Anelastic deformation in Iceland studied using GPS: with special reference to post-tectonic motion following the 1975-1985 krafla rifting episode, and isostatic rebound

Michelle Anne Hofton

How to cite:

Hofton, Michelle Anne (1995) Anelastic deformation in Iceland studied using GPS: with special reference to post-tectonic motion following the 1975-1985 krafla rifting episode, and isostatic rebound. Doctoral thesis, Durham University.

Anelastic Deformation in Iceland Studied Using GPS

with special reference to

post-tectonic motion following the 1975–1985 Krafla rifting episode, and isostatic rebound

by

Michelle Anne Hofton

A thesis submitted in partial fulfilment of the requirements for the degree of Doctor of Philosophy

University of Durham

Department of Geological Sciences

May 1995

Declaration

I declare that this thesis, which I submit for the degree of Doctor of Philosophy at the University of Durham, is my own work and is not substantially the same as any which has previously been submitted for a degree at this or another university.

Michelle Anne Hofton

University of Durham

May 1995

Acknowledgements

Thanks are due to: Pall Einarsson (University of Iceland) and Freysteinn Sigmundsson (Nordic Volcanological Institute) for providing me with my first experience of GPS fieldwork; Professor Dr. Ing. Gunter Seeber, Cord H.-Jahn and Christof Völksen at the Institüt für Erdmessung, University of Hannover, but also the many others from this institute who participated in the 1992 Iceland GPS survey; The scientists at the US Geological Survey, Menlo Park, California, both for their hospitality and their advice throughout my stay, in particular, Al Lindh, Will Prescott, Wayne Thatcher, Bruce Julian, Ross Stein, Grant Marshall and Jerry Svarc; John Rundle at CIRES, University of Colorado at Boulder for providing the original viscoelastic code for adaptation, and extensive suggestions and advice throughout the past two years; Simon Williams and Kathleen Hodgkinson, fellow GPS students at Durham; Neil Goulty; and last (but not least) Gill Foulger, my supervisor, who pushed me through all this.

Funding for this project was provided by N.E.R.C.

ABSTRACT

The Krafla volcanic system is a spreading segment in north Iceland. A decade-long crustal spreading episode began there in 1975. Up to 8 m of rift-normal surface widening occurred along an 80–90 km-long section of the plate boundary. Isostatic uplift in the vicinity of the melting icecap Vatnajökull has been proposed. A third GPS survey of a regional network surrounding the Krafla system was conducted in 1992. In 1991 a 10-point GPS network was installed and measured for the first time around Vatnajökull.

The 1991 and 1992 GPS data were processed using the Bernese software. Differencing the 1992 results with those from 1987 and 1990 revealed a regional deformation field with a maximum, rift-normal expansion rate of 4.4 cm/yr near the rift, decreasing to 3 cm/yr at large distances. The time-averaged spreading rate in north Iceland, 1.8 cm/yr, cannot account for this deformation. The vertical deformation field reveals regional uplift throughout the network area, at its maximum closest to the rift and decreasing with distance.

Three different models were applied to study the postdyking ground deformation, (1) continued opening at depth on the dyke plane in an elastic halfspace, (2) stress redistribution in an elastic-viscous layered medium, and (3) stress redistribution in an elastic layer over a viscoelastic halfspace. The latter model was developed by extending mathematical techniques previously used to model surface displacements resulting from thrust faulting to the case of dyke emplacement.

For the model of continuous dyking at depth, a range of dykes will fit the deformation field. Using the elastic-viscous model, the motion 1987–1990 and 1990–1992 is simulated adequately given the survey errors, but the 1987–1992 deformation is poorly fitted, suggesting that a more realistic geophysical model is required. Using the elastic-viscoelastic approach the effects of historical episodes in the region were subtracted from the observed displacement fields and the remaining motion was modelled as relaxation following the recent Krafla rifting episode. The best-fit model involves a halfspace viscosity of 1.1 x 10^{18} Pa s. The vertical field is noisy, but indicates that the Krafla dyke complex rifted the entire elastic layer. Isostatic uplift centred on Vatnajökull is inconsistent with the vertical deformation field. The model suggests that the Krafla volcano became inactive after 1988/1989. The model further predicts that the width of the "plate boundary zone" is greater than that of Iceland itself.

Contents

Chapter 1

The Structure and Evolution of Iceland

1.1 Introduction

Iceland sits astride the mid-Atlantic ridge and has a unique role in the study of processes taking place at mid-ocean ridge crests. It exhibits the largest exposure of ridge (400 km) and land area (103,000 km^2) anywhere along the mid-ocean ridge system. Over thirty spreading segments and two fracture zones are revealed. The oldest rocks found in Iceland are 16 Ma old and 11% of the land area is covered by lava less than 10,000 years old.

Why does Iceland exist at all, an isolated landmass in the middle of the Atlantic? *Wegener* [1915] suggested that Iceland was a relic of "continental scum" left over from the separation of Greenland and Europe [*Steinthórsson and Jacoby*, 1985], despite his earlier contemplation of a mechanism similar to seafloor spreading [*Wegener*, 1912]. However, that spreading occurs in Iceland, though originally questioned by some [e.g., *Einarsson*, 1967; *Beloussov*, 1970] is now virtually universally accepted and was convincingly demonstrated in action by a recent rifting episode in north Iceland. The spreading process is now the fundamental basis for geological and geophysical interpretations of Iceland, and its subaerial nature there is attributed to excessive lava production caused by an underlying, ridge-centred hotspot.

1.2 Geology

1.2.1 Introduction

Comprehensive reviews of the geology of Iceland are given by *Sæmundsson* [1978, 1979]. The geology is controlled by Iceland's position on the mid-Atlantic ridge, with extensional features predominating. Active deformation occurs in axial rift zones, non-rifting flank zones and along oblique fracture zones that connect offset segments of the axial rift zones either within Iceland or to the submarine mid-ocean ridge axis (Figure 1.1). Flanking the active volcanic zones is a broad expanse of lava-flow sequences that are exposed in cliff or valley sections sometimes over 1 km high.

1.2.2 The Volcanic Pile of Iceland

The volcanic pile of Iceland consists dominantly of tholeiitic basalts (90%) with acid and intermediate rocks constituting 5% and sediment of volcanic origin the remaining 5%. Vertical sections of the volcanic sequence expose up to 1500 m of rocks below which, seismic evidence has shown, a further 2–5 km of extrusives lie. Structural relationships indicate that the pile grew as lenticular units from elongate volcanic systems involving swarms of dykes and fissures usually localised about central volcanoes. Dykes tend to thicken towards the central volcanoes [*Helgason and Zentilli*, 1985]. The majority of faults and dykes are near-vertical, but normal faults with dips of 60–70° also occur, and are believed to be associated with the shallow parts of the fissure swarms.

Detailed studies of deeply eroded, older flood basalts in the east of Iceland show a regional dip of the lava pile towards the active zone, increasing from 0° at the top of the pile to 5–10° at sea level, 1–2 km lower down in the stratigraphic succession. The increase in dip is matched by a thickening of the succession, indicating that the pile tilted as it thickened. Superpositioning indicates that the oldest rocks occur in the furthest northwest and east of Iceland, since age increases with distance from the active zone. This is confirmed by K–Ar dating, with ages in the northwest of around 16 Ma, and 13 Ma in the east.

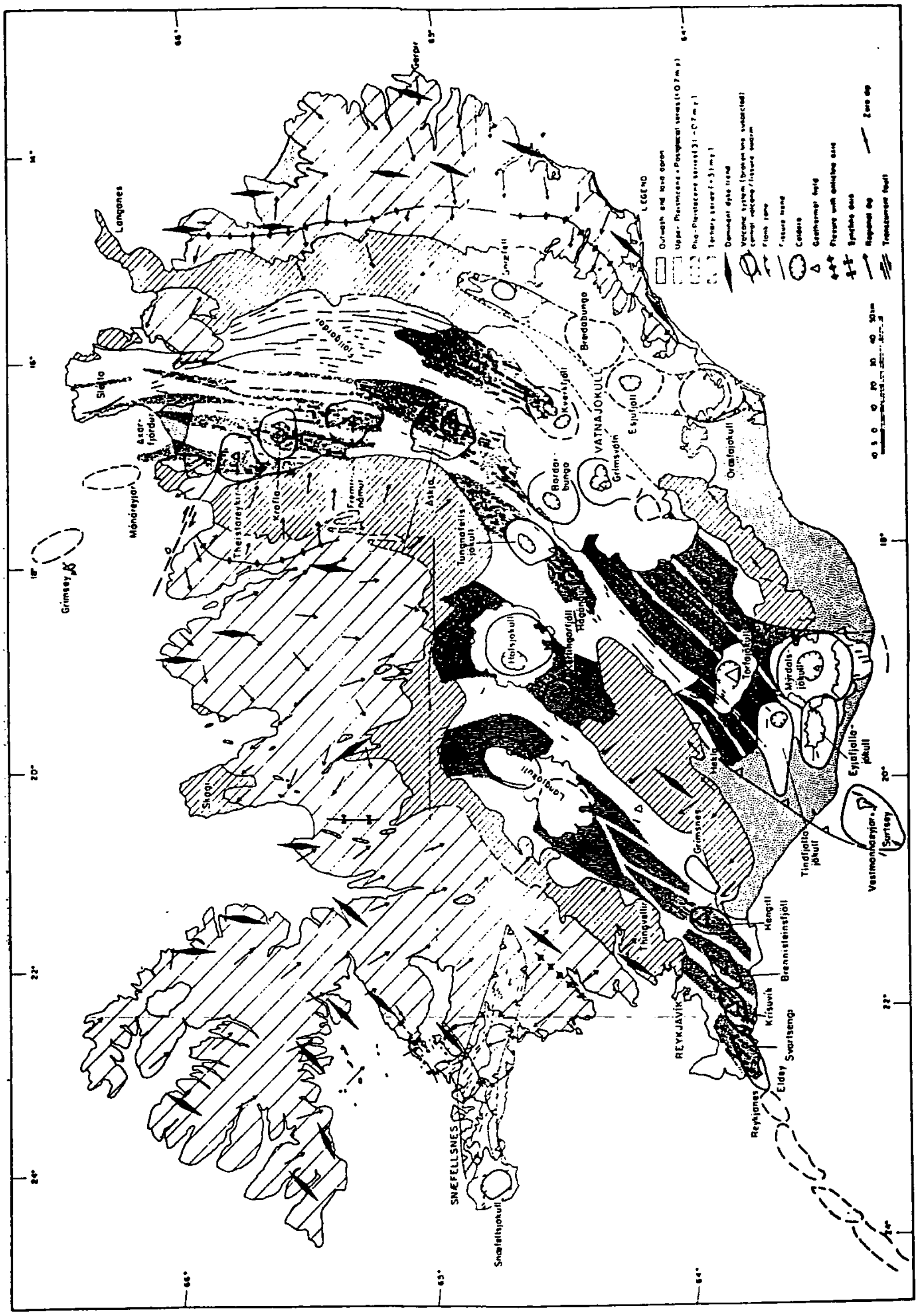

Figure 1.1: Structural geology map of Iceland, after *Sæmundsson* [1986].

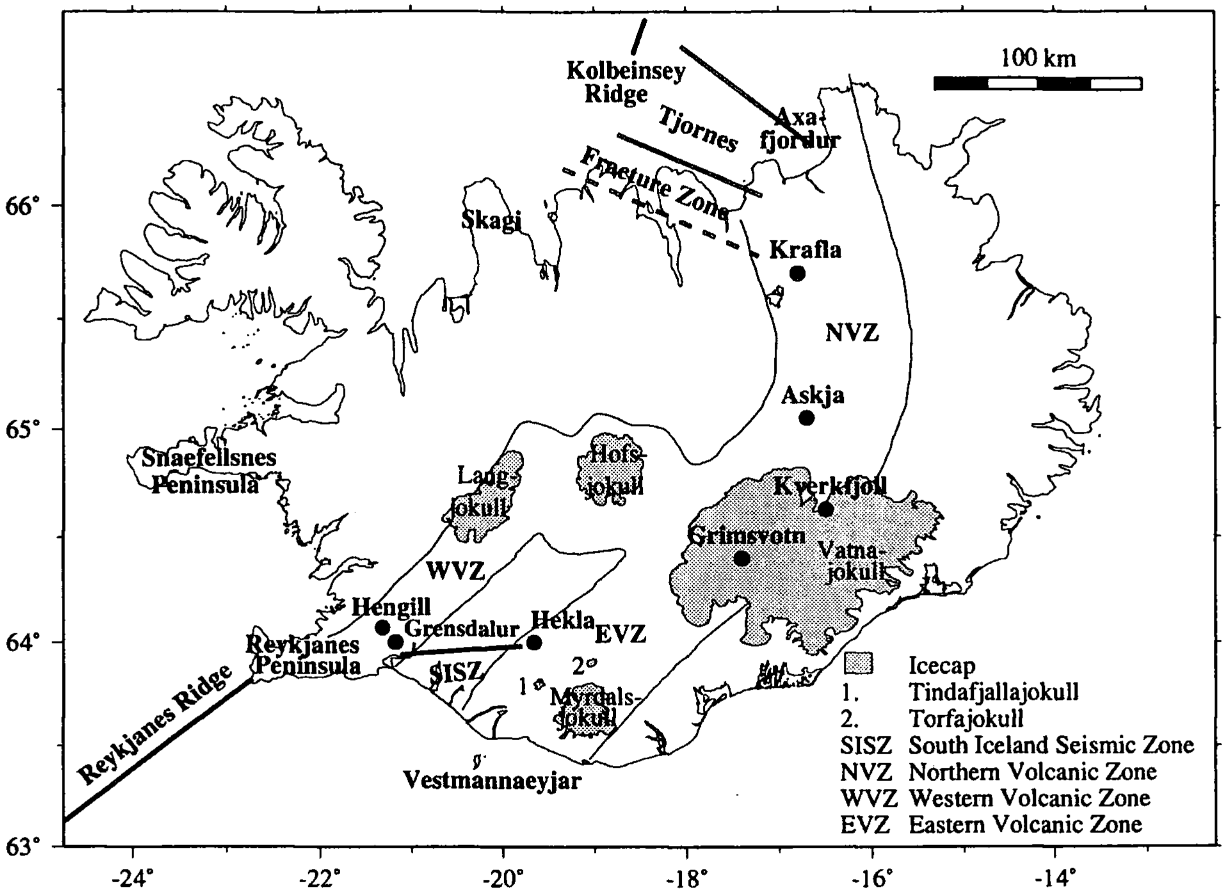

Figure 1.2: Location of place names and areas of Iceland referred to in the text.

1.2.3 The Axial Rift Zones

The axial rift zones are thought to represent the zones where active plate growth is taking place. Their structure is dominated by *en échelon* fissure swarms up to 5–10 km wide and 100 km long. The trend of the swarms is variable but tends to be fairly uniform within each branch of the rift zone. The *en échelon* arrays are either left-lateral or right-lateral, depending on the trend of the individual branch with respect to the direction of relative plate separation (which is near N100°E [*Minster and Jordan*, 1978]). Sinuous, branching, often *en échelon* volcanic fissures and non-eruptive gaping cracks are the dominant surface features of the fissure swarms. Normal faults with dips of greater than ~60° and displacements of 1–100 m also occur. Dyke thicknesses range from less than 1 m to greater than 20 m, but are usually in the 1–3 m range.

Most of the fissure swarms pass through central volcanoes, and together constitute a “volcanic system”. The central volcanoes are the locus of most frequent eruptions and maximum lava production. About one half of the active central volcanoes in the axial rift zones have developed calderas, with diameters of 5–10 km. Caldera collapse is related to explosive eruptions producing sheets of ash or airfall tuffs (e.g., Krafla, Tindafjallajökull, Askja (Figure 1.2)) and to the withdrawal of magma from underlying chambers (e.g., Askja, Grimsvötn (Figure 1.2)). Basaltic flows from central volcanoes are composed of either olivine-poor tholeiites, forming aa lavas, or olivine-rich tholeiites, forming thick pahoehoe flows. The highly fluid nature of these lavas favours the formation of a volcano with gently sloping flanks (unless the eruption occurs subglacially). The axial rift zones contain many large lava shields composed mainly of olivine tholeiites, indicating that they have been fed by subcrustal magma sources. Many of the central volcanoes are also associated with persistent high-temperature geothermal areas, suggesting relatively shallow, long-term intrusive activity.

A certain degree of uniformity in the volcanic processes during the last 10–15 Ma is envisaged by *Pálmason* [1980]. A two-dimensional steady-state plate-tectonic kinematic model of Iceland describing the overall, time-averaged movements of solid crustal elements produced during the accretion process, predicts that the evidence for active volcanic and tectonic processes in the central part of the active zone gradually disappear into the deeper part of the distant crust with time.

Three axial rift zones currently exist in Iceland. The Western Volcanic Zone (WVZ) extends from the Reykjanes Ridge in the southwest to Langjökull in western central Iceland (Figure 1.2). From here the Hofsjökull zone extends eastwards to Kverkfjöll (Figure 1.2), from where the Northern Volcanic Zone (NVZ) extends northwards to Axarfjördur and the Eastern Volcanic Zone (EVZ) extends southwestwards towards the Torfajökull–Vestmannaeyjar flank zone (Figure 1.2).

1.2.4 The Flank Zones

Three active volcanic zones occur that have poorly developed extensional features and are located outside the main axis of accretion. These are the Snæfellsnes volcanic zone, the Torfajökull to Vestmannaeyjar section of the Eastern Volcanic Zone, and the Öræfajökull to Snæfell volcanic zone in southeast Iceland (Figures 1.1 and 1.2). Their volcanic products lie unconformably upon older volcanics that suffered erosion before the volcanism started. Most of the central volcanoes of the flank zones are large stratovolcanoes, many with summit craters and sometimes a caldera. The rate of heat flow in the flank zones is much lower than in the axial rift zones.

The total volume of lava erupted within the neovolcanic zones in the last 10,000 years is estimated at 400–500 km^3 [*Thorarinsson*, 1965; *Jakobsson*, 1972], 85% within the axial rift zones and 15% in the flank zones [*Jakobsson*, 1972].

1.2.5 The Fracture Zones

The South Iceland Seismic Zone (SISZ) (Figure 1.2) connects the Reykjanes Peninsula with the southern end of the Eastern Volcanic Zone, and the Tjörnes Fracture Zone (TFZ) (Figure 1.2) connects the axial rift zone in northern Iceland with the offshore mid-Atlantic ridge segment, the Kolbeinsey Ridge (Figure 1.2). They display a variety of tectonic features along their strike, including oblique spreading segments in *en échelon* arrays as well as older crust broken up by active faulting. Marine geophysical studies also reveal some morphological similarities between oceanic fracture zones and the fracture zones onland in Iceland, enabling a tentative analogy to be drawn between the two.

1.3 Geophysics

1.3.1 The Seismicity of Iceland

The plate boundary in Iceland is seismically active. Figure 1.3 shows the epicentres and focal mechanisms of earthquakes which occurred in the Iceland area during the period 1963–1987. Most large earthquakes in Iceland occur within the two transform zones (the SISZ and TFZ), which are defined primarily by their seismicity, earthquake focal mechanisms and configuration with respect to the spreading axes [*Sykes*, 1967; *Ward*, 1971; *Tryggvason*, 1973]. These two zones are responsible for the largest magnitude earthquakes in Iceland, with magnitudes exceeding 7 (compared to a maximum of up to about 6 for events occurring within the rift zones) [*Einarsson*, 1991]. Plate kinematic considerations suggest right-lateral strike-slip

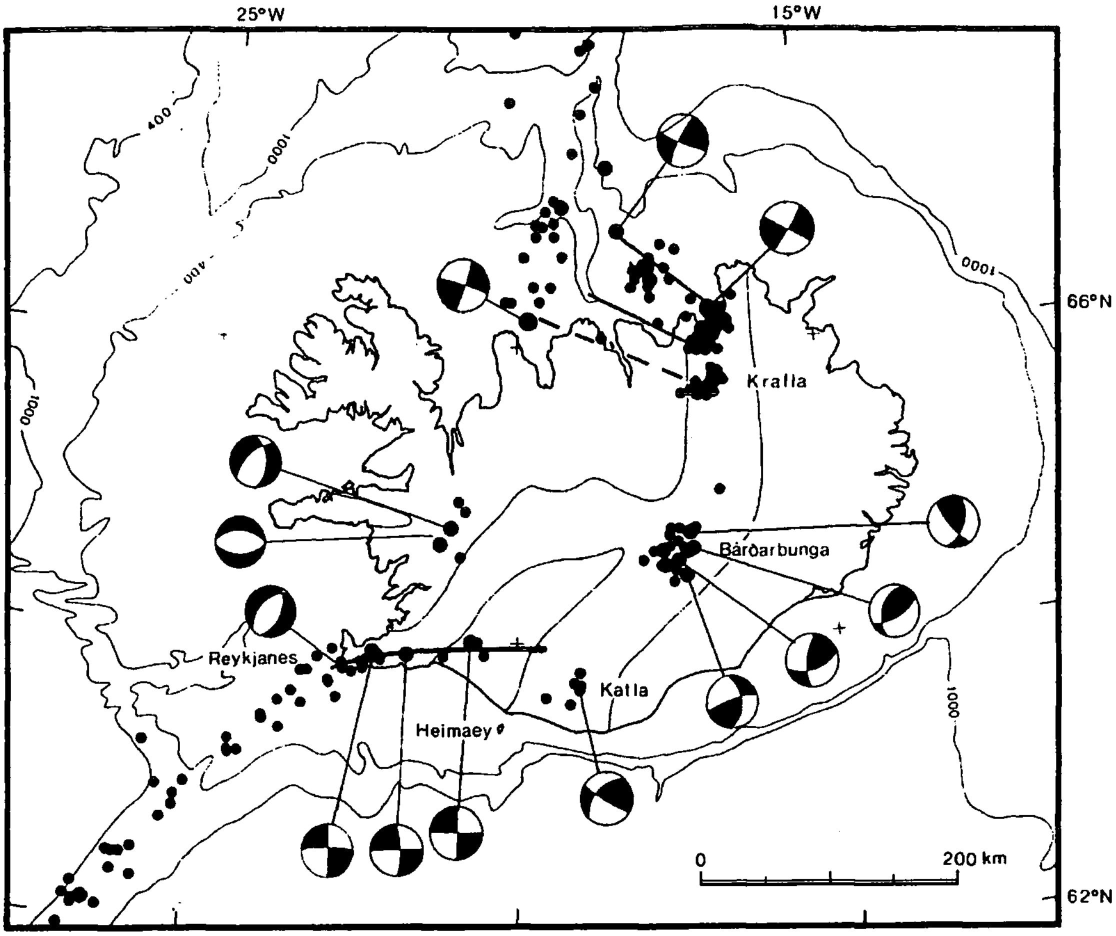

Figure 1.3: Epicentres and single event focal mechanism solutions in the Iceland area. Epicentres are taken from the PDE lists of the US Geological Survey for the period 1963–1981. Only epicentres determined with 10 or more stations are included. Larger dots are events of $M_b=5$ and larger. Focal mechanism solutions are shown schematically in lower hemisphere stereographic projection on the focal sphere. Compressional quadrants are black, after *Einarsson* [1991].

motion in the TFZ and left-lateral strike-slip motion in the SISZ. Focal mechanisms of earthquakes, and the strike of seismic lineations in the TFZ, confirm the right-lateral transform nature of this zone [*Einarsson*, 1991] and that motion is being taken up along three, northwest trending, subparallel faults (Figure 1.3). These faults, from northwest to southeast, are known as the Grimsey, Husavik and Dalvik faults. However, in the SISZ, the destruction areas of individual earthquakes and surface faulting show that each event is associated with faulting on a north–south striking plane. Right-lateral faulting on such planes is a candidate interpretation of focal mechanisms there, so the overall, regional left-lateral transform motion along this zone thus appears to be accommodated by right-lateral faulting on many parallel, north-south faults. Anticlockwise rotation of the blocks between them has been proposed [*Einarsson*, 1991; *Morgan and Kleinrock*, 1991; *Foulger et al.*, 1993]. Hypocentral depths in the SISZ are in the range 0 to 9 km at the western end, but extend down to 12 to 14 km in the east [*Stefansson et al.*, 1993].

The Reykjanes Peninsula (Figure 1.2) is a zone of high seismicity and recent volcanism that forms a transition between the Reykjanes Ridge to the west and the Western Volcanic Zone and SISZ to the east. The plate boundary is thought to be defined by a narrow seismic zone that runs along the peninsula. This seismic zone is less than 2 km wide in most places [*Klein et al.*, 1973, 1977]. Earthquakes mostly occur at a depth of 1–5 km and are not located on any one particular fault. They have been attributed to the deformation of a brittle crust above a deep, aseismic deformation zone [*Einarsson*, 1991]. The stress regime is characterised by a northwest-oriented minimum compressive stress, and as dykes are formed, fissures normal to this direction open up [*Einarsson*, 1991].

The area where the Reykjanes Peninsula plate boundary bifurcates into the Western Volcanic Zone and the SISZ is known as the Hengill triple junction, an area of persistent, geothermal seismicity. The seismicity extends over both the active Hengill volcano and the extinct Grensdalur volcano (Figure 1.2), with hypocentres in the depth range 1–7 km [*Foulger*, 1988a,b]. About half of the events have mechanisms that show normal and strike-slip faulting in response to a northwest-oriented minimum compressive stress. Other events indicate the formation of tensile cracks at depth and have been interpreted as resulting from cooling and contraction of hot rock by circulating geothermal fluids.

A close correlation exists between central volcanoes, high temperature geothermal areas and microearthquake activity [e.g., *Ward and Björnsson*, 1971]. It is likely that much of the background seismicity around central volcanoes is a consequence of the geothermal processes occurring at these sites. However, other seismogenic processes occur, e.g., magma chamber deflation or inflation, magma movements at depth and increase in pore pressure due to glacial melting [*Einarsson*, 1991].

Intraplate earthquakes, not directly related to the plate boundary, also occur. [*Einarsson*, 1991]. One group of such events occurred west of Langjökull (Figures 1.2 and 1.3) and was associated with internal deformation of the North American plate. Most of the hypocentres were at depths of 0 to 8 km but some events extended down to 10 km, indicating that fracturing extended through most of the crust [*Einarsson*, 1989]. A second group of intraplate earthquakes occurred on the insular shelf off eastern and southern Iceland and are thought to have resulted from differential cooling in the crust across the shelf edge [*Einarsson*, 1989, 1991].

1.3.2 The Seismic Structure of Iceland

Over 80 low-resolution (1–4 km station spacing) refraction profiles were analysed in a traditional way by *Pálmason* [1971], who compiled an average velocity model for Iceland. This model has four crustal layers and an upper mantle with an anomalously low P-wave velocity of 7.2 km/s. The velocities of the crustal layers correspond closely to those in oceanic crust. Layer 0, consisting of recent lava flows, has a maximum thickness of 1000 m and has the lowest P-wave velocities of 2.0–3.3 km/s. Layer 1, consisting mainly of highly porous young basalt lavas, has an average thickness of 1 km and P-wave velocities of 4.1 km/s. Layer 2, composed mainly of flood basalts, has an average thickness of 2.1 km and a P-wave velocity of 5.2 km/s. Layer 3 has a P-wave velocity of 6.5 km/s, consists of sheeted dykes and gabbros, and is 4–5 km thick (thicker in northern Iceland). The thicknesses of these layers varies considerably over Iceland with the depth to the base of layer 2 being between 3 and 10 km, and total crustal thickness probably between 10 and 15 km [*Pálmason*, 1971; *Flóvenz*, 1980; *Flóvenz and Gunnarsson*, 1991].

Flóvenz [1980] reanalysed the refraction data, modelling waveforms using synthetic seismograms, and interpreted the results in terms of a structure with velocity gradients rather than layers with constant velocities. The results showed that the Icelandic crust can be divided into two parts, the upper crust, with a velocity continuously increasing with depth (corresponding to layers 0, 1 and 2), and the lower crust with an almost constant velocity (corresponding to layer 3). In this model, the P-wave velocity increases rapidly with depth in the velocity range 2.0–3.5 km/s, followed by an interval with an approximately constant gradient of 0.57 s^{-1} down to the 6.5 km/s level, below which the velocity is virtually constant. Depths to the top of the lower crust do not vary significantly from those predicted for the depth to layer 3 using the layered velocity model (Figure 1.4).

The identification of an anomalously low-velocity upper mantle beneath Iceland arose from several observations. First, the highest upper mantle velocities reported

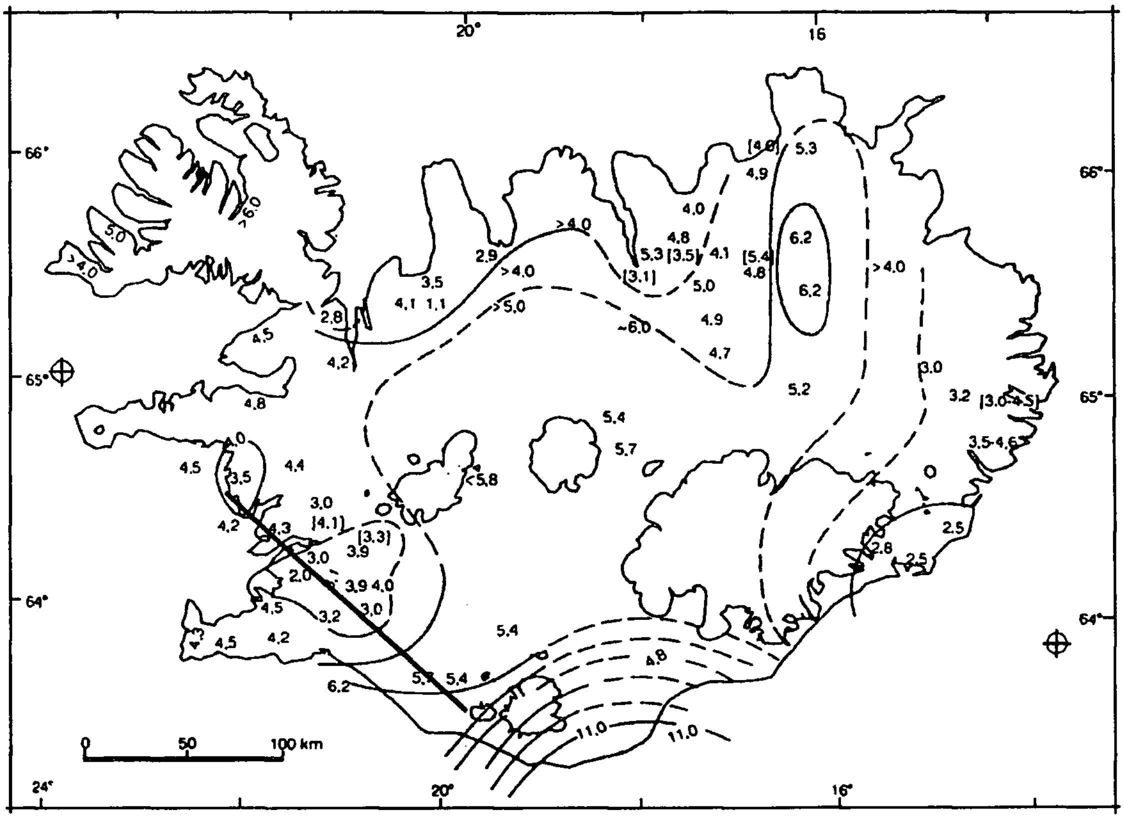

Figure 1.4: Depth to the top of the lower crust in Iceland according to the continuously increasing velocity model of *Flóvenz* [1980]. Data points in brackets are from *Zverev et al.* [1980a,b, 1985] and *Mackenzie et al.* [1982], after *Flóvenz and Gunnarsson* [1991]. The location of a recent refraction study across the WVZ, obliquely through the SISZ to the EVZ is shown by the solid line [*Bjarnason et al.*, 1993].

from older seismic refraction experiments are between 7.0–7.4 km/s [*Båth*, 1960; *Pálmason*, 1971; *Gebrande et al.*, 1980]. Second, teleseismic arrival-time delays measured in Iceland are approximately 1.6 s larger than those measured in Greenland and Europe [*Tryggvason*, 1964; *Long and Mitchell*, 1970] and correspond to upper mantle velocities of 7.4 km/s to depths of 169–240 km. Third, high temperatures at shallow depth beneath Iceland would produce high degrees of partial melt that would depress mantle velocities [*Pálmason and Sæmundsson*, 1974; *Gebrande et al.*, 1980].

In 1977, a long-range seismic refraction experiment (RRISP-77) was carried out along an 800 km-long line across Iceland and along the flank of the Reykjanes

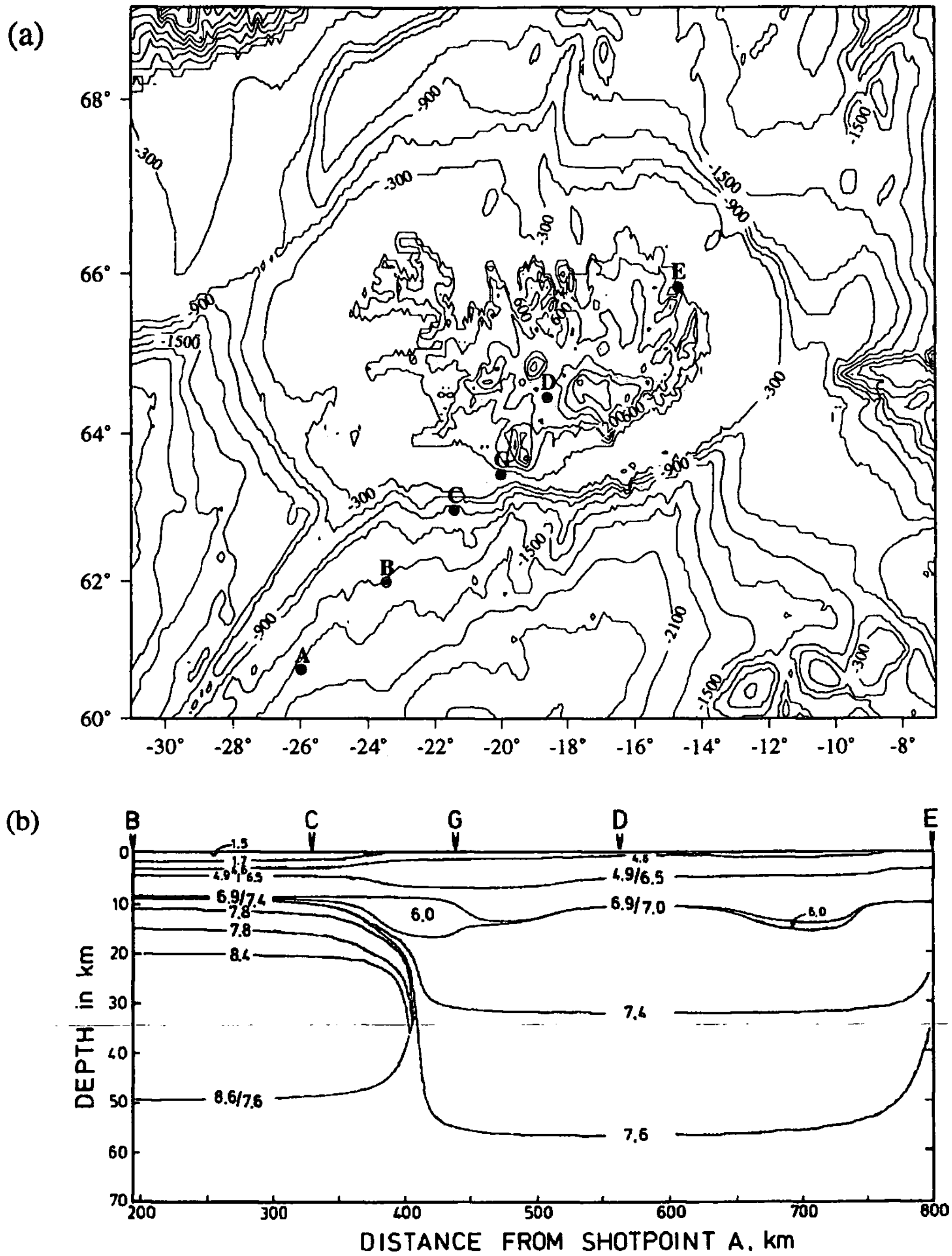

Figure 1.5: (a) Topography and bathymetry of Iceland and its surroundings from the ETOPO5 database [ETOPO5, 1988]. Contours are given every 300 m. Points A to G indicate the positions of shotpoints A to G used in the RRISP-77 project, and are taken from *Angenheister et al.* [1980]. (b) Crust and upper mantle model beneath Iceland and the eastern flank of the Reykjanes Ridge between shot points B to E shown in (a). Distances are given from shotpoint A. Numbers give the velocity at each isocline. The velocity in the two blisters at the base of the crust must be less than 6 kms^{-1} to explain observed travel-time delays, after *Gebrande et al.* [1980].

Ridge (Figure 1.5a). This study determined that 10 Ma old crust on the flank of the Reykjanes Ridge is underlain by low-velocity (7.7 km/s) mantle at 10 km depth and that the velocity increases to 8.2 km/s at 16 km depth [*Goldflam et al.*, 1980]. Beneath Iceland however, upper mantle velocities ranged from 7.0 km/s at the base of the crust at approximately 15 km depth to 7.4 km/s at 30 km depth [*Gebrande et al.*, 1980] (Figure 1.5b). The RRISP-77 experiment thus confirmed interpretations of the relatively normal crustal and upper mantle structure of the Reykjanes Ridge and the anomalously low-velocity upper mantle under Iceland. A normal V_P/V_S velocity ratio of 1.76 was found within the crust, but this ratio was found to reach unusually high values of between 1.96 to 2.2 in the anomalous upper mantle beneath Iceland [*Gebrande et al.*, 1980], probably indicating flow-related anisotropy.

A more recent refraction study along a profile running across the WVZ and obliquely through the SISZ to the western edge of the EVZ, showed a crustal thickness in south Iceland of 20–24 km [*Bjarnason et al.*, 1993] (Figures 1.2 and 1.4). In this interpretation, the P-wave velocity increases smoothly from a surface value of 3.5 km/s to 7.2 km/s at ~22 km depth, beneath which it jumps to 7.7 km/s. This interface at 22 km depth was interpreted as the Moho. The thick crust predicted by this study is in sharp contrast with the results of earlier studies, which determined thicknesses of 7 to 11 km (Figure 1.4) in the same area. However, it is in agreement with theoretical models of geochemical upper mantle melting modes [*McKenzie*, 1984] and rare-earth isotopic inversions [*White et al.*, 1992], which predict 20–30 km thick crusts at hotspots [*Menke and Levin*, 1994].

The seismic structure of the Kolbeinsey Ridge has not been studied in detail [*Flóvenz and Gunnarsson*, 1991]. The structure of the Iceland-Faeroes ridge (southeast of Iceland) is well determined and has a crustal structure similar to that of Iceland, but with a thicker crust (28–35 km) and a subcrustal velocity of 7.8 km/s [*Zverev et al.*, 1976; *Bott and Gunnarsson*, 1980].

1.3.3 Structure From Magnetotelluric Data

Magnetotelluric (MT) measurements made at about 70 sites in Iceland have been used to study lower crustal and upper mantle electrical properties [*Hermance*, 1973; *Hermance et al.*, 1976; *Thayer et al.*, 1981; *Beblo and Björnsson*, 1978, 1980; *Beblo et al.*, 1983]. These measurements have revealed the presence of a regional, low-

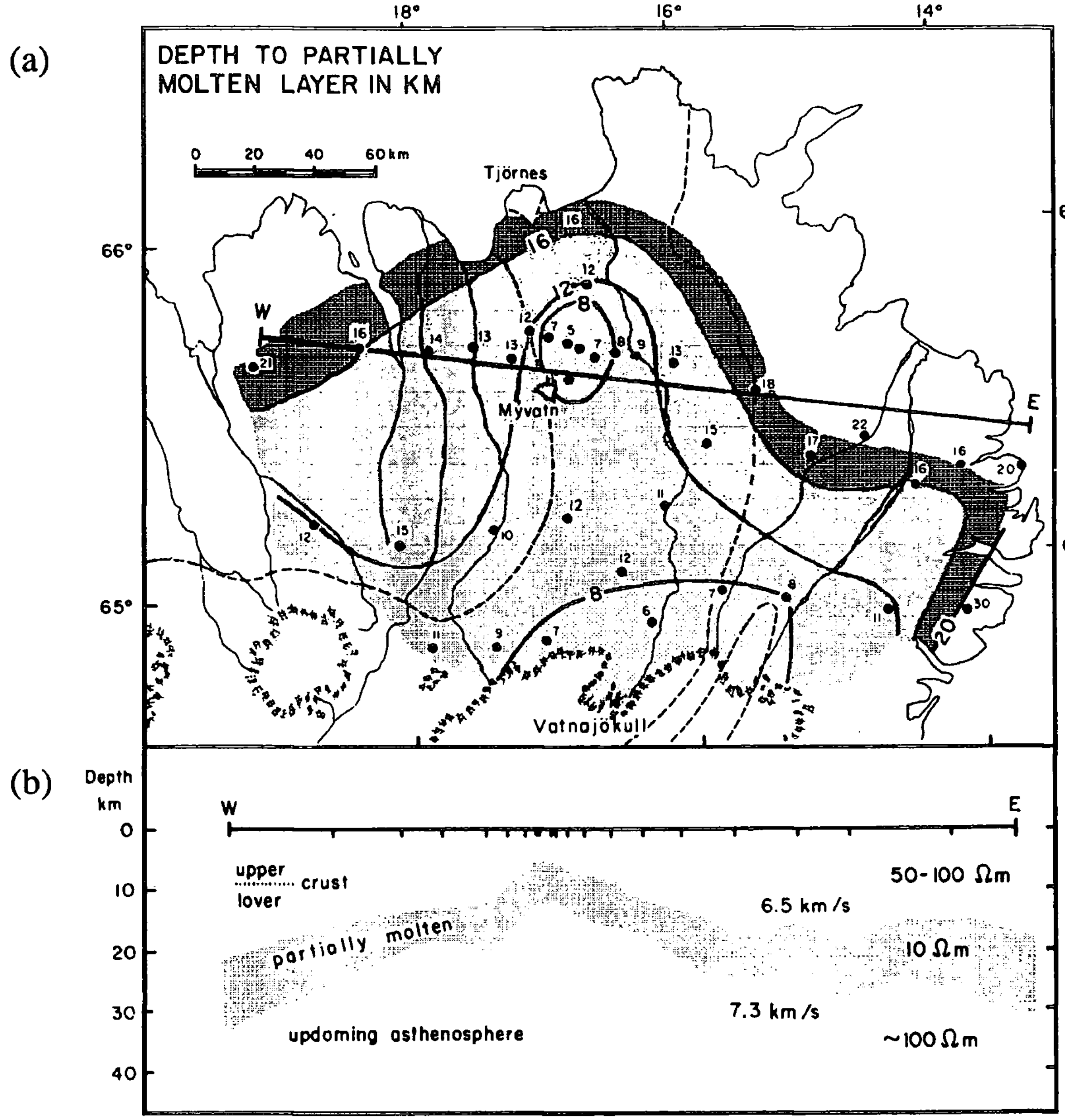

Figure 1.6: Depth to the low resistivity layer in northeast Iceland, thought to correspond to a subcrustal layer of partial melt, after *Björnsson* [1985].

resistivity layer beneath Iceland. In northeast Iceland it lies at a depth of 10 km beneath the axial rift zone, increasing to 20–30 km outside of this zone, and is about 5 km thick [*Beblo and Björnsson*, 1978, 1980; *Beblo et al.*, 1983]. It has a resistivity of about 10 Ωm. Figure 1.6a shows the depth in kilometres to the top of the low-resistivity layer in northeast Iceland. One interpretation of the observations is that basaltic partial melt is migrating upwards and accumulating below Iceland at the crust-mantle interface, an explanation that is supported by laboratory experiments [*Beblo and Björnsson*, 1978]. The region below the low-resistivity layer has a resistivity of about 100 Ωm and is interpreted as partially molten, ultramafic material. A temperature of 1000–1100°C is inferred for the low-resistivity layer.

Beblo and Björnsson [1978] concluded that increasing depth to the partially molten layer with increasing distance from the axial rift zone indicated crustal thickening with age (Figure 1.6b). This agrees with models of the geological structure. The crust is thinner beneath the axial rift zone (~8–10 km) and thickens to over 20 km elsewhere [*Björnsson*, 1985]. The degree of partial melt in the low-resistivity layer is thought to be at least 5% but may be as high as 20% [*Beblo et al.*, 1983] or even 23% [*Schmeling*, 1985]. It must therefore have a very low viscosity [*Björnsson*, 1985]. A second explanation for the low-resistivity layer beneath Iceland is that it is caused by small amounts of highly conductive mineral phases at depth [*Duba et al.*, 1994].

1.3.4 Other Geophysical Research

Iceland is characterised by a bowl-shaped, 100 mGal Bouguer gravity low centred in the northwestern Vatnajökull region (Figure 1.2) [*Einarsson*, 1954], which indicates a major mass deficit in both the crust and mantle [*Hermance*, 1981]. An underplating mechanism and an Airy-type isostatic compensation model, has been used to explain the observations [*Hermance*, 1981]. In this mechanism low density, mantle-derived melt accumulates at the base of the crust beneath the neovolcanic zone and accretes to it as the plates move apart, a model that is in agreement with the observation that the crust thickens with age [e.g., *Pálmason*, 1971; *Beblo and Björnsson*, 1978].

Magnetic anomalies, identifiable northwest and southeast of Iceland, have not

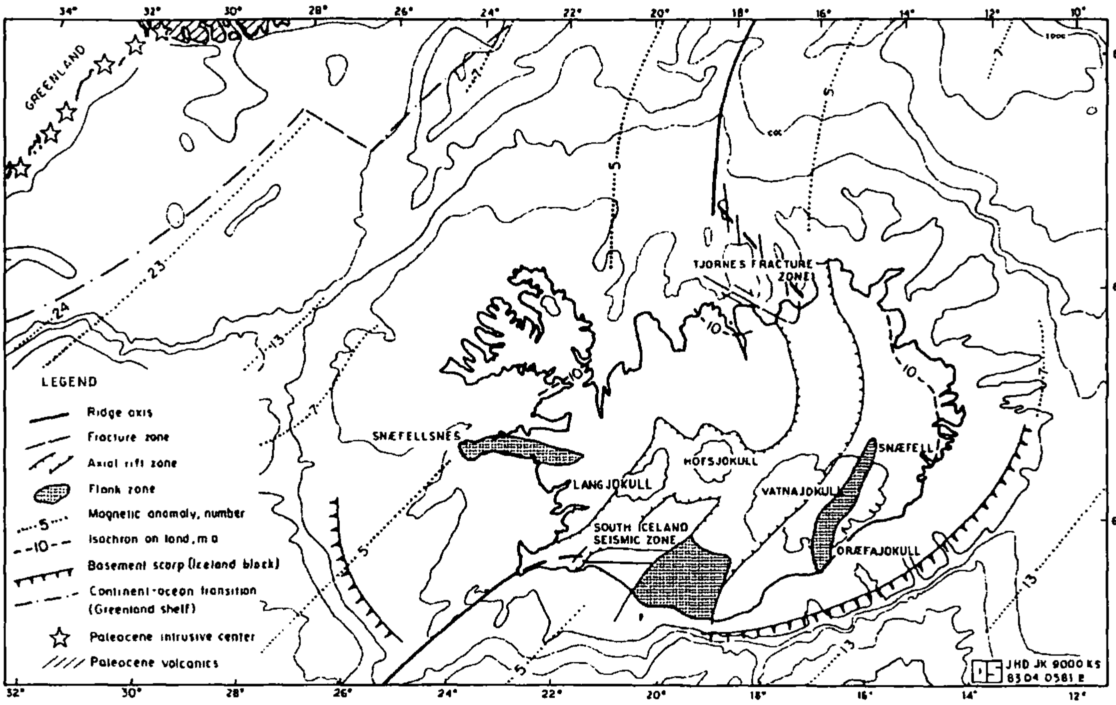

Figure 1.7: Simplified map of the Iceland block showing marine magnetic anomalies, after *Sæmundsson* [1986].

been traced on Iceland, with the exception of anomaly 5 (10 Ma) that is identifiable in the north, northwest and east [*Talwani and Eldholm*, 1977] (Figure 1.7). Magnetic-stripe patterns are obscured by extensive lava flows and by the frequent plate boundary migrations that have occurred on land since anomaly 5 time. The NUVEL-1A global model [*DeMets et al.*, 1994], using data on marine magnetic anomalies, transform fault azimuths and earthquake slip vectors from all major spreading, destructive and transform plate boundaries in the world, predicts that present-day expansion of 1.8 cm/yr is occurring in Iceland.

1.4 The Evolution of Iceland

1.4.1 The Icelandic Hotspot

Several diverse observations indicate that the normal process of crustal accretion which occurs on adjacent sections of the mid-Atlantic ridge is joined by another dynamic process at Iceland. These observations include the high topography of

Iceland, the anomalously thick crust, the culmination of intensity of volcanism in central Iceland and the ~120 km easterly offset of the axial rift zones in Iceland relative to the submerged mid-Atlantic ridge. Geochemical variations in trace-element and isotope compositions of Icelandic rocks compared with those of the oceanic crust also occur, referred to as the Icelandic geochemical anomaly. These observations can be explained by a model of crustal accretion over a mantle plume.

1.4.2 The Evolution of the Icelandic Platform

Iceland and its insular shelf form part of a transverse ridge which crosses the North Atlantic from Greenland to the Faeroe Islands (Figure 1.8) [*Bott*, 1974]. Other components of the ridge are the Iceland-Greenland ridge and the Iceland–Faeroes ridge. The Iceland–Faeroes ridge has crustal seismic velocities similar to those beneath Iceland [*Bott and Gunnarsson*, 1980] but the crust is 30–35 km thick, one of the thickest sections of oceanic crust in the world, and more than four times thicker than normal oceanic crust [*Bott*, 1983b]. The upper mantle beneath the Iceland–Faeroes ridge does not exhibit the exceptionally low seismic velocities observed beneath Iceland and it is believed that this ridge formed at the mid-Atlantic ridge under the influence of the Icelandic hotspot during the early stages of opening of the North Atlantic [e.g., *Bott*, 1983a,b; *Vink*, 1984]. The large crustal thickness can then be attributed to either unusually intense magma differentiation from the mantle during the early evolution of the North Atlantic [*Bott*, 1983a], to subsequent underplating [*Bott*, 1983b], or to lateral flow from the hotspot [*Vink*, 1984].

A reconstruction of marine magnetic anomalies suggests a three-stage evolution history for the Greenland–Faeroes ridge [*Nunns*, 1983]. From 55–44 Ma, a major transform fault existed along the northern edge of the Greenland–Faeroes Ridge, across the Aegir spreading axis to the north and Reykjanes Ridge to the south. Between 44 Ma and 26 Ma, a ridge-ridge-transform triple junction formed, as the Jan Mayen microcontinent separated from Greenland, and sea floor spreading proceeded along the Aegir axis to the north and the new Kolbeinsey axis to the west. After 26 Ma, the Aegir axis became extinct and spreading north of Iceland was taken up on the Kolbeinsey Ridge. At the latitude of Iceland the spreading ridge was displaced eastwards in response to the position of the hotspot that was east of

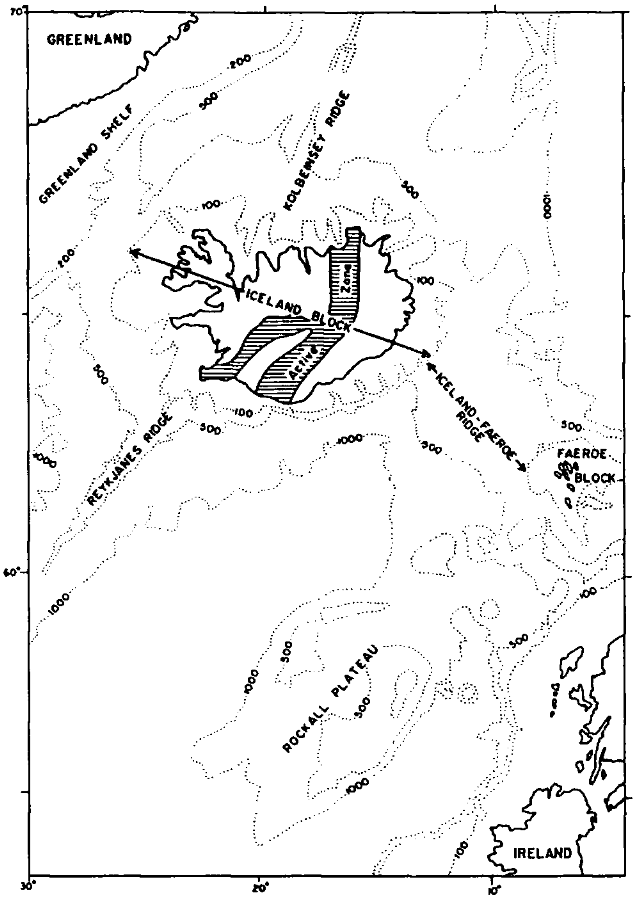

Figure 1.8: The Icelandic platform, adapted from *Bott* [1974].

the Reykjanes and Kolbeinsey Ridges. The Icelandic platform subsequently built up around these ridges asymmetrically [*Bott*, 1985].

The plate tectonic evolution of the north Atlantic has also been reconstructed using magnetic isochrons and a fixed hotspot reference frame [*Vink*, 1984]. In this model, material from the hotspot is assumed to be channelled to the closest section of the mid-ocean ridge (Figure 1.9). According to this reconstruction, the formation of the Iceland–Faeroes ridge was initiated when the hotspot, situated beneath Greenland, started to feed the mid-Atlantic ridge, and was completed when the hotspot emerged from beneath Greenland at about 36 Ma (in contrast to the model of *Nunns* [1983]) and the spreading ridge jumped westwards in response. The Greenland–Iceland section of the Greenland–Faeroes Ridge had been formed by about 20 Ma, since which time a series of eastwards ridge jumps repeatedly repositioned the westward-migrating ridge crest over the hotspot in the neighbourhood of Iceland [*Vink*, 1984].

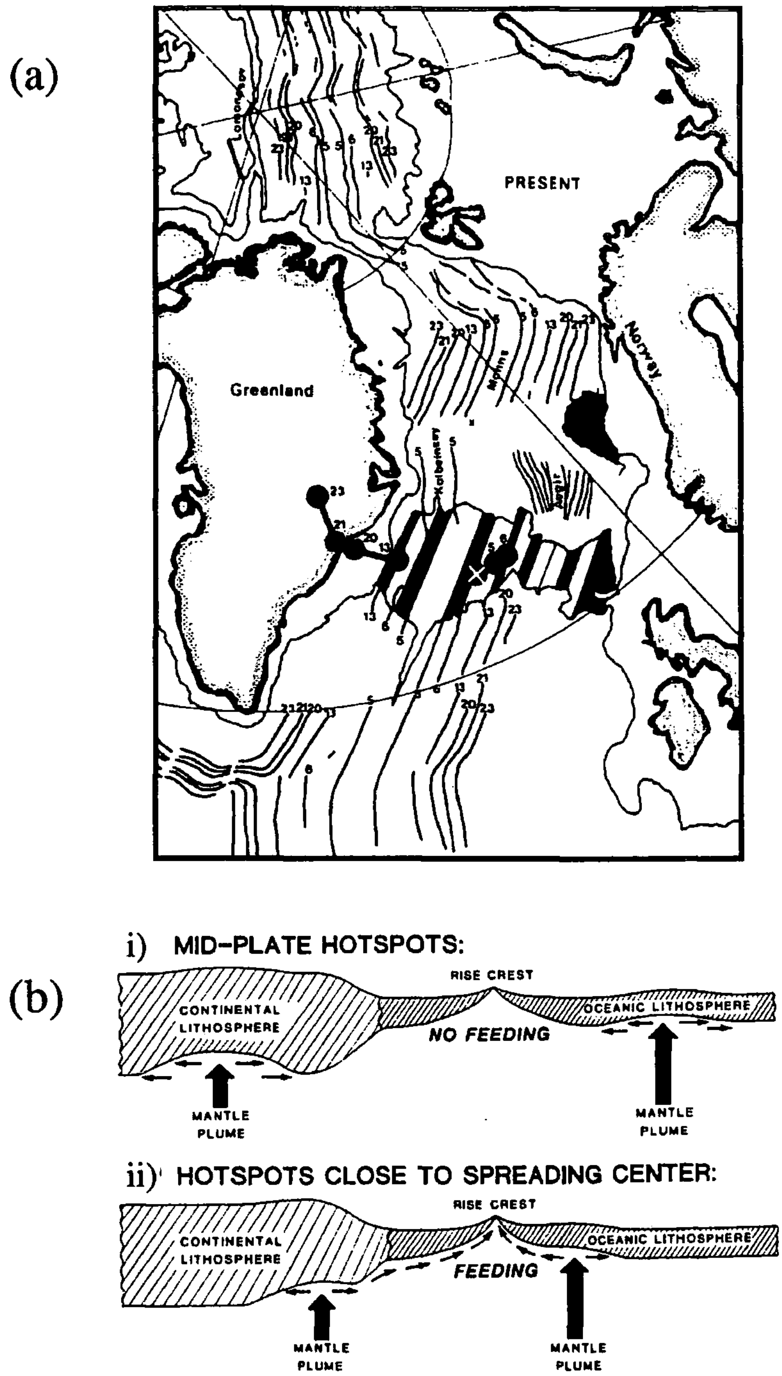

Figure 1.9: (a) The position of the Icelandic hotspot from magnetic anomaly 23 time (55 Ma) to the present. The dots indicate the position of the hotspot through time. The cross marks its present position beneath Iceland. (b) Cross-sectional view of a mantle plume. (i) The heat flux from normal, mid-plate plumes thins the lithosphere. (ii) The proximity of a spreading centre results in excess asthenosphere rising along the base of the lithosphere to the closest section of the spreading centre. In a young ocean basin where the spreading centre is near the ocean-continent boundary, material can feed the spreading centre even though the plume is beneath nearby continental lithosphere, after *Vink* [1984].

1.4.3 Plate Tectonic Evolution

The evolution of the plate boundary in Iceland can be determined to a limited extent only using magnetic anomalies since they are poorly developed on land. *Bott* [1985] suggested that a second active rift zone on Iceland first developed at about 26 Ma when the Aegir spreading axis became extinct. Flexures in the volcanic pile formed by downsagging in response to the piling up of lavas have been used to identify extinct rift zones [*Sæmundsson*, 1979]. Two such zones have been recognised, one on the Snæfellsnes peninsula and the other on Skagi (Figure 1.2). K–Ar dating suggests that volcanism in these zones became extinct at about 6–7 Ma whilst new rift zones were initiated or existing zones to the south and east became more active [*Sæmundsson*, 1979]. As a result the present day Reykjanes–Langjökull zone and NVZ developed (Figure 1.2).

These reorganisations resulted in eastward migration of the rift zones with respect to the mid-Atlantic ridge and occurred alongside the westward drift of the ridge relative to the hotspot [*Sæmundsson*, 1974; *Helgason*, 1985]. The volcanic zone north of the hotspot centre jumped eastwards first and a similar response is currently occurring in the south [*Foulger*, 1988a]. Longitudinal magma flow from the hotspot to the old ridge to the north (the Skagi zone (Figure 1.1)) has died out but is still occurring to the south and maintains activity in the WVZ. The WVZ is slowly being replaced by the EVZ.

A peak in the potassium content of postglacial basalts suggests that the Iceland hotspot is presently centred beneath Kverkfjöll [*Sigvaldason et al.*, 1974] with the Langjökull–Kverkfjöll zone (Figure 1.2) representing its migration trajectory. The Iceland geochemical anomaly (Section 1.4.1) may then be the result of interaction between the hotspot and its own productivity trail [*Oskarsson et al.*, 1985].

The SISZ is thought to be migrating southwards in response to southerly propagation of the EVZ [*Einarsson and Eiríksson*, 1982]. *Sæmundsson* [1979] has suggested alternatively that the SISZ may represent an early stage of the formation of an oblique rift axis that will eventually connect the Reykjanes Peninsula to the southern part of the EVZ.

1.5 Recent Glacial History

At present glaciers and icecaps cover 11,260 km^2 of Iceland or 11%. The biggest icecap is Vatnajökull which covers an area of 8,300 km^2. Icecaps completely covered Iceland several times in recent geological history [*Einarsson and Albertson*, 1988]. During the last (Weichselian) glaciation, the island was covered by an icecap which, at its maximum, was somewhat larger than the current size of Iceland. Ice retreat began around 13,000 BP, followed by postglacial rebound of the Earth's surface which was rapidly completed in about 1,000 years [*Sigmundsson*, 1991].

Since the last glaciation several periods of ice advance and retreat on a much smaller scale occurred. The glacial history of the past 1,000 years has been reconstructed from historical records of fluctuations in the length of outlet glaciers of Vatnajökull, maps and Landsat images [*Sigmundsson and Einarsson*, 1992]. A period of glacial advance is inferred from 900 to 1750, relatively stable conditions from 1750 to 1890, a second period of glacial advance from 1890 to 1930 followed by a period of glacial retreat since 1930 [*Sigmundsson and Einarsson*, 1992]. These fluctuations correspond with climatic variations inferred from historical records and recorded temperature data. From these records it is known that at about the year 1200 climatic cooling began that culminated in a cold period from 1600 to 1900 [*Sigmundsson and Einarsson*, 1992]. This period is known as the Little Ice Age and was a period of worldwide glacial advance [*Grove*, 1988]. From 1890 to 1930 a 1°C warming occurred causing a climatic temperature maximum from 1930 to 1960, since which time the climate has cooled somewhat.

The morphology of volcanic features erupted during glacial periods differs markedly from those formed during interglacial periods. Extensive, flat lava flows formed during interglacial periods, and mounds, ridges of pillow lavas and hyaloclastite rocks characterise subglacial volcanism. Elongate ridges indicate subglacial fissure eruptions, and volcanic table mountains indicate point-source subglacial eruptions.

1.6 Summary

Three distinct morphological units are identified in Iceland; axial rift zones where active plate growth is occurring, non-rifting flank zones, and the surrounding volcanic pile, a monotonous sequence of lava flows which grew from volcanic systems similar to those active today.

The plate boundary in Iceland is seismic and displaced to the east of the mid-Atlantic ridge by two major fracture zones, the left-lateral SISZ in the south and the right-lateral TFZ in the north. These zones generate the largest earthquakes in Iceland. Seismic areas outside these zones are mostly central volcanoes where geothermal processes and magma migration occur. Intraplate earthquakes occur occasionally as a result of internal plate deformation and differential crustal cooling.

The Icelandic crust can be divided into the upper crust, with velocity continuously increasing with depth, and the lower crust with constant velocity. A low-resistivity layer beneath Iceland shallows towards the axial rift zones and the centre of Iceland, and may represent a layer of partial melt at the base of the crust. Geochemistry indicates that the crust is derived from a chemically-anomalous mantle source and, in some areas, from partial melt formed by reworking of the crust.

The existence of Iceland is consistent with excessive volcanism over a ridge-centred hotspot. The hotspot may have started to feed the newly-opened mid-Atlantic ridge from its original position beneath Greenland, and initiated the formation of the Iceland–Faeroes ridge. Migrating eastwards with respect to the plate boundary, it caused the spreading ridge initially to jump westwards in response, leading to the formation of the Greenland-Iceland ridge. Since that time a series of eastwards ridge jumps have progressively repositioned the ridge over the hotspot as the Icelandic landmass developed. The ridge in north Iceland jumped eastwards from the Skagi Zone to form the NVZ. A similar process is currently occurring in the south to form the EVZ. Longitudinal magma flow from the hotspot to the Skagi ridge has ceased but flow is still occurring to the dying WVZ in the south and is thus maintaining activity there.

Two periods of glacial advance, 900–1750 and 1890–1930, have occurred separated by a period of relative stability and followed by glacial retreat up to the present.

Chapter 2

Crustal Deformation in North and East Iceland

2.1 Overview

Major crustal deformation occurs in Iceland, the dynamics and magnitude of which are highly relevant to plate tectonics, in particular crustal spreading. Crucial to our understanding of the deformation is the rate at which the tectonic plates are moving relative to one another. Global models predict that present-day east-west extension of 1.8 cm/yr is occurring in Iceland. These models include the RM2 [*Minster and Jordan*, 1978], NUVEL-1 [*DeMets et al.*, 1990] and the NUVEL-1A [*DeMets et al.*, 1994] models, which use data from marine magnetic anomalies, transform fault azimuths and earthquake slip vectors from all the major spreading and transform plate boundaries in the world, and assume that spreading rates have remained constant throughout the past 10 Ma. The RM2 model predicts relative motion between the North American and European plates of 18.8 ± 1.4 mm/yr at N107.5±2°E and the NUVEL-1 model predicts 19.3 ± 0.5 mm/yr at N106.9±1.2°E. Recent studies showed that the NUVEL-1 model overestimates vectors by ~5% [*Gordon*, 1993], and it has been revised, giving the NUVEL-1A model which estimates 18.5 ± 0.5 mm/yr of spreading at N106.9±1.3°E for Iceland (Table 2.1) [*DeMets et al.*, 1994].

The early continental drift ideas of Wegener implied spreading rates of about 10 to 40 m/yr since they were based on the assumption that Greenland, North America and Europe had separated after the end of the last glaciation, i.e., (as was

Table 2.1: Relative plate motions of the European and North American plates between 65°N 15°W and 65°N 24°W from the RM2 and NUVEL-1 global plate models.

Global Model	Rate mm/yr	Azimuth ° E of N
RM2	18.8 ± 1.4	107.5±2.0
NUVEL-1	19.3 ± 0.5	106.9±1.2
NUVEL-1A	18.5 ± 0.5	106.9±1.3

thought then) in the preceding 50,000 to 100,000 years (see *Vogt* [1986] for summary). Longitude differences, calculated with the aid of radio time signals, between northeastern Greenland and Europe at various times between 1823 and 1927, appeared to support the sense and magnitude of the predicted rates, with a westward drift rate of 0.6 ± 2.4 m/yr calculated by *Wanach* [1926] and 0.32 ± 0.08 m/yr by *Littell and Hammond* [1928].

The modern tectonic view of Iceland began with *Nielsen* [1930] who stated that fissure eruptions and fault structures were "the result of a pull from east to west which has simply split the land into innumerable fissures" (see *Vogt* [1986] for summary). The first effort to measure the extensional rate directly by geodetic means, was made in 1938 by a German expedition. A network of precisely surveyed triangulation points was established across the rift zone in north Iceland [*Niemczyk and Emschermann*, 1943]. A predicted drift rate was made (3.56 mm/yr), based on observations of the widening of fissures splitting postglacial lavas [*Bernauer*, 1943] (see *Vogt* [1986] for summary). This is the same order of magnitude as current estimates of plate motion. The 1938 network was reoccupied and reconstructed in 1964/1965 with considerable improvements in its configuration [*Gerke*, 1974; *Wendt et al.*, 1985].

Distance measurements began in south Iceland across the tip of the Reykjanes Peninsula in 1968 and 1972 [*Brander et al.*, 1976], across the Thingvellir graben in the Western Volcanic Zone in 1967, 1968, 1970, 1971, 1972 and 1973 [*Brander et al.*, 1976; *Gerke*, 1974; *Decker et al.*, 1971, 1976], and across the southern part of the EVZ in 1970 and 1973 [*Decker et al.*, 1976]. These surveys revealed 65 ± 31mm of extension in the 3 year period 1967–1970 in the EVZ [*Decker et al.*, 1971], but no significant motion during the following two years [*Brander et al.*, 1976]. No significant motion was detected in the network in north Iceland around Lake

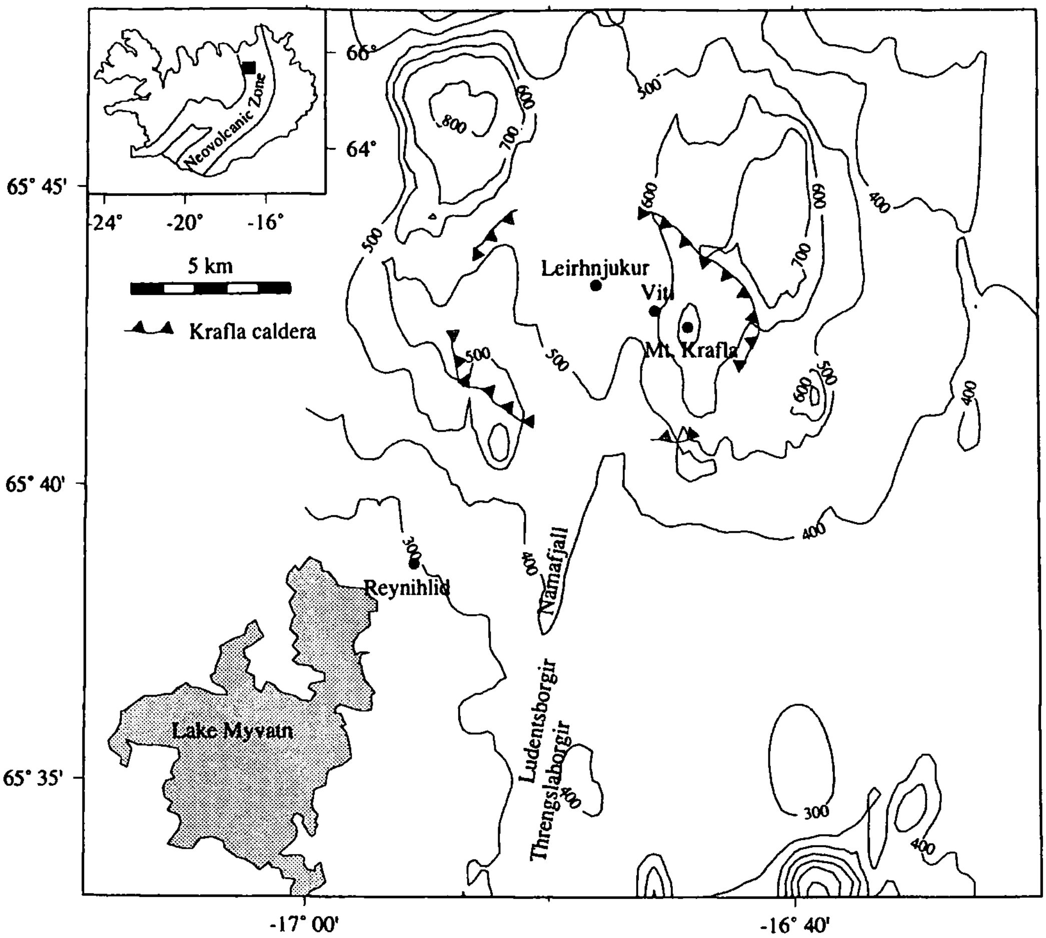

Figure 2.1: Location of places in northeast Iceland commonly referred to in the text. The black box in the inset indicates the location of the main figure.

Mývatn (Figure 2.1) from 1968 to 1972, no more than 3 mm of extension per year in the Thingvellir network during the same period, and a combination of left-lateral motion and extension at ~9 mm/yr at the tip of the Reykjanes Peninsula from 1968 to 1972 [*Brander et al.*, 1976]. These measured extension rates are all much less than those predicted by the global plate models.

Recent advances in surveying technology have made highly accurate, regional scale surveys feasible. Several surveys using Global Positioning System (GPS) satellite surveying techniques have been conducted, including a country-wide survey in 1986 [*Foulger et al.*, 1993], and large regional surveys in 1987, 1989, 1990, 1991, 1992 and 1993 [*Foulger et al.*, 1992; *Heki et al.*, 1993; *Jahn et al.*, 1994; *Hackman*, 1991; *Sigmundsson et al.*, 1992; *Sigmundsson and Einarsson*, 1992; *Sturkell et al.*, 1994]. These surveys covered most densely the Reykjanes Peninsula, the SISZ and the NVZ. Several points in the EVZ were also occupied. They have revealed a picture of crustal deformation in Iceland far more complex than predicted by simple kinematic global models.

2.2 Isostatic Rebound in Southeast Iceland

Load changes on the surface result in deformation of the outer layers of the Earth until isostatic equilibrium is attained. In some areas, e.g., Fennoscandia, the surface is still uplifting in response to deglaciation at the end of the last glacial period. The rate of movement depends on the thickness of the lithosphere, the load distribution, and the rheology of the underlying asthenosphere. Similar uplift took place in Iceland at the end of the last glaciation, but was completed in less than 1,000 years [*Sigmundsson*, 1991]. Marine deposits, 100 m or more above current sea level and 50 km or more from the current coastline, and submerged freshwater peat, reveal the history of ice distribution and vertical movements around Iceland during this time.

Prior to 13,000 BP most of Iceland was covered by an icecap. The icecap retreated to within the boundaries of the present coastline more quickly than the land could uplift in response. Marine organisms colonised deglaciated, submerged coastal areas. The land slowly uplifted and the sea regressed to such an extent that, by about 9,000 BP when isostatic equilibrium was established, relative sea level was 30 m below the present level. Eustatic sea level rise to the present height subsequently occurred. The length of the postglacial-rebound time interval constrains the maximum value of the asthenosphere viscosity to be 1 x 10^{19} Pa s or less [*Sigmundsson* 1991].

Isostatic uplift is believed to be occurring currently in southeast Iceland following deglaciation since about 1930 when the icecap Vatnajökull began retreating in the wake of the Little Ice Age [*Grove*, 1988]. The area and volume of Vatnajökull have decreased by 300 km^2 and 180 km^3 respectively since 1930, inferred from estimates of length changes of outlet glaciers and Landsat images [*Sigmundsson and Einarsson*, 1992]. Modelling the Earth as a Newtonian viscous fluid halfspace overlain by an elastic layer, and assuming a spherical icecap produces 11.4 cm/yr of thinning within the innermost 35 km of the icecap, 23 cm/yr between 35–47.5 km, and 57 cm/yr from 47.5–52.5 km, indicates that the volume decrease should lead to surface uplift immediately around Vatnajökull at a rate of 5–10 mm/yr at the present time and tilt away from the icecap if the viscosity of the asthenosphere beneath Iceland is in the range 1 x 10^{18}–5 x 10^{19} Pa s [*Sigmundsson and Einarsson*, 1992].

2.3 Crustal Spreading at the Krafla Volcanic System

2.3.1 Introduction

The Krafla volcanic system is one of five *en échelon* volcanic systems that together constitute the NVZ. These five systems, from north to south, are the Theistareykir, Krafla, Fremrinámur, Askja and Kverkfjöll systems (Figure 2.2). Each volcanic system consists of a fissure swarm oriented at about N10°E which passes through a central volcano. The direction of plate spreading, deduced from the NUVEL-1A global model [*DeMets et al.*, 1994] is N106°E, about perpendicular to the strike of the fissure swarms. However, the plate boundary, defined by a line joining the central volcanoes [*Björnsson*, 1985], is oblique to the direction of spreading. The NVZ is offset by approximately 120 km to the east from the Kolbeinsey Ridge by the TFZ, a broad zone of sub-parallel seismic lineations and extensional features (Section 1.2.5).

The Krafla volcanic system is characterised by open fissures and faults. Its total length is some 100 km and its width ranges from about 4 to 10 km. The Krafla central volcano has a caldera and is situated just north of the latitudinal mid-point of the swarm. The northern end of the fissure swarm connects with the TFZ in Axarfjördur bay (Figure 2.2). A major rifting episode lasting about a decade started in the Krafla volcanic system in December 1975, providing a unique opportunity to study the spreading process, and in particular the accompanying crustal deformation.

2.3.2 Pre-Rifting Deformation

The 1938 triangulation network in north Iceland, reconstructed and improved in 1964/1965 was remeasured at that time, and again in 1971 and 1975 using EDM (electronic distance measuring) techniques [*Möller and Ritter*, 1980]. The network spanned the fissure swarms of the NVZ for a distance of 110 km east to west (Figure 2.3). The results revealed no significant motion from 1938 to 1965 [*Gerke*, 1974]. Significant contractions of up to 50 cm across the Krafla volcanic system

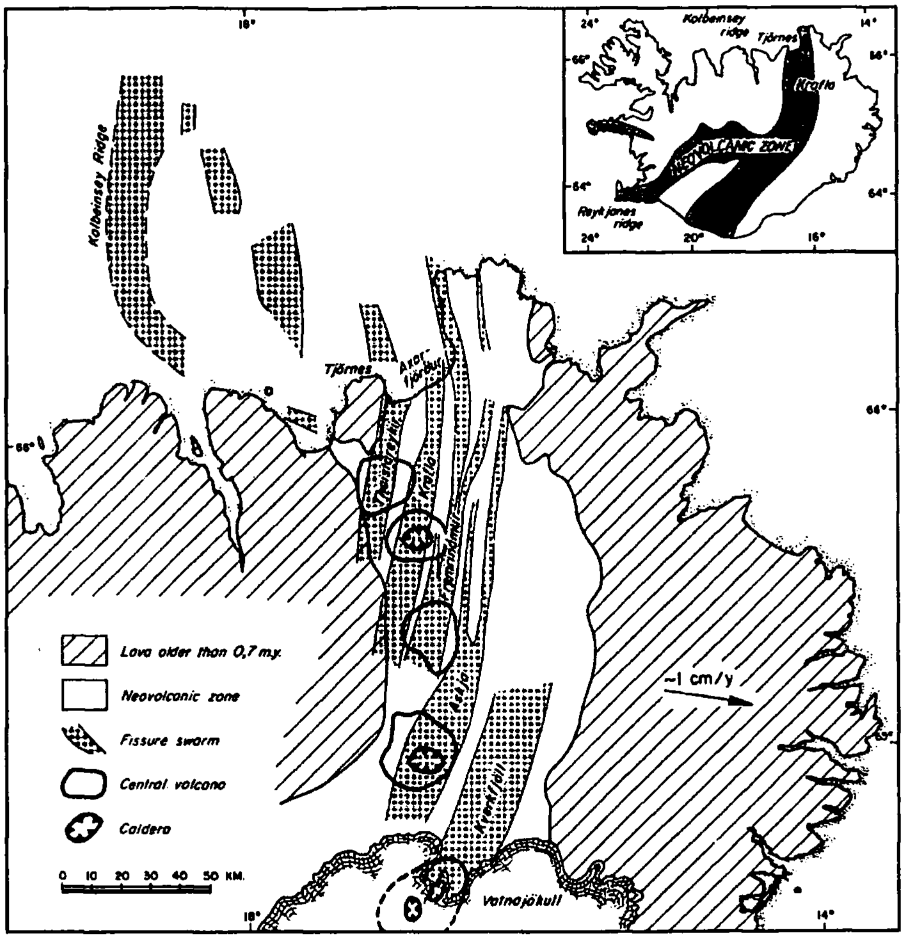

Figure 2.2: Simplified tectonic map of northeast Iceland showing the five elongated, *en échelon* volcanic systems that comprise the rift zone in northeast Iceland. The shaded areas offshore are grabens. The arrow indicates the spreading direction, adapted from *Björnsson* [1985].

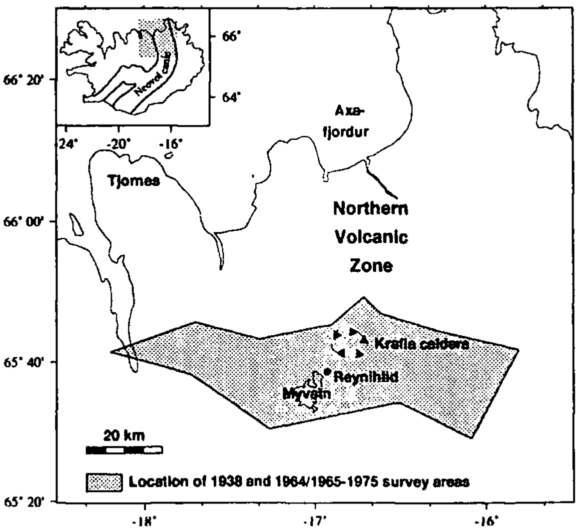

Figure 2.3: Location of the area surveyed in 1938 and between 1964/65–1975 [*Möller and Ritter*, 1980].

were detected from 1965 to 1971. Between 1971 and 1975, the sense of motion reversed and up to 30 cm of expansion occurred, possibly a precursor to the rifting event that followed [*Möller and Ritter*, 1980].

2.3.3 The 1975–1985 Rifting Episode

2.3.3.1 Introduction

During the period 1975 to 1985 the Krafla volcanic system experienced basaltic fissure eruptions, earthquakes, and fissure opening between about latitudes 65°34′N and 66°18′N. About twenty rifting events occurred during the decade-long episode, in short periods of activity every few months. During each event magma flowed rapidly out of a crustal magma chamber underlying the Krafla central volcano into the fissure swarm forming dykes, or, in nine instances, volcanic eruptions. This activity was accompanied by migrating seismicity and ground movements. Between these events the caldera inflated steadily as the magma chamber was filled from below, causing earthquake activity in the caldera floor when the land height rose above its previous maximum. The repeated, sudden extension of the fissure swarm caused extensive faulting and fissuring above the intruded dykes, and resulted in the downthrow of the central part of the fissure swarm and uplift of the flanks.

2.3.3.2 The First Event

The first rifting event started December 20th 1975 and lasted for several weeks. It was preceded by an unusually high level of seismic activity in the Krafla caldera in early 1975, alerting the authorities to the possibility of an eruption and prompting installation of monitoring equipment. On the morning of December 20th continuous tremor was detected close to the caldera. One hour later an eruption began from a 2 km-long fissure in Leirhnjúkur in the centre of the caldera (Figure 2.1). Its vigour decreased rapidly whilst the seismic activity propagated northwards from Leirhnjúkur along the fissure swarm. Within two hours about 40 km of the fissure swarm had been activated. After a few hours the persistent seismicity following the eruption was mainly confined to two separate areas; inside the caldera and in the Axarfjördur region along known faults of the TFZ. There, 42 earthquakes of magnitude 4.5 or larger occurred from December 20th to mid-February. Earthquakes in the Krafla region were between 0 and 4 km deep. The volcanic eruption at Leirhnjúkur proceeded from three craters along a fissure which had been active during a previous eruption, the "Mývatn fires", that accompanied what is now interpreted as a historic spreading episode from 1724–1729 (Section 2.4). The 1975 Leirhnjúkur eruption lasted only 20 minutes except for later minor steam explosions. Within a day only water and steam were being erupted from the craters. The total surface area of erupted lava was 0.36 km^2 [*Björnsson et al.*, 1977].

During this tectonic event down-faulting occurred of a central area of the fissure swarm about 5 km wide (east–west) and 20 km long (north–south). Fissure formation and widening was also observed. Extension across the fissure zone was obvious from the stretching and breaking of telephone lines and fences [*Sigurdsson*, 1980]. The Krafla caldera floor subsided by nearly 2.5 m [*Björnsson et al.*, 1977]. Surface measurements after the event revealed horizontal extension of about 1 m in the Krafla area and 2.0–3.0 m in the Axarfjördur area [*Tryggvason*, 1984]. Relative subsidence of up to 1.5 m within the fissure swarm occurred along with 40 cm of flank elevation [*Sigurdsson*, 1980].

2.3.3.3 Subsequent Activity

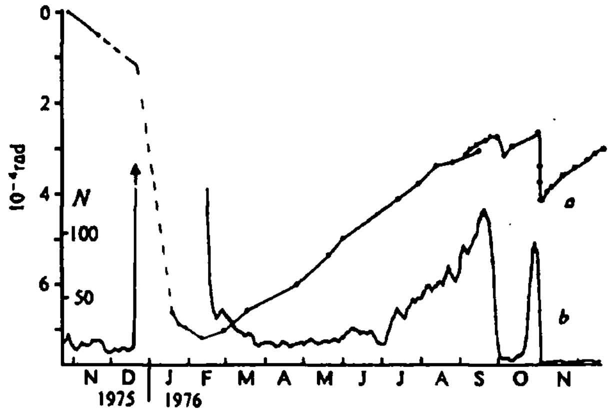

Figure 2.4: Correlation between (a) the north–south tilt of the Krafla power station, and (b) seismic activity within the caldera. Increasing numbers mean tilt down towards the north. N is the five-day running average of the number of earthquakes recorded per day at the seismic station Reynihlid (Figure 2.1) with recorded amplitude above a certain threshold. From 20th December 1975 to 14th February 1976, N was $>$ 130 and most of the time $>$ 1000. The tilt measurements before 20th August 1976 were done by optical levelling, after *Björnsson et al.* [1977].

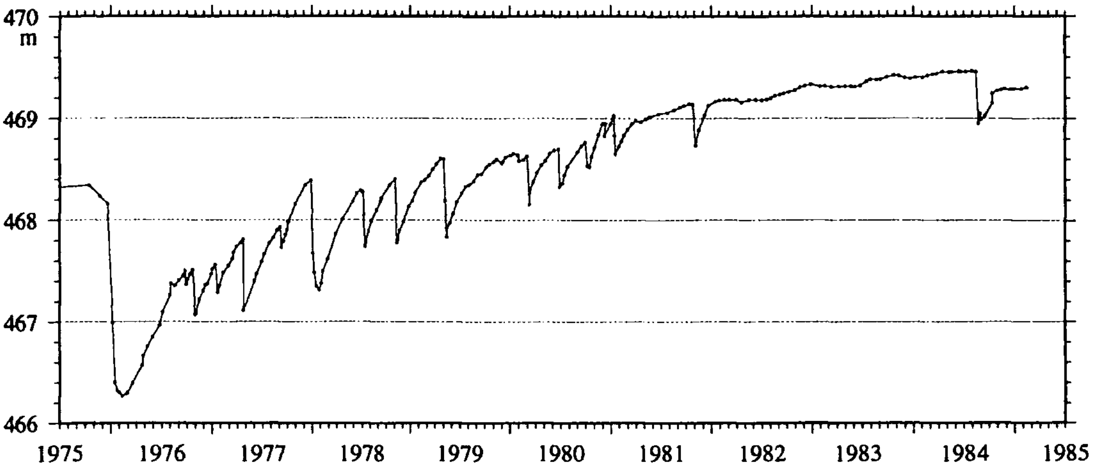

Figure 2.5: Land elevation changes at bench mark FM5596, about 1 km southeast of the centre of the Krafla caldera. The reference benchmark (FM6414) is 20 km away, at the southern end of lake Mývatn (Figure 2.1), adapted from *Jacoby et al.* [1989].

Inflation of the Krafla magma chamber began soon after the end of the earthquake swarm associated with the first rifting event. The rate of uplift, at its maximum near the centre of the caldera, was relatively constant. By May 1976 there was a noticeable increase in earthquake frequency which became more marked until September 28th 1976 when a sudden decrease occurred (Figure 2.4). At the same time rapid subsidence in the Krafla caldera began, lasting 6 days, and amounting to about 25 cm near Leirhnjúkur (Figure 2.5). During the period of most rapid subsidence, bursts of continuous tremor were recorded along with small earthquakes originating in the fissure swarm about 15 km north of the caldera. From this it was concluded that magma had flowed from the Krafla magma chamber north along the fissure swarm to form a dyke. On October 4th the subsidence stopped and the caldera started rising again at a similar rate as before [*Björnsson et al.*, 1977] (Figure 2.5).

This cycle of relatively slow magma-chamber inflation followed by rapid deflation accompanied by seismic activity, fault movements and occasionally volcanic eruptions as dykes were injected into the fissure swarm was repeated numerous times for about 10 years (Figure 2.5). Rifting events occurred only when the caldera was elevated beyond its previous maximum level, i.e., when stress in the magma chamber roof exceeded the previous maximum. Seismic activity in the caldera stopped as soon as the inflation stopped or deflation began. Volcanic tremor accompanied deflation with an amplitude roughly proportional to the deflation rate. Earthquakes

Table 2.2: Magma movements in rifting events, adapted from *Björnsson* [1985].

Subsidence–rifting event (time)	Maximum subsidence at the apex (cm)	Direction of intrusion (N/S of caldera)	Area of extruded lava (km^2)
Dec. 20, 1975 to Feb. 1976	230	N	0.036
Sept 28 to Oct. 4, 1976	17	N+S	
Oct. 31 to Nov. 1, 1976	51	N	
Jan. 20, 1977	32	N	
April 27–28, 1977	81	S	0.001
Sept. 8–9, 1977	24	S	0.5
Nov. 2, 1977	3	N	
Jan. 7–8, 1978	119	N	
July 10–12, 1978	64	N	
Nov. 12–15, 1978	72	N	
May 13–18, 1979	88	N	
Dec. 6–10, 1979	3	?	
Feb. 10–13, 1980	11	S	
March 16, 1980	53	N+S	1.3
June 20, 1980	2	?	
July 10–18, 1980	43	N	5.3
Oct. 18–23, 1980	29	N	11.5
Dec. 22–27, 1980	16	N	
Jan. 30 to Feb. 4, 1981	44	N	6.3
Nov. 18–23, 1981	47	N	17
Sept. 8–14, 1984	60	S	?
Sum total	10.89 m		42 km^2
Estimated total volume	0.6 km^3		0.1 km^3

then propagated from the caldera along the fissure swarm with the propagating dyke tip [*Einarsson*, 1991]. Rifting occurred predominantly to the north of the caldera (Table 2.2).

During each event extensive fissuring and normal faulting occurred above the intruded dyke, the central part of the fissure swarm subsided, and the flanks were uplifted. This is shown by geodetic data. Levelling data collected along a profile 10 km south of the Krafla caldera during the rifting episode reveal vertical land movements from 1974 to 1979 (Figure 2.6). Subsidence of up to 1 m occurred within the fissure swarm during rifting events, along with uplift of tens of centime-

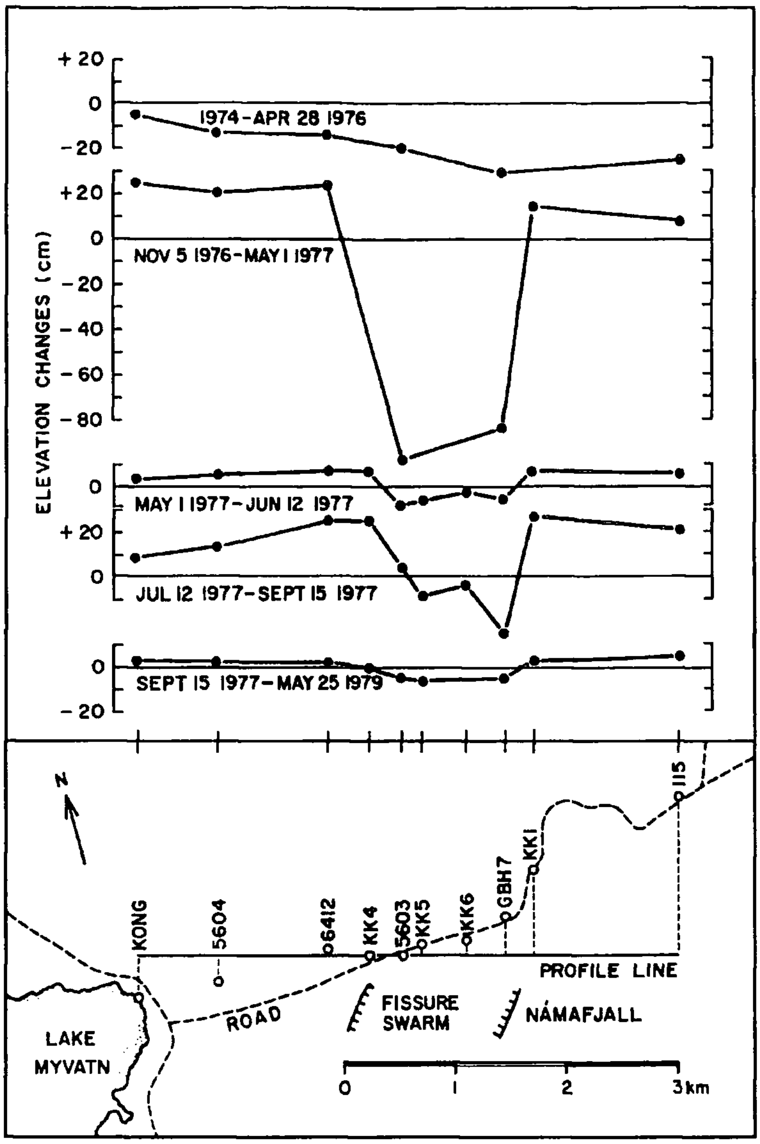

Figure 2.6: Elevation changes along a profile across the Krafla fissure swarm at Námafjall (Figure 2.1), 10 km south of the caldera, from 1974 to 1979, after *Björnsson* [1985].

tres on the flanks. Regional geodetic measurements made over longer time periods revealed horizontal and vertical movements out to over 50 km east and west of the axial rift zone. Trilateration data from a network crossing the axial rift zone in northeast Iceland demonstrated that up to 8 m of extension occurred in the centre of the fissure swarm from 1971 to 1980 and contraction of the flanks [*Möller and Ritter*, 1980; *Möller et al.*, 1982] (Figure 2.7a). Two points, 90 km apart on either side of the rift zone, revealed only ~0.5 m of widening during this same period. Elevation changes on a 140 km-long east–west profile, crossing the active zone near Námafjall (Figure 2.1), indicate a regional uplift of some 0.6 m centred on the Krafla fissure swarm between 1975 and 1980 and subsidence within the central

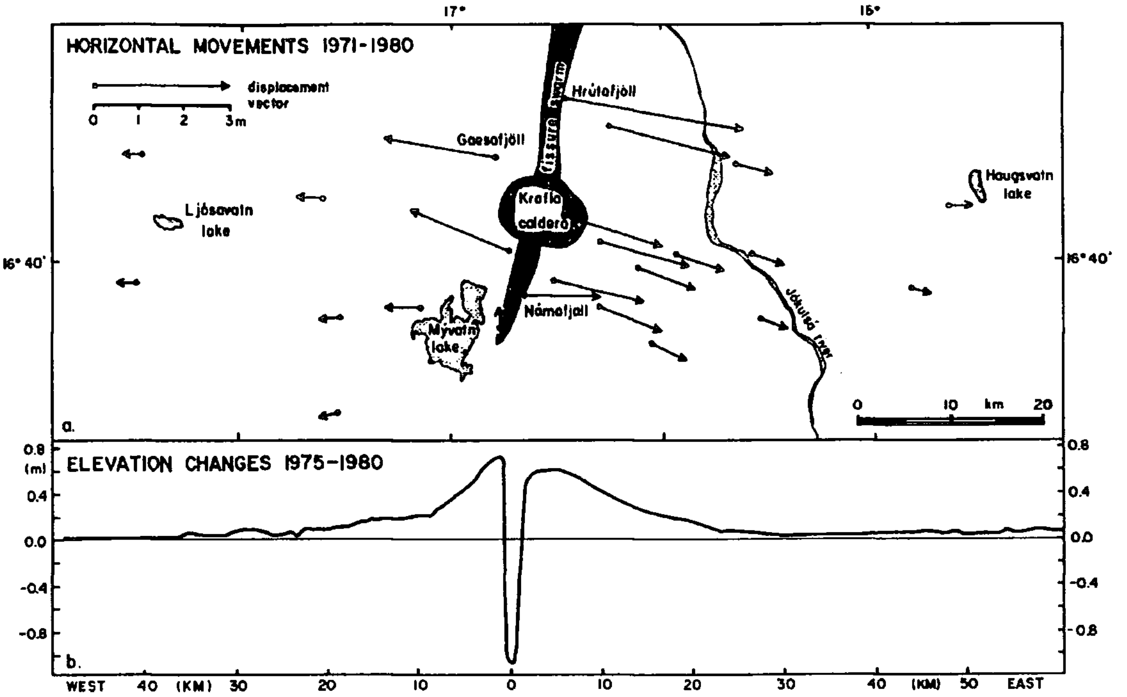

Figure 2.7: (a) Horizontal movements from 1971 to 1980 on a profile across the axial rift zone in the Krafla area. (b) Elevation changes from 1975 to 1980 on an east–west profile, projected onto latitude 16°40', adapted from *Björnsson* [1985].

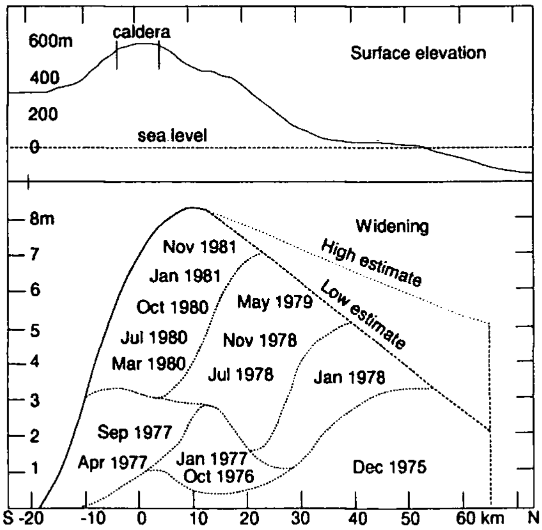

Figure 2.8: An estimate of the accumulated widening of fissures of the Krafla fissure swarm between 1975 and 1982, with crude estimates of the contribution of certain time intervals to the widening. The high and low estimates indicate the possible range of the total widening in the northern half of the rifted zone where no geodetic measurements were made prior to rifting. Land elevation along the Krafla fissure swarm is also shown (top), after *Tryggvason* [1984].

part of the fissure swarm [*Kanngieser*, 1983] (Figure 2.7b). Before July 1980 the deflation events were associated mainly with rifting and subsurface magma transport with only minor surface eruptions. However, from July 1980 the majority of events produced eruptions in addition to surface widening.

Despite the extensive surveying work done, there is still considerable uncertainty in the actual thicknesses of the dykes injected. First, since neighbouring areas contracted when dykes were injected, this must be taken into account for measuring lines of moderate length crossing newly injected dykes. Second, the surface widening is expected to be less than the maximum dyke thickness for dykes that do not reach the surface [*A. Rubin*, pers. comm., 1995]. Third, the dykes are unlikely to have uniform thickness throughout their height. *Tryggvason* [1984] predicts the best set of dyke-thickness estimates available for the whole episode (Figure 2.8).

2.3.3.4 Dyke Injection

Migrating earthquake swarms during the rifting events, and the correlation between caldera subsidence rate and activity in the fissure swarm, suggest that the rifting events were associated with the movement of magma outwards from beneath the volcano into the fissure swarm forming dykes. Modelling of gravity data is consistent with a model where the inflation and deflation of the volcano was caused entirely by the flow of magma into and out of a chamber at about 3 km depth [*Johnsen et al.*, 1980]. S-wave shadows of local earthquakes were used to map a shallow crustal magma reservoir at depths of approximately 3–7 km near the centre of inflation in the caldera. This magma chamber is about 2 x 7 km in area with the long axis oriented east–west and is divided at its top [*Einarsson*, 1978]. Inflow into the chamber was at an average rate of 5 m^3/s [*Björnsson*, 1985].

A total of about 0.5 km^3 of magma was injected into the fissure swarm, estimated from the total accumulated deflation of the Krafla volcano and assuming the crustal magma chamber can be approximated by a sphere, and about 0.1 km^3 was extruded [*Björnsson*, 1985]. Total widening across the fissure swarm was approximately 2 m along 50 km of its length and 6 m along another 30 km, suggesting the average height of the injected dykes to be about 2 km [*Björnsson*, 1985]. These estimates are in agreement with calculations of dyke height made for single rifting events on the basis of widening of surface features [*Tryggvason*, 1984], and on the observed

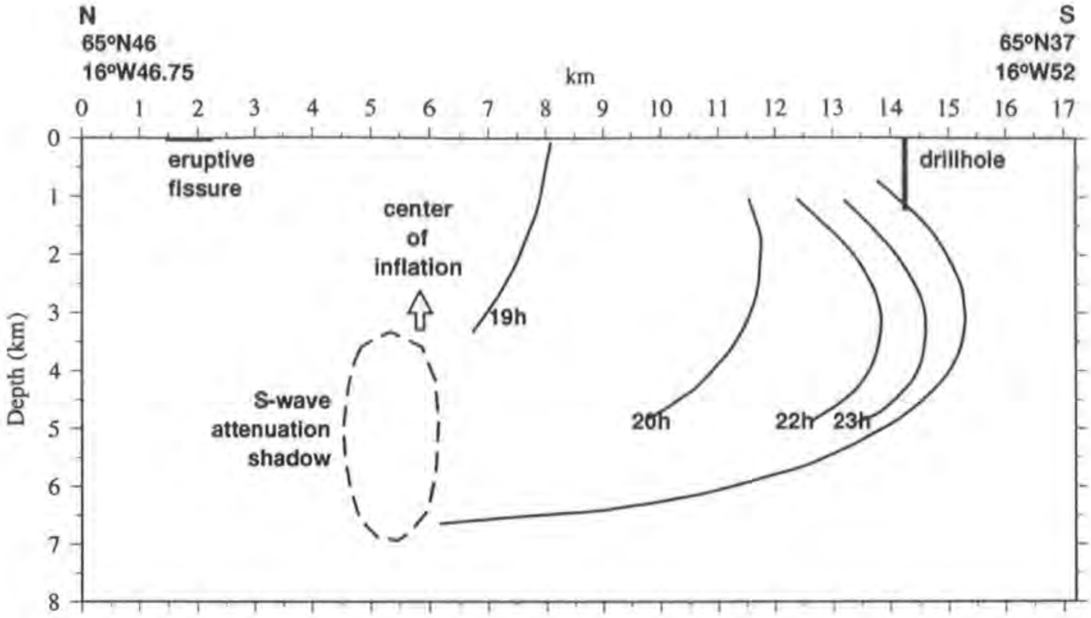

Figure 2.9: A vertical section along the Krafla fissure swarm from 16°W46.75', 65°N46' to 16°W52', 65°N37', showing the September 1977 eruptive fissure, a drillhole at Namafjall through which a small pumice eruption took place in the latter stages of the eruption, the S-wave attenuation zone deduced from seismic data collected during this eruption and thought to map out the position of the magma chamber, and the centre of magma accumulation as determined from elevation and tilt changes. The propagation of the seismic activity along the fissure swarm is shown with curved lines. Isochrons indicate the southern extent of seismic activity at the corresponding time. The final extent of the seismic zone is also shown (rightmost curve), adapted from *Brandsdottir and Einarsson* [1979].

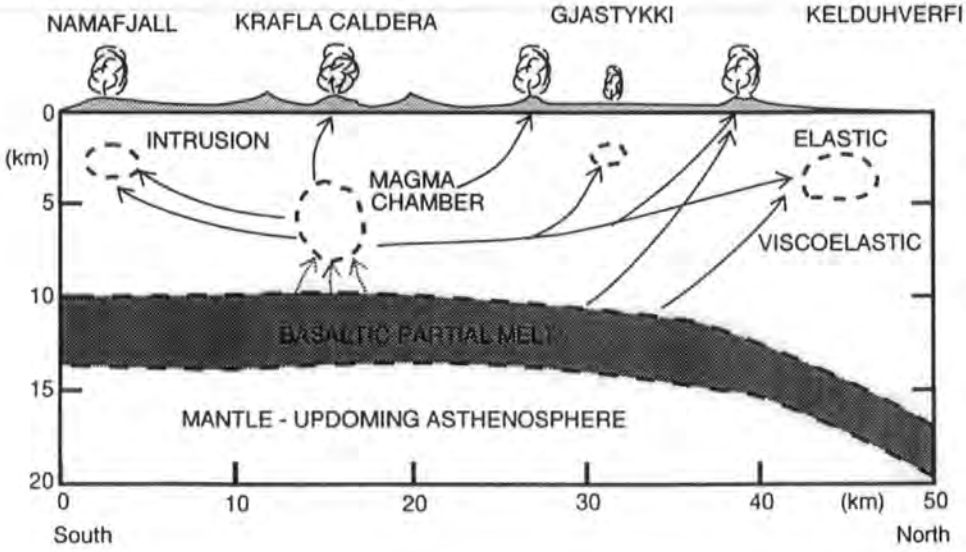

Figure 2.10: A simplified model of the Krafla volcanic system showing a cross section from south to north. The layer of partial melt thought to lie at the base of the crust and the crustal magma chamber are shown. Arrows indicate magma movements, adapted from *Björnsson* [1985].

length of the dyke tip [*Einarsson and Brandsdottir*, 1980].

Estimates for dyke height in eroded dyke swarms in eastern Iceland, are much greater however - of the order of 10 km [*Gudmundsson*, 1983]. Estimates based on the modelling of geodetic data from the Krafla episode are also much larger. Geodetic data collected from 1971 to 1980 across the southern part of the fissure swarm [*Möller and Ritter*, 1980; *Möller et al.*, 1982; *Wendt et al.*, 1985] suggested dykes that extended from the surface to 4-6 km depth [*Marquart and Jacoby*, 1985]. Geodetic data measured in the same region between 1975 and 1980 were also modelled [*Rubin*, 1992]. In this study the several dykes that were injected 1975–1980 were treated as a single dyke intrusion with uniform top and bottom depth and a relative thickness that varies along strike in accordance with the surface horizontal displacement observations. Two normal faults on either side of the dyke were also included. This work suggested a vertical dyke extending from 1.25 to 8.5 km depth [*Rubin*, 1992]. The actual depth extent of the dykes is thus controversial, but it seems clear that they have a greater volume than can be accounted for solely by magma supplied by the magma chamber during deflation events.

Seismic evidence (Figure 2.9) suggests that the dykes were injected laterally from the crustal magma chamber, because there was little seismicity during the rifting events below 4–6 km depth. However, this does not prove that rifting and magma transport were confined to the upper 4 km. Below 4–5 km in the axial rift zone temperatures are high and at some depth viscoelastic behaviour must onset, where stress can be released by creep, and rifting may take place largely aseismically [*Björnsson*, 1985]. Dykes injected from the crustal magma chamber were probably confined to the shallow crust, but dykes at greater depths and at large distances from the caldera may have been engineered by material that ascended from a deeper layer of partial melt [*Björnsson*, 1985] (Figure 2.10). Such a process is supported by the observation that lava with differing chemical composition, that suggests a deeper origin, was erupted far to the north, and within the caldera. An alternative explanation for the observed compositional variations is that the magma was drawn from different depths within a layered magma chamber [*Björnsson*, 1985].

Observations of dyke dips in northwest Iceland show that ~94% of the eroded dykes dip within 5° of the vertical [*Gudmundsson*, 1984]. Modelling of geodetic data from the Krafla episode suggested a vertical dyke [*Rubin*, 1992].

2.3.4 Post-Rifting Deformation

An array of ground tiltmeters has been operated continuously in the Krafla area since the cessation of major tectonism in order to monitor continued activity in the volcano. Data from these meters, which are all within 15 km of the Krafla caldera, indicate alternating periods of uplift and and subsidence [*Tryggvason*, 1994]. From early 1985 to the end of October 1986 vertical ground movements of stations within 5 km of the caldera were negligible. From the end of October 1986 to March/April 1987 uplift occurred with the rate slowing until early 1989 when the sense of motion reversed and subsidence began. Subsidence continued until 1992. Stations 5–9 km from the caldera underwent uplift 1985–1989 followed by no motion or very slight subsidence 1989–1992. Stations more than 9 km from the caldera uplifted 1985–1989 followed by no detectable motion 1989–1992 [*Tryggvason*, 1994]. These observations were interpreted as indicating inflation of the Krafla magma chamber 1985–1989, deflation of this same body 1989–1992 accompanied by inflation of some deeper source and subsidence of the fissure swarm 1985–1992 [*Tryggvason*, 1994] (Table 2.3).

Table 2.3: Summary of the vertical motion in the vicinity of the Krafla magma chamber, detected using tiltmeters 1986–1992 [*Tryggvason*, 1994].

	Distance from caldera		
Epoch	< 5 km	5–9 km	> 9 km
1986–1989	uplift	uplift	uplift
1989–1992	subsidence	no motion/slight subsidence	no detectable motion

Major geodetic surveys using GPS were carried out in northeast Iceland in 1987 and 1990. Differencing the results revealed a large, systematic, rift-normal expansion with a maximum amplitude of ~18 cm [*Foulger et al.*, 1992; *Heki et al.*, 1993; *Jahn et al.*, 1994] (Figure 2.11a). This expansion was clearest around the centre of the fissure swarm where the Krafla dyke complex was injected. The maximum east-west expansion occurred 20–30 km from the rift axis (Figure 2.11b), was approximately three times the time-averaged spreading rate for Iceland (Table 2.1) and decreased somewhat beyond this. Rift-parallel motion was also observed but was of a much smaller magnitude [*Heki et al.*, 1993]. This resulted in a pattern of deformation that had a radial component. Vertical movements were around a few centimetres but were less systematic than the horizontal displacements, possibly because of a

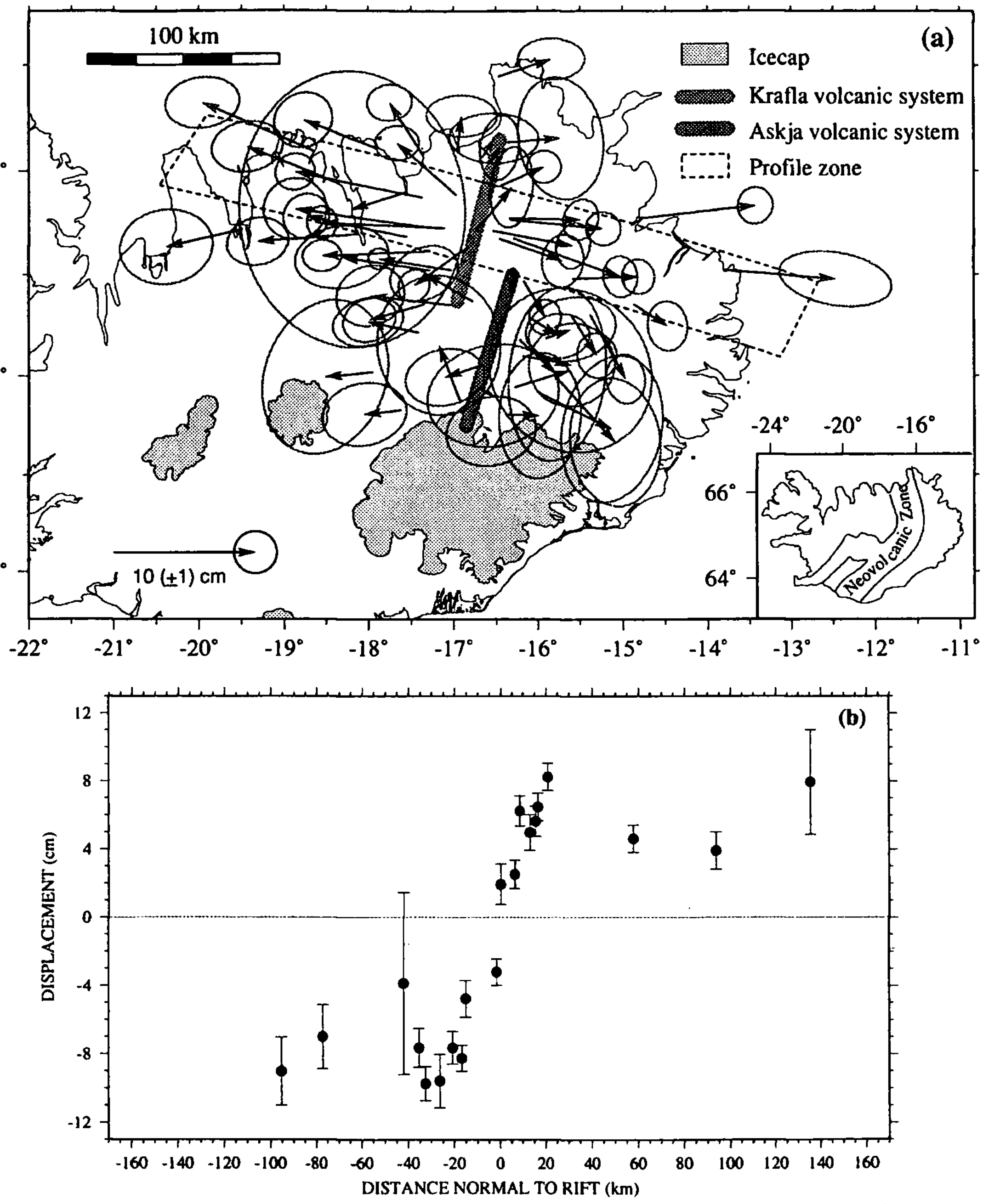

Figure 2.11: (a) Horizontal point displacements between 1987 and 1990. 68% confidence (1.5σ) error ellipses are shown. The dashed profile zone indicates the part of the network around the middle of the intruded dyke complex, extending 26.5 km north of a point on Mt. Krafla to 16.9 km south of it, and perpendicular to the strike of the Krafla volcanic system. (b) The rift-normal motion, as a function of distance from the volcanic system, for the points within the profile zone shown in (a). 1σ confidence bars are shown, adapted from *Heki et al.* [1993].

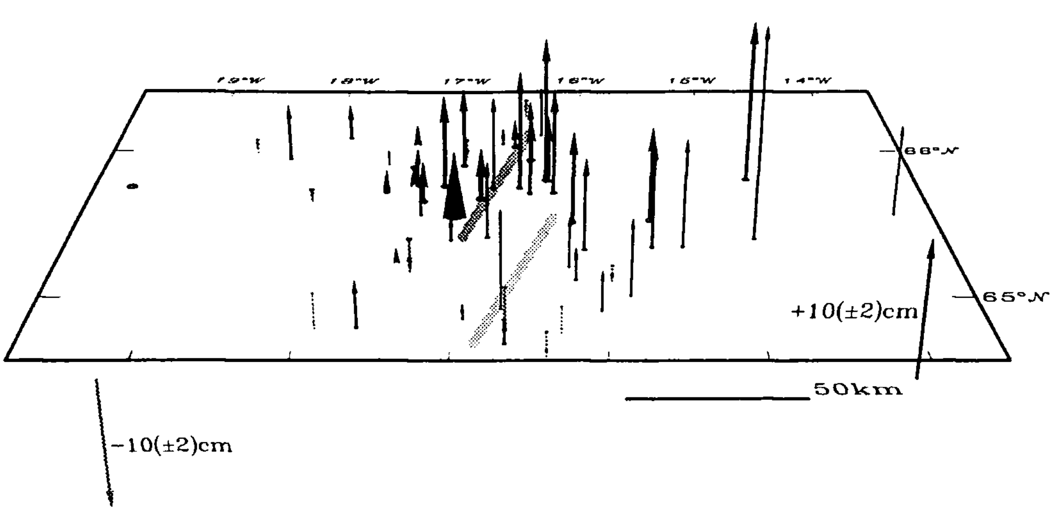

Figure 2.12: Vertical point displacements between 1987 and 1990. The thickness of each displacement arrow is inversely proportional to the positional error. Motions are shown relative to the westernmost point in the network, which is shown as a dot, adapted from *Heki et al.* [1993].

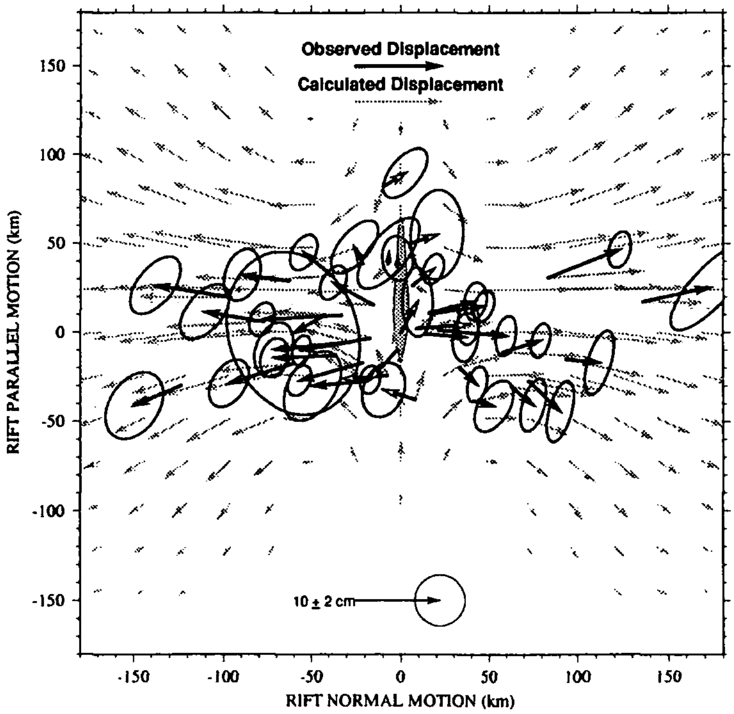

Figure 2.13: Comparison of the observed and simulated displacements 1987–1990, according to the model of *Heki et al.* [1993]. The shaded arrows represent simulated data and solid arrows observed. 68% (1.5σ) confidence error ellipses for the observed displacements are shown. The points within 10 km of the dyke were excluded in fitting the data and are shown with open arrow heads. A stress diffusivity of 10 m^2/s was used, adapted from *Heki et al.* [1993].

lower signal to noise ratio (Figure 2.12).

These movements were interpreted as postrifting relaxation of compressional stress accumulated in the near-boundary region of the plates during the recent Krafla rifting episode [*Foulger et al.*, 1992; *Heki et al.*, 1993]. A simple model was used consisting of a thin, elastic plate overlying a thin, viscous layer [*Elsasser*, 1969; *Bott and Dean*, 1973]. The 1975-1984 series of dyke intrusions was modelled both as a single, instantaneous, infinitely-long dyke (the one-dimensional model) [*Foulger et al.*, 1992], and as a series of such dykes with finite lengths (the two-dimensional model) [*Heki et al.*, 1993]. This latter approach was more consistent with the actual history of dyke emplacement, which involved the multiple injections of thin, rapidly-cooling dykes over a five-year period. This work provides a first order analysis of the data only, since real Earth rheology is known to be better described by viscoelasticity or power-law creep.

The model explained the observations to a first order. Observed and predicted displacements 1987–1990 for the two-dimensional model are shown in Figure 2.13. The poor fit to the data in the vicinity of the dyke was attributed to the response of the elastic crust to inflation of the Krafla magma chamber [*Heki et al.*, 1993], and on these grounds points within 10 km of the dyke were excluded in the inversion process. Another region where the fit was relatively poor was in the northwest, within the TFZ, and this was attributed to postevent motion on the faults in this region modifying the deformation field. The eastward motion of the northernmost point was considered to be reasonable from a plate tectonic viewpoint since it is actually situated on the Eurasian side of the plate boundary (Figure 1.1).

Comparison of the one-dimensional predictions of the stress-diffusion model with the observed displacements along a profile across the dyke (Figure 2.11b) gave an estimate for stress diffusivity of 1 m^2/s, corresponding to a viscosity of 0.3–2 x 10^{19} Pa s [*Foulger et al.*, 1992] [1]. Using the two-dimensional model, a best-fit stress diffusivity of 10 m^2/s was obtained, corresponding to a viscosity of 0.3–2 x 10^{18} Pa s. These estimates are in agreement with that obtained from postglacial rebound studies of 1 x 10^{18} Pa s [*Sigmundsson and Einarsson*, 1992]. The one-dimensional solution involved points close to the rift, i.e., those later thought to be

---

[1] *Foulger et al.* [1992] modelled GPS results calculated using the GEONAP software at the University of Hannover. The results shown in Figure 2.11b were calculated using the Bernese software at the University of Durham.

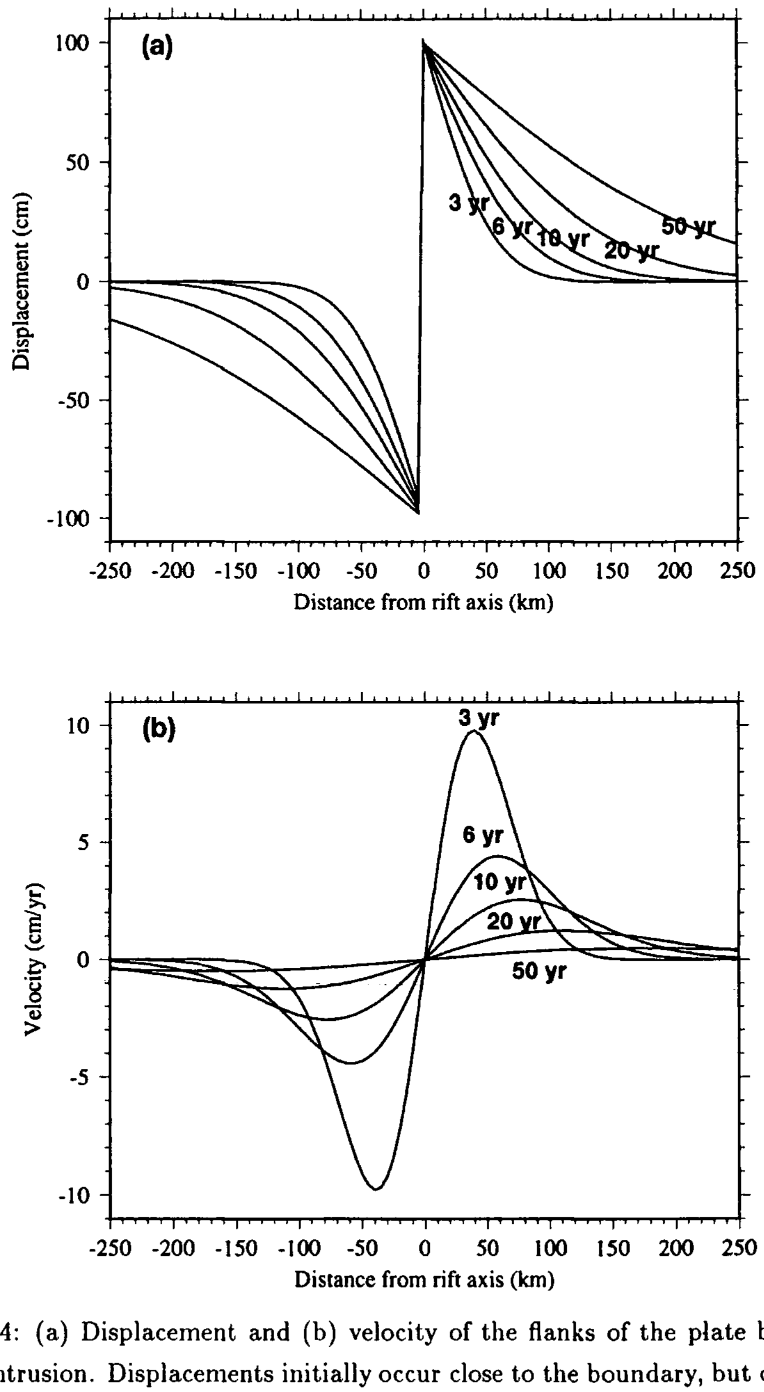

Figure 2.14: (a) Displacement and (b) velocity of the flanks of the plate boundary 3–50 years after the intrusion. Displacements initially occur close to the boundary, but diffuse out over time. Velocity is highest close to the boundary shortly after the intrusion, but the velocity maximum propagates out and decreases in amplitude over time. According to the model of *Heki et al.* [1993] motion results from the relaxation of compressional stresses generated during recurring rifting episodes. A 1-dimensional model was used, dyke thickness 1 m, and stress diffusivity of 10 m^2/s, adapted from *Heki et al.* [1993].

(a) 25 km from boundary

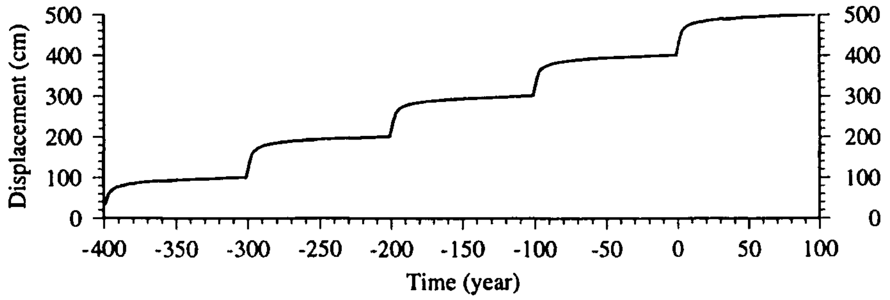

(b) 50 km from boundary

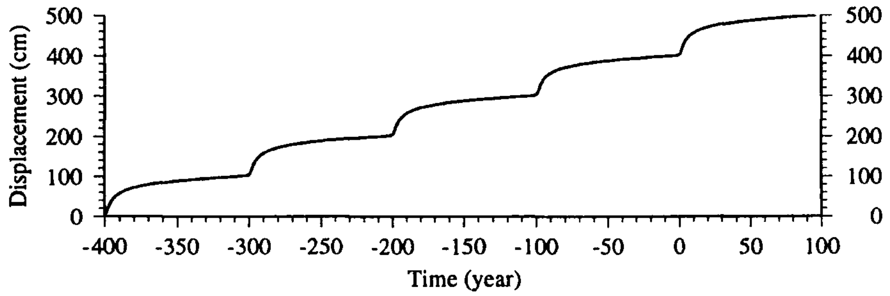

(c) 100 km from boundary

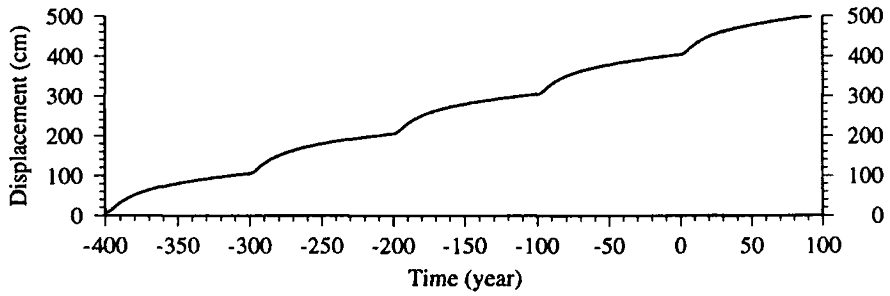

(d) 200 km from boundary

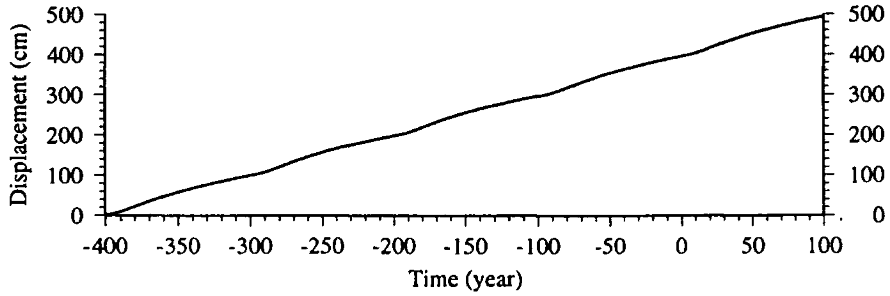

Figure 2.15: Displacement versus time at points (a) 25 km, (b) 50 km, (c) 100 km, and (d) 200 km from the plate boundary. A rifting event is assumed to occur every 100 years when a 1 m thick dyke is intruded. The resultant, average full-spreading rate is 1 cm/yr. Movements change from episodic to continuous with distance from the plate boundary, adapted from *Heki et al.* [1993].

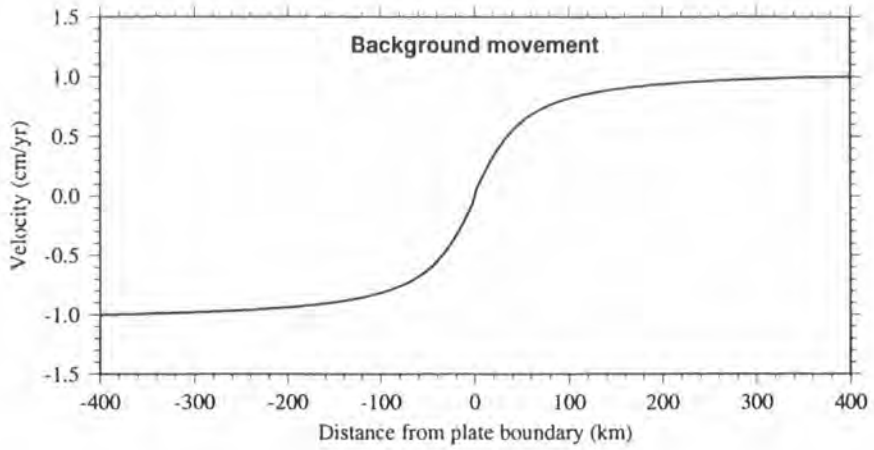

Figure 2.16: Plate velocity as a function of distance from the divergent plate boundary immediately prior to a rifting event, according to the model of *Heki et al.* [1993]. Velocity is constant in the plate interior but is zero at the boundary where the motion is purely episodic, adapted from *Heki et al.* [1993].

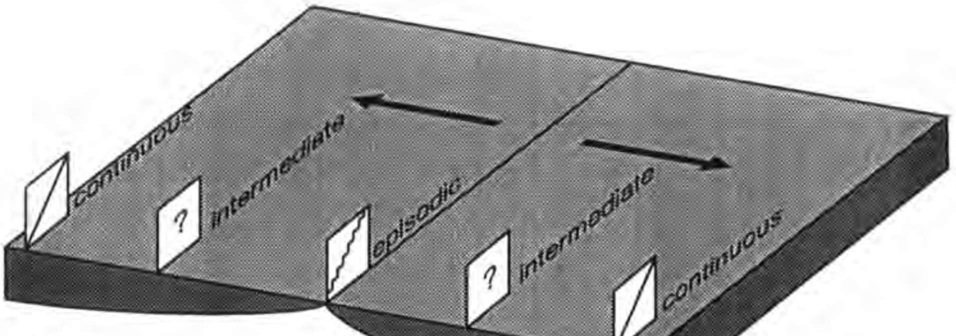

Figure 2.17: Plate motion near an accretionary plate boundary. Movement of most of the plate is continuous, but it is episodic at the boundary, adapted from *Heki et al.* [1993].

most affected by the radial outgoing displacements due to the pressured inflation of the Krafla magma chamber [*Heki et al.*, 1993], giving a lower estimate for the diffusivity as a result. However, this factor could not entirely account for the discrepancy and a real spatial variation in diffusivity was suggested throughout northeast Iceland [*Heki et al.*, 1993].

Plate motion at varying distances from the boundary were inferred using a one-dimensional model and the diffusivity calculated by *Heki et al.* [1993]. The motions at far distance from the boundary from the summation of a number of diffusion pulses produced by regular events at the plate boundary were calculated. Near the boundary, a rifting event causes a sudden displacement similar to a step function (Figure 2.14a). A pulse of velocity ensues that has the largest amplitude immediately after an event, which subsequently decreases (Figure 2.14b). Closest to the boundary (less than 25 km), motion is highly episodic (Figure 2.15a). At 50 km from the boundary, episodicity is less pronounced and continuing movement occurs just before the onset of a new episode (Figure 2.15b). Further (100 km) from the boundary, movement is continuous with only small "ripples" apparent in the velocity rate (Figure 2.15c). Plate motion is nearly constant 200 km from the boundary and essentially indistinguishable from continuous plate motion (Figure 2.15d). Crustal motion just before the onset of a spreading episode is shown in Figure 2.16. The velocity is zero at the boundary and approaches the half-spreading rate with distance. Between these two is a transition zone where movement at intermediate rates occurs, the "plate boundary" zone (Figure 2.17).

It is important to realise that this model is independent of the plate driving forces (ridge push, slab pull, drag on the undersides of the lithospheric plates) and makes no assumptions or predictions in this respect. It merely models the pattern of motion that results from episodic motion at the boundary in north Iceland for this particular Earth structure model.

2.4 Previous Rifting Events in North Iceland

Information on earlier rifting events in the NVZ may be obtained from geology and historical accounts. However, the information available mainly concerns volcanism and felt earthquakes and it is conjectural whether all these events were accompanied by dyking. Tephrochronology gives the detailed history of volcanism in the Krafla area since early postglacial time. Five major volcanic episodes have occurred within the last 3,000 years [*Björnsson et al.*, 1977]. Most eruptions in the Krafla fissure swarm occurred within the Krafla caldera or in the Námafjall area [*Björnsson et al.*, 1979].

There is only one historically documented eruption in the Krafla fissure swarm, known as the "Mývatn fires" which occurred 1724–1729 [*Björnsson et al.*, 1977]. The initial eruption, 17th May 1724, was from the main crater, Víti (Figure 2.1) and was followed by earthquakes, fissure opening and crater formation. In August 1727 a fissure eruption started near Leirhnjúkur, extended southwards to Námafjall in April 1728 and continued until September 1729.

In the Askja fissure swarm (Figure 2.2), steam emissions, intense earthquake activity, and fissure opening occurred 50 km to the north of the caldera from 1874 to 1875. This preceded a small eruption in the caldera and in the newly formed fissures. March 29th 1875 an ash eruption occurred in the Askja caldera and a new caldera with a volume of about 2 km^3 collapsed within the already existing caldera [*Björnsson et al.*, 1977].

Earthquakes and faulting lasting several months were recorded in 1618 in the Theistareykir fissure swarm (Figure 2.2) to the north of the Krafla area [*Björnsson et al.*, 1977]. Periods of volcanic activity have been reported in the Kverkfjöll volcanic system (Figure 2.2) in 1655, 1711, 1717 and 1729 [*Gudmundsson and Sæmundsson*, 1980], but little is known about this activity as that area has always been uninhabited.

2.5 Other Recent, Tectonic Activity in North and East Iceland

In May 1983, a subglacial eruption occurred in the Grimsvötn volcano beneath the Vatnajökull icecap (Figure 1.2) [*Einarsson and Brandsdottir*, 1984]. It was preceded by a significant increase in seismic activity which lasted for about three months, and an intense earthquake swarm on the presumed day of the eruption, the pattern of which closely resembled the increased activity observed in Krafla

Table 2.4: Earthquakes greater than magnitude 6.0 in the Tjörnes Fracture Zone and close to land, 1900–1992. Dates, epicentre locations, and magnitudes are from *Tryggvason* [1973] and *Björnsson et al.* [1977].

Date	Epicentre	Activated fault	Magnitude
Jan. 22 1910	N66.5° W17.0°	Grimsey	7.1
June 2 1934	N66.0° W18.5°	Dalvik	6.3
Mar. 28 1963	N66.3° W19.6°	Dalvik	7.0
Jan. 13 1976	N66.2° W16.7°	Grimsey	6.3

before some of the eruptions and rifting events. The volcanic eruption is believed to have occurred between May 28^{th} and June 5^{th} 1983.

Tilt, levelling and gravity observations at the Askja volcano since 1966 have revealed alternating uplift and subsidence cycles. Within ~10 km of the centre of the Askja caldera subsidence at a rate of a few centimetres a year was detected 1966–1967, uplift 1967–1968, and subsidence 1968–1970. In the same region rapid uplift occurred at a rate of ~20 cm/yr 1970–1972, followed by a net subsidence of 20 cm 1972–1983. Since 1983 subsidence at a rate of 4–6 cm/yr has occurred (see *Camitz et al.* [1995] for summary). The majority of this ground deformation may be explained as a response to pressure changes in a shallow magma chamber [*Tryggvason*, 1984], and on the basis of tilt measurements 1988–1991, *Rymer and Tryggvason* [1993] concluded that 80% of the observed ground deformation could be explained by the deflation of a spherical magma chamber centred at 65° 3.19'N, 16° 46.10'W at a depth of 2.8 ± 0.3 km. This point is approximately at the centre of the Askja caldera. GPS measurements 1990–1993 were interpreted using this result, and imply a maximum subsidence of 11 ± 2.5 cm 1990–1993 and 5.5 ± 1.5 cm 1992–1993 over the centre of the chamber [*Camitz et al.*, 1995]. Outside of a 30–40 km plate boundary zone *Camitz et al.* [1995] report divergent plate movements at a rate of 2.4 ± 0.5 cm/yr for the period 1990–1993.

In addition to what appears to be continuous activity in the magma chamber, two earthquake swarms occurred along a 20 km-long zone trending N57°E, east of the Askja volcanic system in 1982/1983 [*Einarsson*, 1991].

Five large earthquakes greater than magnitude 6.0 have occurred in the TFZ in this century (Table 2.4) [*Tryggvason*, 1973; *Einarsson*, 1991]. Focal mechanisms available for these events show them to be associated with right-lateral, strike-slip motion in the TFZ. The 1976 event was triggered by the first dyke injection of the recent Krafla spreading episode.

Seismic activity has been high in the northwestern Vatnajökull region during the last 30 years or so [e.g., *Einarsson*, 1991]. The most seismically active feature in the area is the central volcano Bardabunga. From 1974–1980, nine earthquakes greater than magnitude 5 occurred there and this was the most significant seismic occurrence in this area for ~50 years [*Einarsson*, 1991]. The activity appeared to correlate with dyke injections during the recent Krafla episode and led *Einarsson* [1991] to hypothesise that they were triggered as a result of a hydraulic link between the central volcanoes of north Iceland, that could be the proposed layer of partial melt at the base of the crust (Section 1.3.3).

2.6 Dynamics of Crustal Spreading

A model for episodic crustal rifting was proposed by *Björnsson* [1985]. The rifting episode in Krafla can be explained by the gradual buildup of extensional stress over a period of a few hundred years, in a narrow zone of the crust near the plate boundary, simultaneously with the slow retreat of the plates (Figure 2.18). The buildup of extensional stress in the axial rift zone results in gradual crustal thinning and subsidence. This stress is periodically, suddenly released in rifting episodes, accompanied by magma intrusions into crustal fissures. Rifting initiates where magma chambers occur since these form weak points in the crust. However, the existence of a magma chamber is not a requisite for the rifting process – magma infiltration through pre-existing or newly-created joints and cracks in the lower crust is also capable of initiating a rifting episode. A volcanic system containing a magma chamber in the roots of its central volcano should rift more frequently than a system that does not have one.

During the Krafla rifting episode repeated dyke injections into the fissure swarm progressively reduced extensional stress in the crust. When the extensional stress in the crust had been released, eruptions occurred since it was no longer easier for the magma to be intruded than erupted. This indicates that the magma supply was not controlled by stress in the shallow crust, but was in fact driving volcano-tectonic activity, whilst the ambient stress field was governing its style. This is

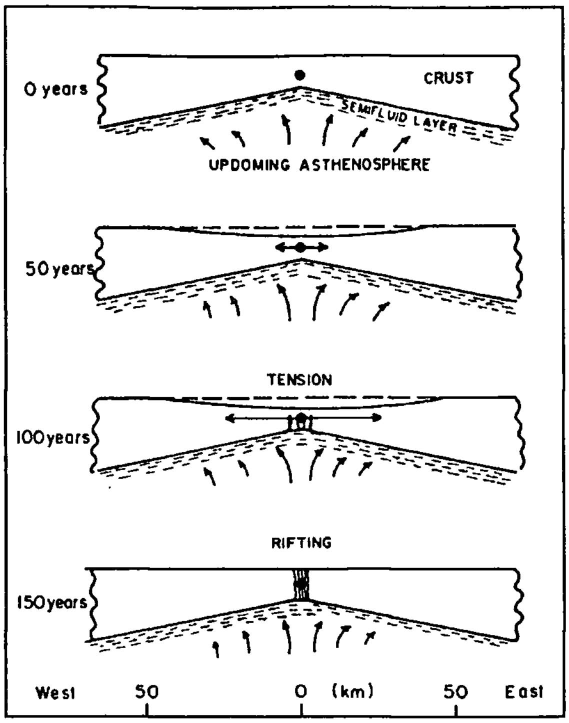

Figure 2.18: A model of episodic crustal rifting in northeast Iceland. The net effect of the plate motions is to build up extensional stresses gradually in the axial rift zone. These are released every few hundred years in a rifting episode, after *Björnsson* [1985].

further illustrated by the fact that the episode came to an end when the supply of magma to the chamber essentially stopped.

Major volcano-tectonic activity is episodic in the rift zone of north Iceland, occurring every 100–150 years. Only one fissure swarm is active at a time [*Björnsson et al.*, 1977; *Sigurdsson and Sparks*, 1978]. Increased compressional stresses produced in the flanks of the rift zone during a rifting episode in one volcanic system will decrease the extensional stress in adjacent, overlapping, *en échelon* volcanic systems and so prevent them from rifting simultaneously.

According to the stress diffusion hypothesis, after the dyking, the stress built up in the adjacent plates diffuses out from the boundary producing a transient deformation field. Pulses from repeated episodes sum in the plate interior to the constant rate of motion observed there. In this manner the spatial transition from episodic to continuous plate motion may be simulated.

2.7 Summary

Geodetic surveying has revealed a picture that is far from simple of crustal deformation in Iceland. In southeast Iceland deglaciation of Vatnajökull throughout this century is thought to be resulting in surface uplift immediately around the icecap. Across the spreading plate boundary in north Iceland, geodetic results reveal up to 50 cm of contraction 1965–1971, 30 cm of expansion 1971–1975, up to 8 m of expansion 1975–1985 and variable, regional expansion at up to three times the time-averaged plate rate of 1.85 cm/yr in the period 1987–1990.

On December 20th 1975 a major, decade-long crustal rifting episode began in the Krafla volcanic system. About 20 rifting events occurred, during which magma flowed out of a crustal magma chamber into the fissure swarm forming dykes. The total widening across the fissure swarm and the volume of intruded magma suggests the average height of dykes from the magma chamber to be 2 km, less than the observed heights of eroded dyke swarms in eastern Iceland (about 10 km) and those obtained from geodetic data inversions (4–8.5 km). This suggests that material from the crustal magma chamber formed the upper parts of the dykes only and the lower and distant parts formed from material from a different source.

GPS measurements in north Iceland 1987–1990 revealed a large, systematic, rift-normal expansion with a maximum amplitude of ~18 cm a few tens of kilometres from the rift axis. These were attributed to the relaxation of compressional stress built up during the Krafla rifting episode. A viscosity estimate of 0.3–2 x 10^{18} Pa s was obtained, but a real spatial variation is likely.

Other volcano-tectonic activity in the region includes activity in the Krafla fissure swarm (1724–1729) and eruptions in the Askja volcanic system (1874–1875). The Askja magma chamber is currently believed to be deflating, and an eruption occurred in Grimsvötn in 1983. Significant, recent seismicity has occurred in the TFZ, the Askja system and Bardabunga.

The picture of crustal spreading that emerges involves slow divergence of the plates and the gradual build up of local extensional stress in a narrow zone of the crust near the plate boundary. Stress is released in periodic rifting episodes that occur every 100–150 years in the Krafla volcanic system. Postdyking, transient stress patterns result.

Chapter 3

Satellite Surveying Using the Global Positioning System

3.1 Introduction

Much of the emphasis of geodetic research in recent years has been placed on methods based on space technology. Three space geodetic techniques are currently widely used for determining the coordinates of points on the Earth's surface. These are Very Long Baseline Interferometry (VLBI), Satellite Laser Ranging (SLR) and the Global Positioning System (GPS). VLBI enables the coordinates of points to be determined using the signals from extra-galactic quasar radio sources whose positions are assumed fixed. SLR involves measuring the times taken for a series of short energy pulses to travel from a transmitter on the ground to a satellite and back. GPS involves determining the travel times of signals transmitted by three or more GPS satellites with known orbits. VLBI and SLR are observatory-based techniques whereas GPS provides a relatively inexpensive, mobile, all-weather method of determining the three-dimensional coordinates of geodetic points. Using terrestrial techniques, two methods would have to be combined to obtain three dimensional coordinates, for example, EDM and levelling.

The GPS system, and data processing principles and methodologies are highly complex and variable and the subject of several substantial publications. Only a broad overview of the basic principles and methods used in this project is possible in this thesis. Readers requiring greater depth are referred to the publications cited in the next section.

3.2 Fundamentals of GPS Satellite Surveying

3.2.1 The GPS System

GPS geodesy is described in detail by many authors including *Dixon* [1991], *Hager et al.* [1991], *Leick* [1990], *Rocken* [1988] and *Wells et al.* [1986]. GPS is a real-time, military navigation system that has been exploited by civilian users for geodetic surveying. It can provide ***absolute*** positioning (i.e., the position of a point in a known coordinate system) to an accuracy of a few metres and *relative* positioning (i.e., the position of a point relative to another point) at the sub-centimetre level.

The full orbital constellation consists of 21 space vehicles, hereinafter referred to as satellites, with orbital periods of just less than 12 hours, at an altitude of about 20,000 km above the Earth's surface. The satellites are distributed in six orbital planes inclined at 55° to the Earth's equator. The system is designed such that at least four satellites are always visible simultaneously from almost any point on the Earth's surface.

Table 3.1: GPS signal characteristics, after *Dixon* [1991].

	Carriers		Code Modulations	
	L1	L2	P	C/A (L1 only)
Frequency (carrier) or chip rate (code modulation)	1.57542 GHz	1.2276 GHz	10.23 MHz	1.023 MHz
Wavelength	19.0 cm	24.4 cm	~ 30 m	~ 300 m

Each satellite transmits signals on two frequencies, known as L1 and L2, with frequencies of 1.57542 GHz (19 cm wavelength) and 1.2276 GHz (24.4 cm wavelength) respectively. These two carriers are modulated with known binary codes that are different for each satellite. The precision (P) code has a period of 267 days and modulates both L1 and L2. The coarse acquisition (C/A) code has a period of 1 millisecond and modulates L1 only (Table 3.1). In addition, a binary satellite message containing the Keplerian orbital elements of the satellites and satellite clock corrections is broadcast. These *satellite ephemerides* are updated every hour, providing orbits that are as accurate as possible at any one time whilst being broadcast in the format of Keplerian elements which yields great economy of information.

3.2.2 Ranging

Instantaneous positioning using GPS is done by *one way ranging.* In order to obtain the position of a point, the ranges to a minimum of three satellites must be determined. The position of the point is then one of the two intersection points of the three spheres having the one-way ranges as their individual radii and the respective satellites as their centres. For observation points on the surface of the Earth, one of these two intersection points may be eliminated (the one in space). In practice, the satellite and receiver clocks are not perfectly synchronised, and ranging to a fourth satellite is necessary to obtain the receiver clock correction. Continuous tracking yields a series of range estimates and reduces the minimum required number of satellites to two.

3.2.3 Measurements

In addition to receiving the broadcast satellite message, GPS receivers can make two kinds of measurements; *code pseudorange* and *carrier beat phase* measurements. These measurements are made at regular, discrete intervals, known as *epochs.* A pseudorange measurement is made by cross-correlating the P- or C/A-code with a replica code generated by the receiver. The time shift required to line up the two codes, multiplied by the speed of light, is the code pseudorange (Figure 3.1). This is equivalent to the distance (range) of the satellite from the receiver, corrupted by the mis-synchronisation of the receiver and satellite clocks. Ranging to four satellites enables both the three-dimensional coordinates of the antenna phase centre and the receiver clock correction to be determined. Correlation of about 1% of the code wavelength can be achieved, so a range measurement precision of about 30 cm is obtained from the P-code and 3 m from the C/A-code (Table 3.1).

The observation equation for the code pseudorange measurement is given by

$$p = c \cdot d\tau, \qquad (3.1)$$

where p is the pseudorange, c is the speed of light and $d\tau$ is the measured time-shift. Taking into account tropospheric and ionospheric delays and the different

(a) Pseudorange Measurement

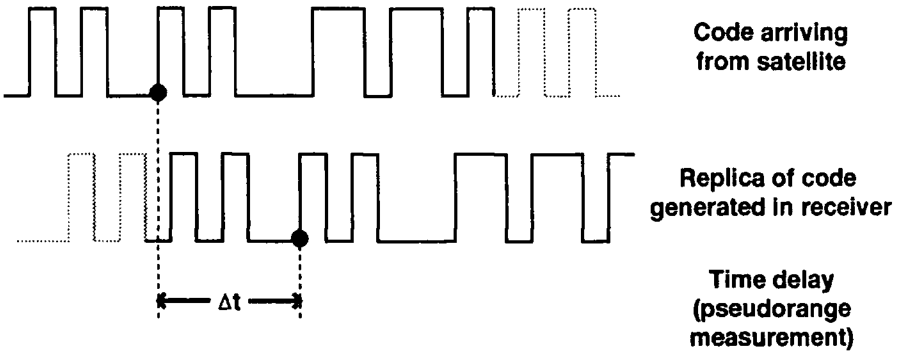

(b) Carrier Beat Phase Measurement

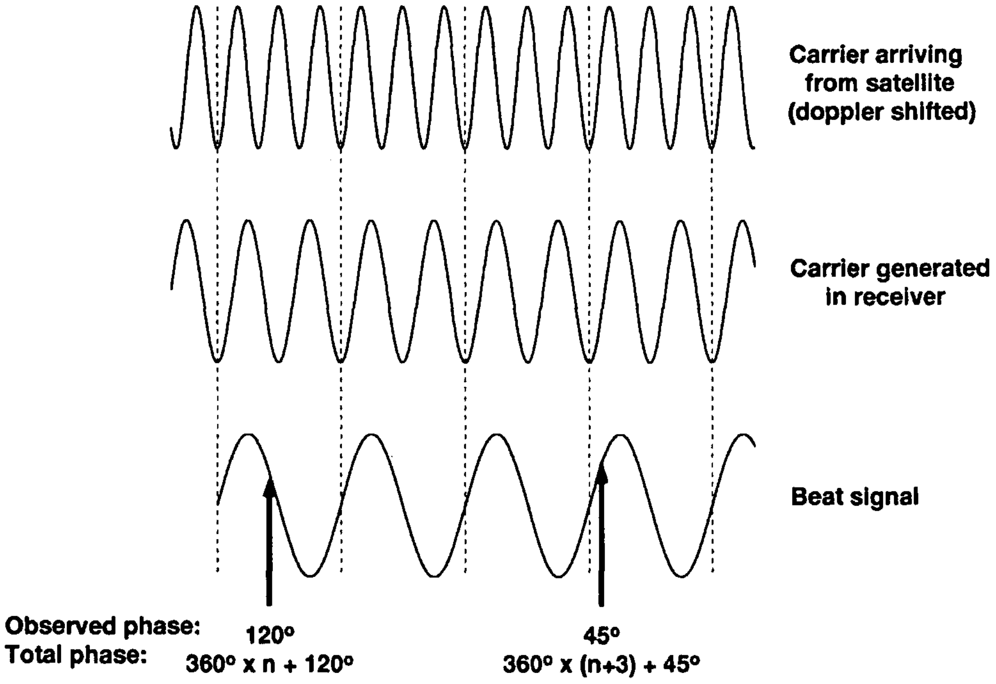

Figure 3.1: The two kinds of range-related measurements made by GPS receivers. (a) Code pseudorange measurements are made by cross-correlating the P or C/A code with a replica generated by the receiver, and is the time delay required to line the two codes up multiplied by the speed of light. (b) Carrier beat phase measurements result when the phase of the incoming, doppler-shifted carrier is differenced with one generated in the receiver at the standard L1 or L2 frequency. The integer number of whole cycles between the satellite and receiver, n, is unknown.

time frames of the receiver and satellite clocks, equation 3.1 becomes

$$p = \rho + c \cdot (dt - dT) + d_{ion} + d_{trop}, \tag{3.2}$$

where ρ is the true range to the satellite, dt and dT are the offsets of the satellite and receiver clocks from true GPS time, and d_{ion} and d_{trop} are the corrections for ionospheric and tropospheric delays.

The carrier beat phase is the phase of the radio carrier which remains when the phase of the incoming, doppler-shifted carrier is differenced with one generated in the receiver (Figure 3.1). Since the wavelengths of the carriers are much shorter than those of either of the codes (Table 3.1), the precision of the pseudorange measured using the carrier beat phase is much greater than that measured using the code, and is about 2 mm for L1. A problem in using carrier beat phase measurements to calculate satellite ranges is that the integer number of whole cycles between the satellite and receiver (i.e., the initial satellite range) is unknown – only changes in range can be measured by phase measurements. This is a problem for phase pseudoranges only since the code sequences are so long that the number of repetitions between satellite and observer on the Earth's surface is unambiguous.

Provided the receiver maintains continuous phase lock on a satellite during the observation session, only one *initial cycle ambiguity* will exist per satellite/receiver pair per session. The total phase, ϕ_{total}, may be expressed as

$$\phi_{total} = Fr(\phi) + Int(\phi; t_0, t) + N(t_0), \tag{3.3}$$

where $Fr(\phi)$ is the measured fractional phase part, $Int(\phi; t_0, t)$ is the integer number of phase cycles from the initial epoch t_0 to epoch t, counted by the receiver, and an unknown integer number N cycles exists between the satellite and receiver at the initial epoch t_0. In other words

$$\phi_{total} = \phi_{measured} + N(t_0). \tag{3.4}$$

The carrier phase observation equation (in length units) is

$$\Phi = -\lambda \phi_{measured}, \tag{3.5}$$

where $\phi_{measured}$ is the carrier phase measurement (in cycles), λ is the wavelength of the carrier and Φ is the phase pseudorange. Including atmospheric effects, the phase pseudorange equation can be written as

$$\Phi = \rho + c \cdot (dt - dT) + \lambda \cdot N - d_{ion} + d_{trop}, \tag{3.6}$$

where N is the initial integer phase ambiguity. The form of this equation is almost identical to the code pseudorange equation (3.2), apart from the sign change of the d_{ion} component which reverses for the following reason. The GPS signal is dispersed by the ionosphere. This is dependent on the refractive index and hence can be modelled using the effect on the signal velocity. Code measurements are dependent on the group velocity, and phase measurements on the phase velocity. Group velocity is the derivative of the phase velocity and hence the sign difference of d_{ion} between the code and phase pseudorange equations.

Various types of receivers are used including dual frequency P-code receivers and dual frequency C/A-code receivers. The former can replicate the P-codes and are able to make code measurements on L1 and L2. The latter type of receiver can replicate the C/A code only, can thus make code measurements on L1 only, and measures the phase of the L2 carrier by multiplying it by itself to remove the (unknown) code. The phase is thus measured at intervals of one-half the wavelength (the squaring technique).

3.2.4 Differencing the Measurements

The two types of ranges recorded by receivers, code and phase pseudoranges, are differenced in various ways to reduce or eliminate errors. These are known as *single, double* and *triple differences.* Single difference equations may be formed between-receivers (Figure 3.2a) and then involve a pair of stations simultaneously observing the same satellite. Differencing the two ranges, r, to the satellites gives

$$\Delta(r) = (r)_{receiver2} - (r)_{receiver1}, \tag{3.7}$$

where Δ denotes the difference between two receivers. The code pseudorange equation then becomes

$$\Delta p = \Delta\rho - c \cdot \Delta dT + \Delta d_{ion} + \Delta d_{trop}. \tag{3.8}$$

The satellite clock error is identical at both receivers and will cancel out. Δd_{ion} and Δd_{trop} are now the differential corrections for the ionospheric and tropospheric delays, and ΔdT is a differential correction for the receiver clock error. Similarly, in the case of phase measurements, the between-receiver single difference pseudorange equation becomes

$$\Delta\Phi = \Delta\rho - c \cdot \Delta dT + \lambda\Delta N - \Delta d_{ion} + \Delta d_{trop}. \tag{3.9}$$

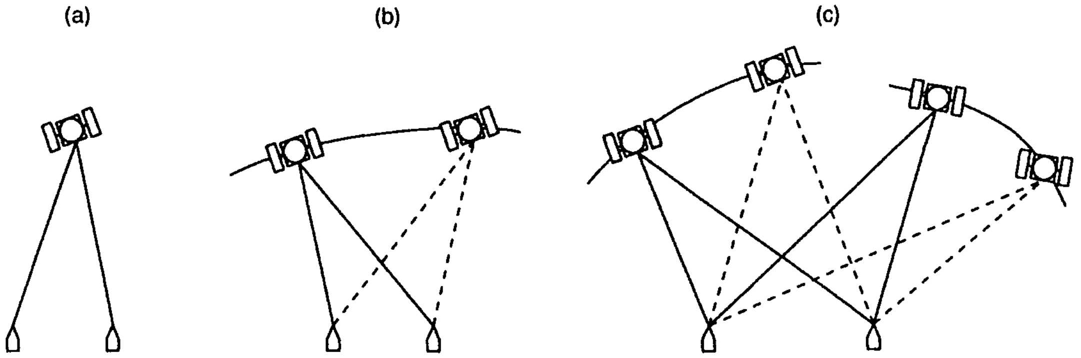

Figure 3.2: Linear differencing of observations by forming (a) between-receiver single differences, (b) receiver-satellite double differences, and (c) receiver-satellite-time triple differences.

Orbit errors and atmospheric delays are correlated over short times and distances, and therefore, providing the survey lines are short (less than a few hundred kilometres), these errors will be smaller in the single differences than they are in the pseudoranges.

Receiver-satellite double differences are obtained by differencing two between-receiver single differences between two satellites (Figure 3.2b). For code pseudorange measurements, the receiver-satellite double difference observation equation is

$$\nabla\Delta p = \nabla\Delta\rho + \nabla\Delta d_{ion} + \nabla\Delta d_{trop}, \tag{3.10}$$

where ∇ denotes differences between two satellites. The receiver clock error, dT, will cancel as it is identical for both satellites. Similarly, for phase measurements

$$\nabla\Delta\Phi = \nabla\Delta\rho + \lambda \cdot \nabla\Delta N - \nabla\Delta d_{ion} + \nabla\Delta d_{trop}. \tag{3.11}$$

Again the errors associated with misalignment between two receiver clocks cancels out.

Triple differences are the change in receiver-satellite double differences from one epoch to the next (Figure 3.2c). In this combination initial integer ambiguities are eliminated in the case of phase measurements. The observation equation for triple-difference phase pseudoranges is

$$\delta\nabla\Delta\Phi = \delta\nabla\Delta\rho - \delta\nabla\Delta d_{ion} + \delta\nabla\Delta d_{trop}, \tag{3.12}$$

where δ denotes differences between two epochs.

3.2.5 Satellite Orbits and Reference Frames

Accurate satellite orbit information is important for GPS positioning. A satellite orbiting the Earth is subject to a force from the Earth's gravitational field. Its equations of motion are described by Kepler's three laws using a quasi-inertial (celestial) reference frame, in which the orientation of the axes remains fixed with respect to the stars and the origin coincides with the Earth's centre of mass. The orbit of satellite is described by an ellipse, with one focus at the Earth's centre of mass.

However, Kepler's Laws do not account for other forces acting on the satellite that are significant for GPS surveying, including the effect of the Earth's equatorial bulge, the gravitational attractions of the sun and moon, solar radiation pressure and atmospheric drag. These forces perturb the orbits of the satellites, and thereby degrade positional estimates unless taken into account.

Survey point coordinates are required in a terrestrial reference frame. A right-handed coordinate system is used with its origin at the Earth's centre of mass. The first axis of this system passes through the intersection of the Greenwich Meridian and the equatorial plane, the third axis is in the average position of the Earth's rotation pole for the years 1900–1905, and the second axis is orthogonal to the first and third axes. The reference frame of the satellites and that of the points are related by the rotational motion of the Earth including precession, rotation, nutation and polar motion which are currently estimated using VLBI measurements.

The time signal broadcast by the satellites is in GPS Time (GPST). This is synchronised with atomic clocks at the GPS master control station at Colorado Springs, which in turn are synchronised with Coordinated Universal Time (UTC). UTC is based on International Atomic Time (IAT), the fundamental time scale of the Earth's time keeping that is obtained from analyses of the atomic standards of many countries. IAT does not account for the slowing of the Earth's rotation with respect to the sun, currently averaging 1 s per year, so to account for this UTC is incremented by 1 s (a leapsecond) when necessary. GPST was set to UTC at 0 hr on 6^{th} January 1980, is not incremented by leap seconds, and at the time of the 1992 GPS survey in Iceland was 7 s offset from UTC.

3.2.6 Intentional Signal Degradation

Two effects have been introduced by the U.S. military to degrade the real-time navigational capabilities of GPS to unauthorised (civilian) users. These effects are *selective availability* (SA) and *antispoofing* (AS). SA is the "dithering" of the satellite clock frequency such that the accuracy of the code pseudoranges is decreased. This mainly affects real-time operations, i.e., navigation. Differencing the pseudoranges at the same epoch between two receivers eliminates the effects. SA also involves truncation of the transmitted navigation message, so the coordinates of the satellites cannot be so accurately computed in real time. Since April 1990, SA has been implemented intermittently.

AS involves turning off the P-code. Authorised (military) personel use the classified Y-code. In order to record data on both the L1 and L2 frequencies, which is necessary to make the substantial ionospheric correction, civilian users must then either count half wavelengths of the L2 carrier ("squaring") or reconstruct the P-code, a technique that increases noise in the P-code pseudoranges. Since October 1993, AS has been turned on permanently.

3.2.7 Error Sources

The accuracy of relative point positions calculated using GPS measurements is dependent on two factors: the measurement accuracy, and the geometric strength of the satellite configuration. The measurement accuracy is affected by *biases* and errors. Three types of bias are important: satellite-, station- and observation-dependent biases. They project into the calculated range and sum to produce the *range bias*. Satellite biases include errors in the satellite ephemeris and clock corrections. Station biases include biases in the receiver clock, and observation-dependent biases include errors from atmospheric delays and the carrier beat phase ambiguity (Tables 3.2 and 3.3).

Errors affecting the measured pseudoranges include phase *cycle slips* and *multipath* effects. A cycle slip results from a mistake in the integer cycle count, and may occur for a variety of reasons, e.g., signal- or receiver-generated noise or loss of lock because of a shaded antenna. The fractional part of the measured phase remains correct but the integer number of cycles is miscounted. Efficient methods

Table 3.2: Error sources of GPS measurements.

BIASES
- Satellite Dependent
    - satellite ephemeris
    - satellite clock
- Station Dependent
    - receiver clock
- Observation Dependent
    - ionosphere delay
    - troposphere delay
    - carrier beat phase ambiguity

ERRORS
- cycle slips
- multipath
- antenna phase centre movement
- random observation error

Table 3.3: Individual contributions to the range bias.

bias	contribution to range bias
satellite clock	300000 m (decreases to 10 m if broadcast correction is used)
receiver clock	10 m to 100 m
ionospheric delay	150 m at horizon to 50 m at zenith
tropospheric delay	20 m at 10° above horizon to 2 m at zenith
carrier beat phase ambiguity	anything

of detecting and correcting cycle slips now exist. Multipath occurs when a signal arrives at a receiver via two or more paths, e.g., because of reflection from nearby buildings. The difference in path lengths causes the signal to interfere at the receiver and may result in a noisy signal or indirect path of the signal recorded.

One measure of the geometric strength of the satellite configuration is the *geometric dilution of precision* (GDOP). GDOP is inversely proportional to the volume of the geometric body defined as having the satellites and the point as corners. This changes with time, as the satellites move. A small value of GDOP indicates well distributed satellites.

3.2.8 Linear Combinations of Dual Frequency Data

To facilitate cycle-ambiguity resolution and to reduce the effect of biases, the double differenced phase pseudoranges measured on the two carrier frequencies are linearly combined. Five combinations may be formed and processed. These are L1 and L2 (the original, double-differenced phase-range measurements), and the L3, L4 and L5 combinations (Table 3.4), obtained by combining L1 and L2 in the following manner [e.g., *Wells et al.*, 1986]:

$$L3 = \frac{f_1^2}{f_1^2 - f_2^2} L1 - \frac{f_2^2}{f_1^2 - f_2^2} L2, \tag{3.13}$$

$$L4 = L1 - L2, \tag{3.14}$$

$$L5 = \frac{f_1}{f_1 - f_2} L1 - \frac{f_2}{f_1 - f_2} L2, \tag{3.15}$$

Table 3.4: Linear combinations of the carriers L1 and L2, after *Wells et al.* [1986].

Carrier	Comment	Wavelength (cm)
L1	carrier wave	19
L2	carrier wave	24
L3	ionosphere-free linear combination	0
L4	geometry-free linear combination	infinite
L5	wide-lane	86

where f_1 is the frequency of carrier L1, f_2 is the frequency of carrier L2 and L1 and L2 are in metres. These linear combinations offer different processing advantages. L1 and L2 have the lowest noise. L3 contains no first-order ionospheric refraction effects and thus virtually eliminates the error from this source. L4 is independent of the receiver clocks and geometry (receiver and satellite positions), and is dependent only on the ionosphere and the ambiguities (for phase measurements). L5 is dependent on the point coordinates, the ionosphere and the difference between the L1 and L2 ambiguities (known as the L5 ambiguities). It has a very long wavelength, and thus resolution of the L5 ambiguities (from which may be derived the difference between the L1 and L2 ambiguities) is relatively easy.

3.2.9 Combining Multiple Point Coordinate Estimates

Combining several estimates of point coordinates is generally necessary in large surveys as multiple occupations of points are made in order to detect blunders and reduce random errors. The basic relationship between the baseline vector components is [e.g., *Heki*, 1992]

$$\vec{b_{ij}} = \vec{p_i} - \vec{p_j}, \tag{3.16}$$

where $\vec{b_{ij}}$ is a baseline vector connecting the ith and jth points, and $\vec{p_i}$ and $\vec{p_j}$ are the ith and jth point position vectors. The observation equation is

$$\vec{y} = A\vec{x} + \vec{v}, \tag{3.17}$$

where $\vec{x}$ is the vector composed of $3m$ parameters $(p_1^x, p_1^y, p_1^z, \ldots, p_m^x, p_m^y, p_m^z)$, $\vec{y}$ is the vector composed of the observations $(b_{12}^x, b_{12}^y, b_{12}^z, \ldots)$ (i.e., the individual session results), and $\vec{v}$ is its error vector. A is a Jacobian matrix composed of 0's and plus and minus 1's. A stochastic model of $\vec{v}$ is obtained by combining the covariance matrices for the individual sessions, Q_i, into Q. The following normal equation is then solved:

$$(A^T WA)\vec{x} = A^T W\vec{y}, \tag{3.18}$$

where W, the weight matrix, is Q^{-1}, and T denotes the transpose matrix, to give an estimate of $\vec{x}$, $\hat{\vec{x}}$, i.e.,

$$\hat{\vec{x}} = (A^T WA)^{-1} A^T W\vec{y}. \tag{3.19}$$

The coordinates are obtained by estimating corrections to a-priori coordinates. One or more points must be fixed or constrained in space since the problem is independent of an arbitrary translation. If fiducial points (points whose coordinates are known accurately) were occupied in the survey, then their coordinates can be fixed and the coordinates of the other points calculated relative to them. Fixing a point eliminates it from the observation equation or constrains it around its a-priori coordinates with a given uncertainty. If fiducial points have not been occupied in the survey, then the most accurately determined network point is used. The final set of point coordinates minimises the weighted sum of the squares of the differences between the individual session, and final coordinates.

3.3 GPS Data Processing

3.3.1 Introduction

The field data, consisting of code and phase pseudoranges and satellites ephemerides, must be processed to calculate precise, point-position coordinates. Several data processing software packages exist, e.g., GIPSY [*Stephens*, 1986; *Lichten and Border*, 1987] and the Bernese software [*Rothacher et al.*, 1990]. The latter software, installed on UNIX SUN workstations at the University of Durham, was used to process the Iceland data.

3.3.2 Overview

The Bernese version 3.2 GPS processing software [*Rothacher et al.*, 1990] creates double differences from the field data and inverts these to estimate the final parameters. Figure 3.3 shows the main components of the software.

1. The transfer component. This comprises a collection of programs to reformat field data with various formats into Bernese v3.2-readable form. The field data are first converted into RINEX format (Receiver INdependent EXchange format [*Gurtner et al.*, 1989]), and then into Bernese format. Separate files containing phase pseudoranges, code pseudoranges and satellite ephemerides are produced.

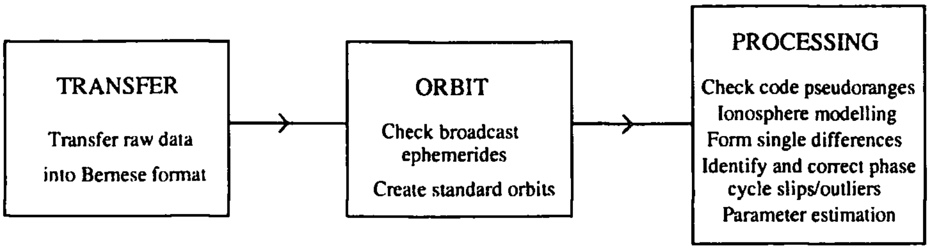

Figure 3.3: Flow diagram of GPS processing using Bernese GPS software version 3.2.

2. The orbit component. Accurate satellite orbits are generated for subsequent data processing. The broadcast orbit files are first checked for outliers then modelled to calculate continuous (tabular) orbits spanning the observation session. The ephemerides, originally transmitted as Keplerian elements, are transferred to an inertial coordinate frame, i.e., one which is either stationary or in uniform motion in space. Then, with each ephemeris treated as a series of data points spanning the hour for which it is valid, smooth (so-called standard) orbits are fitted, that correctly model the gravitational attraction of the sun and moon, higher orders of the Earth's gravitational field and solar radiation pressure. Each measurement session may have its own standard orbit file or one may be generated to cover several sessions. Precise orbits may be imported from some external source and modelled instead of broadcast ephemerides recorded in the field.

3. The processing component. These programs identify and correct outliers and cycle slips and generate an ionospheric model prior to parameter estimation. Parameters that may be determined include cycle ambiguities, point coordinates, troposphere and ionosphere delays and the full covariance matrix. Many steps are required to accomplish this.

Step 1. The code pseudorange data are checked for outliers. This is done by testing the data for short-period smoothness by fitting a low order polynomial.

Step 2. Receiver clock corrections and rough receiver antenna positions are simultaneously calculated using the outlier-free code pseudorange data. The receiver clock offset may be modelled as a polynomial with time, or as an independent offset at each epoch. The clock corrections are written into the phase files. The degree of the polynomial chosen depends on the quality of the receiver oscillator and a degree of 2 + the session length in hours is recommended. The receiver positions are calculated for each epoch using the ranges to the satellites and a single result is determined by computing the least squares solution for the whole measurement session. Absolute positions accurate to ~10 m may typically be determined.

Step 3. An ionospheric model for each measurement session is created for use when processing linear combinations of the pseudoranges other than L3 (in which the ionospheric delay cancels out). The ionosphere is modelled as a shell of infinitesimal thickness containing free electrons at a height of 350 km above the Earth's surface. The electron content of the layer is modelled as a low-order polynomial function of latitude and hour-angle of the sun. Data from all satellites and all stations are used to produce a least-squares model. This produces a smooth, average model, that may be used to make first order corrections for the ionospheric delay. However, it does not model ionospheric-delay fluctuations on the time scale of the recording interval (~30 s). If these "scintillations" are of the order of the wavelength of the phase data they may be confused with cycle slips. Ideally ionosphere modelling should be done after removing cycle slips from the phase data, but in practice it does not make much difference.

Step 4. Between-receiver phase single differences are created.

Step 5. Outliers and cycle slips are identified and corrected in the phase data by checking for smooth variation of the data. For normal data the number of outliers identified should not exceed 10% of the total data, otherwise an unusual problem exists [*K. Heki*, pers. comm., 1991].

Step 6. Parameter estimation is done. Parameters that may be estimated include the initial cycle ambiguities in the carriers, the X, Y and Z coordinates of the points, orbit parameters, ionosphere and troposphere models and the full covariance matrix for all estimated parameters. The greatest precision is achieved if the cycle ambiguities are resolved to their integer values, eliminated from the inversion and as few parameters as possible are estimated. Parameter estimation is conducted in several stages. Selected kinds of parameters are determined at each stage and problems solved progressively.

In the first stage of parameter estimation, the L3 combination is used and cycle ambiguities and point coordinates are estimated. The coordinates estimated in this step are the most precise yet generated, and this solution is known as the *ambiguity-free, ionosphere-free* solution since the ambiguities are not constrained to integers but solved as floating-point numbers. Atmospheric delays are usually made using a standard model, e.g., that of *Saastamoinen* [1972], which assumes standard meteorological conditions. At this stage any remaining cycle slips may be detected through inspection of the residuals of the single differences, in which slips appear as step discontinuities. Outliers and uninterrupted observation periods less than 30 epochs long are manually removed by editing the single difference files and the positions of new cycle slips are marked. The ambiguity-free solution is recalculated and this process repeated until there are no remaining cycle slips in the data.

In the second stage, the coordinates are fixed to the values calculated previously, and the L5 combination is used to estimate the L5 ambiguities as integers. The third stage is optional. The L5 ambiguities are held fixed at the integer values calculated, and the L1 and L2 cycle ambiguities are estimated using the L4 combination. Finally, the L3 combination is used and the point coordinates and any remaining L1 and L2 ambiguities are estimated simultaneously. The third, optional stage may be dispensed with if the data are of high-quality. This final solution is the *ambiguity-fixed, ionosphere-free* solution. Local tropospheric models may also be estimated, but this has been found to give little improvement in Iceland since the troposphere is cool, and thus contains little water vapour, which is the source of the most significant tropospheric delay (the "wet" component) [*Heki et al.*, 1993].

Step 7. In the case of surveys where some or all points were measured multiple times, several point-position estimates are obtained. Network adjustment is the process by which these estimates are combined to form a single, weighted least-squares set of point coordinates (a network solution). One method is to form a standard orbit file covering the entire survey, and to run the parameter estimation program once for all the data from all sessions. This may be a very large computational problem, but the Bernese software will correctly take account of correlations from such sources as common orbits in constructing the covariance matrix. Alternatively, the final coordinates and covariance matrices from the individual sessions may be used to calculate a post-processing, least-squares solution. This method is less computer-intensive but does not take account of all possible correlations.

3.3.3 Processing Procedure

The Bernese software comprises about 50 individual programs, only a few of which are used for a single data set [*Rothacher et al.*, 1990]. The programs used to process the Icelandic data collected as part of this project are specified in bold type. Processing proceeded as follows:

1. Translation of the field data into RINEX (**ASHTORIN**). The field data were separated into S-files, containing the point information, N-files containing ephemeris data, and O-files containing the pseudoranges. The RINEX files contain a-priori station locations, obtained by instantaneous positioning by the receiver using the code pseudoranges.

2. Translation of the RINEX observation files into Bernese v3.2 format (**RXOBV3**).

3. Translation of the RINEX navigation files into Bernese v3.2 format (**RXNBV3**).

4. Scanning of the orbit data files for outliers (**BRDTST**).

5. Translation of the orbit files from an Earth-fixed coordinate system to an inertial reference frame, and the formation of a tabular orbit (**BRDTAB**).

6. Formation of the standard orbit file (**DEFSTD**).

7. Scanning of the code-pseudorange data for outliers (**CODCHK**).

8. Calculation of point positions and clock corrections using the code pseudorange data (**CODSPP**).

9. Graphical examination of the residuals to check the result (**BRES**).

10. Estimation of an ionosphere model (**IONEST**).

11. Graphical examination of the ionosphere model to check the result (**IONGRA**).

12. Formation of single difference files (**SNGDIF**).

13. Cycle slip detection and coordinate estimation using a triple difference solution (**MAUPRP**). Program **MAUPRP** performs three steps; pre-preprocessing, formation of a triple-difference solution and automatic cycle slip detection. In the pre-

preprocessing stage, time intervals are identified within which, with great certainty, no cycle slips are present in the double differences. This is determined by fitting a low-order polynomial to a short time interval of data and marking poorly fitting points as outliers. Cycle slips appear as steps in the double differences. A triple difference coordinate solution is then calculated using the outlier-free data. Using these coordinates, the residuals of the original data are computed and cycle slips in the phase and code pseudorange files are identified and corrected. **MAUPRP** works separately on L1 and L2 in order to check whether detected cycle slips are real, or merely artifacts resulting from a turbulent ionosphere.

If code pseudoranges on both L1 and L2, are available, then steps 12. and 13. are performed in reverse order and cycle slip detection may be performed on the undifferenced phase data using the algorithm **TurboEdit** [*Blewitt*, 1990]. This often performs better than **MAUPRP**. Outliers and cycle slips are detected by comparing subsequent-epoch data. The difference between consecutive epochs must lie within 4 x the standard deviation of the running mean, or else a cycle slip is considered to be detected [*Blewitt*, 1990].

Both **MAUPRP** and **TurboEdit** are insensitive to cycle slips less than 5 or 6 cycles in size, and minimum thresholds of about 5 may be set. Smaller cycle slips are detected by eye and corrected by hand at the parameter estimation stage (14. below).

14. Estimation of the coordinates and ambiguities as floating point numbers, fixing the coordinates of one station (**GPSEST**).

15. Graphical inspection of the single-difference residuals for outliers and cycle slips smaller than the detection threshold of **MAUPRP** or **TurboEdit** (**BRES**).

16. Correction of undetected cycle slips in phase data files by manual insertion of cycle slip flags (**BVI**).

17. Repetition of steps 14.-16. until the data are free of cycle slips.

18. Estimation of L5 ambiguities (program **GPSEST**), fixing all station coordinates to the values calculated in the previous run of **GPSEST** and using the ionosphere model calculated using **IONEST**.

19. Graphical inspection of L5 residuals for any remaining cycle slips (slips that

are the same size in L1 and L2 do not show up in step 15.) (**BRES**).

20. Correction of cycle slips as for step 16. and repetition of steps 18. and 19. until the data are free of slips.

21. Estimation of point coordinates and resolution of the L1 and L2 ambiguities. Two methods were used. The first used the **GPSEST** L4 option where the L1 and L2 ambiguities are resolved and the point coordinates held fixed, followed by the **GPSEST** L3 option in which the remaining ambiguities and station coordinates are estimated simultaneously. The second method used the **GPSEST** L3 option and solved for the L1 ambiguities and station coordinates simultaneously in one step. The first method was used for the 1991 data set and the second method for the high-quality 1992 data set.

22. Network adjustment (**NETADJ** [*Heki*, 1992]).

3.4 Summary

GPS is one of three space-geodetic techniques currently widely used for surveying point positions. The system consists of 21 satellites, each transmitting signals on two carrier frequencies which are modulated with known binary codes. GPS receivers can record transmitted orbital and timing information, and also make code- and carrier-beat phase-pseudorange measurements. These are affected by several error sources, including orbit errors, ionospheric dispersion effects and cycle slips. In addition, the accuracy of relative point positions calculated using these measurements is dependent on the geometric strength of the satellite configuration. To reduce or eliminate these errors, the code- and phase-pseudorange data are combined to form single, double and triple differences.

Satellite orbits are described in a celestial reference frame using Kepler's three laws. Account is also taken of the effect of additional perturbing forces such as solar radiation pressure and atmospheric drag. Station locations are required in a terrestrial reference frame. The time signal broadcast by the satellites is based on International Atomic Time. Two effects have been intentionally introduced by the US military to degrade the real-time navigational capabilities of the system.

Several GPS data processing software packages exist, and can analyse the field data to produce point positions with sub-centimetre precision. The Bernese v3.2 software was used for this project. It can be split into three main components. The first translates field data into Bernese format. The second component enables checking of the broadcast orbit files for smoothness before generating a standard orbit file. The third component includes programs to identify and correct outliers and cycle slips, generate an ionosphere model and estimate parameters. This last step can use five different linear combinations of the double-differenced carrier-phase data to estimate the L1 and L2 ambiguities and produce point coordinates. If points were surveyed independently multiple times a weighted least-squares estimate of the point coordinates is made (network adjustment).

Chapter 4

GPS Satellite Surveying in Iceland

4.1 Introduction

GPS surveying has now been widely applied to determine crustal deformation in Iceland. Several surveys have been carried out including a countrywide survey in 1986 [*Foulger et al.*, 1993], and several regional surveys. These include surveys in 1987 and 1990 in north Iceland to detect ground motion following the rifting episode that began in the Krafla volcanic system in 1975 [*Foulger*, 1987; *Jahn et al.*, 1990; *Heki et al.*, 1993; *Jahn et al.*, 1994], surveys in 1989 and 1992 in the SISZ and on the Reykjanes Peninsula [*Hackman*, 1991; *Sturkell et al.*, 1994], surveys in 1991 around the Vatnajökull icecap and the Hengill triple junction, and a survey in 1993 in the southernmost EVZ to determine motion following an eruption of the volcano Hekla [*Sigmundsson et al.*, 1992].

In addition to a description of the fieldwork, an overview of the most important points concerning the data processing are given in this chapter. The full data-processing computer directory trees are archived electronically at the University of Durham, and all the processing details not covered in this chapter are preserved there.

4.2 Field Procedure

The GPS survey points measured in Iceland usually consist of metal discs or pins embedded in bedrock and on open ground. A small dot is marked in the centre

Figure 4.1: A typical set of GPS field equipment.

of the disc over which the antenna is centred. Identification marks are usually stamped around the rim, indicating the site number and the owner-institute.

A set of GPS field equipment includes a receiver and antenna (and associated connecting cables), a power source for the receiver, a tripod, tribrach, optical plumb and tape measure (Figure 4.1). The procedure for setting up the equipment involves the following basic steps:

1. Antenna positioning. The tripod is accurately centred over the geodetic point using a tribrach and optical plumb. It is first positioned as accurately as possible over the point and coarsely levelled by moving two of the legs. Accurate levelling is achieved by adjustment of the tribrach, which is then centred over the point using the optical plumb. The optical plumb is then removed and the antenna screwed onto the tribrach and oriented north in order to reduce phase centre biases between antennas at different points.

2. Antenna height measurement. The slant height of the antenna rim above the point is measured, usually at three different azimuths in order to provide a check.

3. Equipment power up. The antenna is connected to the receiver which is then switched on.

4. Recording. The receiver is checked periodically to ensure that recording is continuing.

5. Ending the session. The receiver is switched off at the end of the recording session, typically several hours for regional-scale surveys.

6. Antenna height remeasurement. This is done before the tripod is taken down to check that the tripod has not moved, e.g., in the wind.

7. Data download. This is done as soon as possible to, for example, floppy discs.

4.3 GPS Surveys in Iceland

4.3.1 Surveys Prior to 1991

GPS surveys were carried out in Iceland in 1986, 1987, 1989 and 1990 (Table 4.1). The 1986 survey [*Foulger et al.*, 1993] aimed to survey the SISZ to accuracies adequate for geodynamic research, and to measure a country-wide network which would form the basis of a new first-order geodetic network. Site descriptions for this survey are given by *Gudmundsson and Einarsson* [1986].

In July 1987, a GPS survey of north Iceland covering an area of 250 x 250 km, was conducted by the Universities of Durham, Hannover and members of the Icelandic GPS Coordinating Committee [*Foulger*, 1987; *Jahn et al.*, 1990; *Heki et al.*, 1993]. This survey aimed to establish a dense network to study tectonic motion around the spreading plate boundary there. The points occupied were densely spaced within the Krafla volcanic system and sparsely distributed throughout an area extending 130 km into the adjoining plates (Table 4.1; Figure 4.2). The network

Table 4.1: The 1986, 1987, 1989 and 1990 GPS surveys in Iceland.

Date	Location	Number of points	Number of receivers	Total Satellites	Session length	References
13/7/86–24/7/86	all Iceland	51	7 TI4100's	4	50 min (am) 1 hr 50 min (pm)	*Foulger* [1987] *Foulger et al.* [1993]
3/8/87–24/8/87	N Iceland	63	7 TI4100's	6	3 hr 20 min	*Jahn et al.* [1990] *Heki et al.* [1993]
27/7/89–21/8/89	S Iceland	57	6 TI4100's	3–4	6 hr 30 min (am) 5 hr 04 min (pm)	*Hackman* [1991]
30/7/90–19/8/90	N Iceland	61	7 TI4100's	7	4 hr 10 min	*Jahn et al.* [1991] *Heki et al.* [1993]

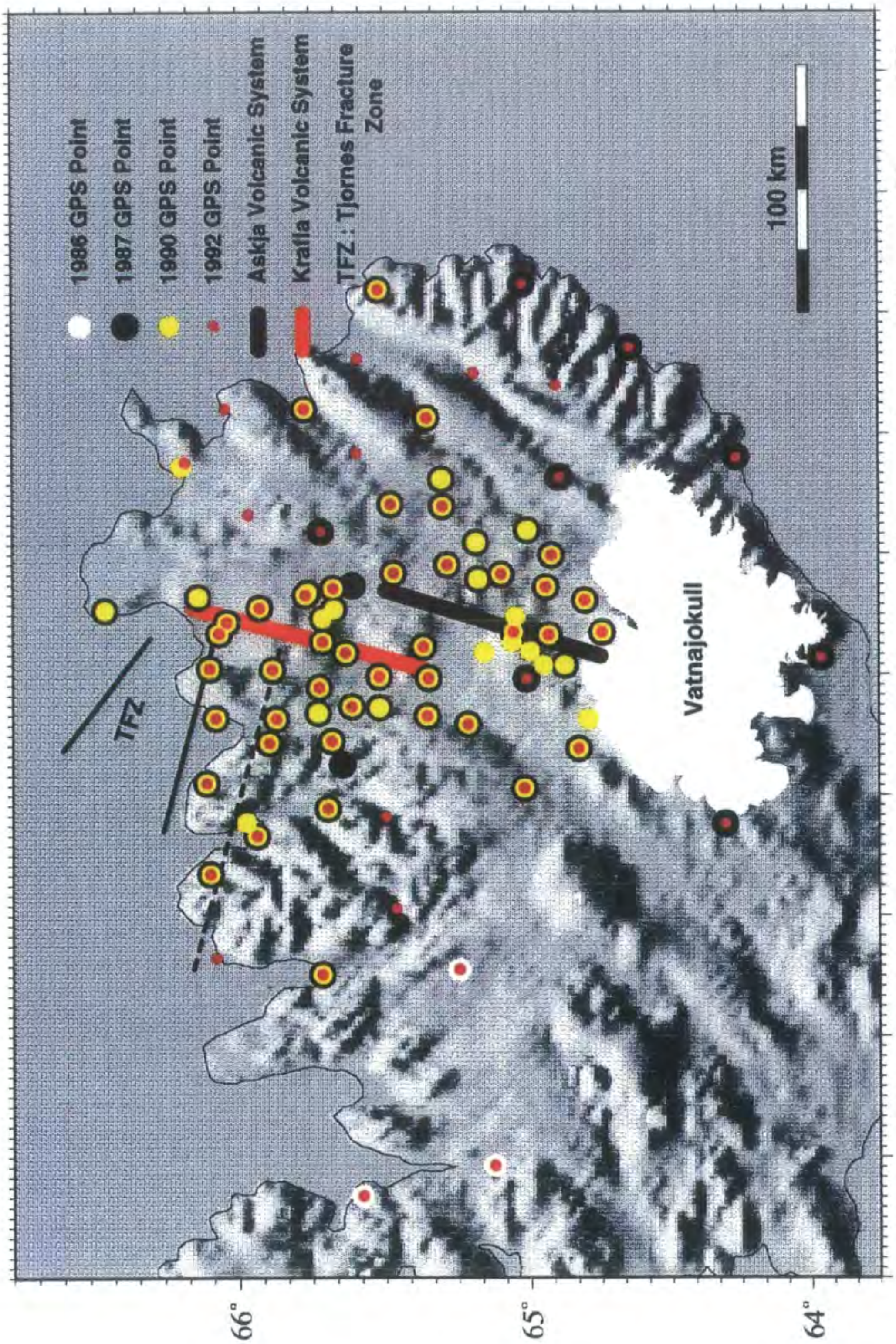

Figure 4.2: The 1986, 1987, 1990 and 1992 Iceland GPS points.

also covered the Askja volcanic system and the TFZ. Site descriptions are given by *Gudmundsson and Einarsson* [1987].

In 1989, the 1986 network in the SISZ, was densified and resurveyed in order to detect crustal deformation in and around the SISZ [*Hackman*, 1991].

In August 1990, most of the 1987 network was remeasured [*Jahn et al.*, 1991; *Heki et al.*, 1993] (Table 4.1). Selective availability was implemented for the first two thirds of the survey. Site descriptions for this survey are given by *Einarsson* [1992].

GPS surveying began very early in Iceland. This has resulted in the Icelandic data providing some of the earliest GPS deformation results in the world. Early surveys suffered from few satellites and having to use TI4100 receivers, which are only capable of tracking four satellites at a time, and these factors degraded accuracy. However, accuracies presently attainable are degraded by SA and AS, so the early results do not compare as badly with the newer ones as might be supposed.

4.3.2 The 1991 Vatnajökull GPS Survey

In July 1991, GPS measurements were made around the Vatnajökull icecap, in order to establish a network to monitor isostatic movements in response to melting during the 20^{th} century. The stations were sited at varying distances from the edge of the icecap in order to detect the variation of uplift with distance from the icecap, since points farther from the icecap are expected to undergo smaller-magnitude isostatic movements. The project was collaborative between the Universities of Colorado, USA, Iceland and Durham. Three Ashtech MDX11 C/A-code GPS receivers, supplied by the Natural Environment Research Council (NERC) UK, recording squared L2 phase data were used. From July 6^{th} to 19^{th}, 10 points east and southeast of the icecap were occupied (Figure 4.3; Table 4.2). Of these, eight were installed during the survey period and the remaining two (Djup and Hofn) were existing survey points occupied in the 1987 survey. Point Hofn was occupied virtually continuously from July 6^{th} to 19^{th} and the other sites were occupied a minimum of three times each. Two observation windows per day were used. The start and end time of these windows varied somewhat from session to session as a result of site accessibility and transport availability. The windows 00:30 to 08:00 (local time) (session 0) and 15:00 to 19:00 (session 1) were usually used. During

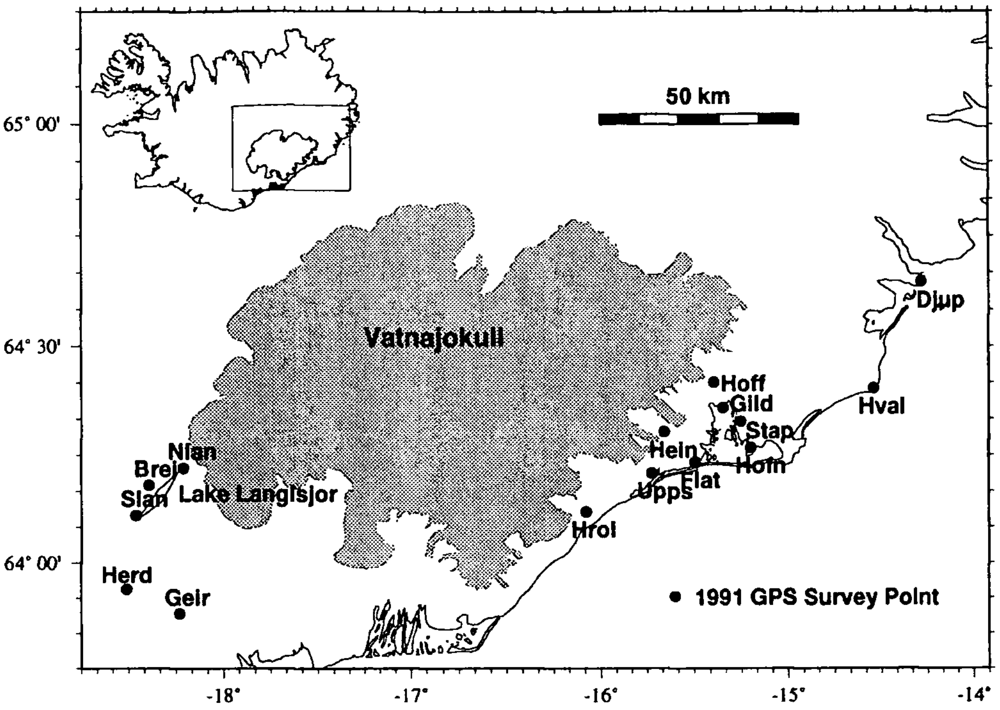

Figure 4.3: The 1991 Vatnajökull GPS network.

these windows up to six satellites were observed simultaneously and up to a total of 15 were observed throughout a single session.

Data were recorded at 10-second intervals during session 0, in order to fit them on a single 1.4 Mbyte floppy disc (the downloading software at the time precluded the splitting of data files), and at five-second intervals during session 1. A 10° minimum satellite elevation angle was used. The data for sessions 188.1, 189.1, 191.1 and 192.1 were collected using a kinematic technique [*P. Einarsson*, pers. comm., 1991], before the author's arrival in the field. The power sources used for the receivers were standard car batteries, and these, the tripods, levels for antenna set-up and other equipment, e.g., tape measures, were supplied by the University of Iceland. Two, four-wheel drive vehicles were used, also supplied by the University of Iceland. Sleeping bag accommodation was provided by a local school in Höfn, where downloading of the data and battery recharging also took place.

From July 27^{th} to 31^{st}, five points southwest of Vatnajökull were occupied using GPS (Table 4.2), and measurements of the water level of Lake Langisjór (Figures 4.3 and 4.4), a glacial lake at the edge of the icecap, were also made. Several sets of

Table 4.2: Point occupation schedule during 1991 Vatnajökull GPS Survey.

		Point														
July	*Session*	Hofn	Stap	Gild	Hoff	Flat	Hein	Upps	Hrol	Hval	Djup	Nlan	Slan	Brei	Geir	Herd
6	187.1	●	●													
7	188.0	●			●											
7	188.1*	●			●											
8	189.0	●		●												
8	189.1*	●		●												
9	190.0	●				●										
10	191.0	●					●									
10	191.1*	●					●									
11	192.0				●	●										
11	192.1*	●	●													
12	193.0					●	●									
12	193.1				●		●									
13	194.0		●	●		●										
13	194.1	●			●						●					
14	195.0	●			●						●					
14	195.1	●					●				●					
15	196.0	●			●											
15	196.1	●	●			●										
16	197.0	●		●				●								
16	197.1	●				●			●							
17	198.0	●						●	●							
17	198.1	●					●		●							
18	199.0	●								●						
18	199.1	●		●						●						
19	200.0				●			●		●						
27	208											●	●	●		
28	209											●	●	●		
29	210											●	●	●		
30	211												●	●	●	
31	212												●		●	●

* Data collected using a kinematic technique, not analysed as part of this project.

Figure 4.4: Lake Langisjór, looking north from the southwestern end of the lake.

Figure 4.5: Measuring the height of a (submerged) strand line relative to the lake level.

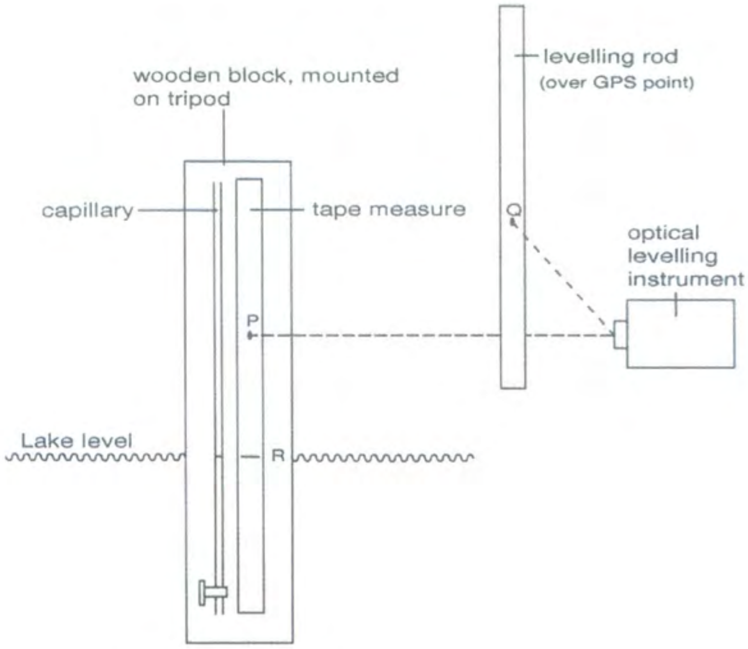

Figure 4.6: The device invented by the University of Iceland to measure lake-level variations on an hourly basis. A levelling rod was erected over the GPS point, and the device was mounted on a tripod in the lake. Points P and Q were level with each other at different azimuths. Their values were read using the optical levelling device. The tap on the capillary was then closed, and the height *PR* read directly from the tape measure. Lake level variations were evident from the differences between P and R.

Figure 4.7: Typical field accommodation during the 1991 Vatnajökull GPS survey.

strand lines are visible around the edge of Lake Langisjór and measurement of the heights of these above the present lake level at the northeast and southwest ends of the lake provided an estimate of tilt of the lake due to recent isostatic movements. Measurements were also taken of the height of a submerged strand line relative to the lake level (Figure 4.5). If the tilt is a result of isostatic uplift due to melting of Vatnajökull, then the difference in height between the strand lines should increase as the icecap is approached. Estimates of the heights above the present lake level were made by laying a tape measure parallel to the dip of the beach, and taking height measurements relative to the present lake level using a levelling rod and an optical level. The position of the optical level was kept fixed and successive height measurements taken at intervals of about 50 cm along the tape measure using the levelling rod and optical level.

Hourly variations in the level of the lake were also measured at both ends of the lake, close to GPS points, using the level and a device invented by the University of Iceland which allows precise differences between a fixed point on a rod and the water level to be read (Figure 4.6). This device consists of a capillary tube with a tap on the lower end, fixed onto a board with a tape measure. The device was mounted on a tripod and positioned in the lake with the tap open. The optical level was then used to make a reading on the level rod placed on the GPS point and then rotated to make a reading from the device tape measure. The tap was then closed and the height of the water in the capillary read using the tape measure. The lake level variations were estimated from the difference in height between the GPS point and the water level in the capillary tube.

Accommodation during the Langisjór survey consisted of two tents (Figure 4.7). Downloading of data onto 1.4 Mbyte floppy disks was done in the field vehicles and powered by the car batteries. Recharging of these batteries was done using petrol powered generators.

4.3.3 The 1992 GPS Survey

From 26th July to 24th August 1992, much of the GPS network in north Iceland that was measured in 1987 and 1990 was remeasured, and additional points were added (Figure 4.2). The fieldwork was colloborative between the Universities of Durham and Hannover. Seven Ashtech MDX11 dual-frequency GPS receivers were

Table 4.3: Point occupation schedule of the Iceland 1992 GPS survey.

	Session																							
Point	209	210	211	213	213.1	216	216.1	217	219	219.1	220	223	224	225	226	227	227.1	230	230.1	231	232	233	234	237
I01			●													●	●						●	
I02			●										●											
I04			●										●											
I05			●																					●
I06			●														●						●	
I08	●		●																					
I09													●		●									
I10	●												●											
I11	●												●											
I13	●														●									
I14	●													●									●	
I17	●													●										
I18									●					●										
I19															●									●
I20	●	●													●									
I22																								●
I23		●													●									
I25		●																						
I26		●													●									
I28		●							●															
I31		●							●	●	●													
I34									●	●	●													
I35											●											●		
I37									●													●		
I38									●													●		
I39												●		●									●	
I40												●		●										
I41												●		●										
I42				●	●							●						●						
I43				●	●	●	●	●										●				●		
I44									●													●		
I46						●	●	●													●	●		
I47												●						●						
I48																		●						
I49																		●	●	●				
I50																		●						
I51																			●					
I52																				●				
I53						●	●	●												●				
I54				●	●																			
I56				●	●															●				
I57				●	●																			
I58				●	●																			
I59				●	●	●		●																
I60						●	●	●																
I61						●	●	●																
I62						●	●	●													●			
I65																		●		●				
I67																				●				
I80			●													●	●							
I82											●													
I83											●													
I84											●													
I85											●										●			
I86																					●			
I87																					●			
I88																					●			
I89												●											●	
I90																●							●	
n05																●	●							
n07																●	●							
n08																●	●							

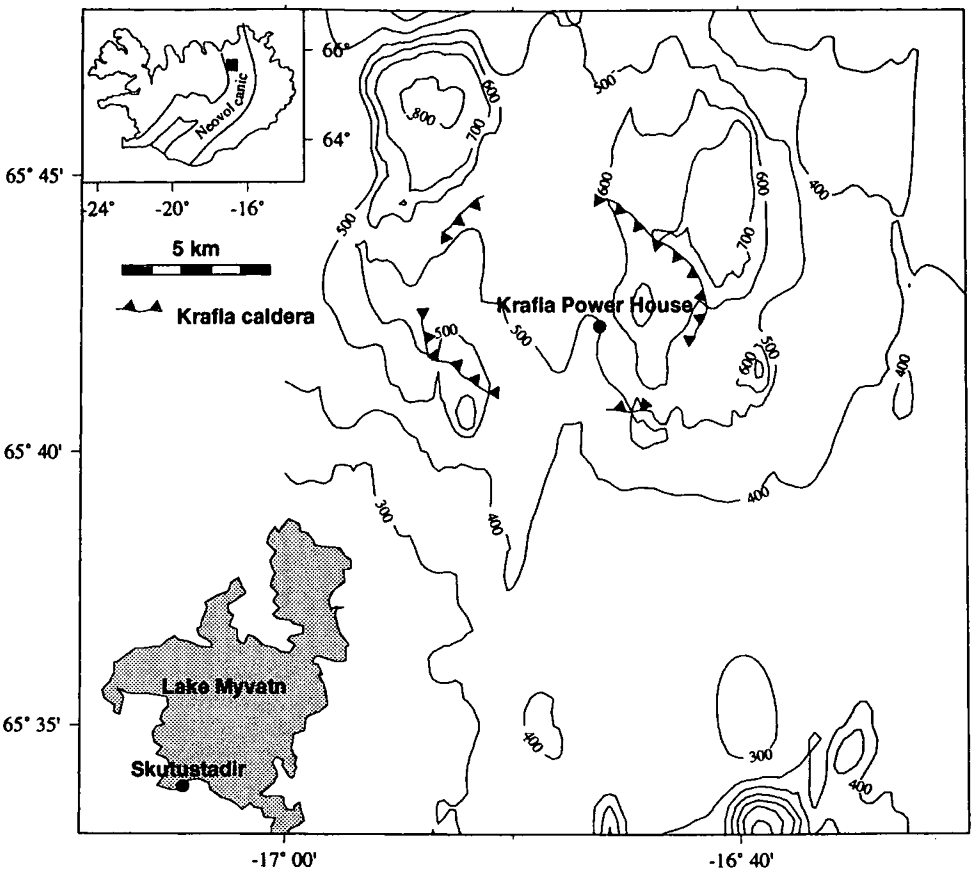

Figure 4.8: Place names referred to in the text.

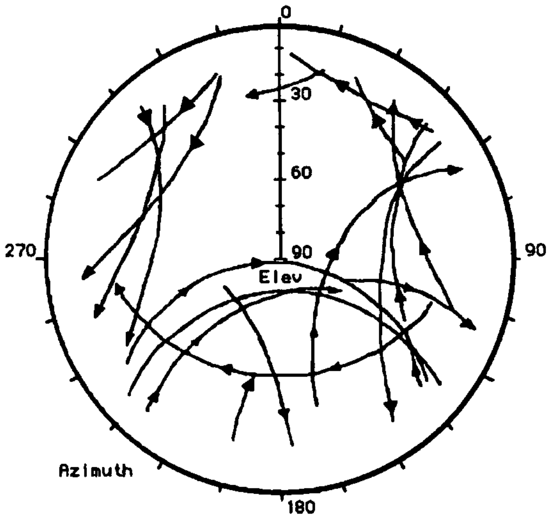

Figure 4.9: Sky chart of satellites observed above a 10° cut-off angle during the period 09:00 to 18:00, 31^{st} August 1992 at 65°N 16°W.

used, three supplied by NERC and four by the University of Hannover. The points measured, and new points added to the network, were selected on the basis of forward extrapolations from modelling the 1987 to 1990 deformation field in north Iceland [*Heki et al.*, 1993]. Some closely-spaced points within the neovolcanic zone measured in previous surveys were omitted, and 14 more distant points were added. Three of these had been occupied using GPS in 1986 and 11 were new GPS points to the east, west and southeast of the network (Figure 4.2). A total of 62 points were measured over a 20-day period (Table 4.3). No observations were made at the weekends as AS was in effect at these times and the receivers could not record under such circumstances.

A five-hour recording session was used, with data being recorded at 15-second intervals. This session was usually during the day, since experience has shown that ionospheric noise is lowest then in north Iceland [*C.-H. Jahn*, pers. comm, 1992]. However, on some occasions data were recorded for considerably longer periods (up to 18 hours) when the drive times to the points were long. The tripods were sometimes reset in the middle of these recording sessions. The reason for this was that the data from these sessions were split to provide two sessions and if the tripods had not been reset, misleadingly good coordinate repeatabilities would have resulted from the absence of tripod set-up errors between the sessions. The second halves of these split sessions are coded .1 in Table 4.3.

The satellite constellation was almost complete at the time of the survey, so observations could be made at virtually any time of the day. No site was occupied continuously as in previous surveys since this had been found to produce no significant improvement in the final results as a consequence of the more numerous long lines with relatively poor accuracy [*C.-H. Jahn*, pers. comm., 1992]. Up to 18 satellites were observed during each session and up to seven satellites simultaneously (Figure 4.9).

Tripods and optical levels (supplied by the University of Hannover) were used for positioning the antennas above the points and the slant height of the antenna above the point was measured using a tape measure. The power sources for the receivers were standard car batteries and these were recharged overnight using mains, petrol generators or car engines. Seven, four-wheel drive vehicles were used, two supplied by the University of Durham and five by the University of Hannover. Field accommodation was in the Krafla power station, a local school at Skútustadir

(Figure 4.8) and in tents or bed-and-breakfast places when points were measured long distances from the survey headquarters in the Mývatn area (Figure 4.8).

Few major problems were encountered. Extreme winds in the Icelandic interior resulted in some tripods being blown down, but the field practice of weighting the legs of the tripods with rocks largely prevented this problem. One antenna was not working at the start of the survey, but a replacement was rapidly delivered by Ashtech. The NERC receivers occasionally lost recorded data from memory when they were switched off at the end of a session, and data were lost on the first day because of this. To prevent this recurring, the data were thereafter downloaded to floppy disk at the survey point before the receivers were switched off. This was done using portable PC's powered by the field-vehicle batteries via the cigarette lighter. The data from the Hannover receivers were downloaded either at Skútustadir or at the Krafla power station. At the end of the survey, the whole data set was archived onto two 60-Mbyte data cartridge tapes using a portable HP workstation, supplied by the University of Hannover.

4.4 Data Analysis

4.4.1 Analysis of the 1986, 1987 and 1990 GPS Data

The 1986 data were processed by scientists at the University of Bern [*Foulger et al.*, 1993]. Analysis was difficult as a result of the short morning satellite window, the small number of satellites available in 1986 and rapid ionospheric variations. An ambiguity-fixed, ionosphere-free solution was produced for the southern part of the network, and an ambiguity-free, ionosphere-free solution for the country-wide network. These two solutions were combined to give the final total survey solution.

The 1987 and 1990 data sets were processed at the University of Durham using the Bernese v3.2 software [*Heki et al.*, 1993]. Resolution of the L1 and L2 ambiguities for the 1987 data set was successful. However, this was more difficult in the case of the 1990 data, due to excessive ionospheric noise at the time of the sunspot maximum. The best solution for the 1990 data was the ambiguity-free, ionosphere-free solution. To reduce multipath effects, 15°–20° satellite cut-off angles were used. The 1987 and 1990 data sets were also processed independently at the University of Hannover using the GEONAP software [*Jahn et al.*, 1994].

4.4.2 Analysis of the 1991 Vatnajökull GPS Data

The data from all sessions were split into two halves for processing, except sessions 187.1, 188.0, 198.1 and 199.1 which were too short to split. Data analysis was conducted as summarised in Section 3.3.3, with details as follows. Processing step numbers correspond to those of Section 3.3.3.

1. Translation of the field data into RINEX format (**ASHTORIN**). The S-files of the first nine sessions were not downloaded to floppy disk because of insufficient space on the floppies. In order to create the RINEX files for these receiver sessions, S-files from different sessions were substituted.

2. Translation of the RINEX observation files to Bernese format (**RXOBV3**). The site information in the Bernese files were checked, in particular the vertical antenna height above the point which is calculated from the slant height and entered manually.

3. Translation of the RINEX navigation files to Bernese format (**RXNBV3**). One file per session was created.

4. Scanning of the orbit file for outliers (**BRDTST**). During some sessions the orbit messages from some otherwise-usable satellites were not broadcast. Substitute data from the Scripps Institute of Oceanography, USA, were used where possible, but some satellite data had to be deleted from the pseudorange and phase files where no orbits were available.

5. Formation of a tabular orbit file (**BRDTAB**).

6. Modelling to form a standard orbit file (**DEFSTD**). One file per session was created. Two iterations were usually required. Typical post-fit RMSs were $\sim$ 1.0 m.

7. Scanning of the code pseudorange data for outliers (**CODCHK**). Typically one outlier per satellite was detected.

8. and 9. Single point positioning to calculate clock corrections and rough absolute station locations (**CODSPP**). The a-priori station positions were obtained from

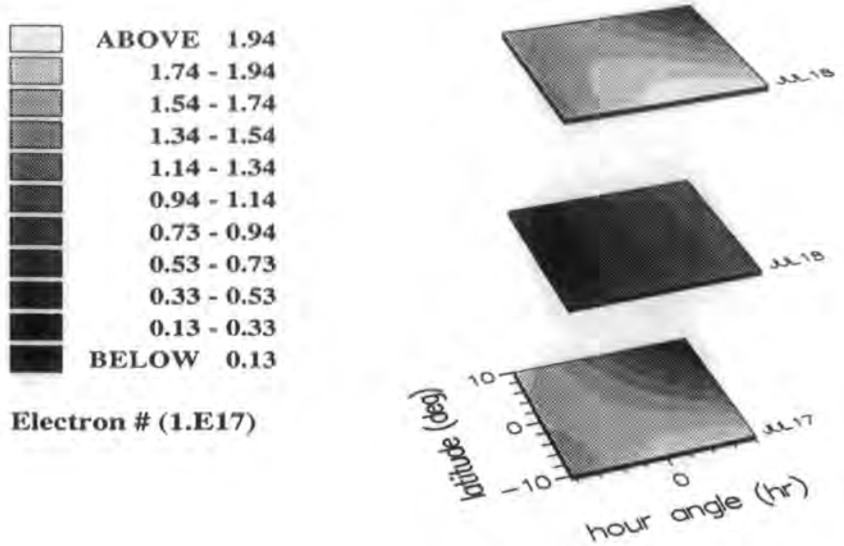

Figure 4.10: Ionospheric models for sessions 198.1 (bottom), 199.0 and 199.1 (top), covering the local time periods 13:18–21:24 (8.1 hours), 23:42-07:24 (7.7 hours) and 13:30–21:42 (8.2 hours) respectively.

the original RINEX files, except for station Hofn for which the 1987 coordinates were used. A 10° cut-off angle was used and the troposphere modelled using a Saastamoinen model. One clock correction per epoch was estimated. RMS residuals of about 20 m for the point coordinates were usually obtained. New–a-priori coordinate differences were generally up to a few 100 m.

10. and 11. Estimation of an ionosphere model (**IONEST**). A 20° cut-off angle was used. Figure 4.10 shows the results for sessions 198.1, 199.0, and 199.1. The electron content varies by about an order of magnitude and the wide variation in ionospheric behaviour between sessions at different times of the day, and the similarity between sessions at the same times on consecutive days is evident. Electron content tends to be lower during the day than at night. Post-fit RMS residuals of 0.1–0.3 m were typically obtained.

12. Formation of single difference files (**SNGDIF**). Stations were paired in such a way as to maximise the amount of single difference data and minimise the distances between paired stations.

13. Outlier and cycle-slip detection and correction in the phase and pseudorange data. Program **MAUPRP** was used. The 1991 data were abnormally noisy and

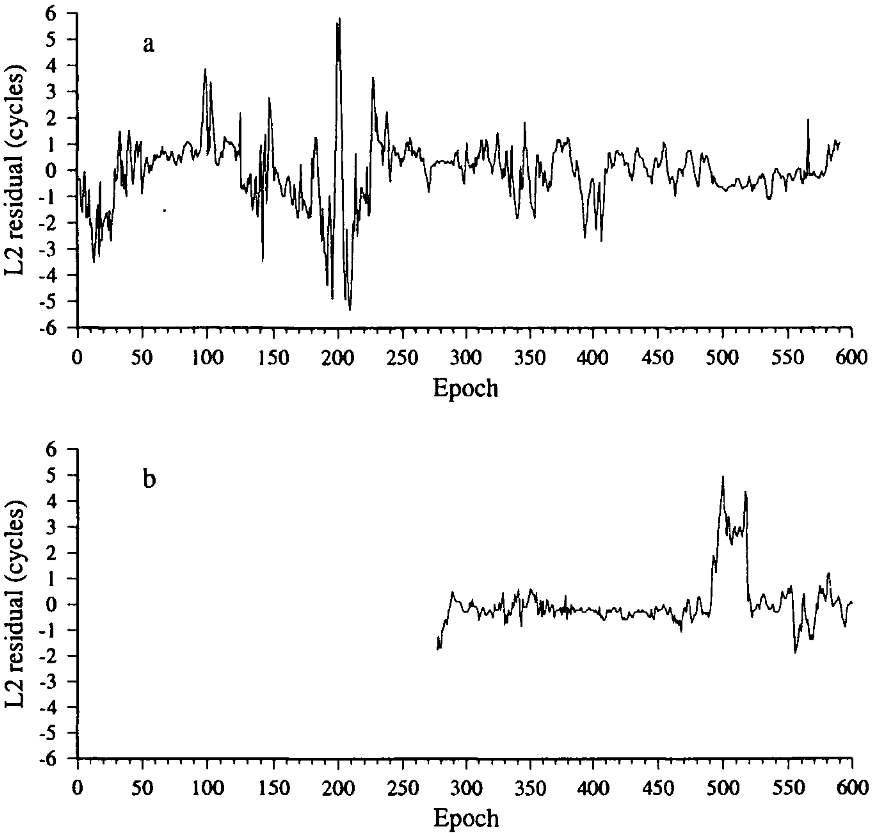

Figure 4.11: L2 residuals (calculated – observed) (post-**MAUPRP**) of single differences between stations Hofn and Hoff for the unsplit session 194.1. The data correspond to the time period 14:38 to 19:38 local time for satellite combinations (a) 11 and 17, and (b) 2 and 16.

such a large number of outliers were identified that it was clear that the program was not working well with these data. The noise probably resulted from both ionospheric scintillations and cycle slips. In order to prevent **MAUPRP** from eliminating many false outliers, it was necessary to increase the maximum ionospheric difference allowable between epochs as a percentage of the L1 wavelength from the recommended 40% to the maximum allowed of 999%, this latter effectively disabling outlier rejection completely. In this case **MAUPRP** functioned solely to produce point coordinates using triple differences.

Figure 4.11 shows the post-**MAUPRP** L2 residuals for single differences between stations Hofn and Hoff on the unsplit session 194.1. The noisy nature of the data is well illustrated in the residuals of satellite pair 11 and 17 (Figure 4.11a). It is impossible to tell whether this noise is ionospheric scintillations at a similar frequency to the measurement frequency (0.1 or 0.2 Hz) or frequent cycle slips. This figure also illustrates the effect of orbital errors. The average residual deviates systematically from zero over long periods as a result of broadcast orbit inaccuracies. The data from satellite combination 2 and 16 (Figure 4.11b) are much less noisy. A cycle slip of 5 cycles occurs near epoch 500.

14. to 17. Estimation of the coordinates and ambiguities as floating point numbers using the L3 combination (**GPSEST**). The coordinates of site Hofn were fixed to the values obtained from the 1987 data processing. Other a-priori coordinates used were the triple difference coordinates calculated by program **MAUPRP**. As the data were so noisy and cycle slip detection using **MAUPRP** worked rarely, many slips remained that had to be detected by inspection of the residuals of the single differences after coordinate estimation. As the L3 combination eliminates most of the ionospheric effect, cycle slips could be unambiguously detected at this stage. The data from some satellites were so noisy as to be unusable, and had to be deleted.

A 20° minimum satellite elevation angle was used. As with previous surveys, local tropospheric parameters were not estimated.

This step was repeated several times and cycle slips gradually eliminated until the data were clean. Approximately 10% of the data were discarded and three sessions were unusable due to the extreme noise levels in the data. These were the second half of session 194.1 and the entire session 195.1. Line-length RMS residuals were of the order of 0.1 m.

18. to 20. Estimation of L5 ambiguities using **GPSEST**. All point coordinates were held fixed to the values calculated in the last run of **GPSEST**. A 15° minimum satellite elevation angle was used. All L5 ambiguities were resolved once all cycle slips had been detected and corrected. Typical RMS residuals of 0.2 m were obtained.

21. Estimation of point coordinates and resolution of the L1 and L2 ambiguities. The **GPSEST** L4 option was used to resolve the L1 ambiguities, followed by the L3 option to resolve the coordinates and remaining L1 ambiguities. Remaining ambiguities were rarely resolved in the L3 option, however, in total, 98% of the L1 and L2 ambiguities were resolved. A 20° minimum satellite elevation angle was used. Typical RMS residuals of 0.15 m were obtained in the L4 option and line-length RMS residuals of 0.2 m in the L3 option.

22. Network adjustment (**NETADJ**). This was done relative to site Hofn. The coordinates of site Hofn were held fixed to the values obtained from the 1987 data processing.

4.4.3 Analysis of the 1992 GPS Data

The 1992 data set was of a higher quality than the 1991 data. This was due to the decrease in sunspot activity following the 1990 sunspot maximum resulting in fewer ionospheric scintillations, the more complete GPS satellite configuration, and the fact that P-code data were recorded. Data analysis was conducted as follows, and very few processing problems were encountered.

1. to 3. Translation of the field data into RINEX (**ASHTORIN**). Translation of the RINEX observation and navigation files to Bernese format (**RXOBV3**, **RXNBV3**). One file per session was created.

4. Scanning of the orbit file for outliers (**BRDTST**).

5. Formation of a tabular orbit file (**BRDTAB**).

6. Formation of a standard orbit file (**DEFSTD**). One file per session was created. Two orbit-modelling iterations were usually required. Typical post-fit RMSs were ~1.5 m.

7. Scanning of the code-observation file for outliers (**CODCHK**).

8. and 9. Single point positioning to calculate clock corrections and station location estimates (**CODSPP**). The a-priori station positions were obtained from the 1987 results, except for new sites whose coordinates were obtained from the RINEX files. A 10° cut-off angle was used, and the troposphere modelled using a Saastamoinen model. One clock correction per epoch was estimated. RMS residuals of about 20 m for the point coordinates were usually obtained. New–a-priori coordinate differences were generally in the range 10–20 m, except for new sites when differences were of the order of a few 100 m.

10. and 11. Estimation of an ionosphere model (**IONEST**). The ionosphere models for each session showed similar trends to the 1991 model (Figure 4.12). Over the survey as a whole, ionospheric variations are not as great as they were during 1991.

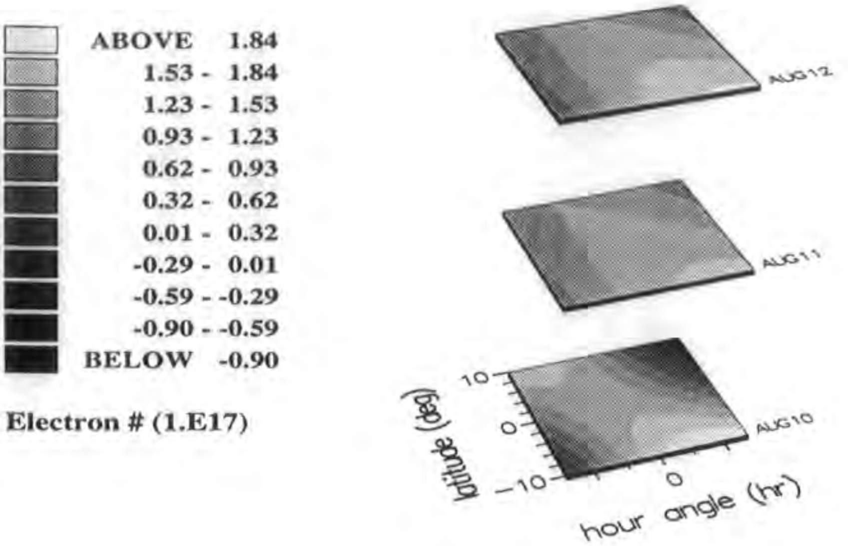

Figure 4.12: Ionospheric models for sessions 223 (bottom), 224 and 225 (top) covering time periods 07:30–19:54 (12.4 hours), 08.54–18:36 (9.7 hours), and 08:06–19:18 (11.2 hours) respectively.

Post-fit RMS residuals of 0.1–0.3 m were typically obtained.

12. Outlier and cycle slip detection and correction in the phase and code pseudorange data. Program **TurboEdit** could be used as P-code data were recorded. Backup copies of the phase and pseudorange files were first made as **TurboEdit** edits the original files. Cycle slips larger than a minimum threshold of six were detected. Typically about five cycle slips were detected in each file. Significantly fewer cycle slips occurred in the 1992 data set than in the 1991 data, and **TurboEdit** performed well with the data.

13. Formation of single difference files (**SNGDIF**).

14. to 17. Estimation of the coordinates and ambiguities as floating point numbers using **GPSEST**. *A-priori* coordinates used were the 1987 results. The coordinates of one site per session was fixed. Since **TurboEdit** worked so well, and the data were so noise-free, few additional cycle slips were detected in the post-fit residuals and those that were detected were smaller than the minimum threshold of **TurboEdit**. A 20° minimum satellite elevation angle and a standard Saastamoinen tropospheric model were used. As with previous surveys, local tropospheric parameters were not estimated. Approximately 1% of the data were discarded and no sessions were unusable. Line-length RMS residuals were of the order of 0.03 m.

18. to 20. Estimation of L5 ambiguities (**GPSEST**). A 15° minimum satellite elevation angle was used. All L5 ambiguities were resolved. Typical RMS residuals of 0.01 m were obtained.

21. Estimation of point coordinates and resolution of the L1 and L2 ambiguities. As the data were high quality, the **GPSEST** L3 option was used to simultaneously resolve the L1 ambiguities and estimate the coordinates. 92% of the L1 and L2 ambiguities were resolved. Line-length RMS residuals of 0.01 m were obtained.

22. Network adjustment (**NETADJ**). This was done relative to site I17, the coordinates of which were fixed to those obtained from the 1987 data processing.

The data were also processed independently at the University of Hannover using the GEONAP (Geodetic NAVSTAR Positioning) software [*Wübbena*, 1989].

4.5 Summary

Several GPS surveys have been carried out in Iceland including a country-wide survey in 1986, and regional surveys in north Iceland in 1987 and 1990.

In July 1991, a first-epoch GPS survey was done around the southeastern and southwestern edges of Vatnajökull to detect glacio-isostatic adjustments following melting of the icecap during the 20^{th} century. This was combined with lake level experiments in the southwest region. Fifteen points were occupied in two recording sessions per day using three Ashtech GPS receivers, squaring L2 data. In July/August 1992, much of the 1987 and 1990 network in northern Iceland was resurveyed and fourteen additional, distant points included. The points were selected on the basis of forward extrapolation of the 1987–1990 postdyking deformation field. 62 points were occupied using seven Ashtech, dual frequency receivers.

Data analysis was performed using the Bernese software. The 1991 data analysis was problematic due to a large amount of noise present in the data. Substantial editing of the data and the exclusion of two unusable sessions were necessary. The 1992 data were high quality and analysis proved relatively unproblematic. The 1987, 1990 and 1992 data sets were also processed independently at the University of Hannover using the GEONAP software.

Chapter 5

GPS Processing Results

5.1 Introduction

The results from repeated GPS surveys of the same network may be differenced to determine crustal deformation within the survey region. However, because the signal:noise ratio for geodetically-determined crustal deformation is often low, the accuracy of the survey results must first be carefully assessed before geophysical interpretations are attempted. Different measures of the quality of survey results include *precision*, *repeatability* and *accuracy.* In the case of the north Iceland surveys, two different GPS software packages were used to process the data independently, and this provides an additional check of the reliability of the results.

5.2 Precision and Accuracy

5.2.1 Introduction

In all physical experiments, errors occur that must be reduced to an acceptable level by experimental technique. It is important, particularly in surveying, to distinguish between precision, repeatability and accuracy. Precision is a measure of the scatter in the data used to determine the result. Repeatability is the consistency of multiple, independent determinations of the same quantity. Accuracy is a measure of how close the result is to the true value. In Figure 5.1 the difference between precision and accuracy is illustrated.

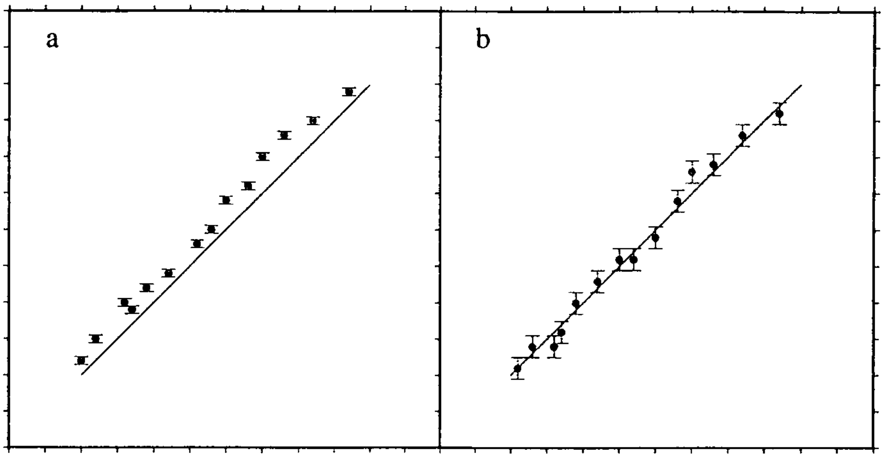

Figure 5.1: The difference between precision and accuracy. The straight line indicates the true values, the dots measurements and the vertical lines RMS error bars. (a) Precise but inaccurate data. (b) Accurate but imprecise data. after *Bevington and Robinson* [1992].

Precision is a measure of *random errors*, whereas repeatability involves errors such as experimental setup errors that may not affect the precision of the determination from a single experiment setup but will degrade the consistency of multiple measurements. Neither, however, can fully quantify *systematic errors* that are common to all the determinations. The accuracy of a determination is degraded by both random and systematic errors in the data. Thus the precision underestimates the true accuracy, and the repeatability underestimates the accuracy somewhat less. Random errors are fluctuations in observations that can be reduced by averaging larger sets of data. Systematic errors are not easily detectable and may result from, for example, incorrect calibration of the equipment.

The precision of a GPS-determined coordinate is obtained from the scatter of the satellite range measurements used. The repeatability is estimated from the variation in repeated determinations of the same coordinate, and will generally indicate much larger errors than the precision of a single determination. It is to be expected that, in the absence of crustal deformation, the repeatability of determinations of coordinates spanning months or years would be even larger than the repeatabilities determined from multiple measurements during a single, short survey. Accuracy is determined from the agreement of the results with those obtained by some other, better technique, e.g., VLBI or SLR. Since there have been no simultaneous occupations of sites in Iceland by GPS and VLBI or SLR instruments (as is sometimes the case for GPS surveys), the accuracy of the results cannot be rigorously determined, but only estimated.

In GPS surveying, the precision of a point coordinate is defined as the formal standard error associated with the individual determination, and is calculated as the RMS residual about the mean of the phase data. Repeatability is defined as the weighted RMS residual about the mean of repeated point coordinate estimates. For a vector distance component (east, north or vertical) this is given by

$$S_{mean} = \sqrt{\frac{\frac{N}{N-1}\sum_{i=1}^{N}\frac{(y_i - \langle y \rangle)^2}{\sigma_i^2}}{\sum_{i=1}^{N}\frac{1}{\sigma_i^2}}}, \tag{5.1}$$

where N is the number of determinations, y_i is the estimate of the component on day i, $\langle y \rangle$ is the weighted mean of the y_i's and σ_i is the formal standard error for the estimate made on day i.

Systematic errors that vary over a longer period than the survey, for example those due to orbital errors, will not be quantified by the repeatability of the results from a single survey. In order to quantify the effects of long-term systematic errors, the repeatability of GPS results derived over a time scale of months to years is required. This is possible in stable regions, and in regions of active tectonics it may be possible if deformation is regular and well understood and may be confidently modelled. However, if the deformation is complicated and not perfectly understood, as is the case in north Iceland, this is not possible.

The network adjustment program **NETADJ** [*Heki*, 1992] calculates the so-called "scaled formal errors" of the coordinates. The program uses the individual estimates of point coordinates to calculate mean values that minimise the weighted RMS, and optimise the repeatability of the whole network (equation 5.1). The factor by which the precision of the whole survey is underestimated can be quantified using the Normal RMS (NRMS), where

$$NRMS = \sqrt{\frac{\sum_{i=1}^{N}\frac{(y_i - \langle y \rangle)^2}{\sigma_i^2}}{N-1}}. \tag{5.2}$$

This is used to scale the precisions (formal errors) of each component. These scaled formal errors provide error estimates that combine both precision and repeatability, and are used in this thesis as the best measure of accuracy available.

The accuracies of individual GPS line-length estimates are dependent on various factors, some of which are dependent and some independent of line length. Length-independent errors are expected from sources such as multipath, receiver noise and tripod setup errors, whilst length-dependent errors may be due to atmospheric and satellite orbit-related errors. Atmospheric errors are dependent on the line length up to a certain length beyond which atmospheric variation becomes uncorrelated at the two ends of the line.

5.2.2 Results

The repeatability of the site coordinates was evaluated using the weighted RMS scatter of the differences between the coordinates from the individual sessions and the network solution (Figures 5.2 to 5.5; Table 5.1). The scaled formal error ellipses for the 1987, 1990, 1991 and 1992 local coordinate solutions are shown in Figures 5.6 to 5.9. Since satellites are visible in one hemisphere only, up-down repeatabilities will be poorer than those in the horizontal directions. Outliers are acceptable if the errors are correspondingly large, but indicate a processing error, e.g., an ambiguity fixed to an incorrect value, if the errors are small.

In 1987 the north-south component was best, and the up-down component poorest (Table 5.1). Several outliers with small errors are evident and may indicate incorrect ambiguity resolution (Figure 5.2).

In 1990 the north-south and east-west components are of a comparable quality with the up-down component poorest. Large errors are present in all components, since more parameters were estimated when forming the final solution (ambiguities as well as coordinates).

The east-west component of the 1991 results is better than the north-south, and the up-down is again poorest. Several outliers, corresponding to points Djup, Gild and Hrol, are present in the north-south and up-down components. The errors are generally small compared to the deviation from the mean and may indicate problems such as incorrect fixed ambiguities or tripod setup errors.

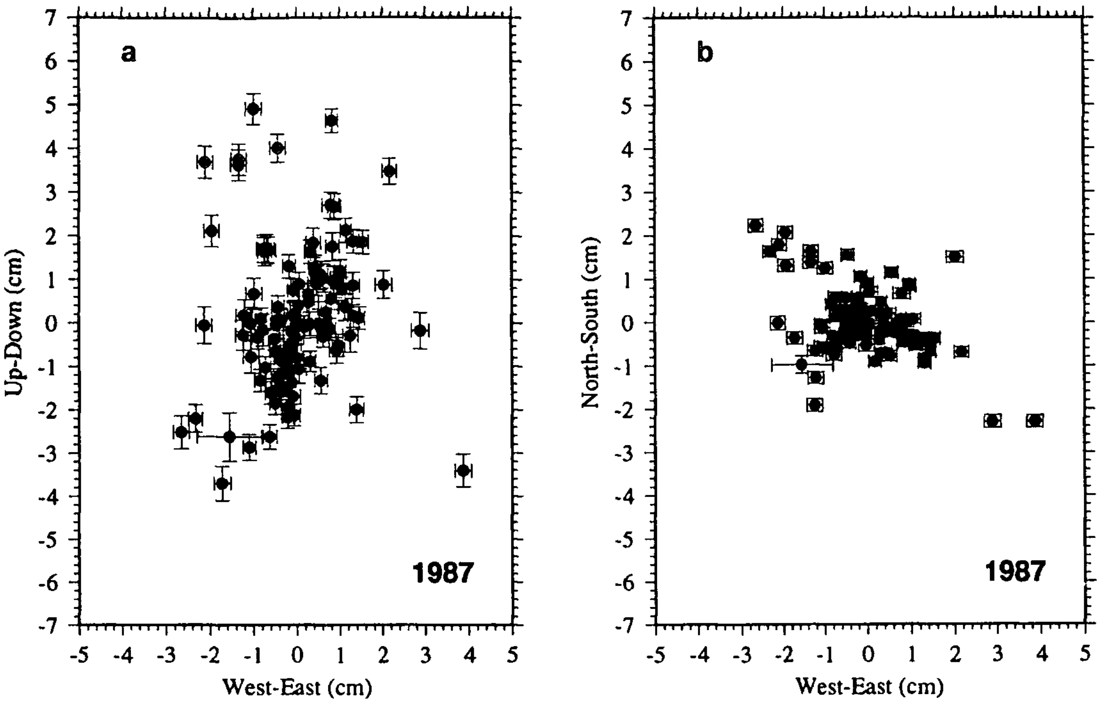

Figure 5.2: Variations about the mean in (a) the vertical and (b) the horizontal for the 1987 results. Error bars represent 1σ scaled formal errors. From the L3 ambiguity-fixed solution determined by *Heki et al.* [1993].

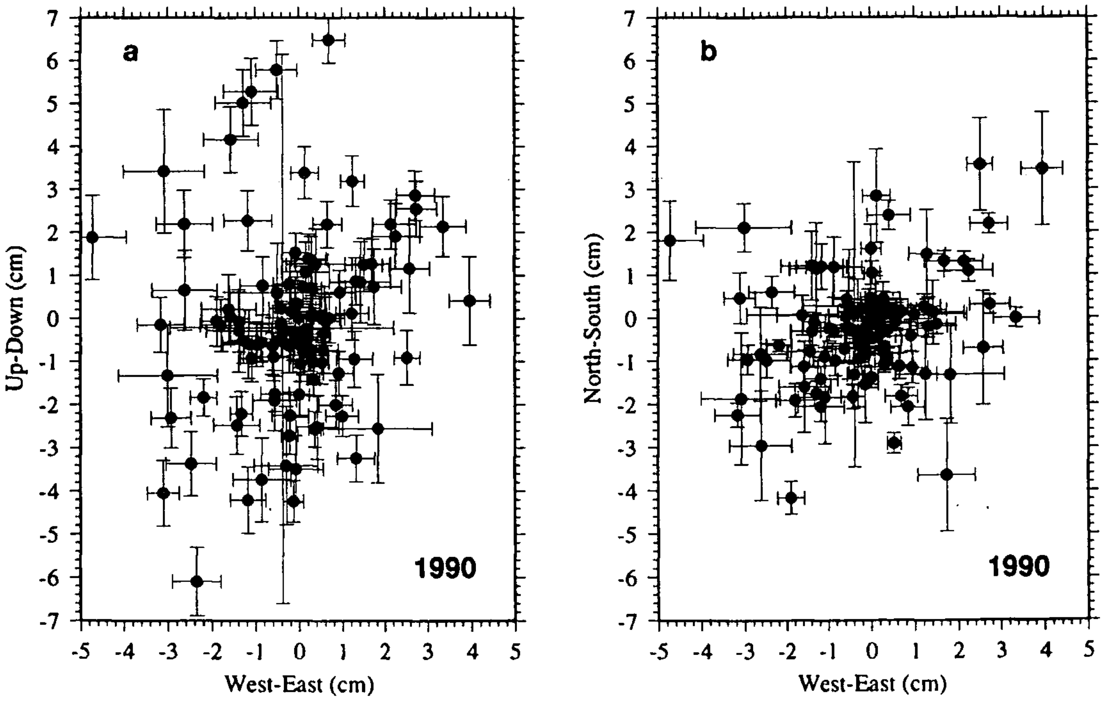

Figure 5.3: Same as Figure 5.2, except for the 1990 L3 ambiguity-free solution determined by *Heki et al.* [1993].

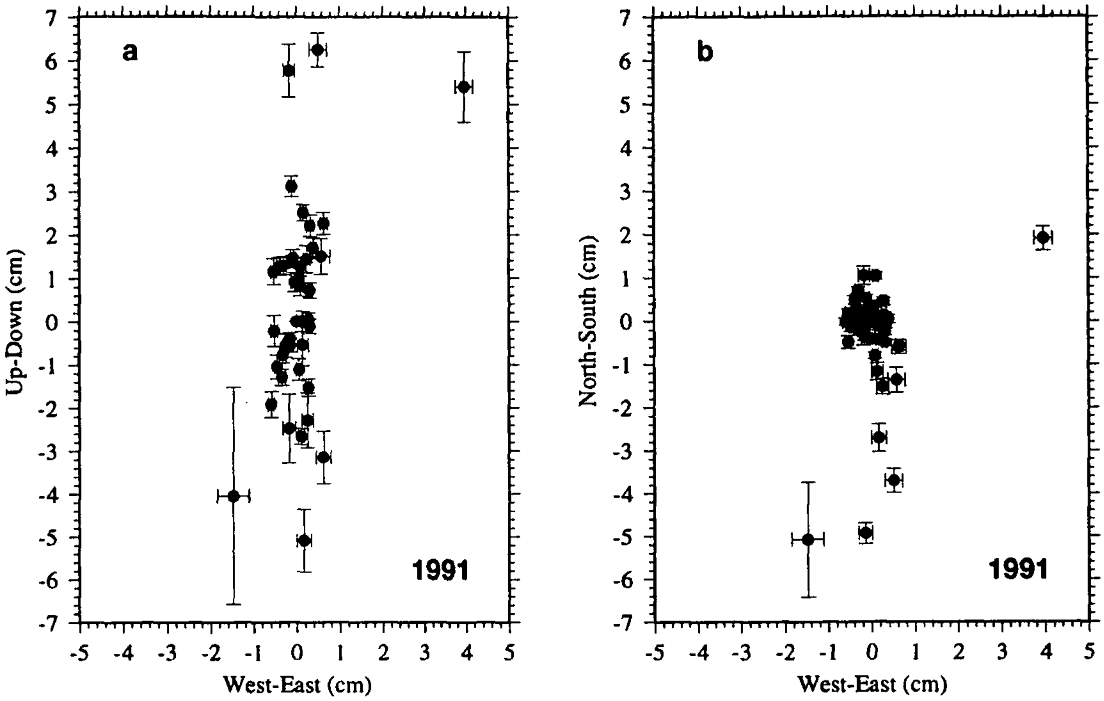

Figure 5.4: Same as Figure 5.2, except for the 1991 L3 ambiguity-fixed solution.

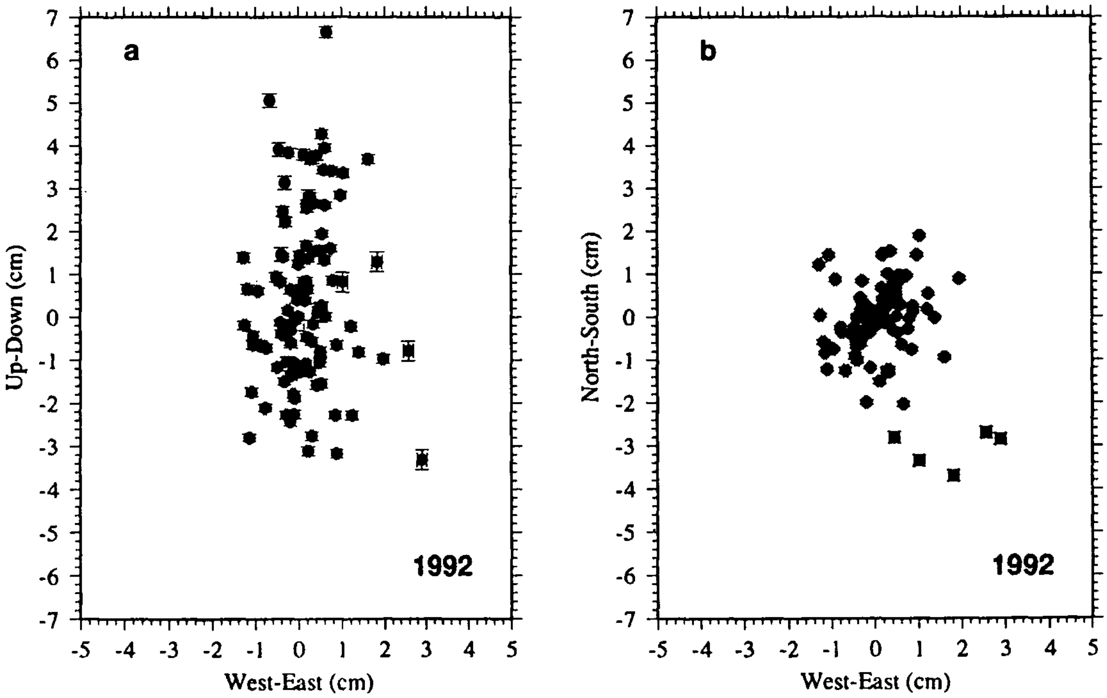

Figure 5.5: Same as Figure 5.2, except for the 1992 L3 ambiguity-fixed GPS solution.

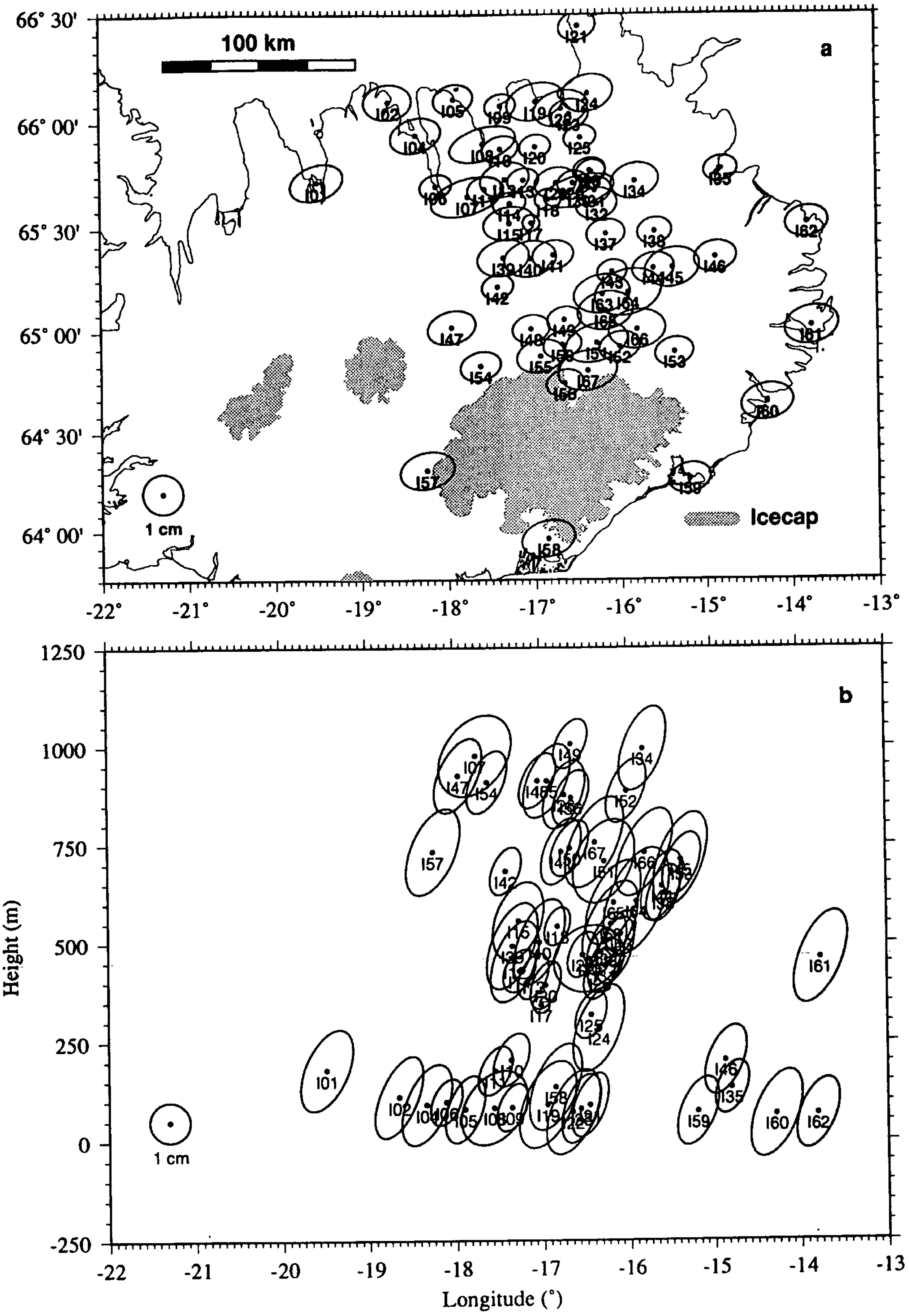

Figure 5.6: Scaled formal error ellipses at the 68% (1.5σ) confidence level for the ambiguity-fixed 1987 solution, (a) horizontal plane, and (b) longitude vs. height.

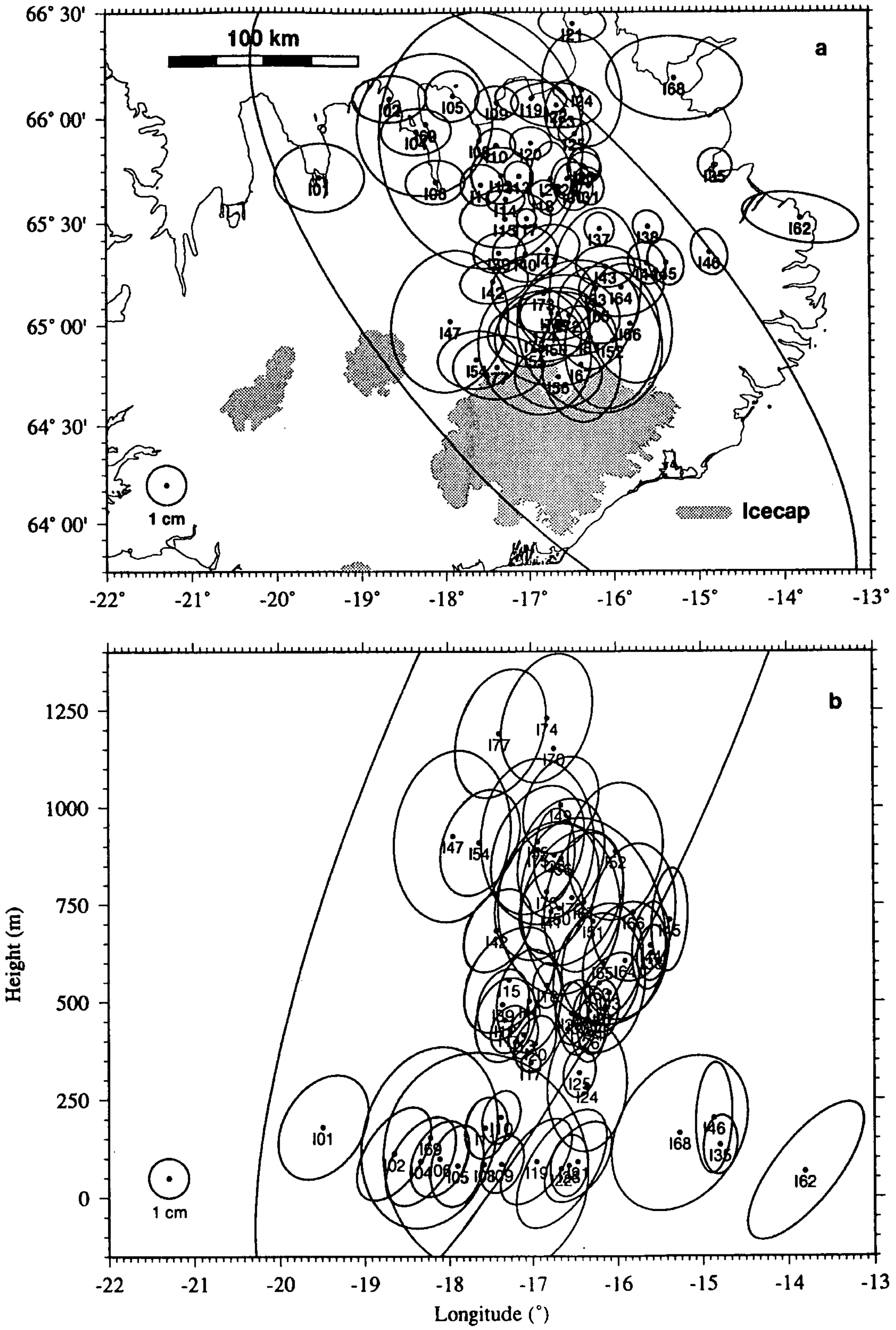

Figure 5.7: Same as Figure 5.6 except for the 1990 ambiguity-free solution. The large scaled formal error associated with point I70 is a result of the single, very short occupation of this point.

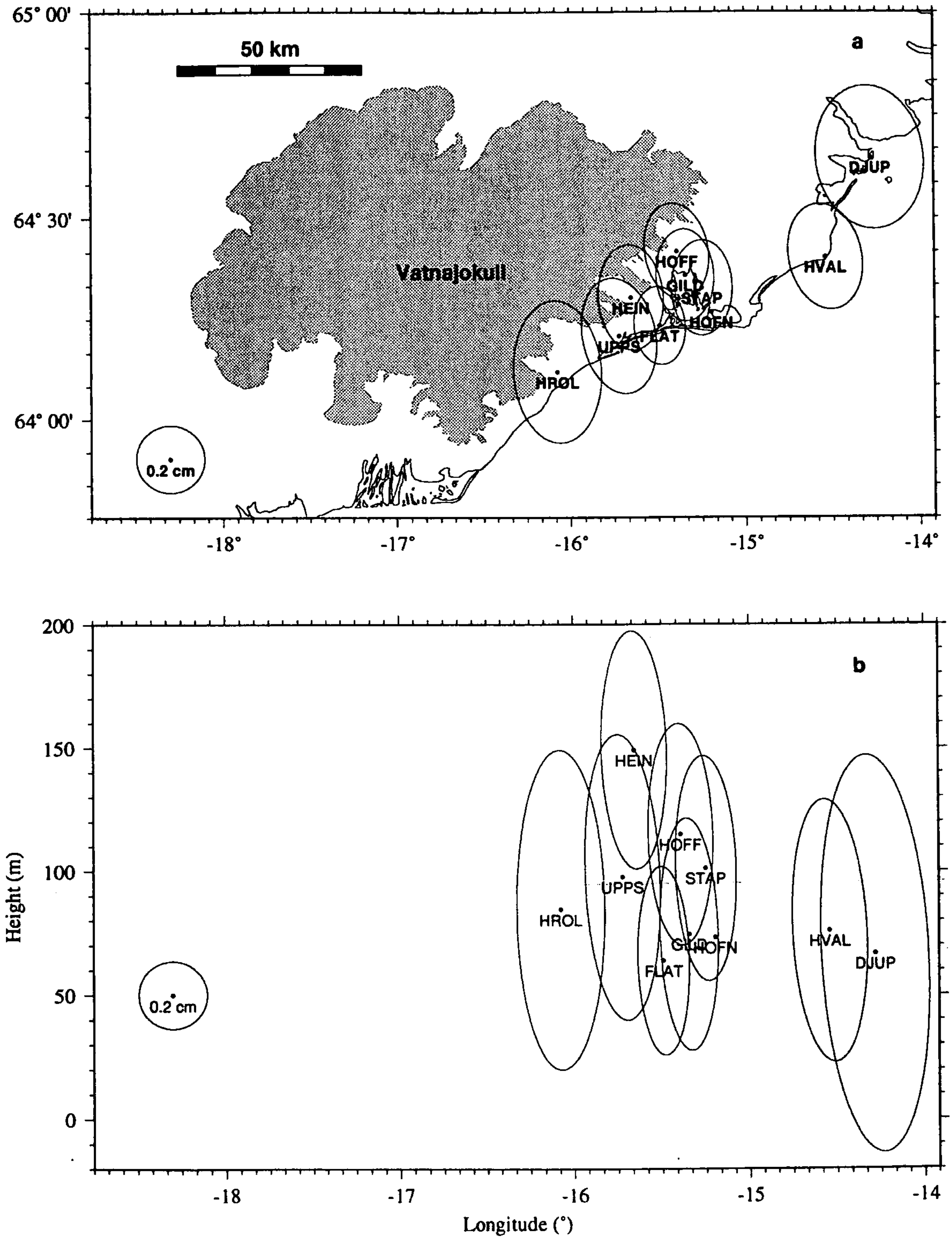

Figure 5.8: Same as Figure 5.6 except for the 1991 ambiguity-fixed solution. Note the different error ellipse scale.

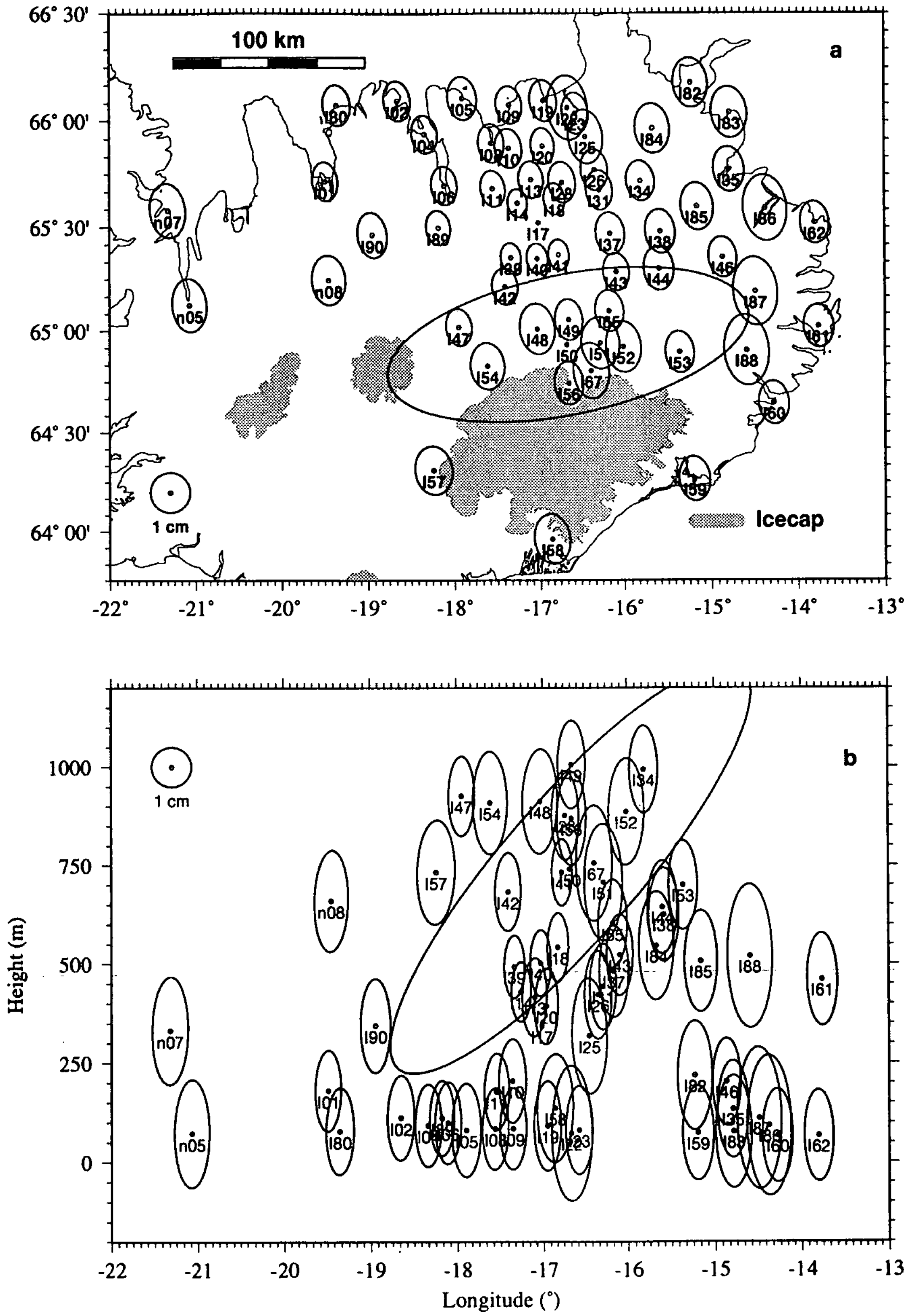

Figure 5.9: Same as Figure 5.6 except for the 1992 ambiguity-fixed solution. The large scaled formal error associated with point I50 is a result of the very short (~1 hr), single occupation of this point.

Table 5.1: Repeatability of site coordinates (equation 5.1) at the 1σ confidence level in the three components for the Iceland GPS surveys.

Survey	North-South mm	East-West mm	Up-Down mm
1987[a]	6.4	9.2	16.7
1990[b]	10.1	11.0	19.3
1991[a]	6.0	4.2	17.1
1992[a]	7.1	6.2	19.0

[a] L3 ambiguity-fixed solution.

[b] L3 ambiguity-free solution.

The north-south and east-west components of the 1992 results are of comparable quality, with the up-down component substantially poorer. Several results are clearly poor (points n05, n07, n08, I80 and I01) indicating some processing problem, probably during session 227.1 when these sites were simultaneously occupied.

The repeatabilities of the 1990 survey are worse than those of the other surveys because of greater measurement noise from ionospheric disturbances which also precluded ambiguity resolution. The north-south repeatabilities of the 1991 and 1992 surveys are comparable to that of the 1987 result. The east-west repeatabilities for the 1991 and 1992 surveys are better than for the 1987 survey because of the improved satellite constellation. Shorter between-point lines were occupied during the 1991 survey leading to greater precisions, and this is reflected in the smaller scaled formal errors (cf., Figures 5.8 and 5.9). The 1992 scaled formal errors are comparable to those of the 1987 survey and are smaller than those from 1990. Thus, the 1987 and 1992 results are of a substantially higher quality than those from 1990.

5.3 Comparison Between Software Packages

5.3.1 Introduction

The quality of the GPS results for 1987, 1990 and 1992 can be studied further by comparing the final coordinates calculated by two software packages, the

Bernese v3.2 GPS processing software [*Rothacher et al.*, 1990] and GEONAP [*Wübbena*, 1989]. The 1987, 1990 and 1992 Iceland GPS data were independently processed at the University of Hannover (Germany) using the GEONAP software [*Jahn et al.*, 1994]. The results were compared with those obtained from the Bernese software using a Helmert transformation. The transformation between two coordinate sets can be represented by the expression

$$\vec{X_B} = \vec{c} + \mu R \vec{X_G}, \tag{5.3}$$

where $\vec{X_B}$ and $\vec{X_G}$ are the vectors representing the Bernese and GEONAP coordinates respectively, μ is a scale factor, $\vec{c}$ is a shift vector and R is a rotation matrix composed of three orthogonal rotations. Three translations, three rotations and a scale factor (seven parameters) were calculated. A least-squares fit is determined for the point coordinates to obtain the minimum transformation parameters. The calculations were done using program **HELMERT**, which is part of the Bernese software.

5.3.2 Results

The 1987 and 1990 results from GEONAP and Bernese processing were compared by *Heki et al.* [1993]. Comparison of the 1992 results was done as part of this project.

Both the 1987 and 1992 GEONAP and Bernese solutions are L3 ambiguity-fixed. For the 1990 survey, two thirds of the ambiguities are fixed in the GEONAP results and none in the Bernese results [*Heki et al.*, 1993]. Tropospheric and orbital parameters were not estimated in any analysis. The results of the Helmert transformation applied to the Bernese results with respect to the GEONAP results are shown in Table 5.2 and the residuals in Figures 5.10 to 5.12.

After application of the Helmert transformation, agreement is within 2 cm, 4 cm and 10 cm for the north-south, east-west and up-down components in 1987 (Figure 5.10). This is within 2σ for the north-south and east-west components but the discrepancy is up to $\sim 5\sigma$ in the up-down. The extent of the disagreement is thus more poorly modelled by the errors in the up-down component.

In 1990 agreement is within 6 cm, 11 cm and 9 cm for the north-south, east-west

Table 5.2: Summary of the Helmert transformations applied to compare the 1987, 1990 and 1992 Bernese and GEONAP final coordinates. x, y and z are axes in the local (east, north, up) coordinate system.

Parameter		Survey		
		1987	1990	1992
Translation (m)	x	2.1 ± 0.003	0.3 ± 0.004	2.5 ± 0.003
	y	6.2 ± 0.003	-1.0 ± 0.004	5.7 ± 0.003
	z	0.2 ± 0.003	-1.4 ± 0.004	-0.4 ± 0.003
Rotation (arcsec)	x	0.01 ± 0.01	0.02 ± 0.02	0.02 ± 0.01
	y	0.02 ± 0.01	0.12 ± 0.02	0.02 ± 0.01
	z	0.01 ± 0.01	0.05 ± 0.01	0.00 ± 0.01
Scale factor (mm/km)		-0.05 ± 0.03	0.16 ± 0.06	0.01 ± 0.04

and up-down components respectively (Figure 5.11). This is up to 6σ for the east-west component, and $\sim 4\sigma$ for the north-south and up-down components.

In 1992 agreement in the north-south and east-west components is within 2 cm (Figure 5.12). In the up-down component it is much larger, up to ~11 cm. This is within 2σ for the horizontal components, but up to $\sim 6\sigma$ for the vertical.

The agreement of the 1987 results is similar to that of the 1992 results. Agreement of the 1990 results is much worse than in either of the other two surveys, except in the vertical component, in which similar agreements are obtained for all three surveys.

Significant translations were required for all three surveys (Table 5.2). However, this is not of importance here as it may result from trivial differences in processing, e.g., variations in the coordinates of the fixed point used, and this study is only concerned with internal network deformations. Two rotations are significant at greater than the 3σ level, about the local y and z axes in Iceland in 1990. A scale factor relatively large and significant at the 2σ level was also found for the 1990 analyses. These results indicate that the GEONAP coordinates show lower elevations of the northern points relative to the southern points compared with the Bernese results, and that they also indicate a more expansive network in 1990 than the Bernese results. For the 1987 and 1992 surveys, no non-translational parameters were significant at the 3σ level. These results are a further indication

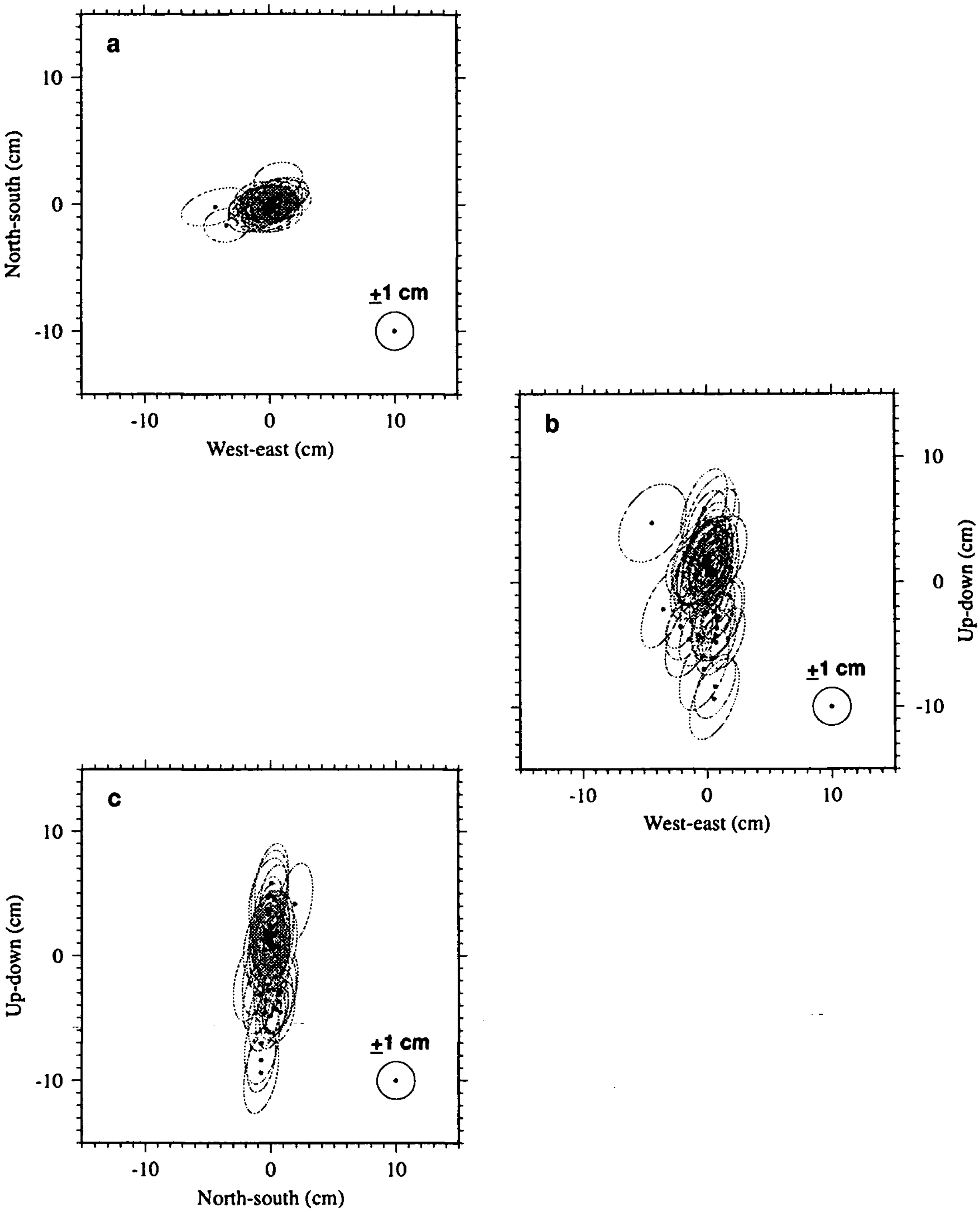

Figure 5.10: Comparison of the final coordinates of the 1987 survey between the Bernese and GEONAP software packages. The black dots represent the residuals after a seven-parameter Helmert transformation (Table 5.2), applied to the Bernese positions with respect to the GEONAP positions. The error ellipses are the Bernese scaled formal errors at the 68% (1.5σ) confidence level. (a) North-south and east-west, (b) west-east and up-down, and (c) north-south and up-down components are illustrated.

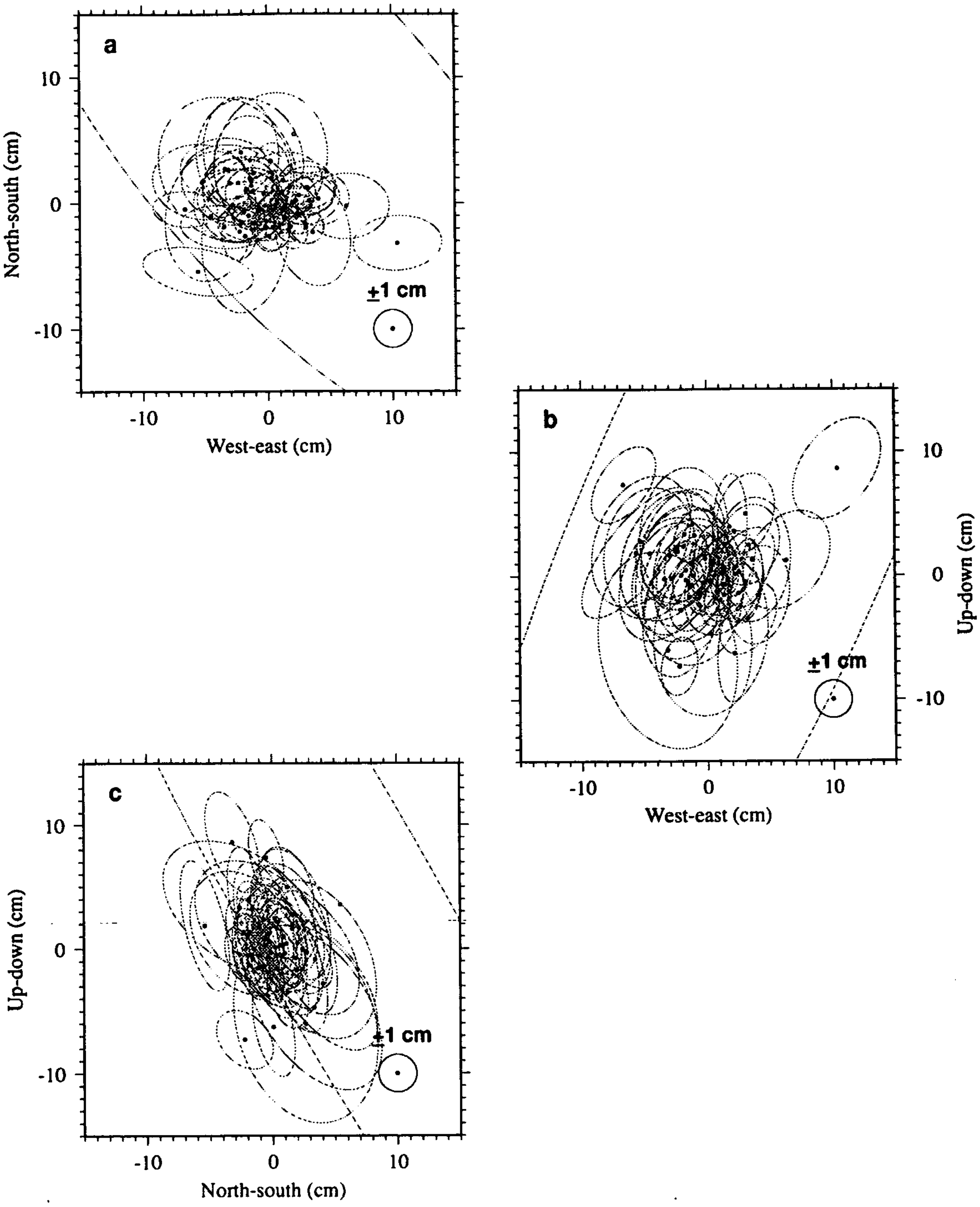

Figure 5.11: Same as Figure 5.10, except for the 1990 survey.

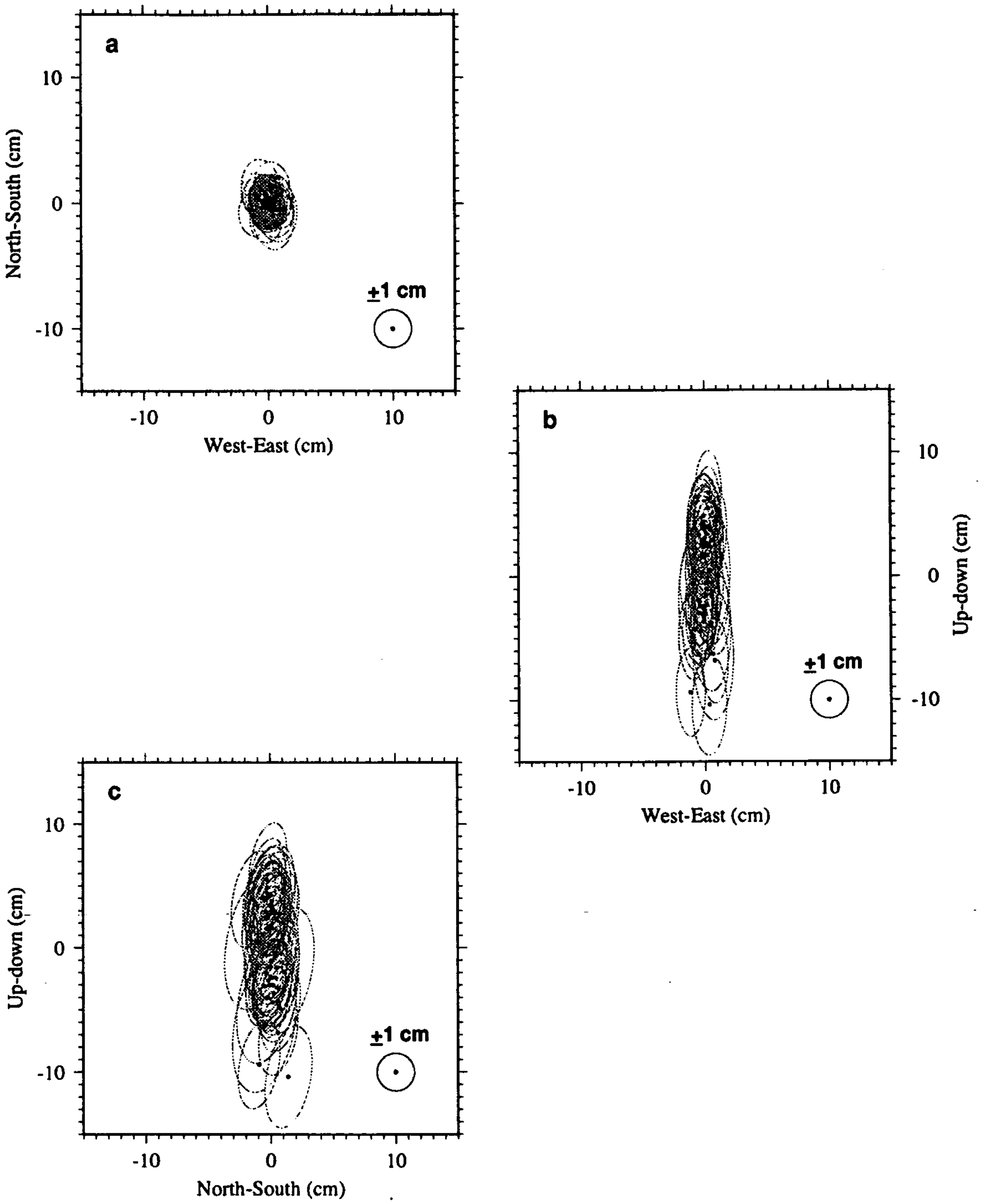

Figure 5.12: Same as Figure 5.10, except for the 1992 survey.

that the 1990 results are the poorest of all.

In addition to these comparisons, the 1987 GEONAP results were compared by *Jahn* [1990] with terrestrial measurements of part of the network made simultaneously by the University of Braunschweig, Germany [*Möller*, 1989]. A scale factor of about 3 ppm with a standard deviation of about 0.5 ppm was detected, which was attributed to miscalibration of the terrestrial survey equipment (see *Jahn et al.* [1994] for summary).

5.4 Derivation of the Deformation Field

The final Bernese coordinates and covariance matrices were used to compare the results between surveys. A weighted Helmert transformation was applied, keeping the three components of a reference site fixed. The results of seven-parameter weighted Helmert transformations are show in Table 5.3. At the 2σ level, all rotations are insignificant for all epochs. Large scale factors significant at greater than the 7σ and 4σ levels are determined for the 1987–1990 and 1987–1992 epochs. This contrasts with the 1990–1992 epoch where no significant scale factor is determined. Expansion of the network is the type of deformation expected to predominate as a result of postdyking stress redistribution in north Iceland. Therefore, the Helmert transformations were repeated without the scale transformation since this transformation would correct for the network deformation due to tectonic motion.

The results of six-parameter weighted Helmert transformations are shown in Table 5.4. Again, no rotations are significant at the 2σ level.

The horizontal deformation fields (Figures 5.13 to 5.15) indicate a large systematic expansion perpendicular to the plate boundary, which is consistent with the results that *Foulger et al.* [1992] obtained using GEONAP results. During the period 1987 to 1990, the maximum amplitude of this expansion was approximately 18 cm [*Heki et al.*, 1993] (Figures 5.13 and 5.16). The largest expansion occurs around the centre of the Krafla rift zone where the dyke complex injected 1975–1984 was widest. A radial component is also evident [*Heki et al.*, 1993]. The relative motion is at a maximum a few tens of kilometers from the spreading axis and decreases with distance from the spreading zone (Figure 5.16a). A very pronounced maximum occurs at distances of ±25 km from the rift zone. Between 60–100 km on either

Table 5.3: Results of seven-parameter weighted Helmert transformations applied to compare the Bernese results of the 1987, 1990 and 1992 surveys.

Parameter		Epoch		
		1987 - 1990	1990 - 1992	1987 - 1992
Translation (cm)	x	355.68 ± 2.24	-350.05 ± 1.66	1.91 ± 3.24
	y	540.97 ± 1.96	-538.45 ± 1.31	-1.15 ± 2.15
	z	-102.07 ± 2.35	105.02 ± 2.59	0.41 ± 6.54
Rotation (arcsec)	x	-0.31 ± 0.23	-0.16 ± 0.20	-0.27 ± 0.30
	y	-0.55 ± 0.32	-0.35 ± 0.32	-0.04 ± 0.35
	z	0.06 ± 0.17	0.11 ± 0.12	0.22 ± 0.14
Scale factor (mm/km)		0.85 ± 0.12	0.06 ± 0.09	0.47 ± 0.09

Table 5.4: Results of six-parameter weighted Helmert transformations applied to compare the Bernese results of the 1987, 1990 and 1992 surveys.

Parameter		Epoch		
		1987 - 1990	1990 - 1992	1987 - 1992
Translation (cm)	x	353.80 ± 2.57	-350.13 ± 1.65	1.04 ± 3.54
	y	542.53 ± 2.25	-538.41 ± 1.31	-2.10 ± 2.35
	z	-103.06 ± 2.72	105.00 ± 2.58	1.24 ± 7.18
Rotation (arcsec)	x	-0.47 ± 0.26	-0.18 ± 0.20	-0.36 ± 0.33
	y	0.52 ± 0.33	-0.33 ± 0.32	-0.31 ± 0.38
	z	0.29 ± 0.20	0.12 ± 0.12	0.23 ± 0.16

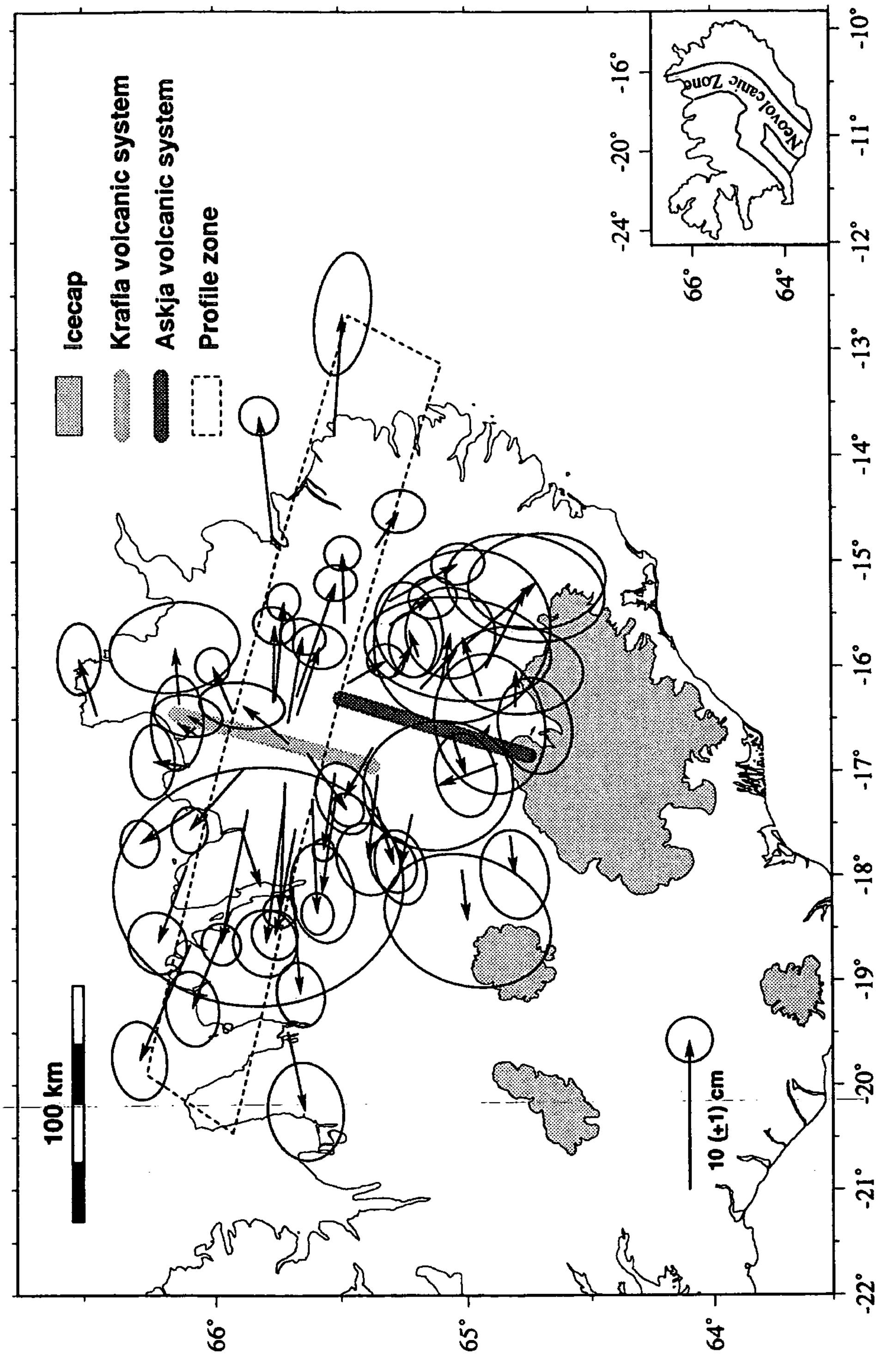

Figure 5.13: Displacements of GPS points 1987–1990 calculated after applying a six-parameter weighted Helmert transformation. Ellipses at each arrowhead indicate scaled formal errors at the 68% (1.5σ) confidence level. The arrow at lower left gives the scale. Two of the five *en échelon* volcanic systems of the neovolcanic zone, the Krafla and Askja volcanic systems, are shown schematically. Inset shows the neovolcanic zone in Iceland. The zone of points used to construct the profiles shown in Figure 5.16 is enclosed in a box.

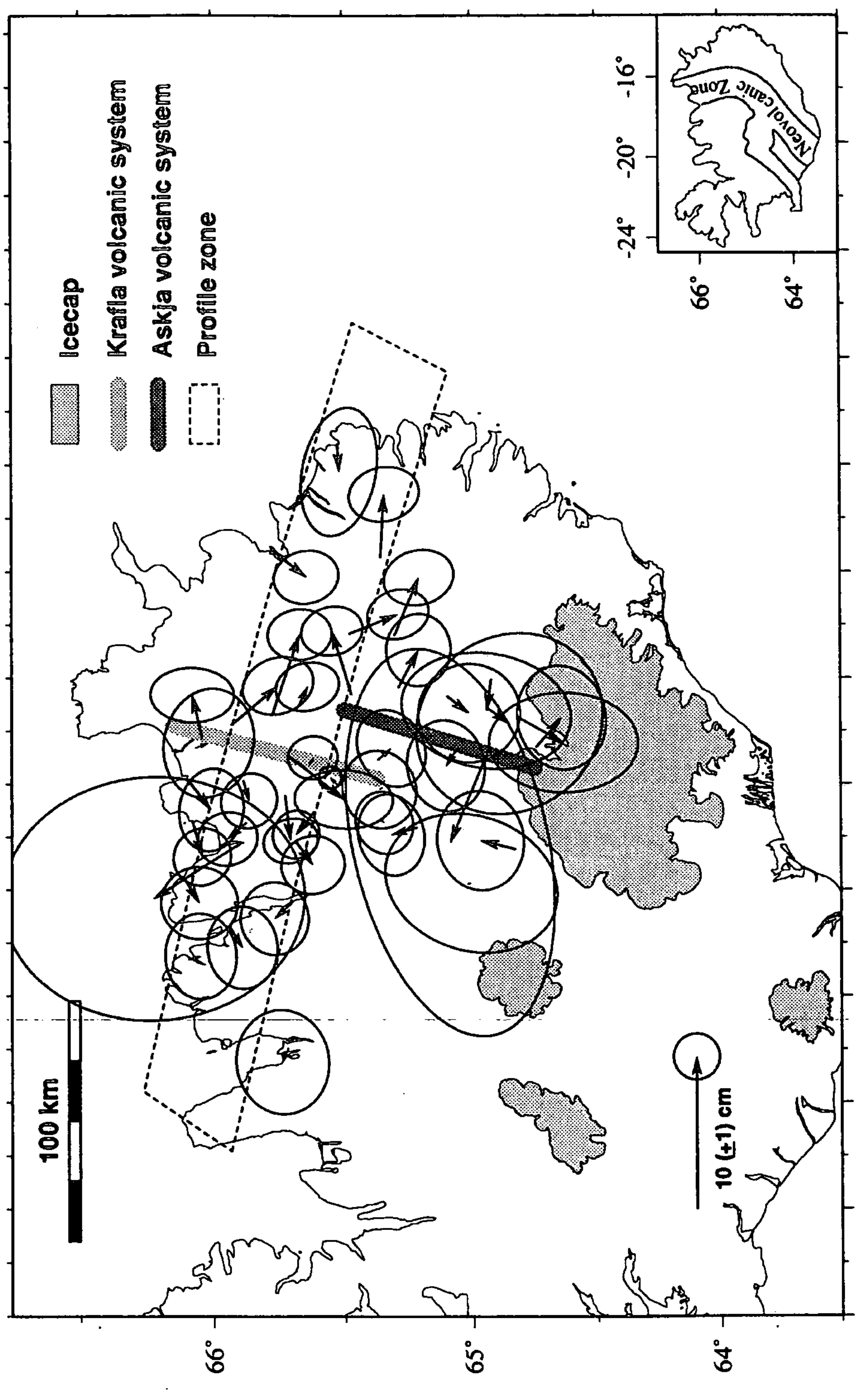

Figure 5.14: Same as Figure 5.13, except for the period 1990–1992.

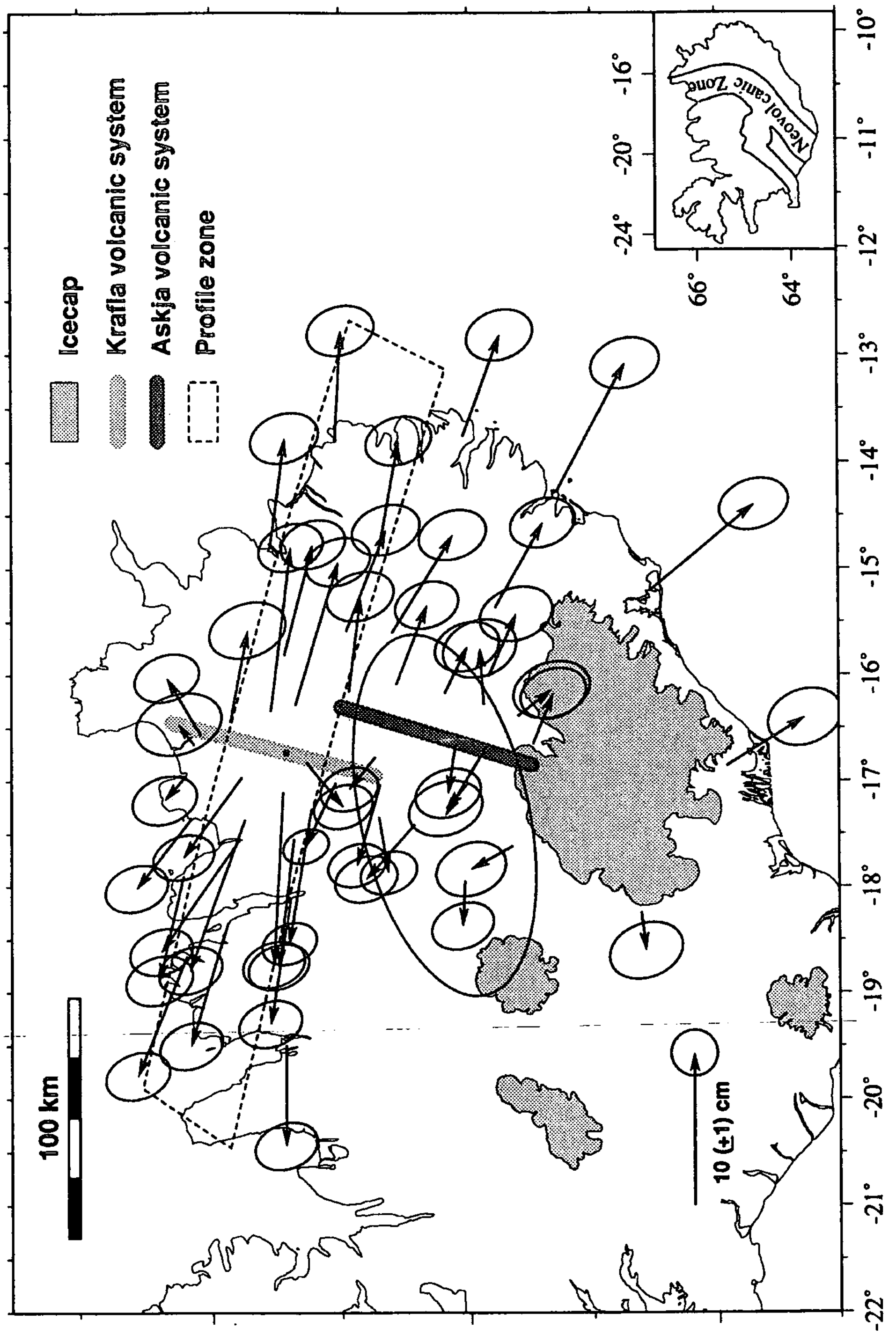

Figure 5.15: Same as Figure 5.13, except for the period 1987–1992.

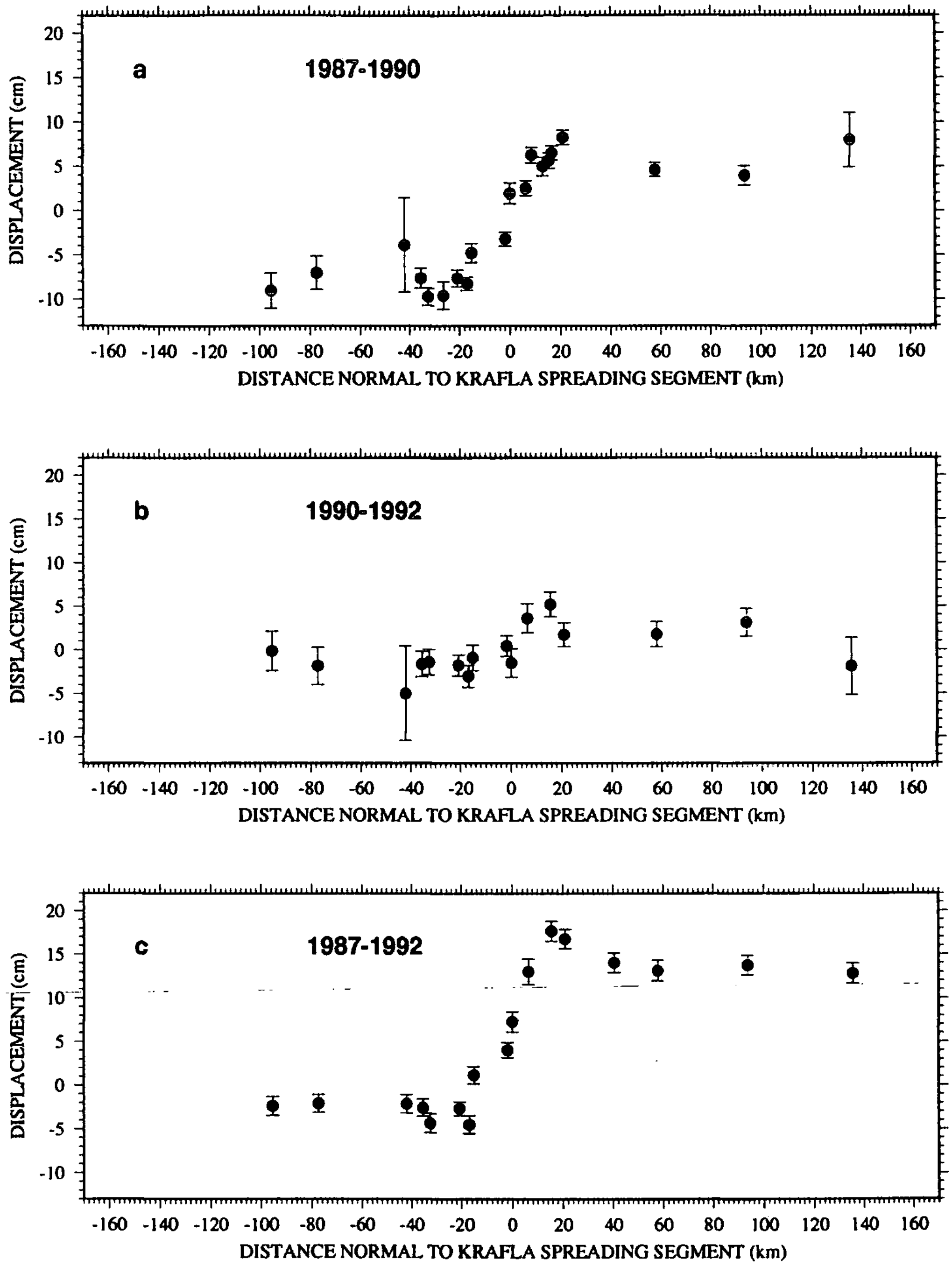

Figure 5.16: Displacements of GPS points within the zone shown in Figures 5.13–5.15, perpendicular to the Krafla volcanic system, as a function of distance from it (i.e., in the u_y direction). The trend of the plate boundary is assumed to be N15°E. The vertical bars indicate 1σ scaled formal errors. Positive displacement occurs to the east of the spreading segment and negative displacement to the west. (a) 1987 to 1990, (b) 1990 to 1992, and (c) 1987 to 1992. The zero reference point for displacements is arbitrary and not consistent between epochs.

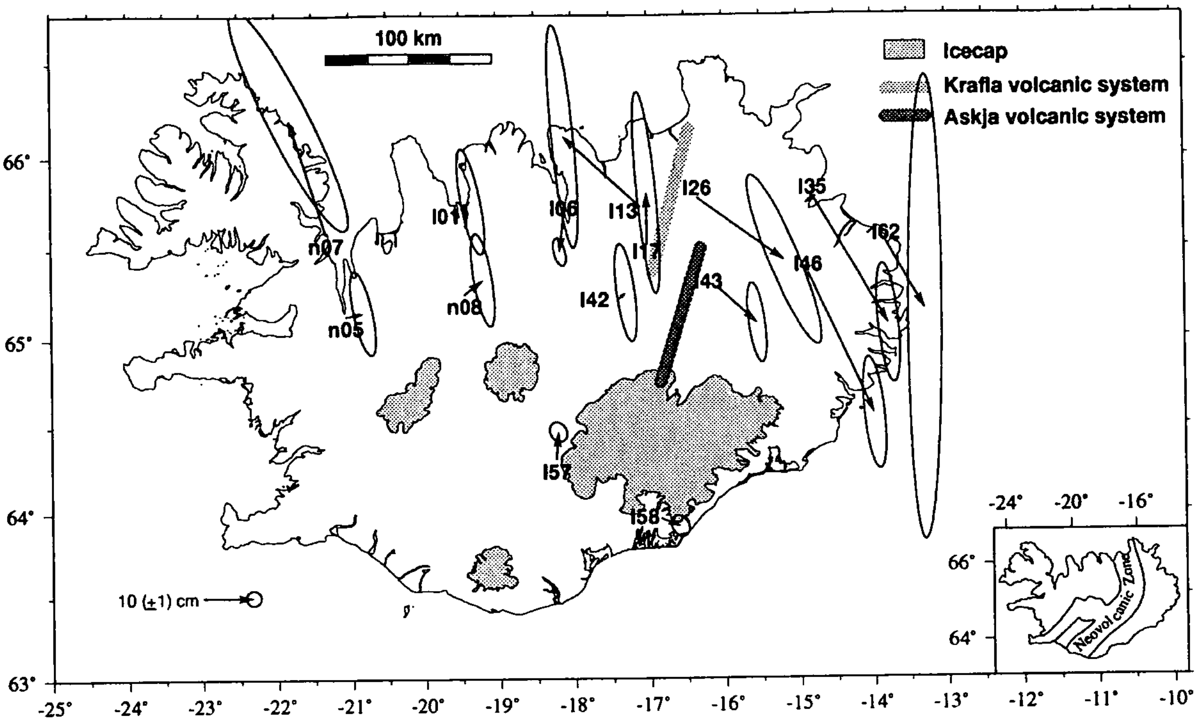

Figure 5.17: Same as Figure 5.13, except for the period 1986–1992.

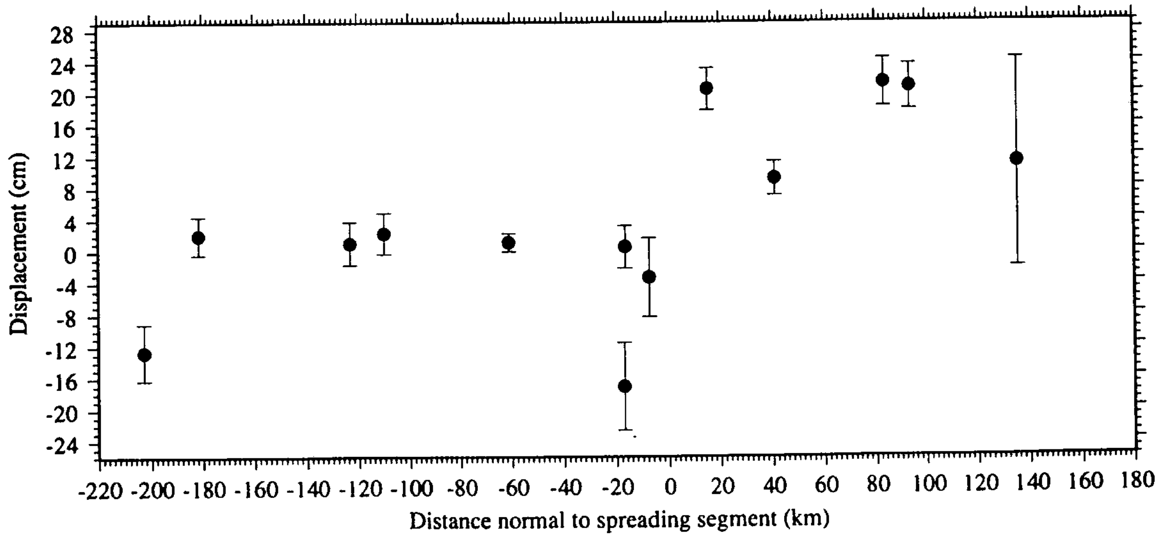

Figure 5.18: Same as Figure 5.16, except for the period 1986–1992. The formal errors of the 1986 data have been scaled by a factor of 5.

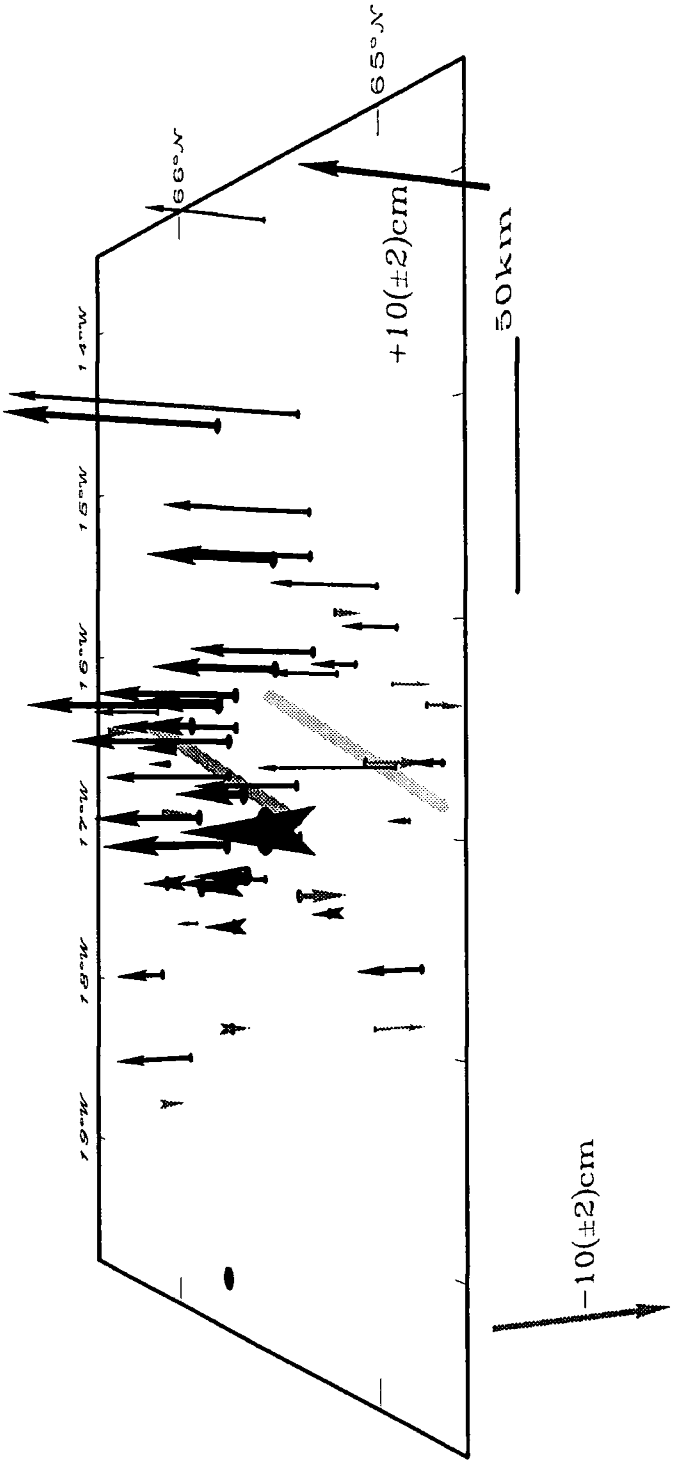

Figure 5.19: Vertical point displacements 1987–1990. The thicknesses of the arrows are inversely proportional to the vertical scaled formal errors. The two arrows at the base of the figure give the scale of the arrows. All velocities are shown relative to the westernmost point in the network, denoted by a black dot. The Krafla and Askja volcanic systems are represented by the parallel, dark and light grey-shaded lines respectively, adapted from *Heki et al.* [1993].

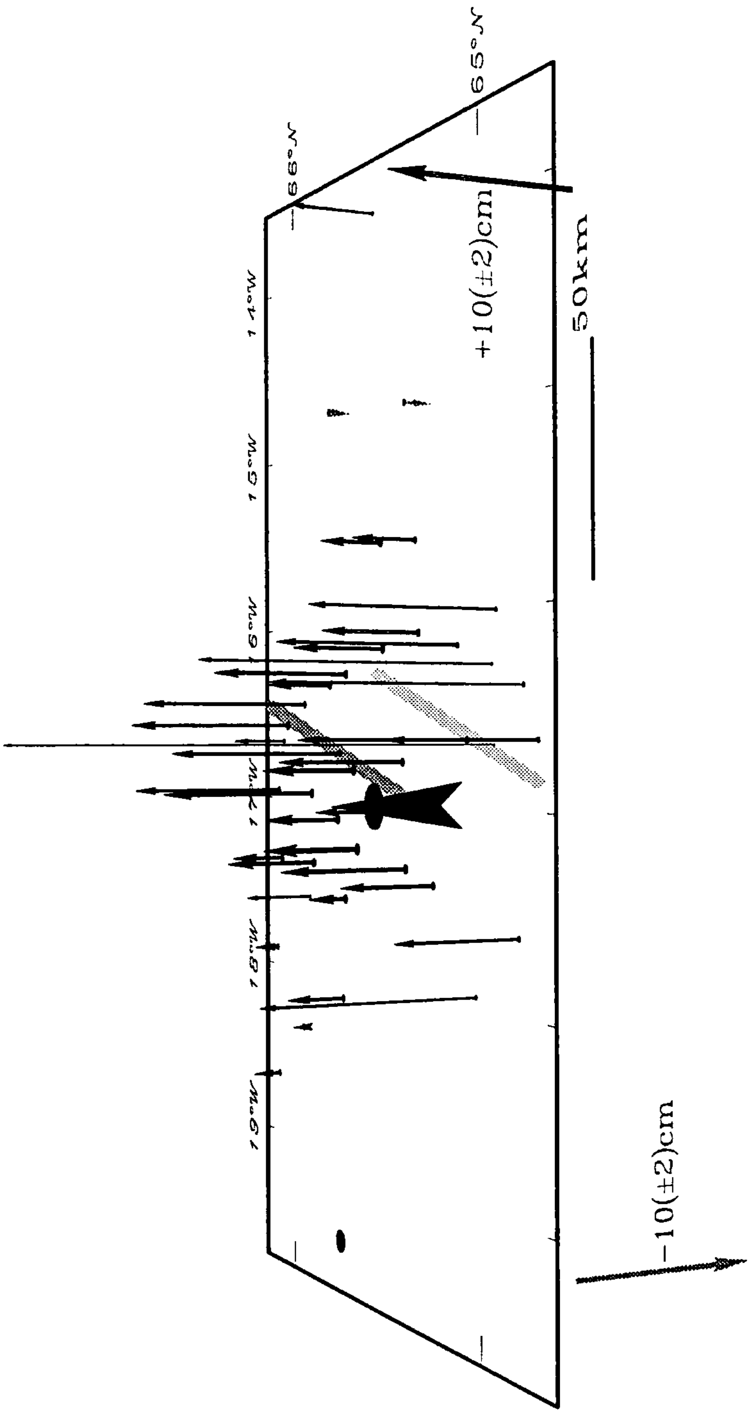

Figure 5.20: Same as Figure 5.19, except for 1990–1992.

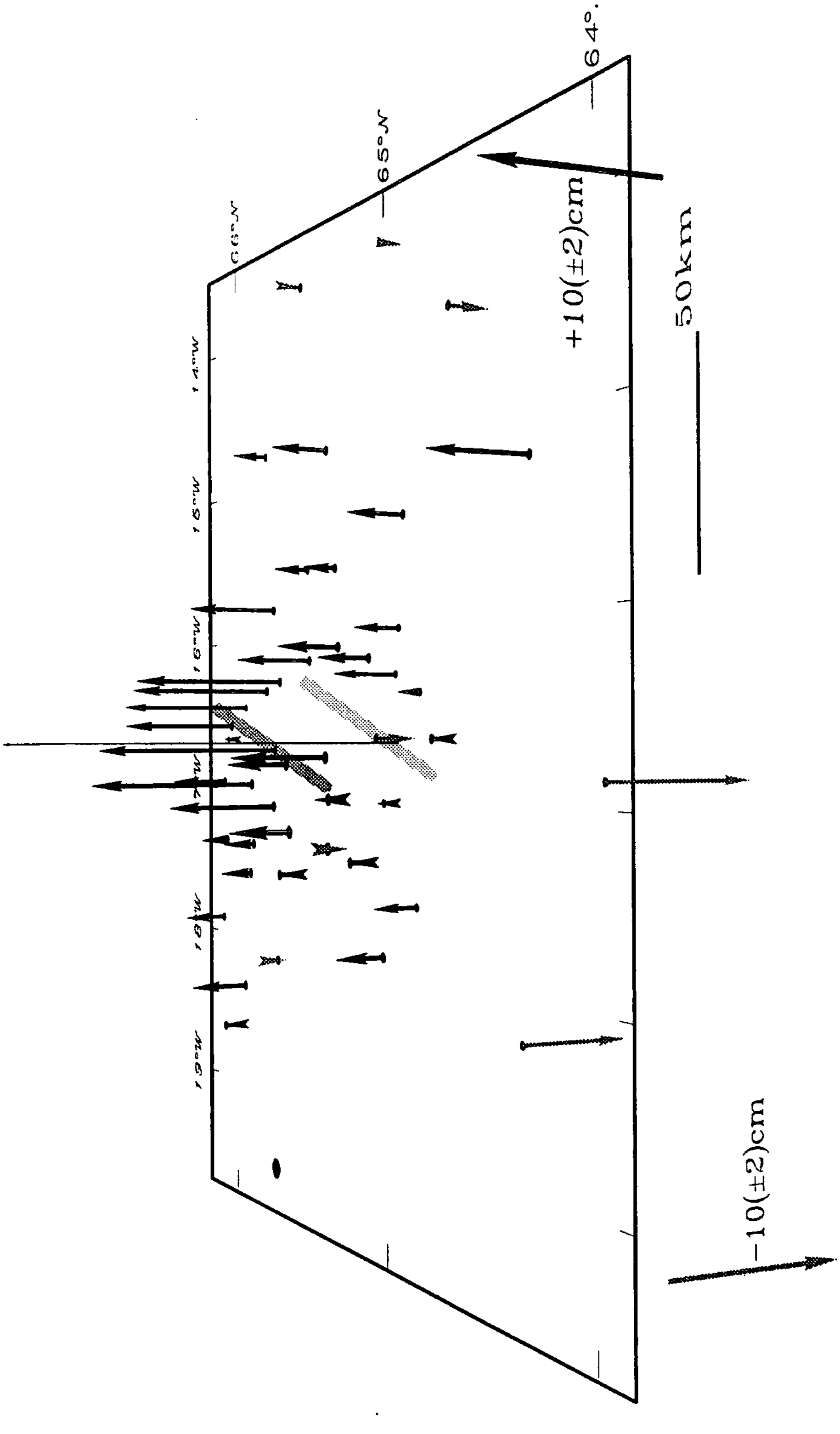

Figure 5.21: Same as Figure 5.19, except for 1987–1992.

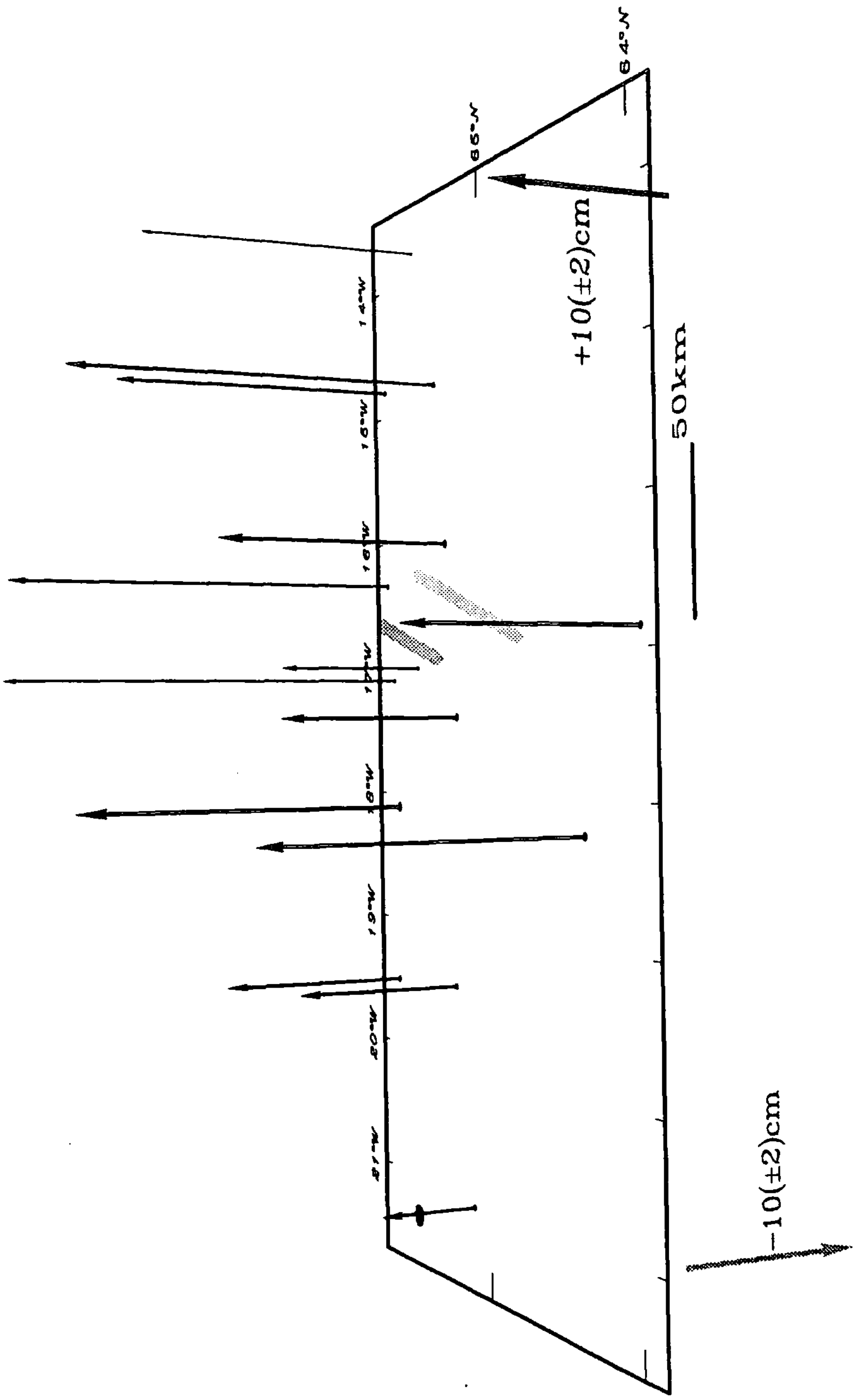

Figure 5.22: Same as Figure 5.19, except for 1986–1992.

side of the rift the motion apparently increases again, and large deformation rates are observed out to the edge of the network.

The results of the 1990 and 1992 surveys (Figures 5.14 and 5.16b) indicate the continuation of the east-west expansion observed between 1987 and 1990. This motion is barely significant at the 1σ level, probably because of the short inter-survey time, resulting in a small expansion, and the large errors associated with the 1990 results. The maximum is about 8 cm during that two year period. A pronounced maximum again occurs at distances of about 20 km from the rift zone. Little relative motion is detected at large distances from the rift.

The best-defined deformation field is obtained by comparing the 1987 and 1992 results (Figures 5.15 and 5.16c) due to the higher quality of both the 1987 and 1992 results compared to the 1990 results and the larger deformation signal. A better-defined deformation-field is obtained, and a clear east-west expansion is evident. The expansion is up to approximately 22 cm within a few tens of kilometres of the rift, decreasing to approximately 14 cm farthest from the central axis. The radial deformation pattern is clearly seen. The maximum expansion occurs at distances of ±20 km from the rift zone. Between 60 and 100 km from the rift zone a slight increase in the deformation rate is observed, but at 60–140 km a relatively constant rate of motion is observed. High deformation rates extend to the edge of the network.

The first order features of the 1987–1992 horizontal displacement field is well-illustrated by the profiles shown in Figures 5.16a–c. The deformation field is fairly symmetrical about the Krafla spreading segment. The rate of motion is variable, with higher velocities close to the rift and decreasing by about 30% further away. The expansion rate appears to have decreased with time between 1987 and 1992. From 1987 to 1990 the maximum expansion rate was about 6 ± 0.5 cm a^{-1}, this decreased to about 4 ± 0.9 cm a^{-1} for the period 1990 to 1992, and was 4.5 ± 0.3 cm a^{-1} for the total period 1987 to 1992. The time-averaged plate motion in northeast Iceland, 1.8 cm/yr [*DeMets et al.*, 1994], cannot account for this expansion.

A comparison of the 1986 and 1992 data (Figures 5.17 and 5.18) reveals a horizontal deformation field that agrees with the trend shown in the 1987, 1990 and 1992 results. There appear to be several outliers in the field (points I43, I62, I13 and n07; Figure 5.18). Additional information on the distant motion is provided by points n05 and n08. That provided by n08 however, duplicates that of I01, and therefore adds little except confidence in the motion of I01. The motion of point n05 suggests that the high rate of motion observed extends to 120–180 km from the rift zone.

The vertical displacement fields (Figures 5.19 to 5.22), shown relative to the westernmost point in the network, exhibit considerable scatter which is to be expected as the errors in this component are several times greater than those in the horizontal. The vertical deformation observed from 1987 to 1990 is of the order of a few centimetres and the southern points appear to subside with respect to the more northerly points [*Heki et al.*, 1993]. General uplift appears to be occurring around the Krafla rift zone, with maximum uplift closest to this zone. Virtually all the points 1990–1992 appear to uplift relative to the westernmost point, especially in the region of the Krafla volcanic system where maximum uplift occurred closest to the rift. The best-constrained vertical deformation field is that determined for 1987–1992. Within the Krafla region points near the rift axis uplift relative to more distant points. The 1986–1992 vertical deformation field shows uplift of all points relative to the westernmost point. Again, points closest to the Krafla rift zone undergo maximum uplift, decreasing with distance from the rift zone. Apparent reversals in the direction of the vertical motion occurred. For example, from 1987–1990 the two stations furthest from the fixed point underwent substantial uplift, whereas for 1990–1992 the situation appeared to reverse.

5.5 Summary

The precisions and repeatabilities of the Iceland GPS results were assessed using standard statistical techniques. Both the repeatability, evaluated using the WRMS scatter between the individual coordinate solution and the network solution, and the scaled formal errors output by **NETADJ**, show that the 1987, 1991 and 1992 results are of a comparable and high quality, with better repeatabilities and smaller scaled formal errors than the 1990 results. This is a consequence of substantial ionospheric turbulence at the time of the 1990 survey.

The 1987, 1990 and 1992 data sets were independently processed using two different software packages, and the results compared using seven-parameter Helmert transformations. The 1987 and 1992 results agree well but significant rotations were detected for the 1990 results, confirming that this survey is the least accurate of the three.

Differencing the results of the 1987, 1990 and 1992 surveys reveals a systematic expansion perpendicular to the plate boundary, with maximum amplitude occurring a few tens of kilometres from the rift axis, decreasing slightly beyond this, but continuing at a high level to at least 180 km from the rift. The deformation rate was variable. From 1987 to 1990, a maximum of 6 cm/yr of rift-normal expansion was detected, decreasing to 4 cm/yr 1990–1992. The best-defined deformation field, 1987–1992, indicated a total of 22 cm of expansion, decreasing to 15 cm far-field. The time-averaged plate motion in northeast Iceland cannot account for this deformation. The vertical deformation field reveals regional uplift throughout the network area. Uplift is at its maximum close to the rift zone and decreases with distance from it.

Chapter 6

Geophysical Models of Post-Rifting Crustal Deformation

6.1 Introduction

An important goal of modern crustal deformation studies is to understand the transient, postevent ground deformation sometimes seen following a large, sudden tectonic event, e.g., an earthquake or dyke emplacement. There are several possible explanations for this transient strain. These include stress relaxation in nonelastic material below a surface elastic layer [e.g., *Thatcher and Rundle*, 1984; *Thatcher et al.*, 1980; *Cohen*, 1984], and continued slip at depth on the fault or continued dyking.

Several methods are used to predict co- and postevent deformation fields. Usually these involve modelling the dynamics of a finite or infinitely long fault in an elastic or viscoelastic halfspace, or in a structure that involves both of these rheologies. An elastic halfspace structure provides an adequate description of the co-event deformation field from an earthquake or dyke injection, but is unable to explain continuing transient strain following the event without introducing a source that has a time-dependent mechanism. Many authors have proposed homogeneous or layered elastic halfspace models involving different dislocation sources [e.g., *Steketee*, 1958; *Maruyama*, 1964; *Knopoff*, 1958; *Chinnery*, 1961; *Press*, 1965; *Okada*, 1985; *Jovanovich et al.*, 1974].

Recent work has focussed on models involving viscoelastic material below a surface elastic layer. Postevent displacements may then be explained by the gradual relaxation of stresses built up by tectonic events through yielding of the viscoelastic material. Models involving various fault geometries and a variety of external effects have been studied. One-dimensional models (infinitely long faults and vertically averaged stresses) have been proposed by, for example, *Savage and Prescott* [1978] and *Rydelek and Sacks* [1990], to explain motion resulting from transform and thrust faulting. The cumulative effect of successive earthquakes on the same fault has been evaluated by *Thatcher and Rundle* [1984], *Cohen and Kramer* [1984] and *Rundle* [1986], and the effects of self-gravitation have been incorporated [e.g., *Rundle*, 1982; *Melosh*, 1983; *Cohen*, 1984]. The displacement fields from finite faults have also been modelled. Several mathematical methods have been applied, including analytical methods where the stresses at an elastic layer/viscoelastic halfspace boundary are approximated by the average stresses in the elastic layer [e.g., *Lehner et al.*, 1981], numerical methods using, for example, finite element methods [e.g., *Yang and Toksöz*, 1981], and the derivation of exact analytical solutions [e.g., *Rundle and Jackson*, 1977; *Rundle*, 1978].

Much work deals with strike-slip and thrust sources, but models have also been proposed for dilational sources. One of the first authors to deal with this type of source was *Mogi* [1958], who used a centre of dilation in an elastic halfspace to interpret the ground deformation attributed to the inflation and deflation of magma chambers. This model has been applied to areas such as Kilauea, Hawaii [e.g., *Fiske and Kinoshita*, 1969], Long Valley Caldera, California [e.g., *Savage and Clark*, 1982] and Krafla, Iceland [e.g., *Björnsson et al.*, 1977]. *Bonafede et al.* [1986] solved the problem of a centre of dilation in a viscoelastic halfspace by applying the correspondence principle (Section 6.4.6) to the solutions obtained by *Maruyama* [1964] for an elastic halfspace. *Pollard et al.* [1983] used a boundary element method for interacting cracks in elastic material to simulate a system of two-dimensional, injected dykes in a homogeneous, elastic halfspace. *Roth* [1993] presented a solution for an opening crack contained in a layered halfspace that could be extended to model a system of dykes, and *Bott and Dean* [1973] proposed a viscous diffusion model to predict stress relaxation at divergent plate boundaries following short-lived, extensional episodes. However, most modelling of dilational sources has dealt with the coemplacement strain fields and very little has been done on the postemplacement response. The remainder of this chapter will focus on approaches to modelling postdyking strain transients.

6.2 Continuous Dyke Intrusion at Depth

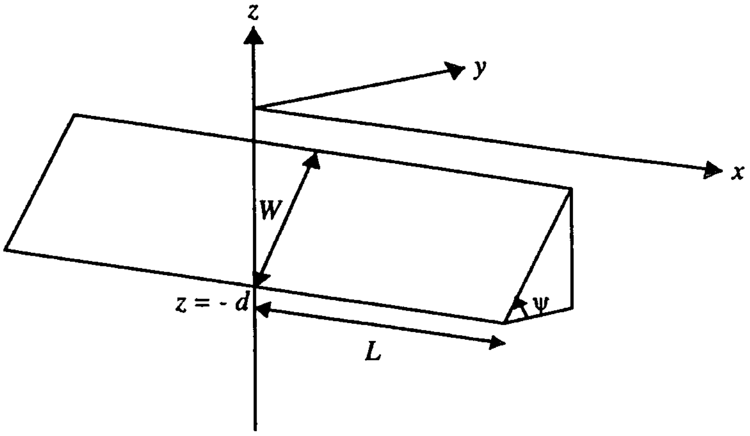

Figure 6.1: Geometry of source model, after *Okada* [1985].

One possible explanation for transient, postdyking deformation is that continued, aseismic dyke intrusion occurs at depth following the main dyke injection event. Modelling of this process is easily performed using elastic halfspace methods.

From the formulae of *Okada* [1985], the surface displacements, u_x, u_y and u_z, resulting from opening of amount U, on a three-dimensional dyke in an elastic halfspace (Figure 6.1), are given by

$$u_x = \frac{U}{2\pi}\left[\frac{q^2}{R(R+\eta)} - I_3 \sin^2\psi\right]\Bigg\|, \tag{6.1}$$

$$u_y = \frac{U}{2\pi}\left[\frac{-\hat{d}q}{R(R+\xi)} - \sin\psi\left\{\frac{\xi q}{R(R+\eta)} - \tan^{-1}\frac{\xi\eta}{qR}\right\} - I_1 \sin^2\psi\right]\Bigg\|, \tag{6.2}$$

$$u_z = \frac{U}{2\pi}\left[\frac{\hat{y}q}{R(R+\xi)} + \cos\psi\left\{\frac{\xi q}{R(R+\eta)} - \tan^{-1}\frac{\xi\eta}{qR}\right\} - I_5 \sin^2\psi\right]\Bigg\|, \tag{6.3}$$

where

$$I_1 = \frac{\mu}{\lambda+\mu}\left[\frac{-1}{\cos\psi}\frac{\xi}{R+\hat{d}}\right] - \frac{\sin\psi}{\cos\psi} I_5, \tag{6.4}$$

$$I_3 = \frac{\mu}{\lambda+\mu}\left[\frac{1}{\cos\psi}\frac{\hat{y}}{R+\hat{d}} - \ln(R+\eta)\right] + \frac{\sin\psi}{\cos\psi} I_4, \tag{6.5}$$

$$I_4 = \frac{\mu}{\lambda+\mu}\frac{1}{\cos\psi}\left[\ln(R+\hat{d}) - \sin\psi\,\ln(R+\eta)\right], \tag{6.6}$$

$$I_5 = \frac{\mu}{\lambda+\mu}\frac{2}{\cos\psi}\tan^{-1}\frac{\eta(X+q\cos\psi)+X(R+X)\sin\psi}{\xi(R+X)\cos\psi}, \tag{6.7}$$

and

$$
\begin{aligned}
p &= y\cos\psi + d\sin\psi, \\
q &= y\sin\psi - d\cos\psi, \\
\hat{y} &= \eta\cos\psi + q\sin\psi, \\
\hat{d} &= \eta\sin\psi - q\cos\psi, \\
R^2 &= \xi^2 + \eta^2 + q^2, \\
X^2 &= \xi^2 + q^2 \,.
\end{aligned}
\tag{6.8}
$$

The along-strike coordinate is x, y is the strike-normal coordinate, ψ is the dip angle, d is the distance from the surface to the bottom of the dyke, L is the dyke half-length, W is its downdip width and λ, μ are the Lamé elastic moduli of the halfspace (Figure 6.1).

Chinnery's notation [*Chinnery*, 1961], $\|$, is used to represent the substitution

$$f(\xi,\eta)\| = f(x,p) - f(x,p-W) - f(x-L,p) + f(x-L,p-w).$$

6.3 The Elastic-Viscous Model

6.3.1 One-Dimensional Model

A second possible explanation for postdyking, transient strain fields is that of stress relaxation in a nonelastic layer below a surface elastic layer. In the simple model shown in Figure 6.2, a thin elastic plate overlies a thin viscous layer, which is underlain by a rigid halfspace.

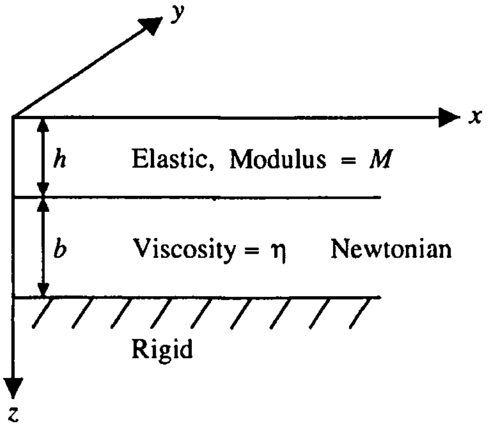

Figure 6.2: Schematic diagram of the 1-D stress diffusion model, after *Foulger et al.* [1992].

The source is considered to be a vertical dyke, infinitely long in the y direction, where x is the horizontal distance normal to the dyke and t is time. By balancing the viscous traction at the base of the elastic layer with the elastic forces within, and assuming plane-stress conditions, the equation of motion for $u(x,t)$, the only non-zero component of the horizontal displacement, is found to be identical to the one-dimensional heat diffusion equation [*Elsasser*, 1969; *Bott and Dean*, 1973]. The area of the elastic layer adjacent to the line $x = 0$ is considered to be initially at rest, and then displaced to the right or left by an amount U_0 when a dyke of thickness $2U_0$ is intruded at time $t = 0$. The appropriate solution to the diffusion equation is then [*Carslaw and Jaeger*, 1959]

$$u(x,t) = U_0 erfc\frac{x}{2\sqrt{\kappa t}}, \tag{6.9}$$

and the horizontal velocity is

$$\frac{\partial u}{\partial t} = \frac{U_0}{t\sqrt{\pi}}\frac{x}{2\sqrt{\kappa t}}e^{-x^2/4\kappa t}, \tag{6.10}$$

where

$$\kappa = \frac{bhM}{\eta}, \tag{6.11}$$

is the diffusivity, b and η are the thickness and viscosity of the viscous layer, h is the thickness of the elastic layer and M is the elastic modulus relating horizontal stress and strain within the elastic layer. For the plane-stress conditions assumed in the x-z plane, $M = 4\mu\ (\lambda + \mu)/(\lambda + 2\mu)$, where λ and μ are the Lamé moduli.

6.3.2 Two-Dimensional Model

For a dyke of finite length, two non-zero components of horizontal displacement exist, $u(x,y,t)$ in the x direction and $v(x,y,t)$ in the y direction. By proceeding as for the one-dimensional case, and modifying the three-dimensional version of Hooke's Law to the two-dimensional case assuming plane-stress conditions (to obtain the normal and shear stresses in the x and y directions), the equations of motion for u and v are given by [*Heki et al.*, 1993]

$$\frac{\partial u}{\partial t} = \kappa_1\frac{\partial^2 u}{\partial x^2} + \kappa_2\frac{\partial^2 v}{\partial x\partial y} + \kappa_3\frac{\partial^2 u}{\partial y^2}, \tag{6.12}$$

$$\frac{\partial v}{\partial t} = \kappa_1\frac{\partial^2 v}{\partial y^2} + \kappa_2\frac{\partial^2 u}{\partial y\partial x} + \kappa_3\frac{\partial^2 v}{\partial x^2}, \tag{6.13}$$

where

$$\kappa_1 \stackrel{def}{=} (\lambda' + 2\mu)\frac{bh}{\eta}\,, \qquad \kappa_2 \stackrel{def}{=} (\lambda' + \mu)\frac{bh}{\eta}\,, \qquad \kappa_3 \stackrel{def}{=} \frac{\mu bh}{\eta}\,, \tag{6.14}$$

and

$$\lambda' \stackrel{def}{=} \frac{2\lambda\mu}{\lambda + 2\mu}\,. \tag{6.15}$$

Note that κ_1 is the same as κ in the one-dimensional case (equation 6.11).

The solutions to equations 6.12 and 6.13 may be found analytically [e.g., *Crouch and Starfield*, 1983], or non-analytically, e.g., using a finite-difference method [*Heki et al.*, 1993]. The boundary conditions imposed on the displacement solution are for zero displacement at an infinite distance from the the dyke axis and zero shear stress at the dyke axis, i.e., $\sigma_{xy} = \frac{1}{2}\left[\frac{\partial u}{\partial y} + \frac{\partial v}{\partial x}\right] = 0$.

6.4 The Elastic-Viscoelastic Model

6.4.1 Introduction

Following the method of *Rundle* [1978, 1980] and *Hofton et al.* [1995] (preprint in pocket at back of thesis), a model is constructed for a finite, two-dimensional, rectangular dyke in an elastic layer overlying a viscoelastic halfspace. The mathematical method used to obtain the near field, time-dependent displacements proceeds as follows :

Step 1. The Green's functions for a dilational point source in an elastic layer over an elastic halfspace are computed.

Step 2. The correspondence principle [*Lee*, 1955] is applied to introduce viscoelastic properties into the halfspace.

Step 3. The resultant Green's functions are integrated over the finite source region.

The choice of materials in the viscoelastic region is limited to those whose rheological properties have linear constitutive laws, and the rheology chosen is that of a Maxwell viscoelastic solid, i.e., one that behaves as an elastic solid on short timescales and as a Newtonian fluid on long timescales. For times short compared to a year the Earth behaves elastically, while for longer times permanent, non-elastic deformations occur and it is these observations that influence the choice of rheological properties for this model. The Maxwell solid is the simplest kind of medium that exhibits this dual behaviour. A Maxwell element is shown in Figure 6.3. If a constant displacement is suddenly applied to the free end, the spring will immediately stretch, and over the course of time it will gradually contract again as the piston in the dashpot moves. The applied force is analogous to stress and displacement to strain.

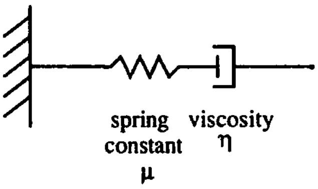

Figure 6.3: A Maxwell Element.

Gravitational effects are also included in the model. For deformation at the surface of an elastic halfspace, gravitational effects become important over distances greater than 1000 km [*Rundle*, 1981] but have little effect near the source region. However, in viscoelastic structures this is not the case. There, stresses in some regions of the media decrease as flow occurs. This is because the initial elastic stresses induce flow in the media, producing time-dependent displacements and generating gravitational stresses as a result. Equilibrium is eventually attained between the gravitational and elastic stresses in the flowing region. Gravitational effects are important over long time periods, and when an event is assumed to recur periodically, but are small over short time periods [*Rundle*, 1981].

Gravitational effects are dependent on two factors; the vertical component of the surface gravitational acceleration, g, and the Gravitational constant, G_0. To compute the displacement solutions that involve terms associated with g and G_0 (referred to as the "full solution" hereafter), Step 1 must be subdivided into two separate problems [*Rundle*, 1980]. First, the equations for an infinite elastic-gravitational halfspace are solved. Then using these solutions, the Green's functions for a point source in an elastic-gravitational layer over a elastic-gravitational halfspace are calculated.

The calculation of the Green's functions for a point source in a layered, elastic-

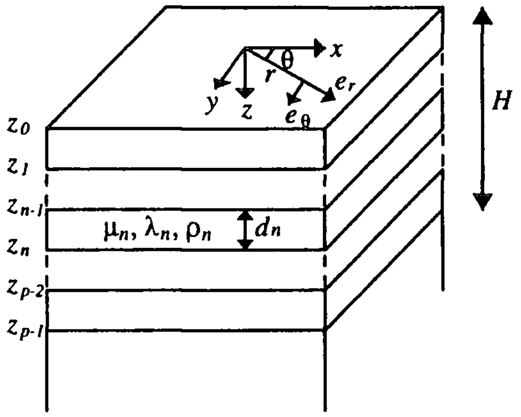

Figure 6.4: Coordinate system and geometry of layered halfspace, after *Rundle* [1980].

gravitational halfspace involves the Haskell-Thomson propagator matrix method [*Haskell*, 1953; *Thomson*, 1950], which simplifies the algebra involved in relating the solution in one layer to that in the next. In the full solution, eight quantities, organised into an 8 x 8 matrix, must be propagated. These quantities are the kernel functions, three of which are for displacement, three for normal tractions and two for the gravitational potential and its gradient minus a multiple of the vertical displacement. *Rundle* [1981] showed that most of the gravitational effects for dislocations arise from the terms associated with g, not G_0. Using this fact the number of quantities propagated from one layer to another can be reduced from eight to six. This reduced "full solution" is presented here.

6.4.2 Solution to the Infinite Space Problem

For purposes of clarity, it is necessary to review briefly earlier work [*Rundle*, 1980, 1981]. *Rundle* [1980] used a polar coordinate system (r, θ, z) with unit vectors $\hat{e_r}$, $\hat{e_\theta}$, $\hat{e_z}$, the z axis oriented into the medium and the origin at the surface of a layered elastic-gravitational halfspace (Figure 6.4). The elastic moduli in the nth layer are denoted by λ_n and μ_n, the density by ρ_n and the thickness by d_n. The depth to the top of the halfspace is H, which is the sum of the d_n. In the structure there are $p - 1$ layers with the halfspace being the pth layer. The interface between layers n and $n + 1$ is defined as z_n, hence $z_0 = 0$ is the free surface and $z_{p-1} = H$ is the boundary between the deepest layer and the halfspace.

The equations to be solved in the full solution are the vector static perturbation equations of elastic-gravitational equilibrium [*Love*, 1911],

$$\nabla^2\vec{u} + \frac{1}{1-2\sigma}\nabla\nabla\cdot\vec{u} + \frac{\rho_0 g}{\mu}\nabla(\vec{u}\cdot\hat{e}_z) - \frac{\rho_0}{\mu}\nabla\phi - \frac{\rho_0 g}{\mu}\hat{e}_z\nabla\cdot\vec{u} = 0, \tag{6.16}$$

$$\nabla^2\phi = -4\pi\rho_0 G_0\nabla\cdot\vec{u}, \tag{6.17}$$

where $\vec{u}$ and ϕ are the displacement and gravitational potential perturbations evaluated at a deformed coordinate x, g is the vertical component of the unperturbed surface gravitational acceleration, G_0 is the Gravitational constant, σ is Poisson's ratio, ρ_0 is density and μ is rigidity.

To simplify the problem somewhat, g is assumed to be constant and a linear functional of the density. In addition, g is assumed to be invariant with depth since this contributes a higher-order effect to this first-order problem. All perturbed quantities are presumed to tend to zero as $z \to \infty$ and the free surface is assumed to be stress free.

Using the fact that for displacements resulting from an event in a layered elastic-gravitational medium, self-gravitational effects arising from G_0 are generally much smaller than g [*Rundle*, 1981], equations 6.16 and 6.17 can be reduced to

$$\nabla^2\vec{u} + \frac{1}{1-2\sigma}\nabla\nabla\cdot\vec{u} + \frac{\rho_0 g}{\mu}\nabla(\vec{u}\cdot\hat{e}_z) - \frac{\rho_0 g}{\mu}\hat{e}_z\nabla\cdot\vec{u} = 0\ , \tag{6.18}$$

since setting $G_0 = 0$ implies ϕ is constant. It is the solutions to this reduced equation that must be found.

Rundle [1980], using the orthonormal basis vector functions

$$\vec{P_m} = J_m(kr)e^{im\theta}\hat{e}_z, \tag{6.19}$$

$$\vec{B_m} = \frac{1}{k}\nabla(J_m(kr)e^{im\theta}) = \left(\frac{\partial J_m(kr)}{\partial kr}\hat{e_r} + im\frac{J_m(kr)}{kr}\hat{e_\theta}\right)e^{im\theta}, \tag{6.20}$$

$$\vec{C_m} = \frac{1}{k}\nabla\times\vec{P_m} = \left(im\frac{J_m(kr)}{kr}\hat{e_r} - \frac{\partial J_m(kr)}{\partial kr}\hat{e_\theta}\right)e^{im\theta}\ , \tag{6.21}$$

where $J_m(kr)$ are cylindrical Bessel functions, $i = \sqrt{-1}$ and k is the wavenumber in dynamical problems [cf., *Ben-Menahem and Singh*, 1968], expanded $\vec{u}$, the perturbed displacement, as

$$\vec{u} = \sum_{m=0}^{\infty}\int_0^{\infty} k\,dk[W_m(z)\vec{P_m} + U_m(z)\vec{B_m} + V_m(z)\vec{C_m}]. \tag{6.22}$$

Substituting equation 6.22 into 6.18 yields the ordinary differential equations for the functions $W_m(z)$, $U_m(z)$ and $V_m(z)$. The solution given by $V_m(z)$ is found to be identical to the solution in the non-gravitating case [*Singh*, 1970] and will be derived in the next section. The functions $U_m(z)$ and $W_m(z)$ are given by [*Rundle*, 1981]

$$\begin{pmatrix} U_m(z) \\ V_m(z) \end{pmatrix} = \begin{pmatrix} 1 \\ p_1^+(k) \end{pmatrix} e^{a_1 z} + \begin{pmatrix} 1 \\ p_1^-(k) \end{pmatrix} e^{-a_1 z} + k \begin{pmatrix} 1 \\ p_2^+(k) \end{pmatrix} e^{a_2 z} + k \begin{pmatrix} 1 \\ p_2^-(k) \end{pmatrix} e^{-a_2 z}, \tag{6.23}$$

where

$$\pm a_1 = \pm(k^2 + k\eta\sqrt{\zeta})^{1/2}, \tag{6.24}$$

$$\pm a_2 = \pm(k^2 - k\eta\sqrt{\zeta})^{1/2}, \tag{6.25}$$

$$\zeta = \frac{1-2\sigma}{2(1-\sigma)}, \tag{6.26}$$

$$p_j^{\pm}(k) = \pm 1 - \frac{k\eta\sqrt{\zeta}}{(a_j + k)} \frac{1+\sqrt{\zeta}}{a_j - k\sqrt{\zeta}}, \qquad j = 1, 2, \tag{6.27}$$

and

$$\eta \overset{def}{=} \frac{\rho_0 g}{\mu} \overset{def}{=} \rho g, \tag{6.28}$$

$$\rho = \frac{\rho_0}{\mu}. \tag{6.29}$$

The quantities a_j and p_j (j=*1*,*2*) are either real or complex, depending upon whether k is greater than or less than a quantity termed the "gravitational wave number", k_g, and which is found by solving the equation $a_2 = 0$. Hence, k_g is given by

$$k_g = \eta\sqrt{\zeta}. \tag{6.30}$$

6.4.3 Solution to the Layered Half Space Problem

For an elastic, uniform, infinite space, the vector displacements $\vec{u}$ satisfy the Navier equation,

$$\nabla^2 \vec{u} + \frac{1}{1-2\sigma} \nabla\nabla \cdot \vec{u} = 0. \tag{6.31}$$

The solution in the nth layer is given by [*Singh*, 1970; *Rundle*, 1980]

$$\vec{u}^n = \sum_{m=0} \int_0^\infty k\, dk\, \vec{u}_m^n\,. \tag{6.32}$$

If the source is at the interface between two layers, $\vec{u}^n_m$ may be considered to be a solution to the homogeneous problem such that

$$\vec{u}^n_m = x^n_m \vec{P}_m + y^n_m \vec{B}_m + z^n_m \vec{C}_m. \tag{6.33}$$

P_m, B_m and C_m are the orthonormal basis vectors given by equations 6.19 to 6.21. The displacement kernel functions, x^n_m, y^n_m and z^n_m, are given by

$$x^n_m = p_1^- e^{-a_1 z} B^-_{mn} + p_1^+ e^{a_1 z} B^+_{mn} + k p_2^- e^{-a_2 z} D^-_{mn} + k p_2^+ e^{a_2 z} D^+_{mn} \ , \tag{6.34}$$

$$y^n_m = e^{-a_1 z} B^-_{mn} + e^{a_1 z} B^+_{mn} + k e^{-a_2 z} D^-_{mn} + k e^{a_2 z} D^+_{mn} \ , \tag{6.35}$$

$$z^n_m = e^{-kz} C^-_{mn} + e^{kz} C^+_{mn} \ , \tag{6.36}$$

where B^-_{mn}, B^+_{mn}, C^-_{mn}, C^+_{mn}, D^-_{mn} and D^+_{mn} are constants to be determined. Similarly, the perturbed normal tractions across a plane $z =$ constant in the nth layer are

$$\vec{T}_n = \sum_{m=0} \int_0^\infty k\,dk\,\vec{T}^n_m, \tag{6.37}$$

where

$$\vec{T}^n_m = X^n_m \vec{P}_m + Y^n_m \vec{B}_m + Z^n_m \vec{C}_m, \tag{6.38}$$

and X^n_m, Y^n_m and Z^n_m are the normal traction kernel functions given by

$$X^n_m = \frac{\mu}{k(1-2\sigma)} \left\{ (1-\sigma)\ (x^n_m)' - \sigma k y^n_m \right\} \ , \tag{6.39}$$

$$Y^n_m = \frac{\mu}{2} \left\{ (y^n_m)' + k x^n_m \right\} \ , \tag{6.40}$$

$$Z^n_m = \mu (z^n_m)', \tag{6.41}$$

and

$$(x^n_m)' = a_1(-p_1^- e^{-a_1 z} B^-_{mn} + p_1^+ e^{a_1 z} B^+_{mn}) + k a_2(-p_2^- e^{-a_2 z} D^-_{mn} + p_2^+ e^{a_2 z} D^+_{mn}) \ , \tag{6.42}$$

$$(y^n_m)' = a_1(-e^{-a_1 z} B^-_{mn} + e^{a_1 z} B^+_{mn}) + k a_2(-e^{-a_2 z} D^-_{mn} + e^{a_2 z} D^+_{mn}) \ , \tag{6.43}$$

$$(z^n_m)' = k(e^{-kz} C^-_{mn} + e^{kz} C^+_{mn}) \ . \tag{6.44}$$

Inspection of equations 6.34 to 6.36 and 6.39 to 6.42 reveals that the problem can be divided into two separate parts, the "R" problem involving the x^n_m, y^n_m, X^n_m and Y^n_m, i.e., the $\vec{P}_m$ and $\vec{B}_m$, terms (a 4 x 4 matrix problem) , and the "L" problem involving the z^n_m and Z^n_m, i.e., the $\vec{C}_m$, terms (a 2 x 2 matrix problem) [*Singh*, 1970; *Rundle*, 1980].

In order to solve the "R" problem, two column matrices, $[A_m^n(z)]$ and $[K_m^n]$, are defined as [*Singh*, 1970]

$$[A_m^n(z)] = [x_m^n(z), y_m^n(z), X_m^n(z), Y_m^n(z)]^{\mathbf{T}}, \tag{6.45}$$

$$[K_m^n] = [B_{mn}^-, B_{mn}^+, D_{mn}^-, D_{mn}^+]^{\mathbf{T}}. \tag{6.46}$$

Using the expressions for x_m^n, y_m^n,X_m^n and Y_m^n given above, $[A_m^n(z)]$ can be written as

$$[A_m^n(z)] = [Z^n(z)][K_m^n], \tag{6.47}$$

where the elements of $[Z^n(z)]$ are [*Rundle*, 1981]

$$\begin{aligned}
(1,1) &= p_1^- e^{-a_1 z},\\
(1,2) &= p_1^+ e^{a_1 z},\\
(1,3) &= kp_2^- e^{-a_2 z},\\
(1,4) &= kp_2^+ e^{a_2 z},\\
(2,1) &= e^{-a_1 z},\\
(2,2) &= e^{a_1 z},\\
(2,3) &= ke^{-a_2 z},\\
(2,4) &= ke^{a_2 z},\\
(3,1) &= \mu_n(\sigma_n[a_1 p_1^- - k] - a_1 p_1^-)e^{-a_1 z}/([1-2\sigma_n]k),\\
(3,2) &= \mu_n(a_1 p_1^+ - \sigma_n[a_1 p_1^+ + k])e^{a_1 z}/([1-2\sigma_n]k),\\
(3,3) &= \mu_n(\sigma_n[a_2 p_2^- - k] - a_2 p_2^-)e^{-a_2 z}/(1-2\sigma_n),\\
(3,4) &= \mu_n(a_2 p_2^+ - \sigma_n[a_2 p_2^+ + k])e^{a_2 z}/(1-2\sigma_n),\\
(4,1) &= \mu_n(kp_1^- - a_1)e^{-a_1 z}/2k,\\
(4,2) &= \mu_n(kp_1^+ + a_1)e^{a_1 z}/2k,\\
(4,3) &= \mu_n(kp_2^- - a_2)e^{-a_2 z}/2,\\
(4,4) &= \mu_n(kp_2^+ + a_2)e^{a_2 z}/2.
\end{aligned} \tag{6.48}$$

The matrix $[Z^n(z)]$ is used to calculate the Haskell-Thomson propagator matrix $[a^n]$ associated with the layer n. By inverting equation 6.47 to obtain

$$[K_m^n] = [Z^n(z)]^{-1}[A_m^n(z)], \tag{6.49}$$

and considering the layer $n-1$, it can be easily seen that [*Singh*, 1970]

$$[K_m^n] = [Z^n(z_{n-1})]^{-1}[A_m^n(z_{n-1})]. \tag{6.50}$$

Hence, equating and rearranging equations 6.49 and 6.50 gives

$$[A^n_m(z_{n-1})] = [a^n][[A^n_m(z_n)], \tag{6.51}$$

where $[a^n]$ is given by

$$[a^n] = [Z^n(z_{n-1})][Z^n(z_n)]^{-1}. \tag{6.52}$$

To compute $[a^n]$, the origin is shifted temporarily to $z = z_n$ [*Singh*, 1970], so equation 6.52 becomes

$$[a^n] = [Z^n(-d_n)][Z^n(0)]^{-1}, \tag{6.53}$$

and the elements of matrix $[a^n]$ can be determined.

The continuity condition at the interface $z = z_{n-1}$ yields the expression

$$[A^{n-1}_m(z_{n-1})] = [A^n_m(z_{n-1})]. \tag{6.54}$$

The point source is considered to be situated on the z-axis at a depth c below the free surface. The source layer is designated as layer s, with boundaries $z = z_{s-1}$ and z_s. Layer s is divided into two layers of identical properties, s_1 and s_2. s_1 is bounded by the layers $z = z_{s-1}$ and z_{s_1}, and z_2 is bounded by the layers $z = z_{s_1}$ and z_{s_2}. The introduction of the point source will therefore give jump discontinuities in x^n_m, y^n_m, X^n_m and Y^n_m across the plane $z = z_{s_1}$. Hence, using equation 6.54

$$[A^{s_2}_m(z_{s_1})] - [A^{s_1}_m(z_{s_1})] = [D_m]. \tag{6.55}$$

The vector $[D_m]$ is a vector of discontinuities for a particular source, and has been derived for various source functions by *Singh* [1970].

Using equations 6.51, 6.54 and 6.55, and the relation [*Haskell*, 1953]

$$[a^{s_1}][a^{s_2}] = [a^s], \tag{6.56}$$

it is found that

$$[A^1_m(0)] = [U][A^p_m(H)] - [V][D_m], \tag{6.57}$$

where

$$[U] = [a^1][a^2]\ldots[a^{p-1}], \tag{6.58}$$

$$[V] = [a^1][a^2]\ldots[a^{s_1}]. \tag{6.59}$$

The boundary conditions specify that the free surface must be stress free, and that zero displacements and stresses occur at infinity, hence equations 6.45 and 6.46 become

$$[A^1_m(0)] = [x^1_m(0), y^1_m(0), 0, 0]^{\mathbf{T}}, \tag{6.60}$$

$$[K^p_m] = [B^-_{mp}, 0, D^-_{mp}, 0]^{\mathbf{T}}. \tag{6.61}$$

Substituting these two expressions in equation 6.57, it is found that

$$[x^1_m(0), y^1_m(0), 0, 0]^{\mathbf{T}} = [E][B^-_{mp}, 0, D^-_{mp}, 0]^{\mathbf{T}} - [F_m], \tag{6.62}$$

where

$$[E] = [U][Z^p(H)], \tag{6.63}$$

$$[F_m] = [V][D_m]. \tag{6.64}$$

Solving equations 6.62 for the coefficients B^-_{mp} and D^-_{mp} yields the expressions for the kernel functions [*Singh*, 1970]

$$x^1_m(0) = \{E|^{14}_{13}(F_m)_3 + E|^{13}_{31}(F_m)_4 - E|^{34}_{13}(F_m)_1\}/E|^{34}_{13}, \tag{6.65}$$

$$y^1_m(0) = \{E|^{24}_{13}(F_m)_3 + E|^{23}_{31}(F_m)_4 - E|^{34}_{13}(F_m)_2\}/E|^{34}_{13}, \tag{6.66}$$

where

$$E|^{ij}_{kl} = E_{ik}E_{jl} - E_{il}E_{jk}. \tag{6.67}$$

E_{ij} are the components of matrix $[E]$ defined by equation 6.63 and $(F_m)_j$ are the components of vector $[F_m]$ defined by equation 6.64.

The "L" problem is tackled in a similar manner to obtain [*Singh*, 1970]

$$z^1_m(0) = \{E^L_{11}(F^L_m)_2 - E^L_{21}(F^L_m)_1\}/E^L_{21}, \tag{6.68}$$

where the superscript L distinguishes $[E^L]$ and $(F^L_m)_j$ from their counterparts in the "R" problem.

Equations 6.65 to 6.68 define a solution for the displacements which have zero tractions at $z = 0$ and vanish as $z \rightarrow \infty$.

6.4.4 Source Functions

The source vectors $[D_m]$ and $[D_m^L]$ for the six elementary dislocations have been determined by *Singh* [1970]. In the notation of *Steketee* [1958], these six elementary dislocations are : *(i,j) = (1,1), (2,2), (3,3), (2,3), (1,3)* and *(1,2)* (Figure 6.5), where i refers to the direction of the corresponding force system at the source and j refers to the normal to the plane across which the force system is applied. For example, the source *(1,2)* relates to a vertical strike-slip fault and *(2,3)* to a dip-slip fault.

To find the source function for a dyke with dip ψ, the coordinate system must be rotated through the same angle about the origin. Using the rotation

$$(i',j') = [\Omega](i,j)[\Omega]^{-1}, \tag{6.69}$$

where the matrix $[\Omega]$ is given by

$$[\Omega] = \begin{pmatrix} \cos\psi & \sin\psi \\ -\sin\psi & \cos\psi \end{pmatrix}, \tag{6.70}$$

the expression for the source function for a dyke with dip ψ is

$$(i',j') = (3,3)\cos^2\psi + (2,2)\sin^2\psi - (2,3)\sin 2\psi. \tag{6.71}$$

The components are [*Singh*, 1970]

$$\begin{array}{lll} (i,j) = (2,2); & (D_0)_1 = 2\gamma\frac{3\delta-1}{\delta+1}, & (D_0)_4 = \mu\gamma\frac{7\delta-1}{\delta+1}, \\ & (D_2)_4 = \mu\gamma, & (D_2^L)_2 = -2\mu\gamma i, \\ (i,j) = (3,3); & (D_0)_1 = 2\gamma, & \\ (i,j) = (2,3); & (D_1)_2 = -2\gamma i, & (D_1^L)_1 = -2\gamma, \end{array} \tag{6.72}$$

and $\gamma = \Delta U d\Sigma/4\pi$, where ΔU is the relative displacement across the dyke, $d\Sigma$ is an element of area on the dyke and δ=1/(3-4σ). Hence, three force systems are included in the dyking problem; one describing opening in the vertical direction (*m=0*), a second describing opening in the horizontal direction (*m=2*) and a third describing shearing (*m=1*).

6.4.5 Surface Displacements From a Dilating Point Source

Using equations 6.32, 6.33 and 6.71, the displacement vector at the surface resulting from a dilating point source in an elastic layer over an elastic halfspace, both of

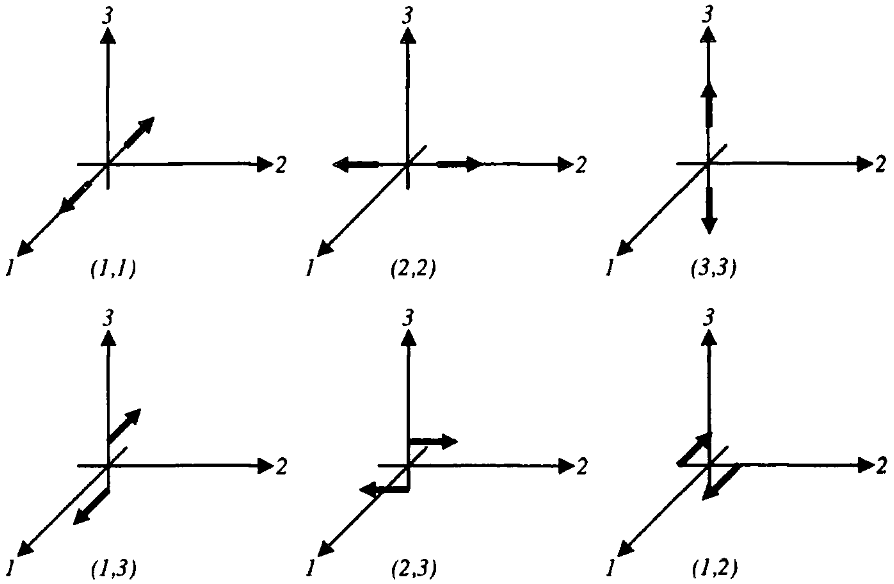

Figure 6.5: The force couples corresponding to the six elementary dislocations.

which are subject to gravitational effects, may be written as

$$\begin{aligned}\vec{u} &= \int_0^\infty k\,dk\Big\{\Big[x_0^{1(33)}(0)\vec{P}_0 + y_0^{1(33)}(0)\vec{B}_0\Big]\cos^2\psi \\ &+ \Big[x_0^1(0)\vec{P}_0 + y_0^1(0)\vec{B}_0 + x_2^1(0)\vec{P}_2 + y_2^1(0)\vec{B}_2 + z_2^1(0)\vec{C}_2\Big]\sin^2\psi \\ &- \Big[x_1^1(0)\vec{P}_1 + y_1^1(0)\vec{B}_1 + z_1^1(0)\vec{C}_1\Big]\sin 2\psi\Big\}, \qquad (6.73)\end{aligned}$$

where $x_m^1(0), y_m^1(0)$ and $z_m^1(0)$ are given by equations 6.65 to 6.68. The superscript $(3,3)$ distinguishes the kernel functions of the $(i,j) = (3,3)$ component from the $(i,j) = (2,2)$ component.

Substituting equations 6.19 to 6.21 for $\vec{P}_m$, $\vec{B}_m$ and $\vec{C}_m$, obtaining the real part of the expression and splitting the displacement vector into its three components gives

$$\begin{aligned}u_r &= -\int_0^\infty k\,dk\Big\{y_0^{1(33)}(0)J_1(kr)\cos^2\psi + \Big(y_0^1(0)J_1(kr) \\ &- \Big[y_2^1(0)\Big(\frac{J_1(kr) - J_3(kr)}{2}\Big) - \frac{1}{i}z_2^1(0)\Big(\frac{J_1(kr) + J_3(kr)}{2}\Big)\Big]\cos 2\theta\Big)\sin^2\psi \\ &- \Big[\frac{1}{i}y_1^1(0)\Big(\frac{J_0(kr) + J_2(kr)}{2}\Big) + z_1^1(0)\Big(\frac{J_0(kr) + J_2(kr)}{2}\Big)\Big]\sin\theta\sin 2\psi\Big\}, \\ &\qquad (6.74)\end{aligned}$$

$$
\begin{aligned}
u_\theta &= \int_0^\infty k\,dk\Big\{\Big[\frac{1}{i}z_2^1(0)\Big(\frac{J_1(kr)-J_3(kr)}{2}\Big) \\
&- y_2^1(0)\Big(\frac{J_1(kr)+J_3(kr)}{2}\Big)\Big]\sin 2\theta\sin^2\psi + \Big[\frac{1}{i}y_1^1(0)\Big(\frac{J_0(kr)+J_2(kr)}{2}\Big) \\
&+ z_1^1(0)\Big(\frac{J_0(kr)-J_2(kr)}{2}\Big)\Big]\cos\theta\sin 2\psi\Big\}, \qquad (6.75)
\end{aligned}
$$

and

$$
\begin{aligned}
u_z &= \int_0^\infty k\,dk\Big\{x_0^{1(33)}(0)J_0(kr)\cos^2\psi + x_0^1(0)J_0(kr)\sin^2\psi \\
&+ x_2^1(0)J_2(kr)\cos 2\theta\sin^2\psi + \frac{1}{i}x_1^1(0)J_1(kr)\sin\theta\sin 2\psi\Big\}. \qquad (6.76)
\end{aligned}
$$

The following relations have been used to simplify these expressions:

$$
\begin{aligned}
J_{m-1}(kr) + J_{m+1}(kr) &= \frac{2m}{kr}J_m(kr) \\
J_{m-1}(kr) - J_{m+1}(kr) &= 2\frac{d}{d\,kr}J_m(kr). \qquad (6.77)
\end{aligned}
$$

6.4.6 Introduction of Time Dependence

The correspondence principle [*Lee*, 1955] is used to add appropriate viscous properties to the halfspace. This principle states that if the elastic solution to a problem is known and the inertial forces are negligible, the quasi-static solution for a linear, viscoelastic medium is obtained by replacing all the time-dependent quantities by their transformed quantities and then inverting the resulting expression. In practice, this requires that μ, λ and $UH(t)$ in each component of the elastic solution $u(t)$, be replaced by $s\bar{\lambda}(s)$, $s\bar{\mu}(s)$ and U/s to obtain $\bar{u}(s)$, where the bar signifies the Laplace transformed quantity and s is the parameter conjugate to time. $H(t)$ is the Heaviside step function and is the time dependent part of the applied dislocation. It indicates that the displacement is zero when $t < 0$. The function $\bar{u}(s)$ is then inverted to give $u_v(t)$, the solution to the viscoelastic problem. In order to compute the Laplace transformed solution, an approximation method appearing to give smooth time-domain results in the time interval studied, and involving as few function evaluations as possible, is used [*Rundle*, 1982]. This method involves the Prony series where $u_v(t)$ is approximated by a function $u_v^\star(t)$ comprising of a series of decaying exponentials [*Schapery*, 1961; *Cost*, 1964]:

$$u_v(t) \cong \sum_{ij}^{N} A_i \tau_i (1 - e^{-t/\tau_i}) = u_v^\star(t). \tag{6.78}$$

The A_i are a set of constants that can be determined by a least squares method and the $\{\tau_i\}$ are a set of N relaxation times and were set equal to:

$$\{0.5\tau_a, \tau_a, 5\tau_a, 10\tau_a, 50\tau_a, 100\tau_a\}. \tag{6.79}$$

Both elastic moduli of the halfspace, λ_H and μ_H, may possess stress relaxation properties. However, the variation of both parameters with time produces results that differ by only a few percent from those obtained using a model in which only μ_H is varied [*Rundle*, 1982]. Hence, only the Maxwell constitutive relation for $\mu_H(t)$ is used so that

$$s\bar{\mu}_H(s) = \frac{s\mu_H}{s + 2/\tau_a}, \tag{6.80}$$

where τ_a is the characteristic relaxation time given by $\tau_a = 2\eta/\mu_h$. η and μ_h are the viscosity and the elastic modulus of the Maxwell fluid. The required solution is then obtained by integrating $u_v^\star(t)$ over the source region.

6.4.7 Results

6.4.7.1 Introduction

The deformation field predicted by the elastic-viscoelastic model is strongly dependent on many parameters, the most important of which are H, W/H, AL, τ_a and ψ. Much of the model behaviour can be summarised with dimensionless figures, and this policy is adopted in this section. The variation of parameters peripherally relevant to the situation in north Iceland (e.g., ψ) was explored by *Hofton et al.* [1995]. In this section the models most relevant to north Iceland are explored in detail, including the effects of varying H, W/H, AL and τ_a.

6.4.7.2 Varying H, W/H, AL and τ_a

Total postdyking displacement is illustrated for the case of a vertical dyke 200 km long with an elastic layer thickness of 30 km at time $2\tau_a$ after intrusion (Figures 6.6

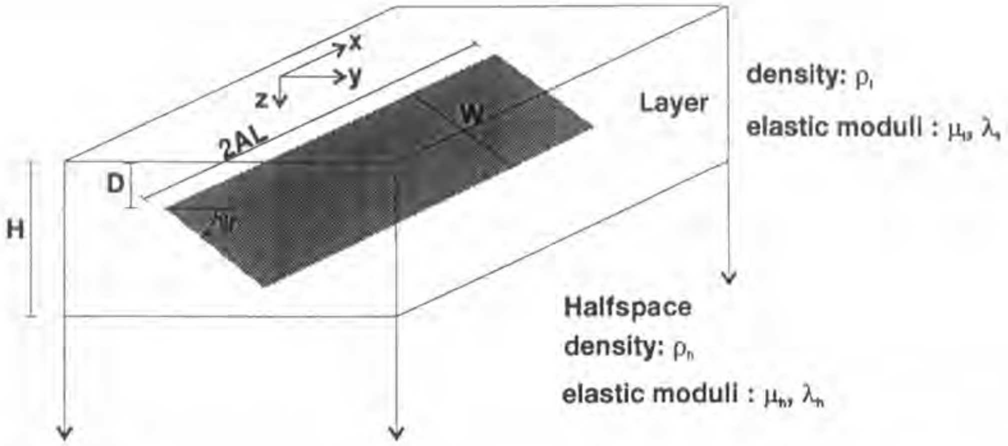

Figure 6.6: Geometry and coordinate system for a rectangular, dipping dyke in an elastic-gravitational layer over a viscoelastic-gravitational halfspace. H is the thickness of the layer, D is the depth to the top of the dyke, $2AL$ is the along-strike length, W is the downdip width, and ψ is the dip.

to 6.10). Gravitational effects are included in all the figures, which show nondimensional motion perpendicular to the dyke over an area scaled by H. Strictly speaking this is not rigorous as independent length scales exist in the gravitational problem, for example, H, the layer thickness, k_g^L, the gravitational wave number for the layer, and k_g^H, the gravitational wave number for the halfspace. A nondimensionalising of the kernel functions for the gravitational problem results in a ratio of gravitational effects, represented by $\rho g H$, to elasticity effects μ, e.g., $\rho g H/\mu$ [*Rundle*, 1982]. However, for the short time scale most relevant to the deformation in north Iceland (Chapter 7), scaling by H is a reasonable approximation (e.g., compare Figures 3 and 4 of *Hofton et al.* [1995]).

The horizontal and vertical total postdyking displacement fields for $t = 2\tau_a$ resulting from a dyke extending completely ($W/H = 1$) and partially ($W/H = 0.5$ and $W/H = 0.25$) through the elastic layer are shown in Figures 6.7 (in profile) and 6.8 (in map view). The dyke-normal horizontal displacement field for a dyke extending completely through the elastic layer shows little deformation in the very near-source region, but beyond this, substantial displacement at distances of up to several downdip dyke widths from the source (Figure 6.7a). Substantial uplift is produced above the dyke, much less motion on either side (i.e., in the flank zones) at distances comparable to the thickness of the elastic layer, and uplift further away of the same order of magnitude as that produced immediately above

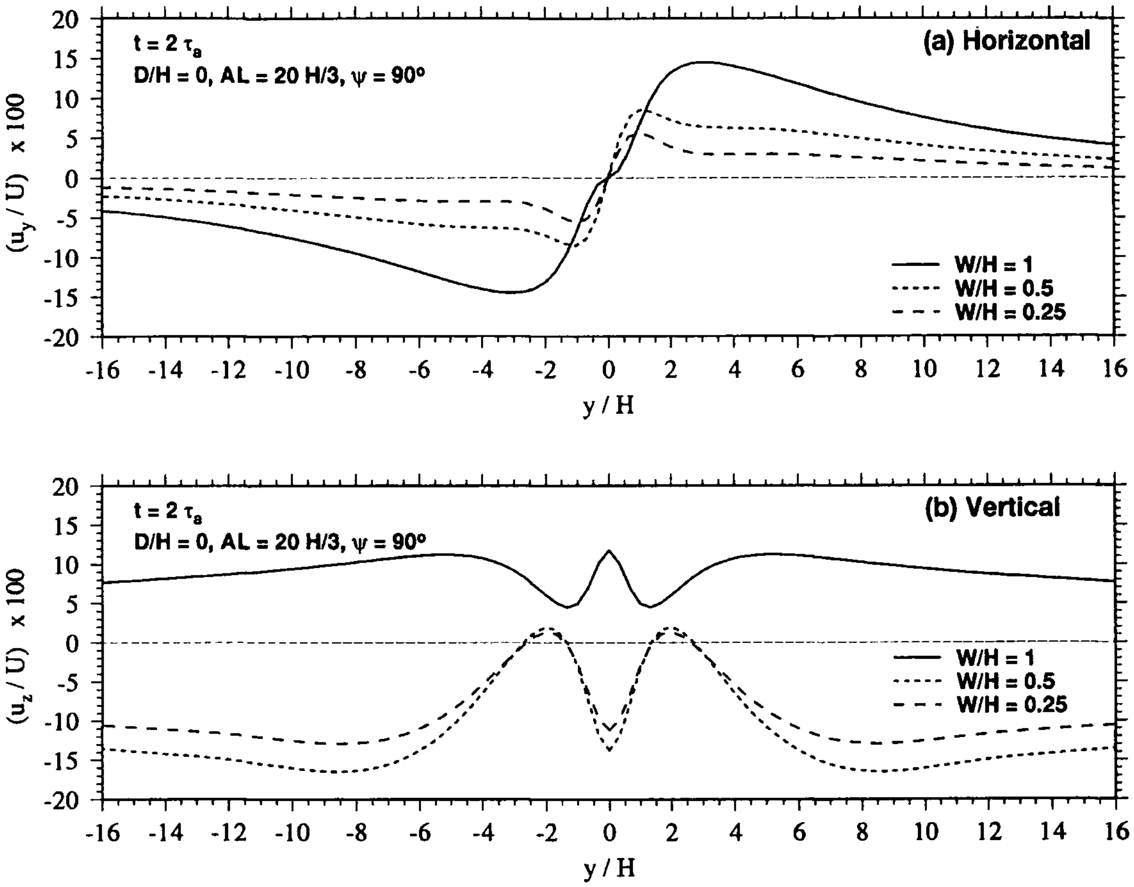

Figure 6.7: Nondimensional (a) horizontal and (b) vertical total postdyking surface displacement against distance normal to the dyke at time $2\tau_a$ after dyke emplacement. Model parameters are $H = 30$ km, $2AL = 20H/3$, $\rho_l = \rho_h = 3.0$ g/cm^3, $\mu_l = \mu_h = \lambda_l = \lambda_h = 3 \times 10^{10}$ Pa, $D/H = 0$, and $\psi = 90°$. The profiles from a surface dyke extending completely ($W/H = 1$), and partially ($W/H = 0.5$ and $W/H = 0.25$) through the elastic layer are shown by the solid and dashed curves. Each displacement profile has been evaluated at the midpoint of the dyke. U is the full dyke thickness.

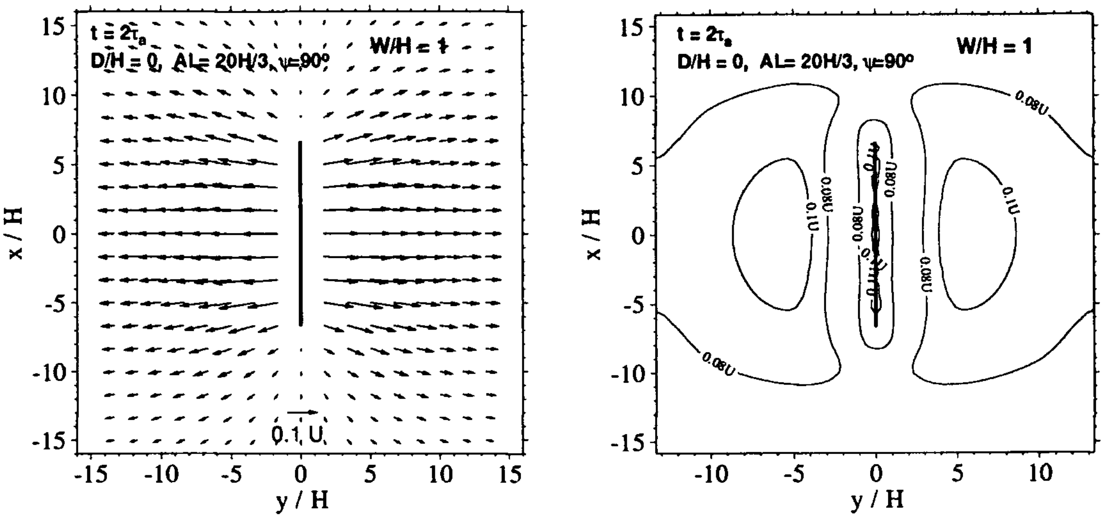
(a) Horizontal

(b) Vertical

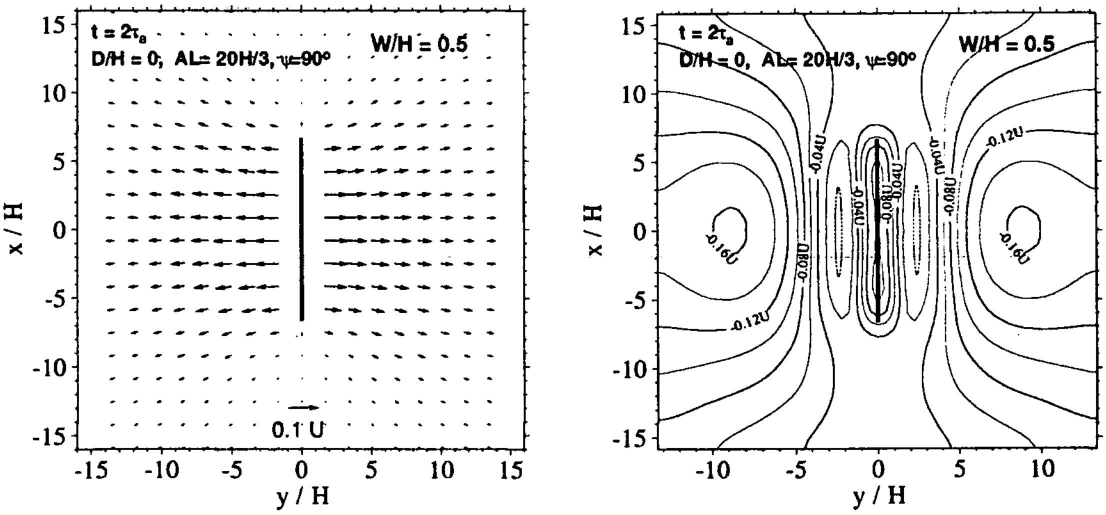
(c) Horizontal

(d) Vertical

Figure 6.8: Nondimensional total postdyking surface displacement at time $2\tau_a$ after dyke emplacement. Model parameters are identical to those in Figure 6.7. (a) Horizontal and (b) vertical deformation fields for $W/H = 1$ and (c) horizontal and (d) vertical fields for $W/H = 0.5$. The dyke is shown by the solid line in the centre. Vertical contours are every 0.02U.

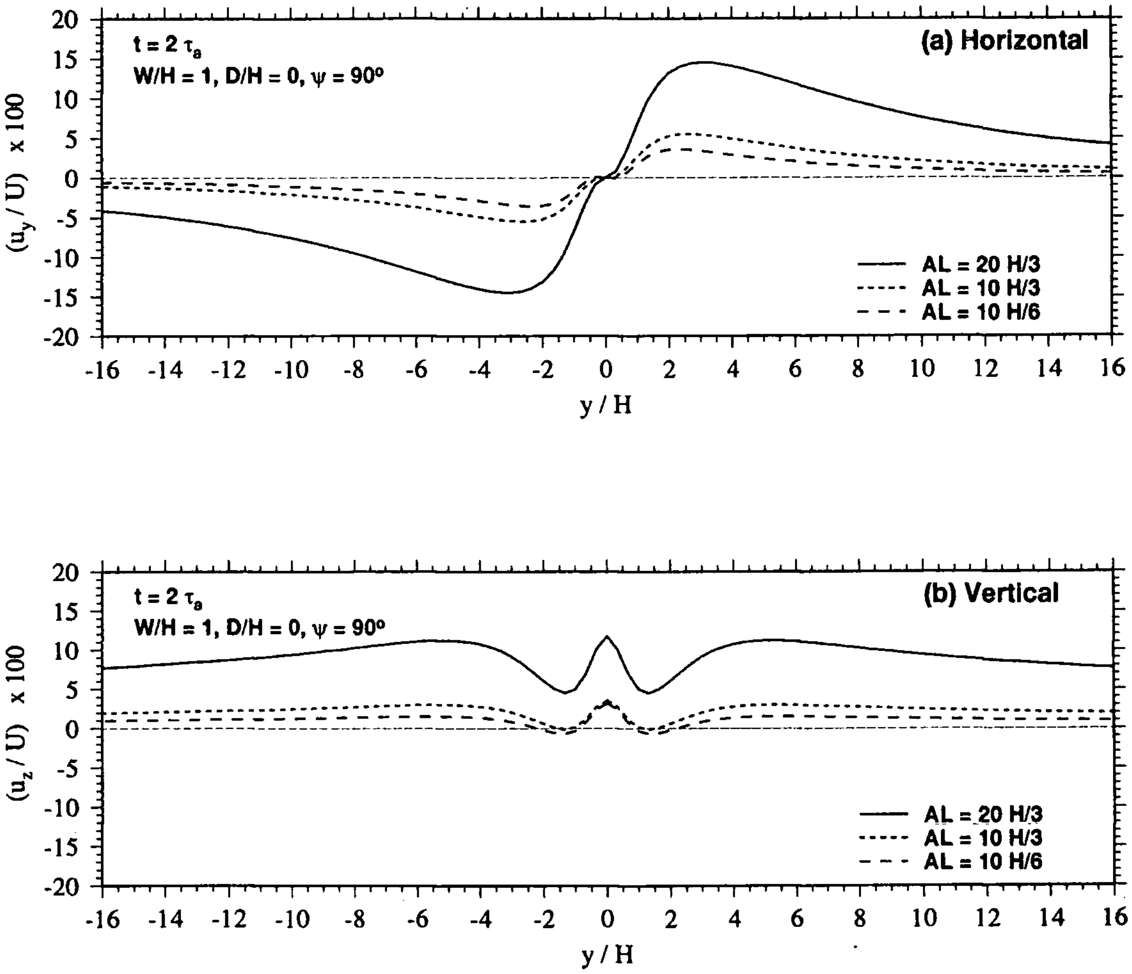

Figure 6.9: Same as Figure 6.7, except the effects of varying AL when $W/H = 1$ are illustrated.

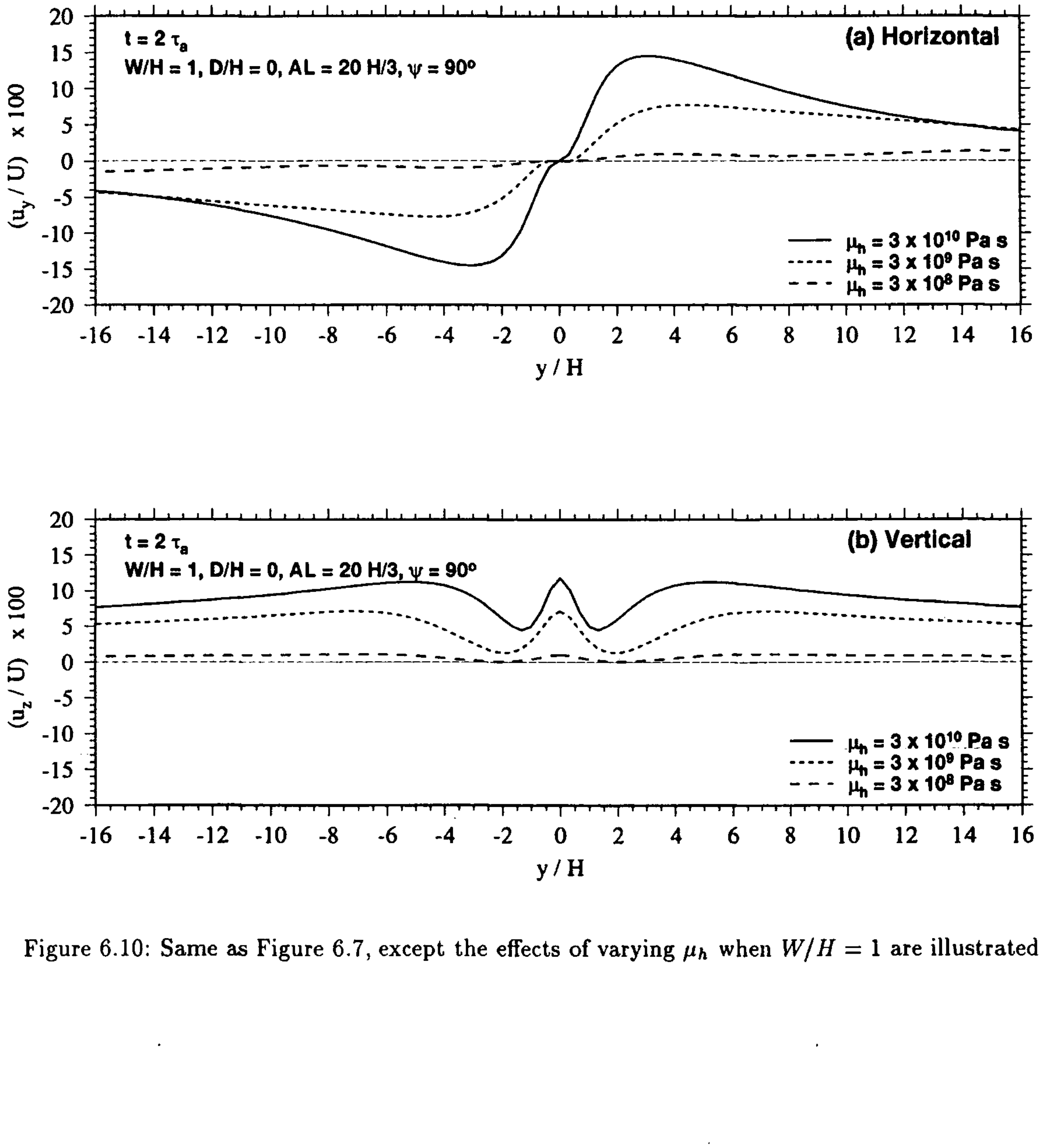

Figure 6.10: Same as Figure 6.7, except the effects of varying μ_h when $W/H = 1$ are illustrated.

the dyke (Figure 6.7b). Decreasing the downdip width of the dyke causes a corresponding decrease in the amplitude of the postdyking horizontal displacement field and a pronounced peak at a distance comparable to the thickness of the elastic layer. The vertical deformation field is substantially altered with subsidence predicted above the dyke, uplift of the flank zones and subsidence beyond this. These effects are caused by the reduction of the source size and by the increase in distance from the base of the dyke to the top of the viscoelastic halfspace which causes the viscoelastic effects to diminish.

Outward, radial horizontal motion from the dyke is predicted in all areas (Figures 6.8a and c). However, the displacements at the ends of the dyke are much smaller than those predicted elsewhere. The maximum motions occur at distances of about $2H$ from the dyke. When $W/H < 1$ motion decays at smaller distances from the dyke than when $W/H = 1$. When $W/H = 1$ uplift of all points is predicted, with the maximum uplift of $0.1U$ occurring above the dyke and in the flank zones, and the local minimum occurring within $2H$ of the dyke (Figures 6.7b and 6.8b). When $W/H = 0.5$ subsidence is predicted in all areas, except at distances of $\sim 2H$ on either side of the dyke where a small amount of uplift occurs. The maximum subsidence occurs at $\sim 9H$ from the dyke (Figures 6.8b and d).

The elastic-viscoelastic model predicts outward motion parallel to the dyke at the dyke ends. This contrasts with the elastic-viscous model which predicts inward motion there. *Heki et al.* [1993] found that the elastic-viscous model fits the 1987–1990 dyke-parallel motion very poorly, and in this aspect in particular the elastic-viscoelastic model clearly provides a superior fit to the observations.

Decreasing the dyke length decreases the magnitude and range of the horizontal and vertical postdyking displacement (Figure 6.9) since the source size has been reduced. However, the shape of the displacement field is not substantially affected.

The amplitudes of the postdyking horizontal and vertical displacement fields increase with μ_h (Figure 6.10), which also leads to a more pronounced peak in the horizontal field several dyke widths from the source. Increasing μ_h corresponds to an increase in viscosity since $\tau_a = 2\eta/\mu_h$, assuming τ_a is constant. This means that the viscoelastic halfspace has become "stiffer", and produces a larger magnitude response to a dislocation in the elastic layer.

6.4.7.3 Variation in Deformation With Time Following a Single Event

The elastic-viscoelastic model predicts that the deformation field will vary with time. This is illustrated for an infinitely-long example dyke in Figure 6.11 over time scales of 0 to 10,000 τ_a. The elastic (codyking) horizontal displacements are large close to the dyke and decrease rapidly with distance (Figure 6.11a). The postdyking response shows a general increase in accumulated displacement over time at large distances. Very close to the dyke (at distances less than 10 km) the amount of postdyking displacement decreases with time. At intermediate distances (~20–150 km) the motion is more complex and varies considerably at different distances. Large displacements outward from the dyke occur early on, but later the direction of motion reverses and the total outward displacement decreases.

Codyking subsidence is predicted within ~20 km of the dyke, which decreases rapidly with distance (Figure 6.11b). The postdyking motion is in the opposite sense with uplift occurring in the vicinity of the dyke, the amount of which increases with time. A pattern of local subsidence and uplift further away is predicted 10–150 km either side of the dyke, that migrates out with time. No significant vertical motion is predicted further than 150 km from the dyke.

The total displacement field (i.e., the elastic plus the viscoelastic effects) from a single event is shown in Figure 6.12. Postdyking anelastic deformation causes horizontal displacements outwards from the dyke to accumulate at all distances shortly after the intrusion (Figure 6.12a). This results in the rather surprising phenomenon of excess displacement in the flank areas (at distances of less than ~150 km from the dyke in this case). The direction of motion in these areas reverses at some time, and after a long period the accumulated displacement at all distances is approximately equal to the amount of dyke opening. Within 350 km of the dyke the amount of displacement is underestimated by a few percent. This is a result of the boundary conditions inherent in the model (as $y \rightarrow \pm\infty$ the displacement field is constrained to converge to zero) and the approximation technique used to perform the Laplace inversion. In this inversion the $\{\tau_i\}$ were roughly approximated (in order to save computational time), when strictly speaking they are determined by the poles of the function $u_v(t)$.

Postdyking anelastic vertical deformation causes the initial subsidence to decrease over time in the vicinity of the dyke (Figure 6.12b). Additional subsidence accu-

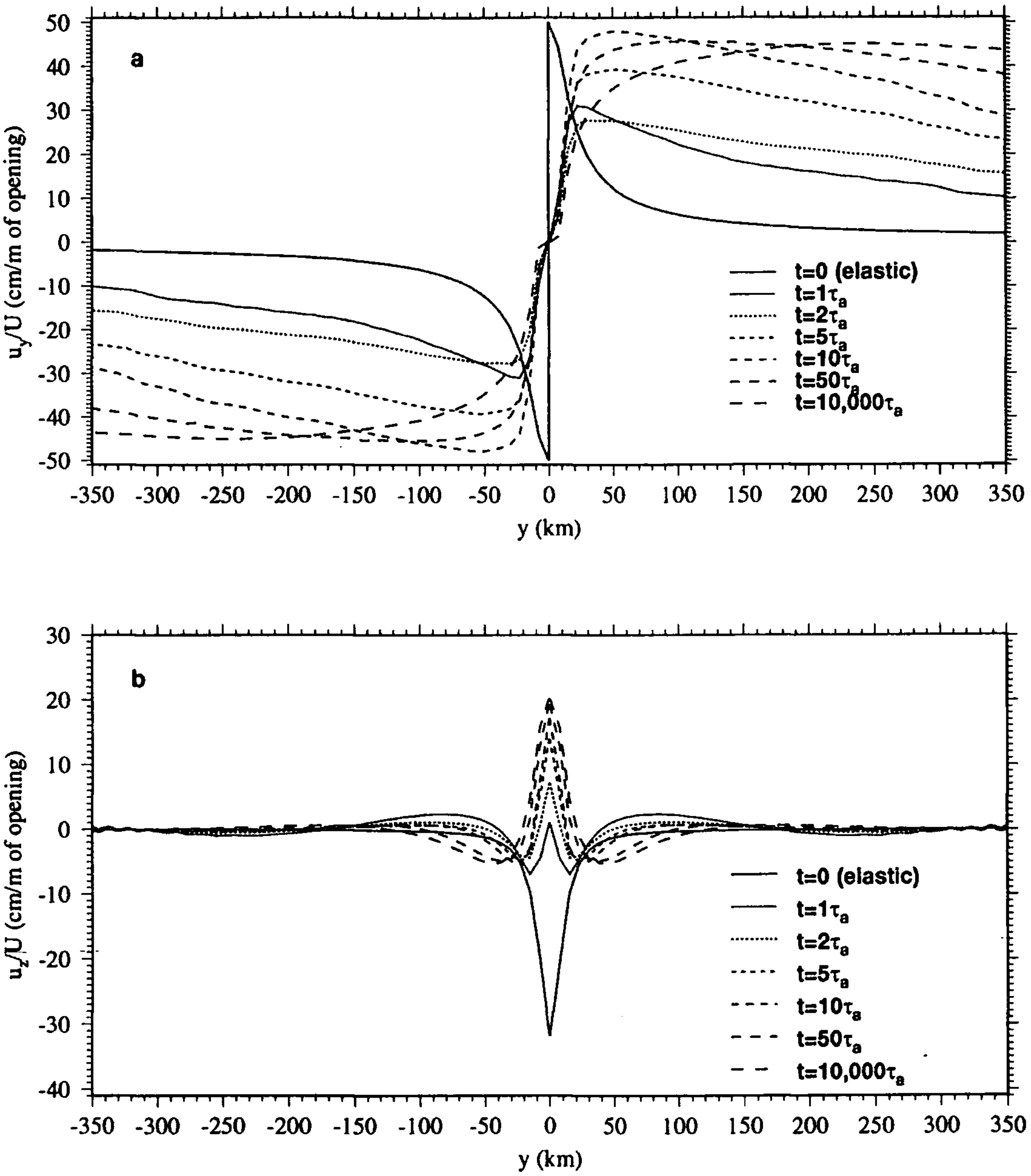

Figure 6.11: Predicted (a) horizontal and (b) vertical displacement including the elastic response and the postdyking displacement ($t > 0$) due to an infinitely-long dyke using the elastic-viscoelastic model. Model parameters are $H = W = 10$ km, $\rho_l = 2.8$ g/cm^3, $\rho_h = 3.1$ g/cm^3, μ_l=2.7 x 10^{10} Pa, λ_l =4.9 x 10^{10} Pa, μ_h =4.1 x 10^{10} Pa, λ_h =9.9 x 10^{10} Pa, and $\psi = 90°$. The profiles are evaluated at the midpoint of the dyke. The small oscillations in the vertical predictions when $y > \pm 300$ km are due to the fineness of the integration interval, the level of which is set to produce a practical computation runtime (no more than a few hours using a Sparc station 10).

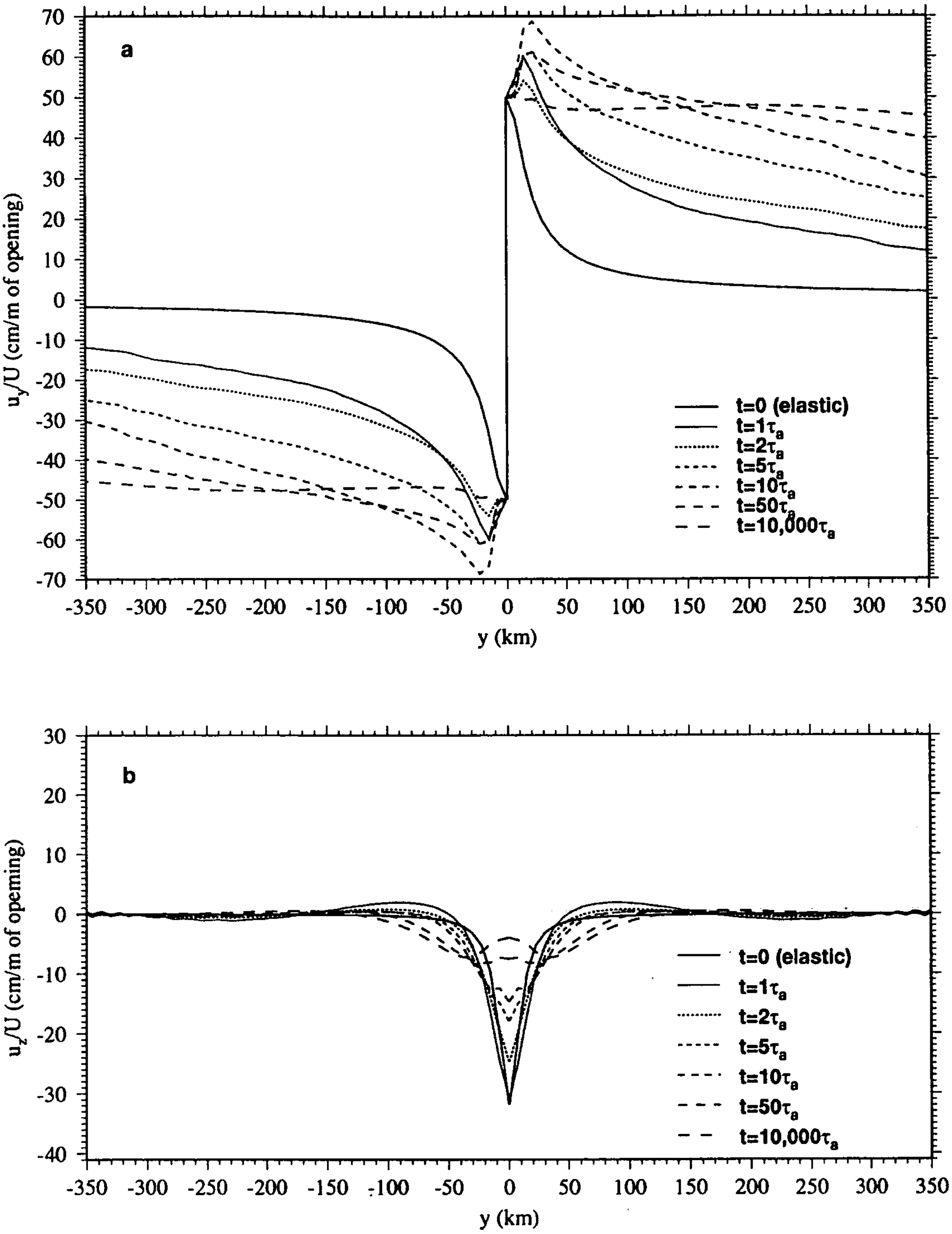

Figure 6.12: Same as Figure 6.11, except total (elastic plus viscoelastic) displacement from $t = 0$ (a) horizontal and (b) vertical.

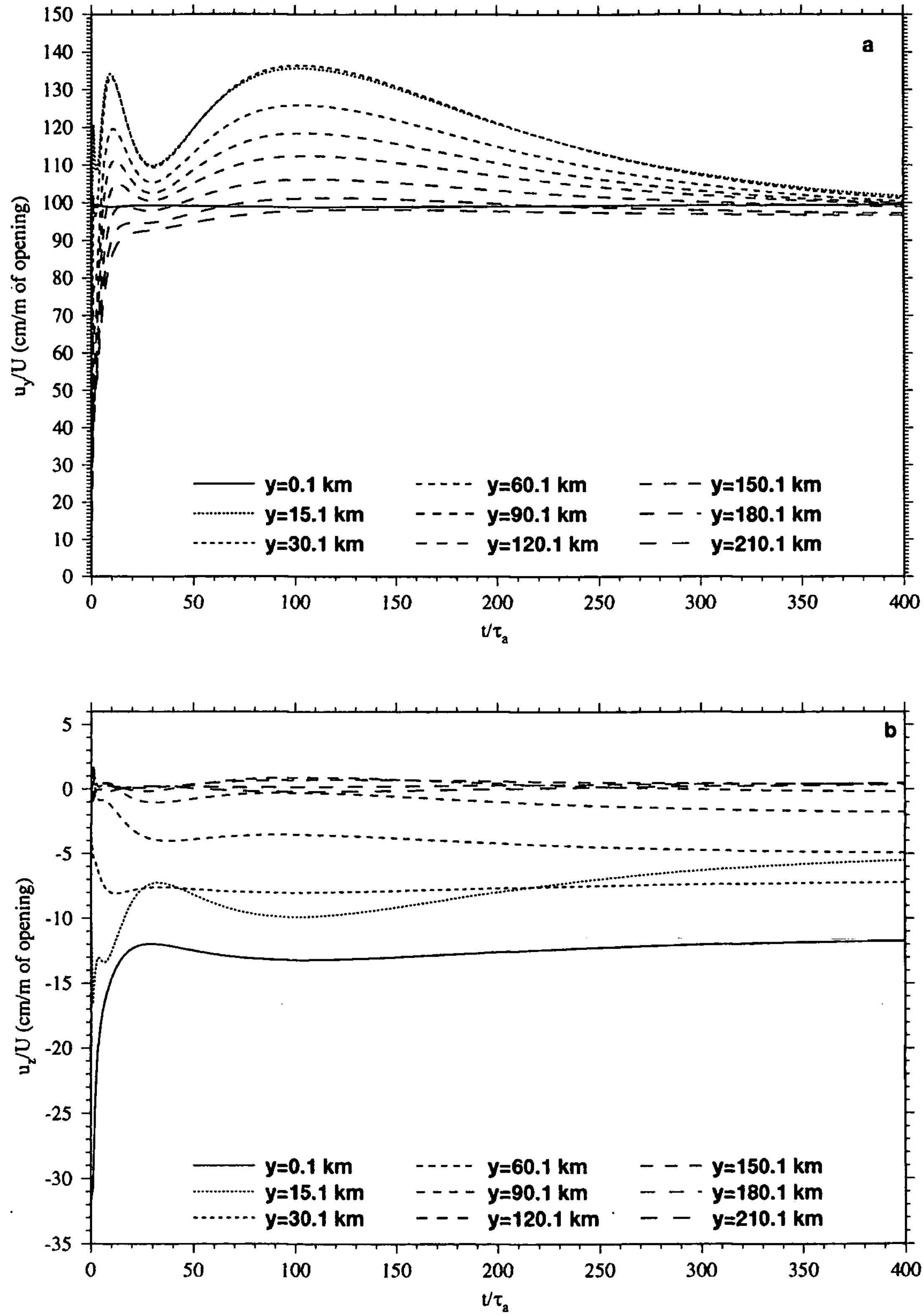

Figure 6.13: The variation of cumulative (a) horizontal and (b) vertical surface deformation from $t = 0$ with distance from the axis with time, due to a single dyking event. Model parameters are identical to those used for Figure 6.11.

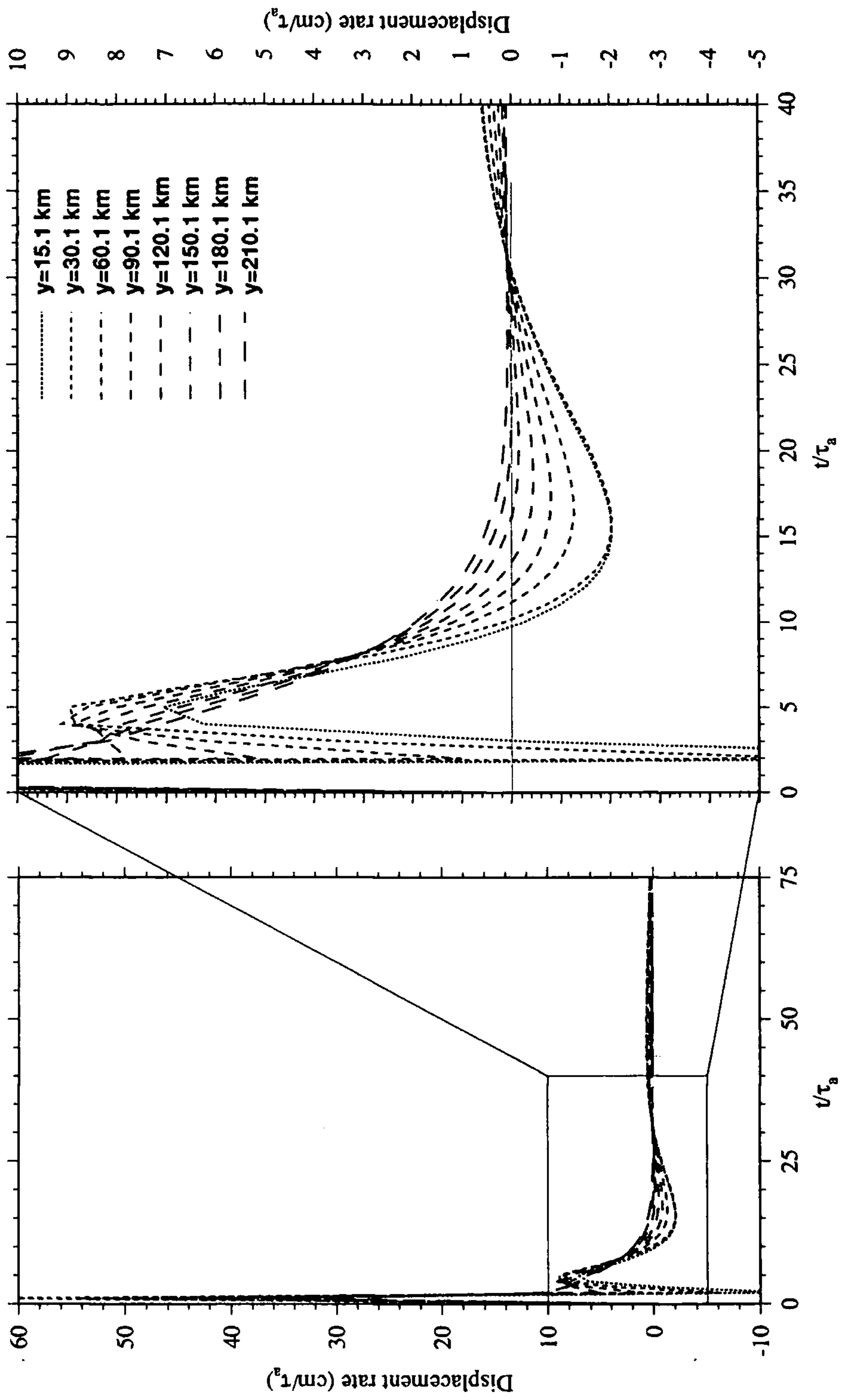

Figure 6.14: The variation of horizontal displacement rate with distance from the axis and time after a single dyking event. The area enclosed by a box in the figure on the left is shown enlarged in the figure on the right. Model parameters are identical to those used for Figure 6.11.

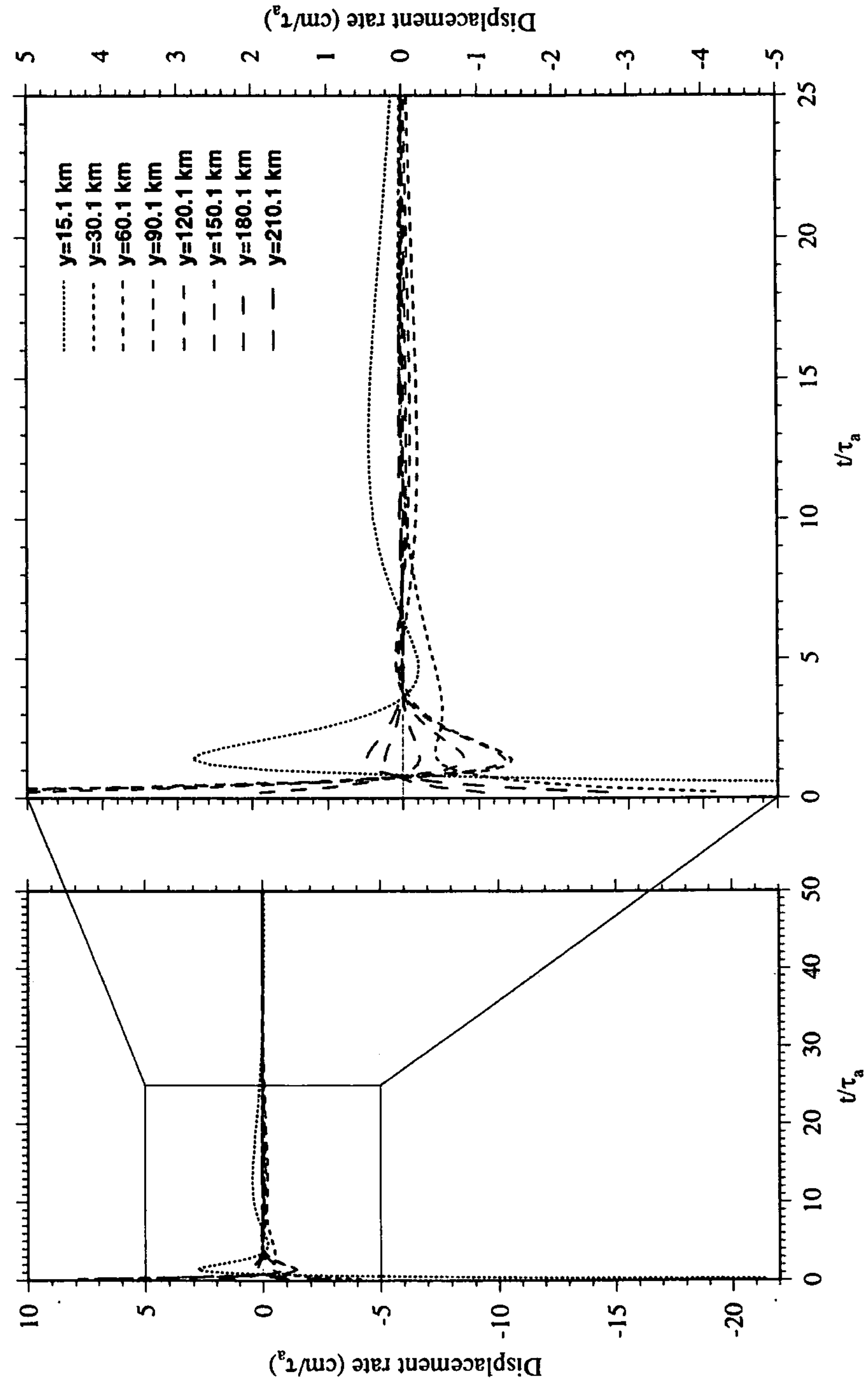

Figure 6.15: Same as Figure 6.14, except for the vertical field.

mulates at distances of ~20–120 km. After a long time period net subsidence is predicted within ~100 km of the dyke, with local, relative uplift within ~20 km of the dyke.

Following a single event, the same amount of horizontal deformation eventually results everywhere as a result of stress redistribution in the viscoelastic halfspace. However, the evolution of the displacement field with time depends on distance from the boundary. Close to the plate boundary very little transient motion is observed (Figure 6.13a), and the majority of the final displacement occurs at the time of the event. Further away from the plate boundary (e.g., at ~15 km), the total amount of displacement increases until ~$10\tau_a$ after the event. The sense of motion then reverses and contraction towards the dyke occurs until ~$30\tau_a$, at which time a second reversal occurs and expansion begins again. The maximum amount of displacement occurs at ~$100\tau_a$ after the event and exceeds the amount of dyke opening by 35%. This general displacement pattern occurs at all points out to distances of ~150 km from the boundary, with the amplitude of the displacements decreasing with distance (Figure 6.13a). Beyond distances of ~150 km from the boundary, e.g., at ~210 km, little excess displacement occurs and a simple pattern of evolution of displacement with time is predicted. There, the curve can be divided into two stages. In the first stage the displacement quickly increases to near its maximum value (within ~$15\tau_a$ of the event). Following this is a much more gradual increase as the displacement reaches its final and maximum value over the next ~$50\tau_a$.

The vertical field clearly shows that within ~120 km of the dyke, net subsidence is predicted following a single rifting event (Figures 6.12b and 6.13b). Close to the dyke (within 15 km) the amount of subsidence decreases with increasing time until ~$25\tau_a$, at which time a slight, relative increase occurs. Decreasing subsidence is again predicted after ~$100\tau_a$. Between 30 and 90 km from the dyke axis the amount of subsidence progressively increases to a maximum at ~$50\tau_a$. At distances of greater than ~120 km there is insignificant vertical response to the intrusion.

A deformation rate that is highly variable spatially and temporally is thus predicted. Close to the axis a maximum expansion of ~60 cm/τ_a is predicted shortly after the event (Figure 6.14). This quickly decreases and within ~$2\tau_a$ of the event contraction at a rate of up to 10 cm/τ_a is predicted within ~120 km from the dyke. The rate of motion then increases and at $5\tau_a$ after the event an expansion of up to

9 cm/τ_a occurs. The rate of motion subsequently decreases, and at ~50 τ_a after the event the expansion rate has decayed to ~1 cm/τ_a. The rate decreases to zero at all distances within ~100τ_a of the event. As was apparent in Figure 6.13a, the counter-intuitive reversal of sense of motion is discernible, in the cases studied here, out to distances of ~120 km.

The predicted vertical displacement rate also shows a complicated pattern (Figure 6.15). Within ~15 km of the dyke a high subsidence rate of up to 20 cm/τ_a initially occurs. The rate then reverses and within 2τ_a an uplift rate of up to ~3 cm/τ_a is predicted close to the dyke. Low rates of uplift and subsidence are then predicted until ~30τ_a when the rate becomes zero. At distances of ~30 km from the dyke a subsidence rate of ~4cm/τ_a is predicted within 1τ_a of the event. This decreases to near-zero by ~5τ_a after the event. Between ~60 km and ~120 km uplift of up to 7 cm/τ_a is predicted shortly after the event, followed by subsidence of up to 1 cm/τ_a by 2τ_a after the event. Motion subsequently decreases to zero. From 180–210 km subsidence at a rate of up to 3 cm/τ_a is predicted shortly after the event, decreasing to zero by ~3τ_a after the event.

6.4.7.4 The Summation of Repeated Events

If an event is assumed to recur periodically the pattern of motion will vary with time and distance from the axis. The case for a recurrence time of 100 τ_a is illustrated in Figure 6.16. Motion at the boundary is highly episodic, with most of the motion occurring at the time of the event and little or none just before the onset of the next episode. Further away (e.g., ~30 km from the boundary) episodic motion occurs at the time of the event. For a short while the motion decreases, and then sharply increases to a peak at ~10τ_a after the event, after which it decreases to zero. From ~30τ_a after the event to just before the next event, very little motion occurs. At larger distances (e.g., ~90 km) from the boundary a similar though attenuated pattern of motion occurs, and at distances of over 200 km from the plate boundary, most of the motion occurs during the first 15τ_a, after which little motion occurs until the next event. An important prediction of the viscoelastic model, for the case where the dyke ruptures the entire elastic layer, is that the average motion at all points is the same.

Unlike the horizontal motion, the average vertical motion is not the same at all

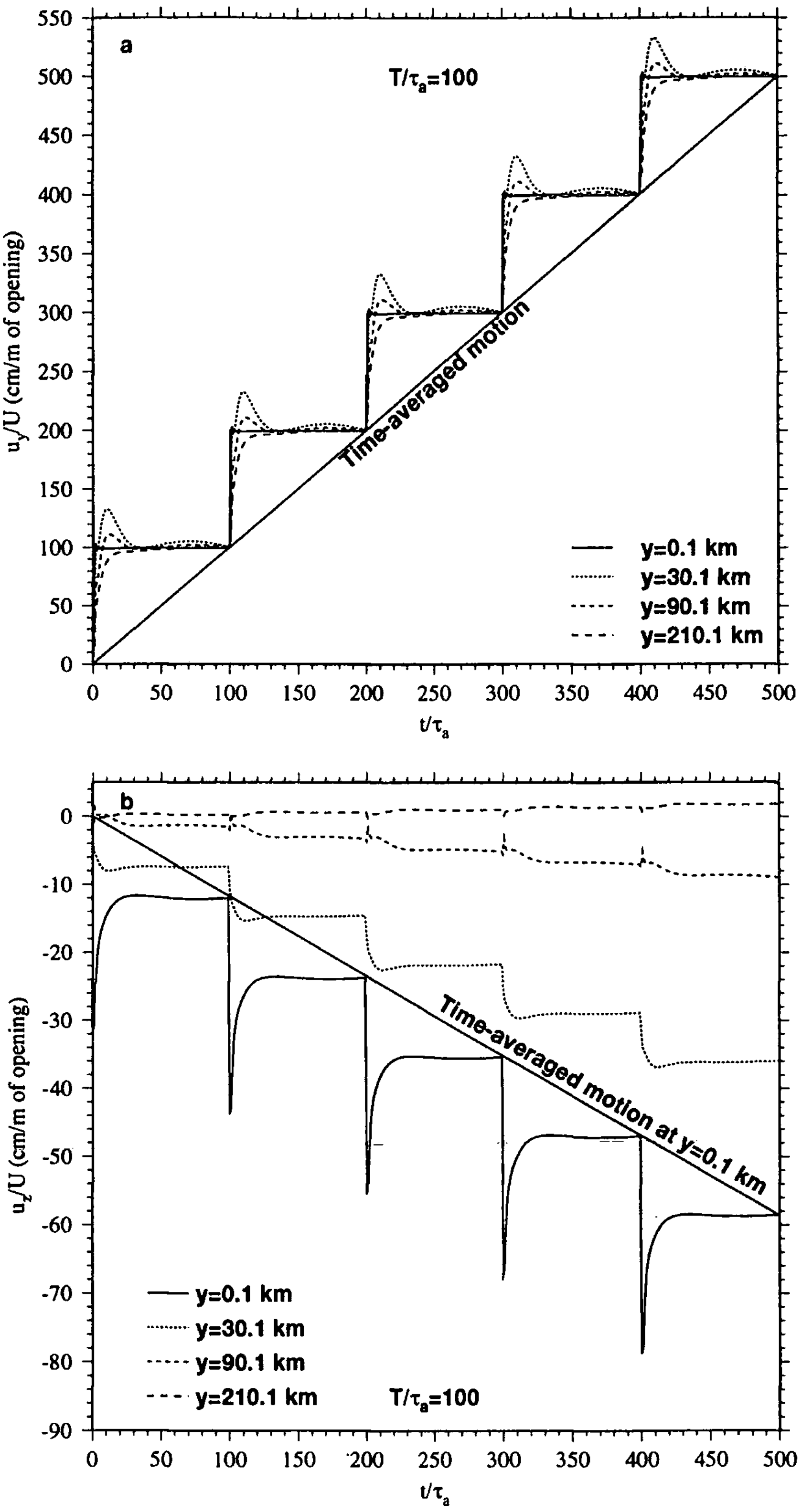

Figure 6.16: (a) Horizontal (b) vertical displacement against dimensionless time at 0.1 km, 30.1 km, 90.1 km and 210.1 km from the plate boundary. An event is assumed to recur every $100\tau_a$. A large number of previous events are assumed to have occurred prior to time $t/\tau_a = 0$ in order for the displacement field to reach a steady state. T is the event recurrence time. As a result of increasing computational inaccuracies with distance, the y=210 km curve is an approximation only, and has been displayed assuming the net displacement is equal to the time-averaged displacement.

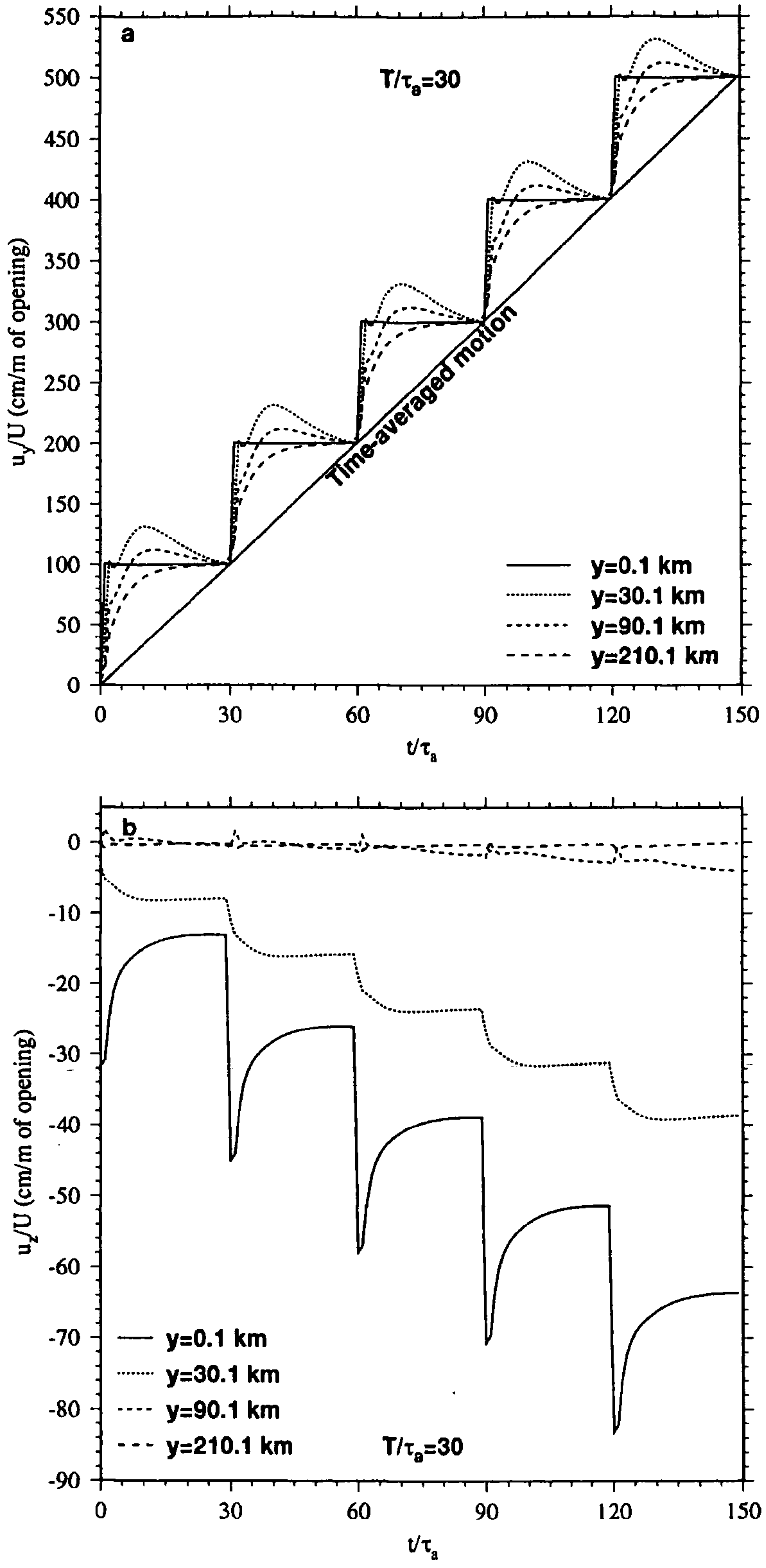

Figure 6.17: Same as Figure 6.16, except an event is assumed to recur every $30\tau_a$.

distances from the dyke. Close to the dyke a net subsidence is predicted, the amount of which decreases with increasing distance from the dyke (Figure 6.16b). Vertical motion at the boundary is also highly episodic with substantial subsidence occurring at the time of the intrusion followed by uplift for a short time after the event and no significant motion immediately prior to the next event. At larger distances from the dyke, a similar but attenuated deformation pattern occurs with virtually no motion beyond about 150 km.

If the recurrence interval is made shorter (or equivalently, the relaxation time is increased for these plots where t is scaled by τ_a) the spatial scale of the transient motion changes (Figure 6.17a). Motion is discernible throughout the interevent period for distances of up to ~100 km from the dyke, and at distances of ~200 km motion is more continuous than for long recurrence intervals, though still clearly episodic. The vertical field (Figure 6.17b) is very similar to that predicted when T=100 τ_a, and thus the predicted vertical field appears to be less dependent on the recurrence time than the horizontal field.

The width of the "plate boundary zone", i.e., the zone within which transient, time-dependent deformation occurs, is shown thus to be dependent on the relaxation time. If apparent continuous, uniform "plate" motion is to occur within about 200 km of the plate boundary, the recurrence time must be of the order of ~15 τ_a, i.e., the next event must occur before the displacement gradient change occurs for a point at that distance (Figure 6.13a).

6.5 Simulating Plate Motion

It can be seen from the example in the preceding section that models involving repeated, infinitely-long dykes rupturing the entire elastic layer can simulate the continuous motion of the plates if dyke thicknesses are chosen to be consistent with the event recurrence times and the time-averaged plate velocity. This was also illustrated graphically for the elastic-viscous model by *Heki et al.* [1993], who gave the total displacement, $U(x,t)$, for the one-dimensional solution as

$$U(x,t) = u(x,t) + \sum_{n=1}^{\infty} u(x,t+nT), \tag{6.81}$$

where T is the recurrence interval of the events (Figure 2.15). This model predicts that the transient velocity pulses from the events at the plate boundary diffuse out and sum to produce the constant motion of the plate interiors. The viscoelastic model does not show the same "diffusion" pattern as the viscous model, but is similar in as much as the deformation is initially predicted to be greatest close to the dyke, and to spread to greater distances with time. This model does not imply the origin of plate driving forces, and a similar result would be obtained if an infinitely-long destructive or transform plate boundary were modelled. The continuous dyking model involves elastic responses only and in order to simulate continuous plate-like motion, continuous dyking at the appropriate rate and over the whole observation period is required.

6.6 Summary

Fundamentally different explanations have been invoked to predict transient, post-dyking ground deformation; continued opening at depth on the dyke plane and stress relaxation in a nonelastic region situated below a surface elastic zone. The first of these is easily modelled using elastic-halfspace methods.

Two methods are used to model postdyking deformation resulting from the relaxation of a nonelastic region. The first assumes that dyking occurs in a surface elastic layer underlain by a viscous (Newtonian) layer. Stress, assumed to originate in the rifting episode, obeys the classical, linear-diffusion equation. The second method involves dyking in an elastic layer overlying a Maxwell viscoelastic halfspace, both of which are subject to gravitational effects. This method involves computing the Green's functions for a dilational point source in an elastic-gravitational layer over an elastic-gravitational halfspace. The correspondence principle is applied to give the functions for a source in an elastic-gravitational layer overlying a viscoelastic-gravitational halfspace. Finally these functions are integrated over the finite source region to give the required horizontal and vertical surface displacements.

Example calculations involving a vertical dyke that extends to the surface indicate that the greater the length and downdip width of the dyke, the greater the deformation. Changing the viscosity of the viscoelastic region substantially affects the deformation pattern. All examples predict substantial motion at large distances from the dyke and at early times, in contrast to the elastic-viscous model.

Alternating periods of expansion and contraction with very variable displacement rates are predicted following a single rifting event. For an infinite dyke, and after a long time, the amount of cumulative horizontal displacement at all distances is approximately equal to the amount of dyke opening. In the vertical, net subsidence is predicted in the vicinity of the dyke, the amount of which decreases with increasing distance. If an event is assumed to recur periodically the nature of the horizontal displacement field is dependent on the ratio of the recurrence time of the event to the relaxation time. The vertical field is less sensitive to this ratio. Continuous plate motion may be simulated by the summation of the displacements from a large number of events rupturing the entire plate boundary, using either the elastic-viscous or elastic-viscoelastic model.

Chapter 7

Modelling the Measured Deformation in North and East Iceland

7.1 Introduction

Suggested explanations for the deformation observed 1987–1992 in north and east Iceland involve several conceptually different processes. Continuous, aseismic dyke intrusion at depth beneath the Krafla spreading segment has been suggested that may be modelled using an elastic halfspace [*J. Savage*, pers. comm., 1994]. The deformation field has been attributed to postdyking stress relaxation in viscous or viscoelastic structural elements following the recent Krafla rifting episode. Modelling of the deformation using these processes and structures has the potential to place constraints on tectonic processes and the rheology of the Earth beneath Iceland.

An Earth model incorporating viscoelasticity is the most realistic of these processes, and the case of the viscous model has been dealt with in depth by *Heki et al.* [1993]. This latter model, and that of continuous dyking, will thus be treated only briefly in this chapter, which concentrates mainly on modelling using a structure that involves viscoelasticity.

7.2 Continuous Dyking in an Elastic Halfspace

In this approach the surface displacements observed in Iceland 1987–1992 (Figure 7.1) are attributed to continuous, aseismic dyke intrusion at depth beneath the Krafla spreading segment. This process is modelled using an elastic halfspace and the formulae of *Okada* [1985] (Section 6.2).

End-member example cases of short, thick and tall, thin dykes for the infinitely long case are shown in Figure 7.2. Observed displacements within a narrow profile spanning the Krafla dyke are superimposed on the modelled displacement profile to decrease the effects of the finite length of the dyke complex intruded in the Krafla episode on the data plotted.

The models predict horizontal displacement fields that increase steeply to a peak within a few tens of kilometres from the spreading axis, and then fall off more slowly at greater distances (Figure 7.2a). Zero vertical motion is predicted along the spreading axis, substantial uplift on either side, peaking somewhat closer to the spreading axis than the horizontal motions, and decreasing with distance to zero further away (Figure 7.2b).

Figure 7.2 shows that this model predicts the overall shape of the observed deformation field, and suggests that a range of dykes with various depths and dimensions intermediate to those shown will fit the observations from the profile zone. The short, thick dyke fits reasonably the horizontal displacements close to the spreading axis but predicts poorly the motion further away. The tall, thin dyke underestimates the motion close to the axis but provides a reasonable fit for the more distant points. The short, thick dyke fits the observed vertical displacements fairly well, whereas the tall, thin dyke predicts a deformation field with somewhat larger displacements far from the spreading axis than those observed.

A well-fitting case with dyke length comparable to that of the recent Krafla episode is shown in Figures 7.3 and 7.4. In order to approximate the motion of the furthest points a tall, thin dyke is required. The observed horizontal motion is large close to the rift and decreases slightly with distance. A maximum of 10 cm is predicted close to the rift, decreasing to about 6 cm approximately 100 km from the axis. Residuals significant at greater than 2σ occur in the vicinity of the dyke and in the far southeast of the network, where residuals of up to 7 cm occur. The vertical

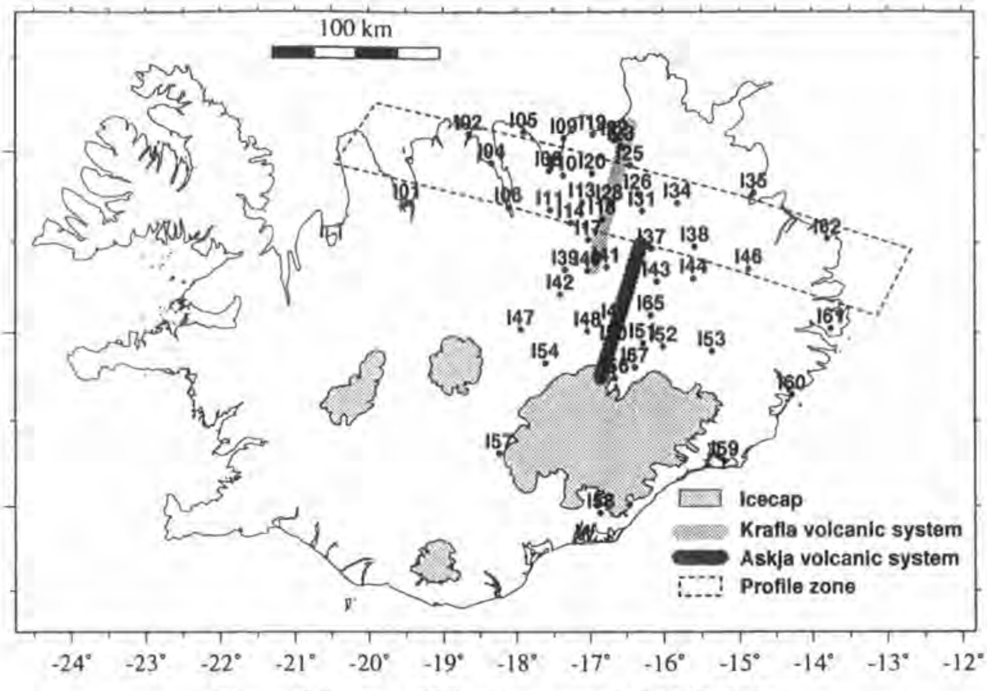

Figure 7.1: The GPS points occupied 1987–1992.

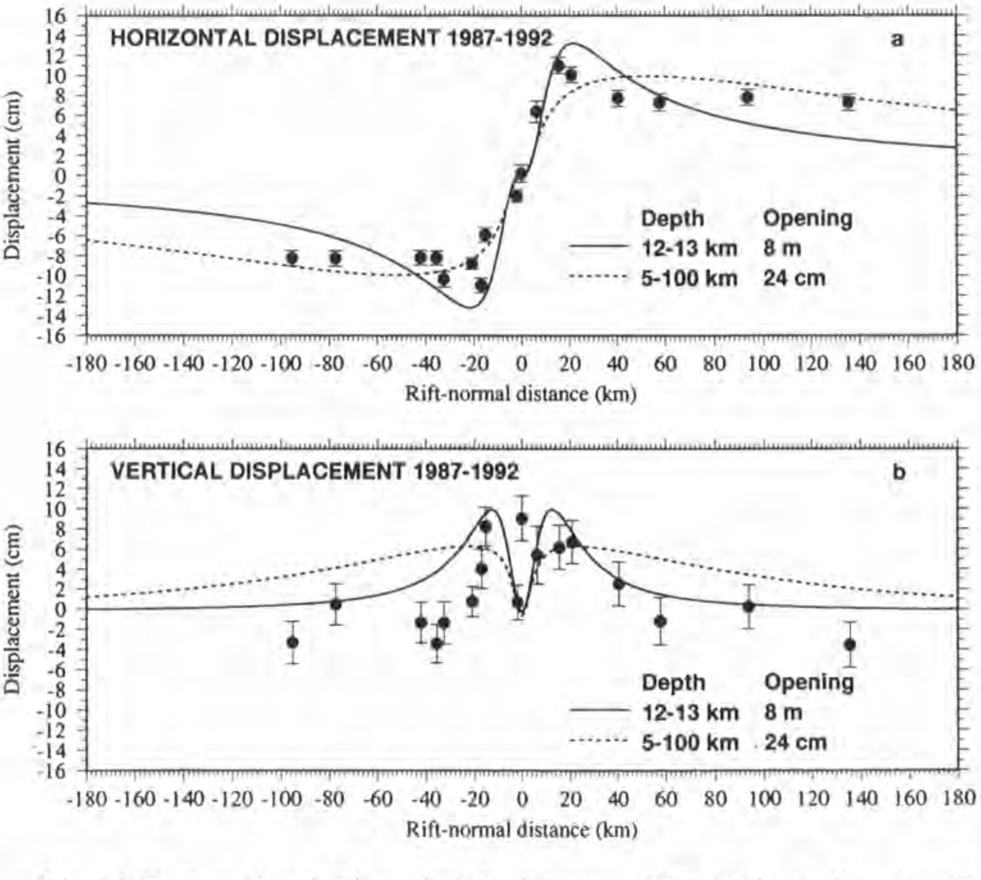

Figure 7.2: (a) Horizontal and (b) vertical displacements 1987–1992 as a function of distance from the plate boundary for the points within the profile zone shown in Figure 7.1. Vertical bars indicate 1σ errors. Lines are theoretical curves for models of continuous dyke intrusion at depth in an elastic halfspace. The depth extent and amount of opening for the modelled dykes are given in the figures. Two end-member cases are shown, a short, thick dyke and a tall, thin dyke.

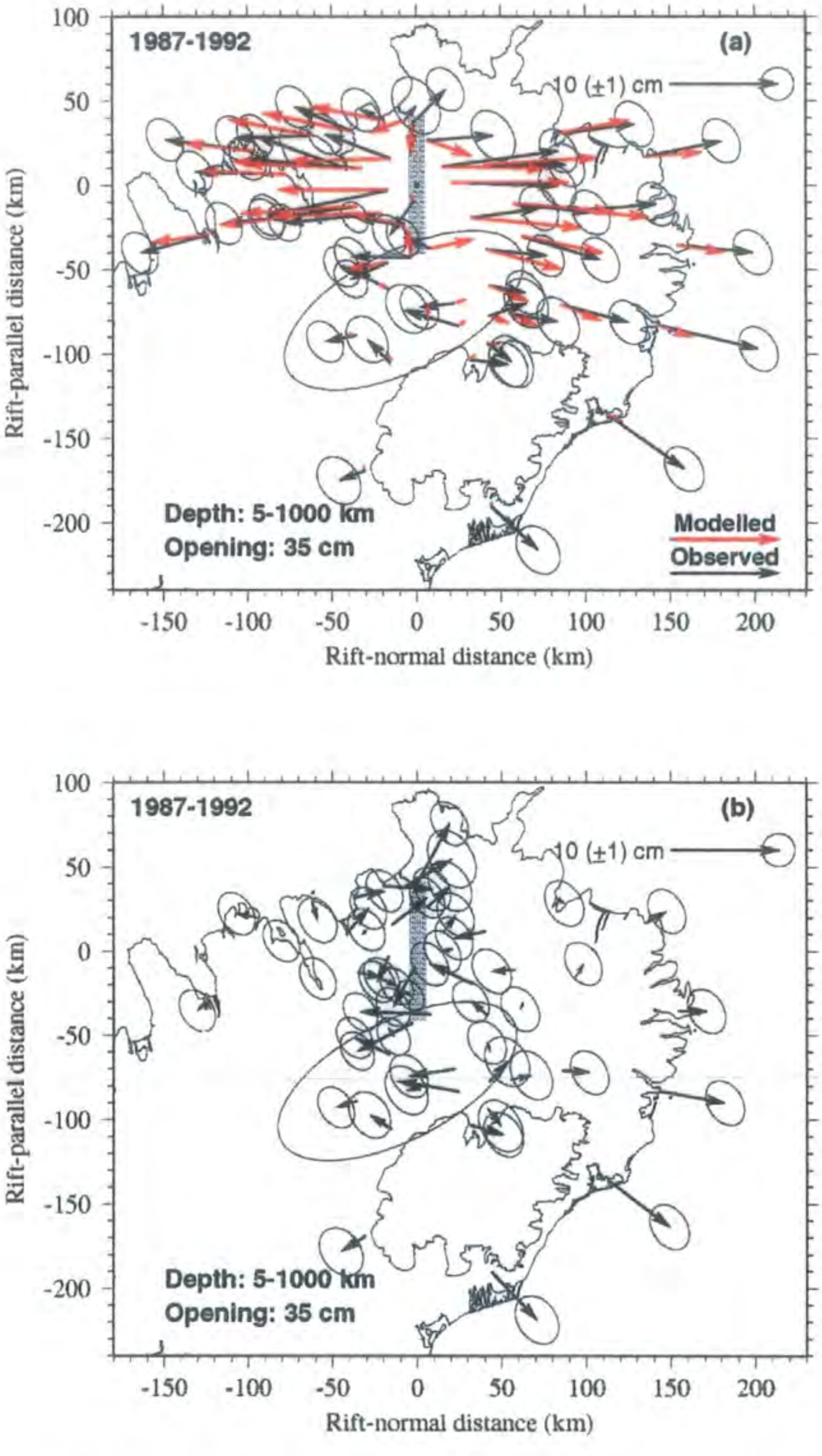

Figure 7.3: (a) Comparison of observed and simulated horizontal displacements 1987–1992 using the model of continuous dyke intrusion at depth in an elastic halfspace. An 80 km long dyke is assumed. The solid arrows represent observed data and red arrows simulated. 68% (1.5σ) confidence error ellipses are shown. The dyke axis is shown shaded. The residual vectors are shown in (b).

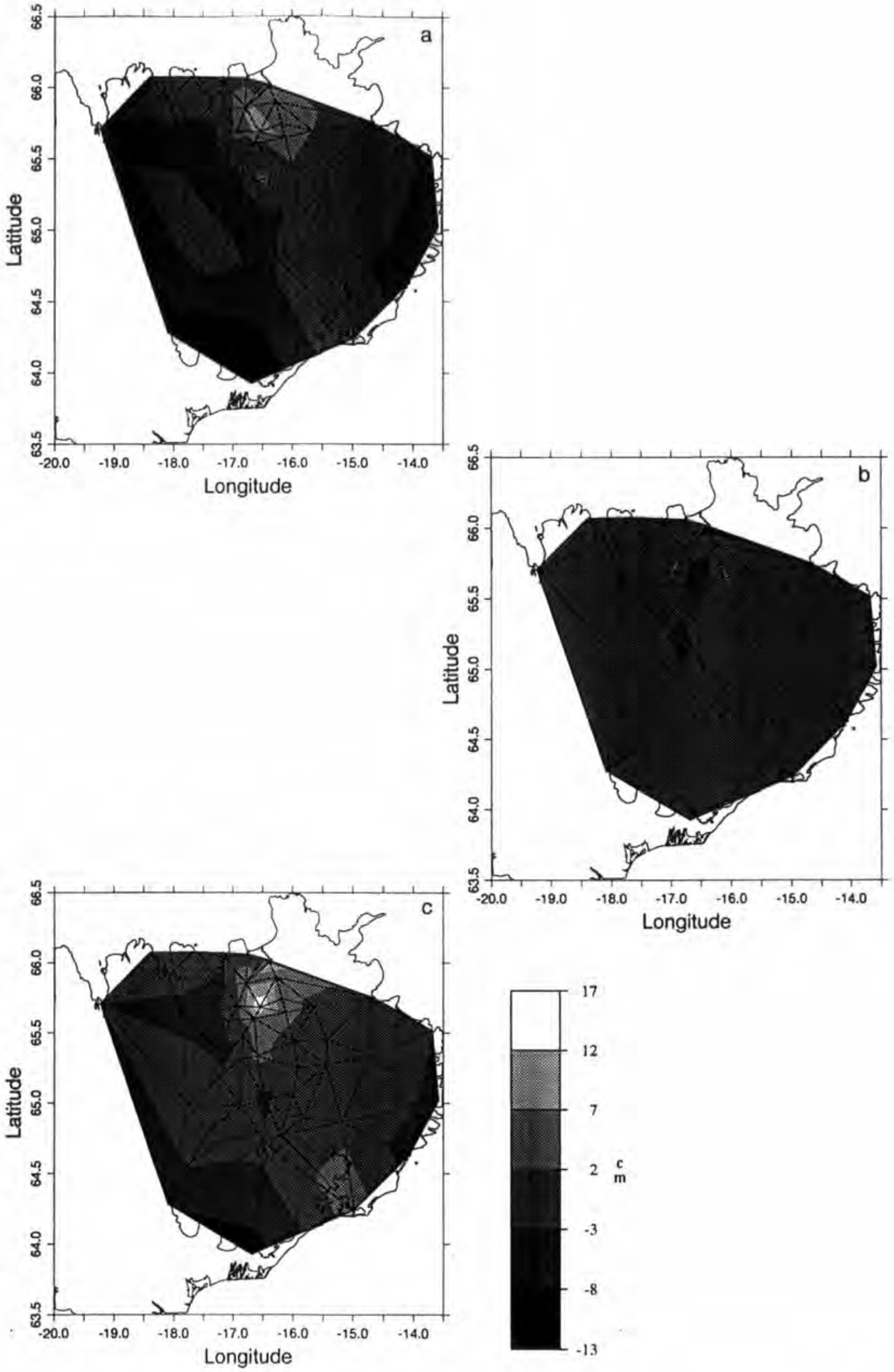

Figure 7.4: (a) Observed, (b) simulated, and (c) residual vertical displacements 1987–1992 using the same model as Figure 7.3. The vertical motions of the points, whose positions are at the corners of the triangles, have been calculated, followed by bilinear interpolation between them, and contouring. Clearly, no observational geodetic evidence exists between the points, and this illustrative method is adopted for clarity only. The scale bar gives vertical displacement in centimetres.

simulated field (Figure 7.4b) has a maximum uplift of 5 cm close to the dyke axis, decreasing to zero with distance. Residuals of up to 15 cm, and significant at greater than 2σ occur in the south of the network, and in the vicinity of the dyke (12 cm).

A quantitative measure of the quality of fit to the data is given by the reduced χ^2 statistic [e.g., *Bevington and Robinson*, 1992], given by

$$\chi_\nu^2 = \frac{\sum_{i=1}^{N} \frac{(v_i^{obs} - v_i^{mod})^2}{\sigma_i^2}}{N - M}, \tag{7.1}$$

where v^{obs} and v^{mod} are the observed and predicted displacements, σ is the scaled formal error, N is the number of data points, and M is the number of adjustable model parameters. Values of χ_ν^2 much larger than 1 indicate that the measurement errors cannot account for all of the data misfit, and suggest either an incorrect representation of the physical situation (an incorrect model or model parameters) or incorrect estimates of the errors. If χ_ν^2 is less than 1 the errors in the data are likely to have been overestimated or else measurement error is being modelled. χ_ν^2 is 3.7 in the horizontal and 5.3 in the vertical for the model shown in Figures 7.3 and 7.4.

Clearly, further improvement to the fit could be achieved by making the model more complicated by using several dykes with different dimensions and times of intrusion. However, this line of research is not pursued further here.

7.3 Stress Diffusion in an Elastic Layer Overlying a Viscous Layer

Following the method of *Foulger et al.* [1992], a one-dimensional stress diffusion model was applied to the 1987–1990, 1990-1992 and 1987–1992 displacements, which were viewed as instantaneous velocities 11 and 13 years after the dyke intrusion event. The best-fitting form (in a least-squares sense) of the one-dimensional horizontal velocity equation (equation 6.10) to the observations was found and estimates of the dyke thickness and diffusivity obtained. The position of the dyke is well known from previous geodetic measurements and was held to a fixed location.

Table 7.1: Summary of the diffusivities and dyke half thicknesses obtained using the stress diffusion model.

Epoch	Diffusivity (m^2/s)	Half dyke thickness (m)
1987–1990	1.10 ± 0.30*	1.00 ± 0.10*
1987–1990	1.78 ± 0.38	1.43 ± 0.12
1990–1992	0.64 ± 0.35	0.72 ± 0.17
1987–1992	3.11 ± 0.68	1.27 ± 0.14
1986–1992	0.65 ± 0.33	1.30 ± 0.67
1987–1990	10.0 †	–

* Estimates obtained by *Foulger et al.* [1992] using the GEONAP results.

† Estimate obtained by *Heki et al.* [1993] using the two-dimensional model.

Best-fit models to profiles perpendicular to the rift axis within the zone shown in Figure 7.1 yield estimates for the thickness of the dyke complex (averaged throughout the elastic layer) of 0.72–1.43 m and stress diffusivities of 0.64–3.11 m^2/s (Table 7.1, Figure 7.5). Whilst the motion in the proximity of the rift can be predicted well by this simple model, the motion of points further than 60 km from the rift is poorly modelled. The predicted relative motion from a single intrusion is zero whereas substantial motion is observed at these distances. This is most clearly seen in the 1987–1992 epoch (Figure 7.5c). Increasing the diffusivity to 10 m^2/s (the value calculated by *Heki et al.* [1993] by two-dimensional modelling of the 1987–1990 epoch) gives a better fit for these far points, but at the expense of the fit to the points close to the rift. The estimates for the dyke half thickness suggest a value of 2–3 m for the average full thickness of the dyke complex, i.e., smaller than the 3.5–8 m of surface widening observed during the rifting episode. The diffusivity and dyke thickness calculated using data from the 1986–1992 epoch are less reliable since the 1986 results are of low quality and there are few points close to the rift where point velocities are most variable.

The two-dimensional deformation fields for 1990–1992, 1987–1992 and 1986–1992 were compared with the predictions of *Heki et al.* [1993] (a diffusivity of 10 m^2/s, and dyke thicknesses as estimated by *Tryggvason* [1984]) (Figure 7.6). The discrepancy between predicted and observed deformation, highlighted by the one-dimensional analysis where the predictions using a diffusivity of 10 m^2/s are shown (Figure 7.5), is again seen (i.e., a reasonable fit to the far- and poor fit to the near-rift points). The model can predict most of the motion for the 1987–1990 and

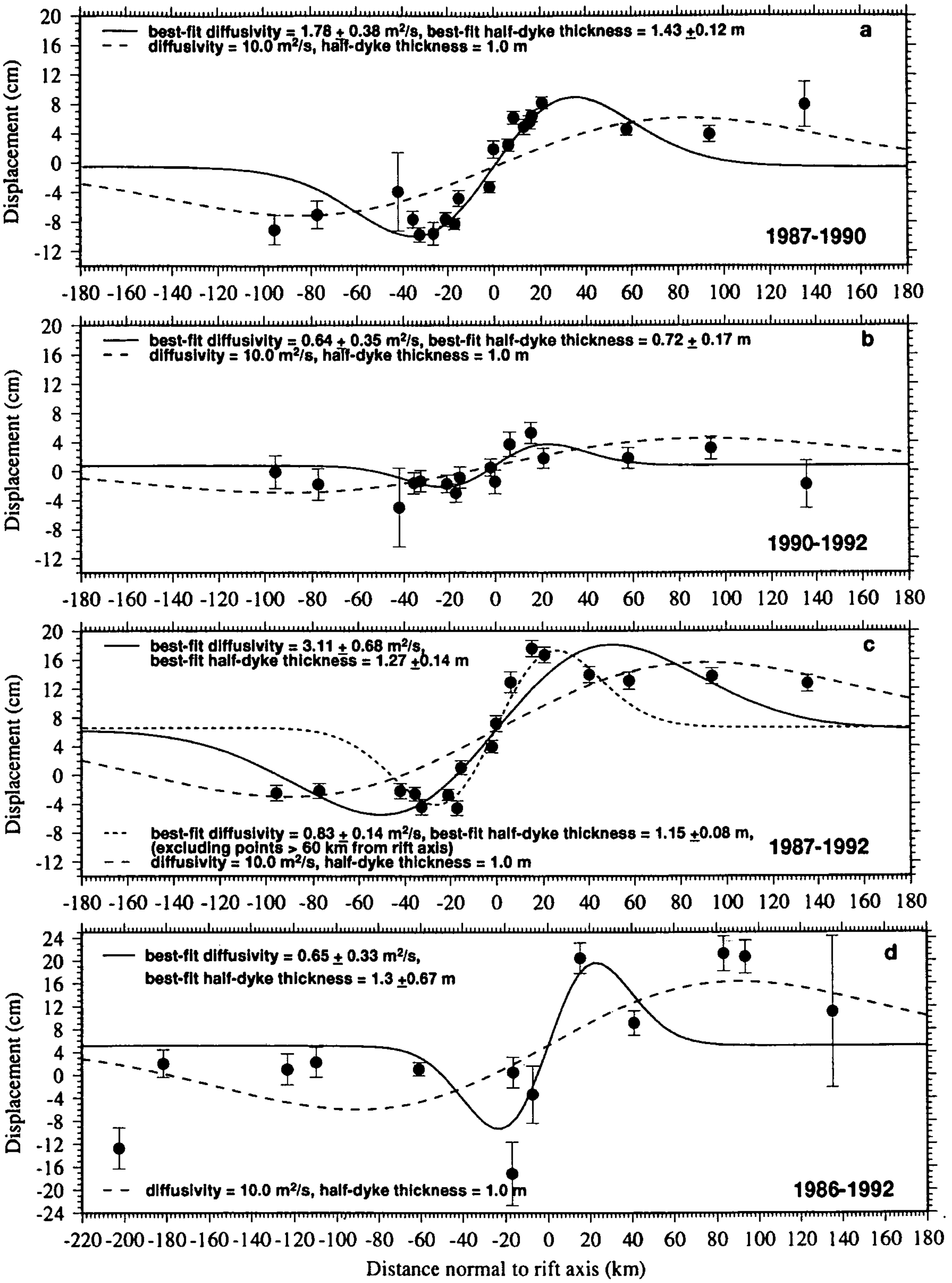

Figure 7.5: Horizontal displacements (a) 1987–1990, (b) 1990–1992, (c) 1987–1992, and (d) 1986–1992, as a function of distance from the spreading axis for the points within the profile zone shown in Figure 7.1. Vertical bars indicate 1σ errors. The best-fit curves for models of stress diffusion in an elastic layer overlying a viscous layer are superimposed. A one-dimensional model (infinitely-long dyke) was used.

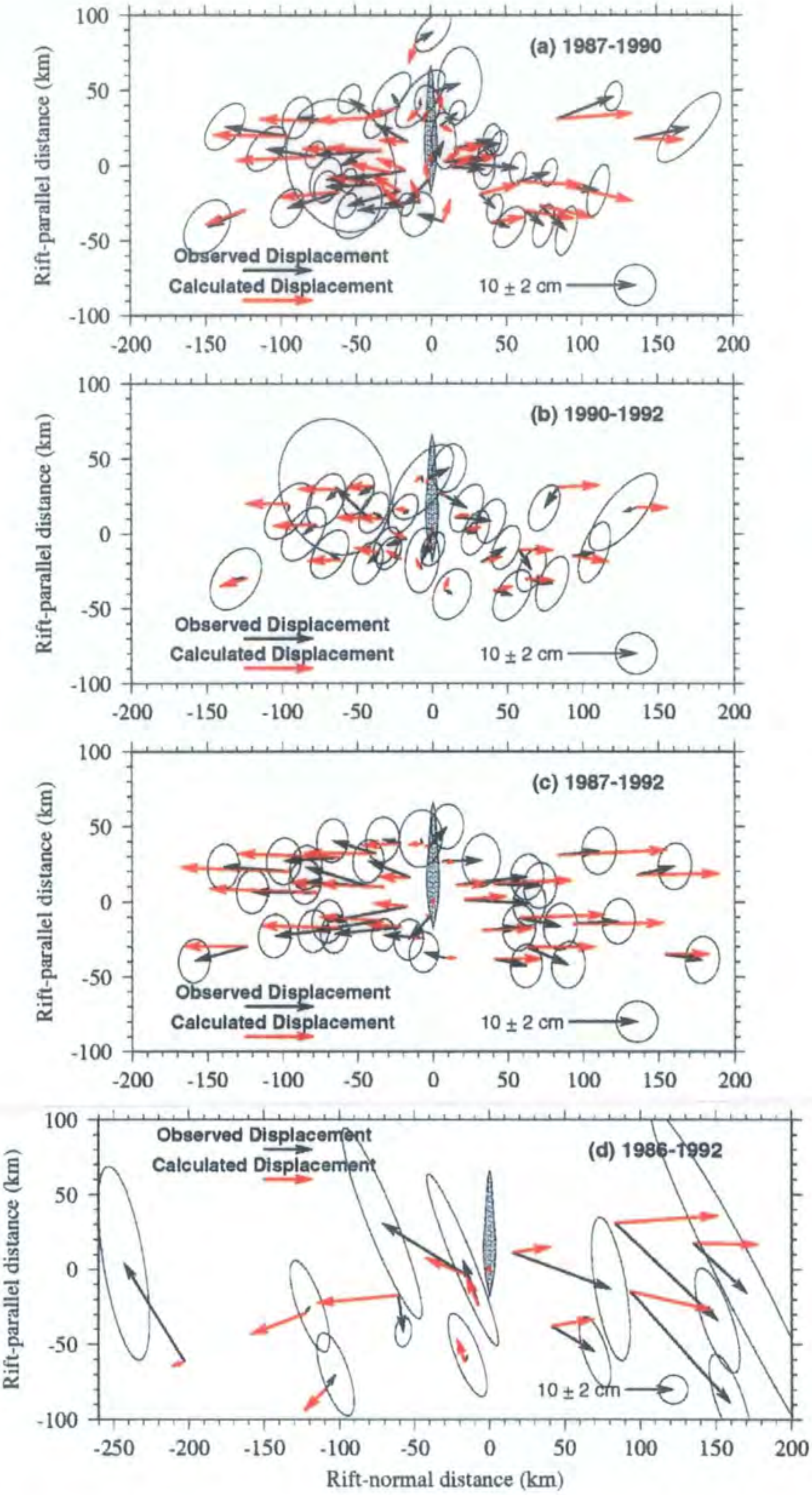

Figure 7.6: Comparison between observed and simulated displacements for (a) 1987–1990, (b) 1990–1992, (c) 1987–1992, and (d) 1986–1992 using a two-dimensional model and a diffusivity of 10 m^2/s (the best-fit diffusivity for the 1987–1990 epoch from *Heki et al.* [1993]). 68% (1.5σ) confidence error ellipses are shown. Points within 10 km of the dyke have not been included in the analysis. The dyke complex is shown shaded. (a) is adapted from *Heki et al.* [1993]. χ^2_ν is 2.6, 1.3, 4.4, and 3.8 for the 1987–1990, 1990–1992, 1987–1992, and 1986–1992 epochs respectively.

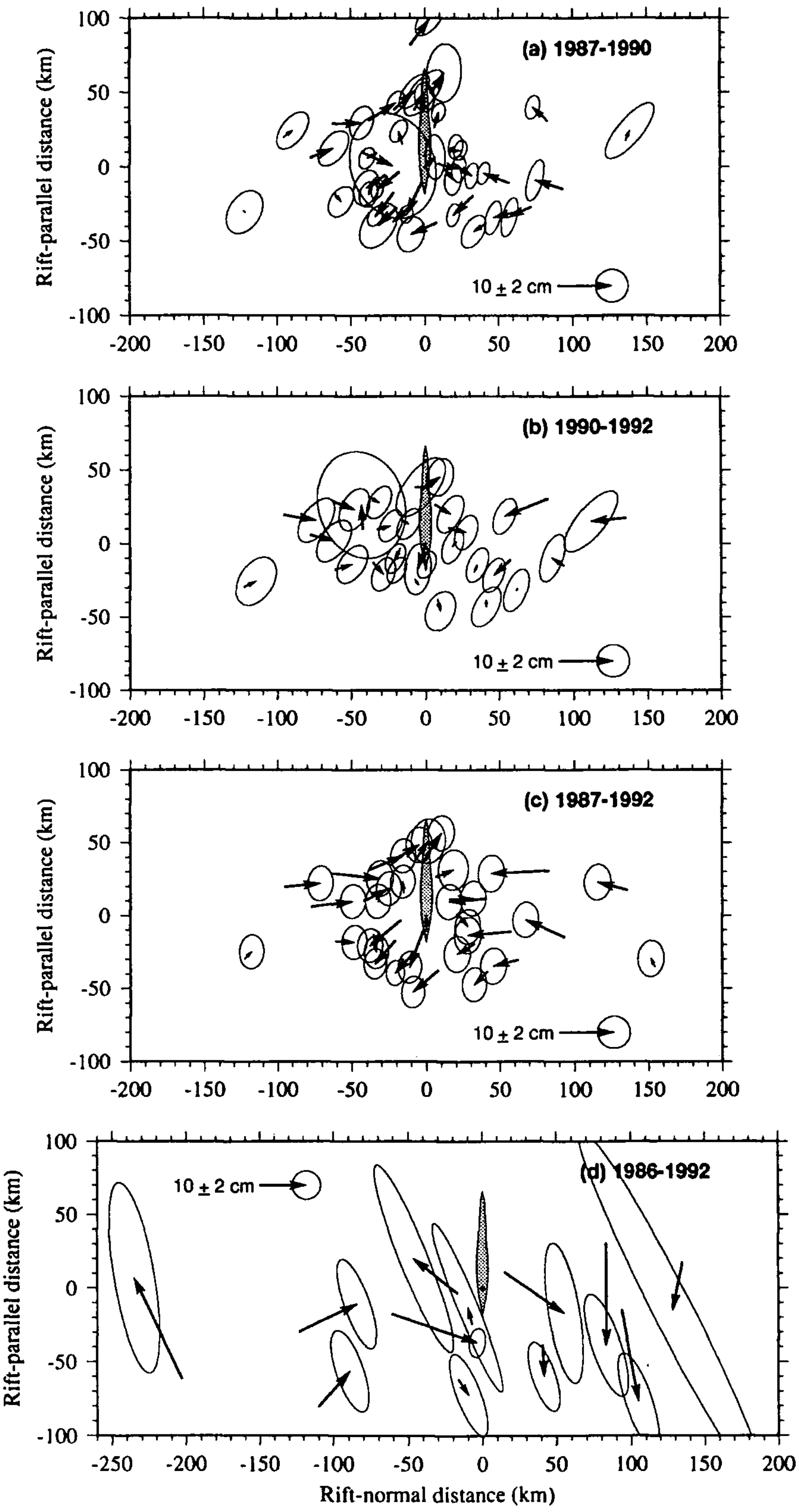

Figure 7.7: Residual vectors (a) 1987-1990, (b) 1990-1992, (c) 1987-1992, and (d) 1986-1992 between the observed and simulated displacements shown in Figure 7.6.

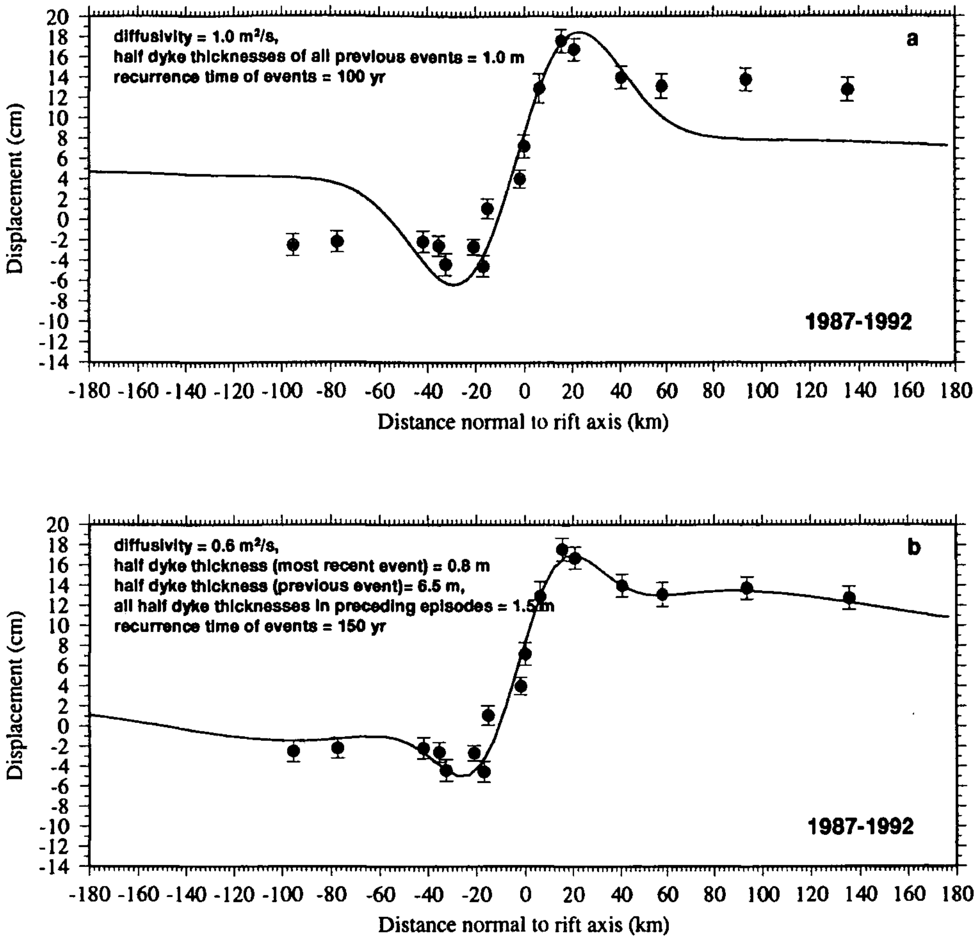

Figure 7.8: Same as Figure 7.5 for the period 1987–1992 except an infinite number of previous episodes were assumed to occur. (a) Dyke thicknesses and event recurrence times are consistent with the value for the time-averaged half plate velocity in Iceland of 1.0 cm/yr, and (b) an example of a model which fits well but requires an unrealistically large dyke thickness for the preceding event (in this case about six times the thickness of the dyke complex intruded in the recent Krafla episode).

1990–1992 epochs, but clearly works poorly in the case of the better-constrained 1987–1992 epoch (Figure 7.7). The poor quality 1986 data again gives poor results for the 1986–1992 epoch. These results suggest that a more realistic geophysical model is required.

If the effects of previous events are taken into consideration (equation 6.81), with dyke thicknesses and recurrence times consistent with current estimates of the time-averaged plate velocity in Iceland, the fit is improved somewhat as the motion at distance from the rift does not fall off to zero. However, a substantial discrepancy still exists between the predicted and observed motion of the furthest points (Figure 7.8a). The motion at these far points can be modelled, but unrealistically large dyke thicknesses are required for the preceding event, e.g., 6.5 m (Figure 7.8b).

7.4 Stress Redistribution in an Elastic Layer Overlying a Viscoelastic Halfspace

7.4.1 Introduction

An improved fit to the observations, and advance in our understanding of the spreading process and structure is to be expected if a more realistic geophysical model is used. Here, a model incorporating an elastic layer overlying a viscoelastic halfspace, and including gravitational effects, is applied. However, as the early work using stress diffusion principles highlighted, before modelling of the Krafla episode can be correctly conducted the effects of other processes that contribute to the deformation must be taken into account. These processes include older dyke intrusions in the Krafla volcanic system, past rifting episodes in the other systems of the NVZ, earthquakes in the TFZ, and other known tectonism, for example, inflations and deflations of the central volcanoes. There is much uncertainty about some of these processes, but fortunately their effects are minor, as will be shown below.

7.4.2 Deformation From Processes Other Than the Krafla Spreading Episode

7.4.2.1 Model Parameters

In order to reduce the number of variables, certain model parameters for which strong, independent constraints exist, are assumed known and their values held fixed during the modelling process. These include the thickness of the elastic layer, H, the height of the dyke, W, the dip of the dyke, ψ, the elastic moduli of the elastic layer, μ_l and λ_l, and the halfspace, μ_h and λ_h, and the densities of the layer and the halfspace, ρ_l, and ρ_h (Table 7.2).

A value of 10 km was assumed for the elastic layer thickness. This is the depth to the regional, low resistivity layer beneath north Iceland in the neighbourhood of Krafla, inferred from magnetotelluric evidence [*Björnsson*, 1985]. This value is further supported by the observed depth range of earthquakes [*Einarsson*, 1991], and later

Table 7.2: Model parameters held fixed during modelling of the events and processes described in Sections 7.4.2.2–7.4.2.6.

Model parameter	Symbol	Value
Elastic layer thickness	H	10 km
Dyke height	W	10 km
Dip	ψ	90°
Elastic moduli: layer	μ_l	2.7 x 10^{10} Pa
	λ_l	4.9 x 10^{10} Pa
halfspace	μ_h	4.1 x 10^{10} Pa
	λ_h	9.9 x 10^{10} Pa
Layer density	ρ_l	2.8 g/cm^3
Halfspace density	ρ_h	3.1 g/cm^3
Viscosity	η	1.1 x 10^{18} Pa s

modelling of the recent Krafla episode (Sections 7.4.3.1 and 8.2.3.2.2). The dykes are assumed to rupture the entire elastic layer, i.e., W=10 km, in accordance with the model of *Björnsson* [1985] and the results of *Rubin* [1992] (Section 2.3.3.4). This model implies that all the far-field, plate-like motion is the summed effect of the Krafla episode and other large spreading episodes and earthquakes along the plate boundary (Section 6.5).

The dykes are assumed to be vertical, in agreement with field geological observations [*Gudmundsson*, 1984]. Seismic refraction experiments suggest an average value for V_p of 5.5 km/s at 0–10 km depths, and 7.0–7.4 km/s at 10–30 km depths [*Gebrande et al.*, 1980]. The V_p/V_s ratio for the crust is about 1.76, and 1.96–2.2 for the upper mantle [*Gebrande et al.*, 1980]. Using the standard seismological relations: $\mu = V_s^2\rho$ and $\lambda = V_p^2\rho - 4/3\mu$, and a velocity–density relationship of $\rho = 1530 + 230V_p$ [*Christensen and Wilkins*, 1982], values for the densities and elastic moduli of the layer and halfspace were calculated (Table 7.2).

A value of 1.1 x 10^{18} Pa s was used for the viscosity of the halfspace. This value is based on numerous forward models of the dyke complex intruded in the Krafla episode. A large majority of the deformation detected using GPS 1987–1992 results from this episode, and modelling it as such can constrain the viscosity to within about 10%. In the absence of a full inverse modelling program and in view of

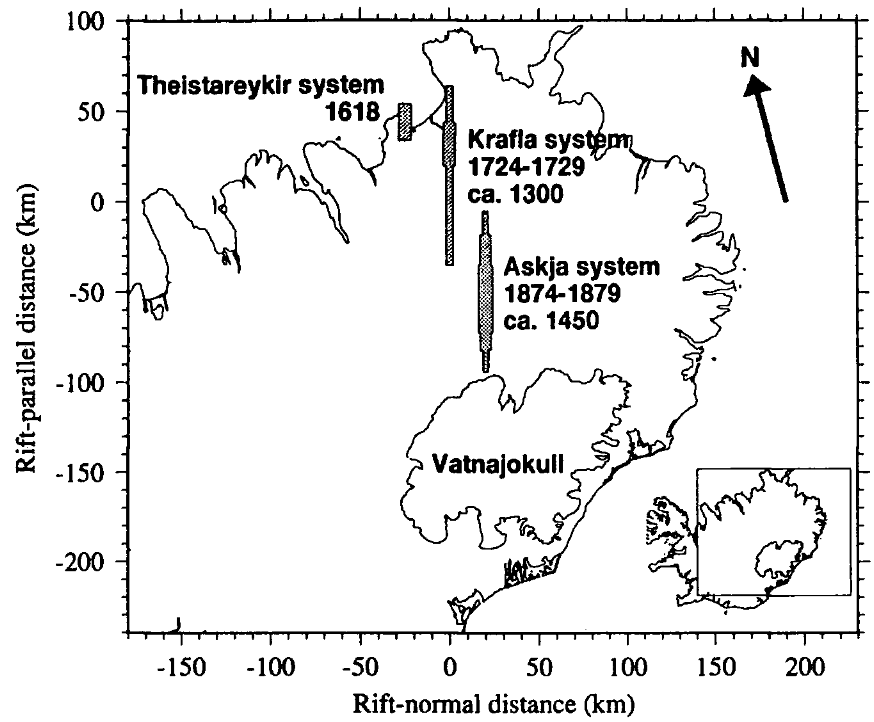

Figure 7.9: Map of northeast Iceland showing the date, location, and dimensions of previous rifting episodes in the NVZ. The Krafla caldera is positioned at $x = y = 0$.

the fact that their effects are minor, this was the most reasonable approach to selecting a halfspace viscosity for modelling the minor contributing tectonic events other than the Krafla episode.

Dyke thicknesses for the historic spreading episodes in the NVZ (Figure 7.9) (Section 2.4) were estimated assuming that the average widening at all points along the rift is 2 cm/yr. In addition, it is assumed that during a dyking episode no thicker dyke can be injected than corresponds to the amount of potential extension accumulated since the last episode at that latitude. This implies that the dykes taper where they overlap one another along the strike of the rift zone. However, this has to be approximated by square-ended dykes for modelling purposes. It is assumed that no unreported rifting events occurred since the 1618 Theistareykir episode (Figure 7.9).

Rifting is thought to recur every 100–150 years in north Iceland [*Björnsson*, 1985]. It is assumed that 150 years prior to the 1618 Theistareykir episode, rifting occurred in the Askja system, and 150 years prior to that in the Krafla system. These assumptions result in estimates of the dyke thicknesses of the Askja 1875 episode and the Mývatn fires episode of 1725 that are about the same as that known for the recent Krafla episode, a reasonable result (Figure 7.9). Thicknesses of 8 m and 7 m respectively are obtained.

These assumptions about the thickness of the early dykes in the NVZ are based on very little information. However, the modelling results show that their effect is small, and thus errors from this source do not greatly affect later modelling of the recent Krafla episode. The assumed dyke lengths were based on observations of fissure swarm widening and eruptive activity at the times of the eruptions.

7.4.2.2 The 1618 Theistareykir Episode

A value of 7 m was used for the thickness of the dyke complex inferred to have been injected in the Theistareykir system in 1618. This value is probably an upper bound as the dyke is thought to be fairly short (~20 km), and a thickness of 7 m yields an aspect ratio of 0.29 x 10^3 which is somewhat high for Icelandic dykes [*Gudmundsson*, 1984].

The horizontal displacements at the GPS network points for the period 1987–1992 that result from this intrusion are shown in Figure 7.10. All points in the network are undergoing motion towards the dyke. A maximum displacement of 0.25 cm is predicted, occurring close to the dyke. The displacement decreases with distance from the dyke. The southernmost points are unaffected by this dyke intrusion.

The vertical displacement field 1987–1992 shows that the maximum uplift is about 0.06 cm and it occurs above the dyke (Figure 7.11). The maximum subsidence, which is about 0.1 cm, occurs at distances of ~50 km either side of the dyke. The amount of subsidence decreases with increasing distance from about 50 km from the dyke, and points in the southern part of the network underwent subsidence of only 0.02–0.04 cm due to this intrusion.

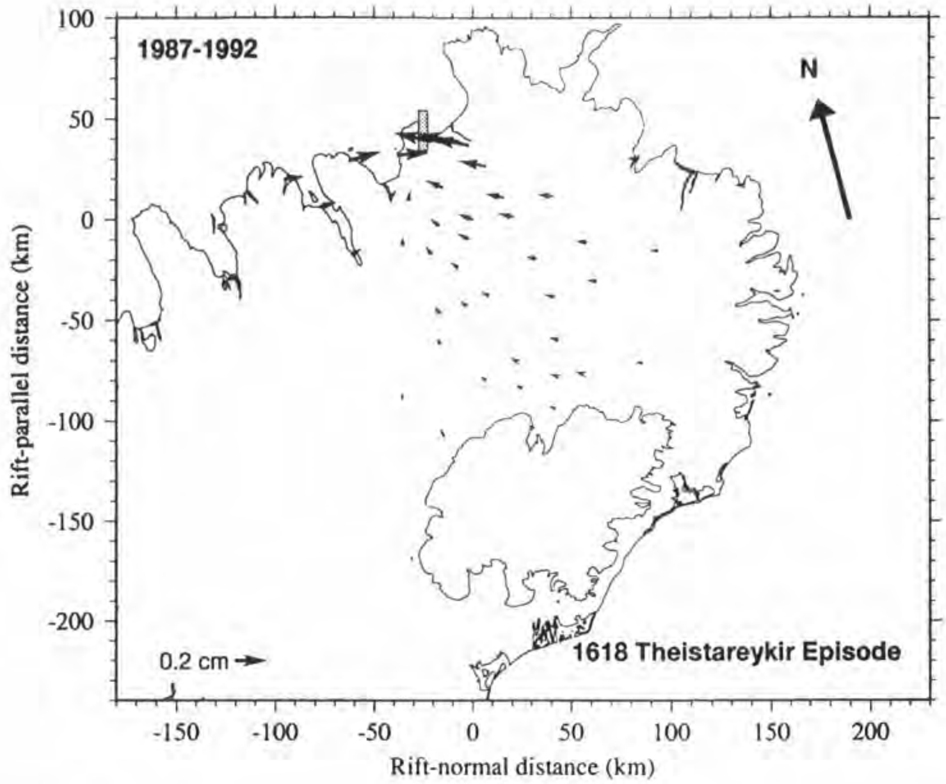

Figure 7.10: Horizontal displacements 1987–1992 of points of the GPS network as a result of the 1618 Theistareykir rifting episode. The position of the dyke is shown shaded. A dyke thickness of 7 m was assumed. All other dyke and model parameters are given in Table 7.2. The Krafla caldera is at $x = y = 0$.

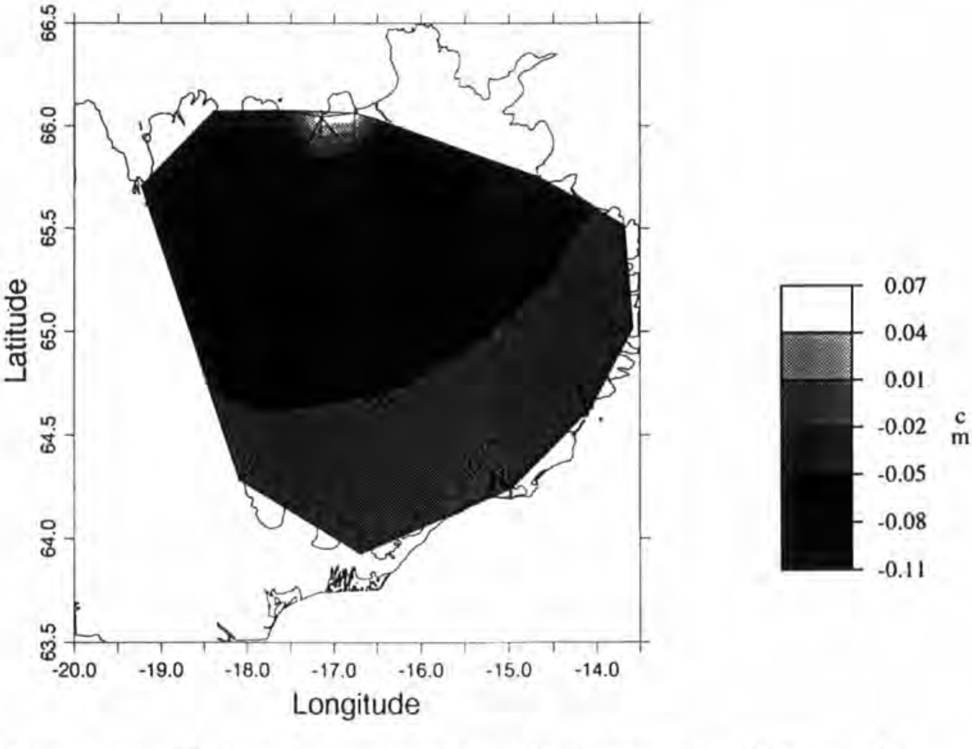

Figure 7.11: Vertical motions 1987–1992 as a result of the 1618 Theistareykir rifting episode. Diagrammatic representation as for Figure 7.4.

7.4.2.3 The 1724–1729 Mývatn Fires Episode

To estimate the dyke thickness of the 1724-1729 Mývatn fires episode, a previous episode was assumed to have occurred in the Krafla volcanic system ca. 1300. This yielded a dyke thickness estimate comparable with that of the recent Krafla dyke complex (up to 7 m). A dyke of variable along-strike thickness was used, that tapers where there is overlap with the preceding 1618 Theistareykir dyke. Three end-to-end dykes, simultaneously intruded in 1729, were used to simulate the intrusion, a northern and a southern one with thicknesses of 4 m, and a central one with a thickness of 7 m (Figure 7.9).

The predicted horizontal and vertical deformation fields 1987–1992 (Figures 7.12 and 7.13) show similar patterns to those predicted for the Theistareykir episode, but of larger amplitude. A horizontal contraction of the network 1987–1992 is predicted with maximum displacements of 1.2 cm occurring closest to the central part of the dyke complex. Displacement decreases with distance from the dyke. Points south of the dyke undergo very little motion, as do the points further than ~80 km from the dyke.

Uplift occurs in the vicinity of the dyke to a maximum of 0.2 cm, and subsidence of up to 0.6 cm at distances of ~50 km on either side of the dyke axis. The amount of subsidence decreases at larger distances from the rift, with the southernmost points in the network predicted to experience a maximum 0.2 cm of subsidence as a result of this dyke intrusion episode.

7.4.2.4 The 1874 Askja Episode

In order to determine the thickness of the hypothesised dyke intruded in 1874 in the Askja system, the previous episode there was assumed to have occurred ca. 1450, an assumption based on the episodicity of spreading in the NVZ. This gives a dyke which is 8 m thick along much of its length, which is comparable to the thickness of the recent Krafla dyke complex. Five end-to-end, simultaneously-injected dykes were used, which had dyke thicknesses of 3 m, 6 m, 8 m, 6 m and 3 m.

The horizontal deformation field predicts an expansion of the network during 1987–1992 as a result of this episode (Figure 7.14). A maximum displacement of 2 cm

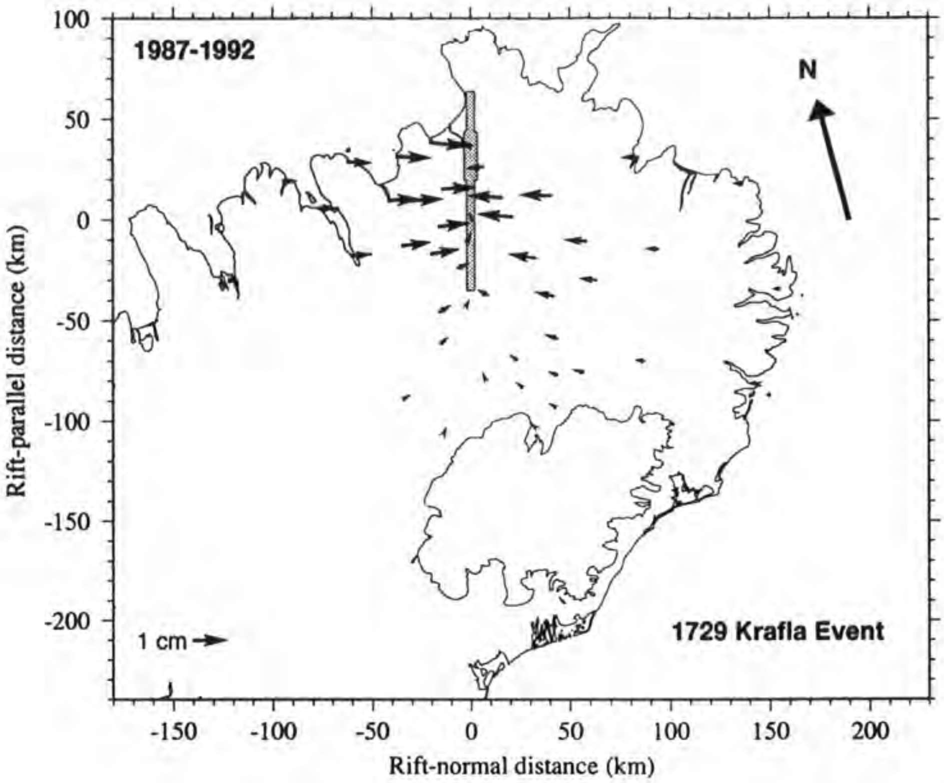

Figure 7.12: Same as Figure 7.10, except for the 1724–1729 Mývatn fires episode.

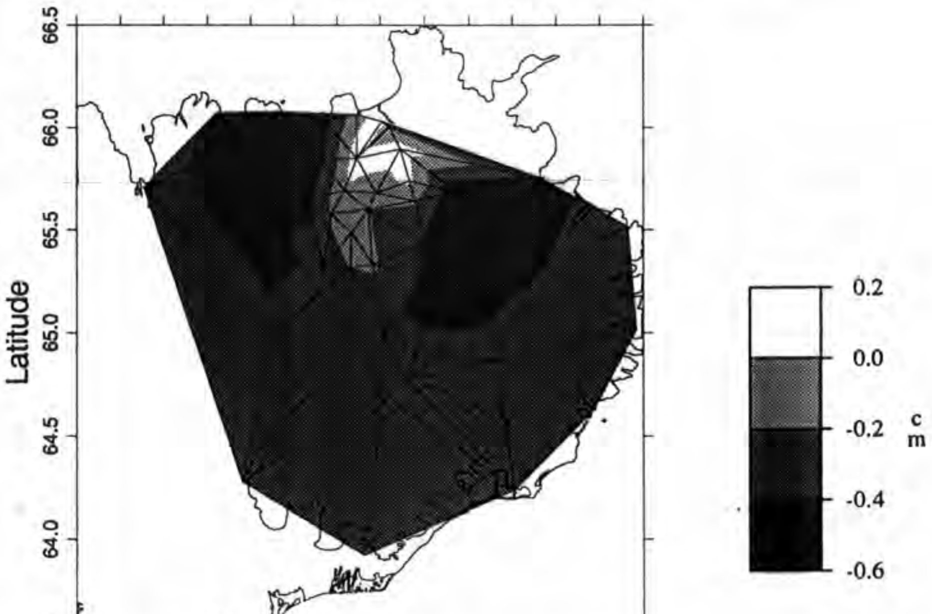

Figure 7.13: Same as Figure 7.11, except for the 1724–1729 Mývatn fires episode.

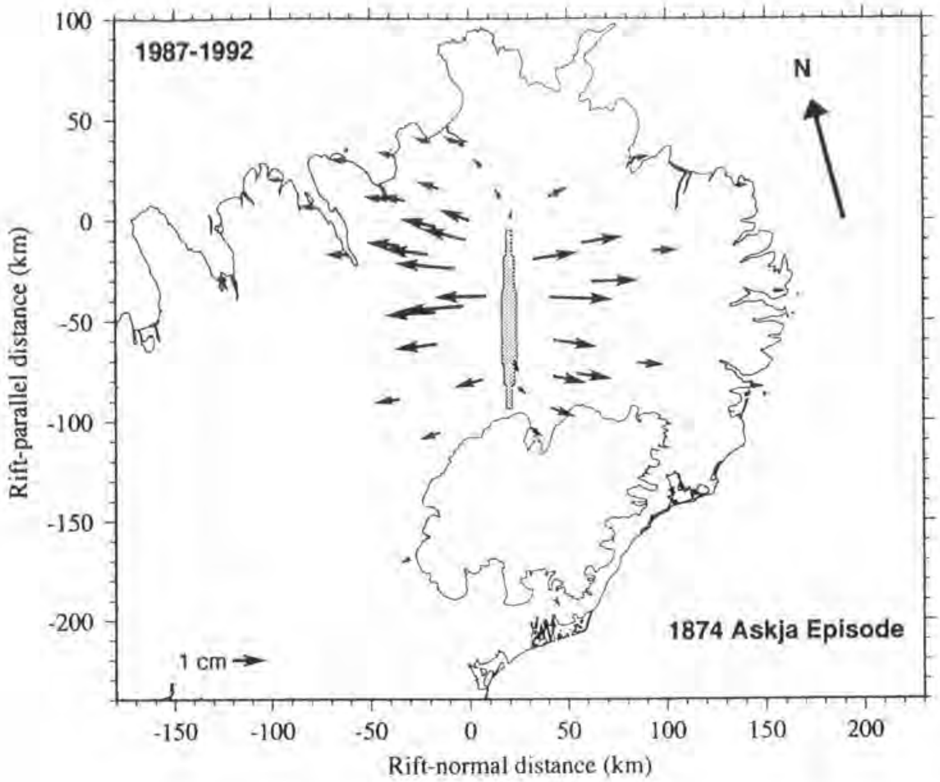

Figure 7.14: Same as Figure 7.10, except for the 1874 Askja rifting episode.

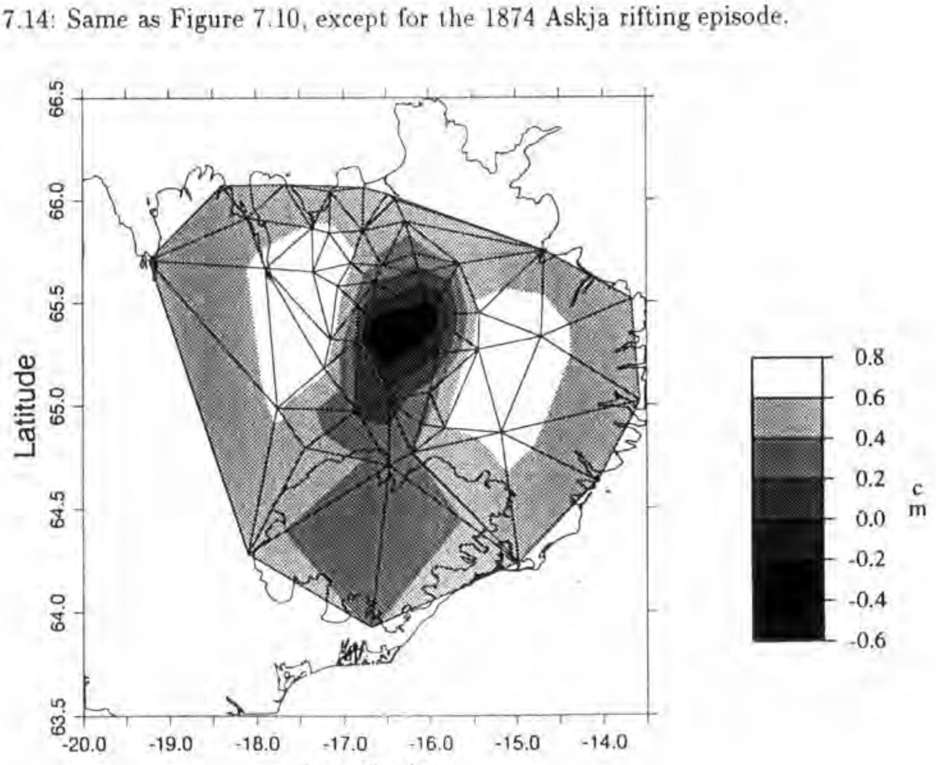

Figure 7.15: Same as Figure 7.11, except for the 1874 Askja rifting episode.

is predicted within a few tens of kilometres of the dyke. Motion decreases with distance from the dyke and is very small at large distances. Points to the south and north of the dyke also experience little motion.

The vertical field (Figure 7.15) shows that most of the network experienced uplift as a result of the intrusion, except for points in the region of the dyke complex which underwent subsidence of up to 0.6 cm. The maximum uplift of about 0.8 cm occurred at distances of ~50 km on either side of the dyke. Vertical motion of the farthest points was ~0.4 cm, decreasing with increasing distance from the dyke.

7.4.2.5 Recent, Large Earthquakes in the Tjörnes Fracture Zone

The deformation resulting from recent, large earthquakes in the TFZ also contributed to the 1987–1992 displacement field. The events in this region are predominantly right-lateral strike-slip. All events large enough, close enough or recent enough to significantly affect points of the GPS network were selected (Table 7.3). Their effects were modelled using a version of the elastic-viscoelastic modelling program adapted for strike-slip sources [*T. T. Yu*, pers. comm., 1995].

Table 7.3: Earthquakes greater than magnitude 6.0 in the Tjörnes Fracture Zone and close to land, 1900–1992. Dates, epicentre locations, and magnitudes are from *Tryggvason* [1973] and *Björnsson et al.* [1977].

Date	Epicentre	Magnitude	Fault length (km)	Dislocation (m)
Jan. 22 1910	N66.5° W17.0°	7.1	50	2.0
June 2 1934	N66.0° W18.5°	6.3	25	0.5
Mar. 28 1963	N66.3° W19.6°	7.0	50	2.0
Jan. 13 1976	N66.2° W16.7°	6.3	20	0.5

Estimates of the fault length and dislocation for each event were made (Table 7.3) using the relations $M = 2/3 \log M_0 - 10.7$ [*Hanks and Kanamori*, 1979], where M is the magnitude and M_0 is the seismic moment (in dyne cm), and $M_0 = \mu A \bar{u}$ [e.g., *Aki and Richards*, 1980], where μ is the rigidity, A is the area of fault slip, and $\bar{u}$ is the amount of slip. The TFZ is segmented on a scale of ~25 km [*Einarsson*, 1991]. Assuming magnitude 6 and 7 events rupture one and two segments respectively this suggests fault lengths of about 25 km and 50 km for these events. The estimates for the magnitude 6.3 events are supported by the length of the 1976 aftershock zone.

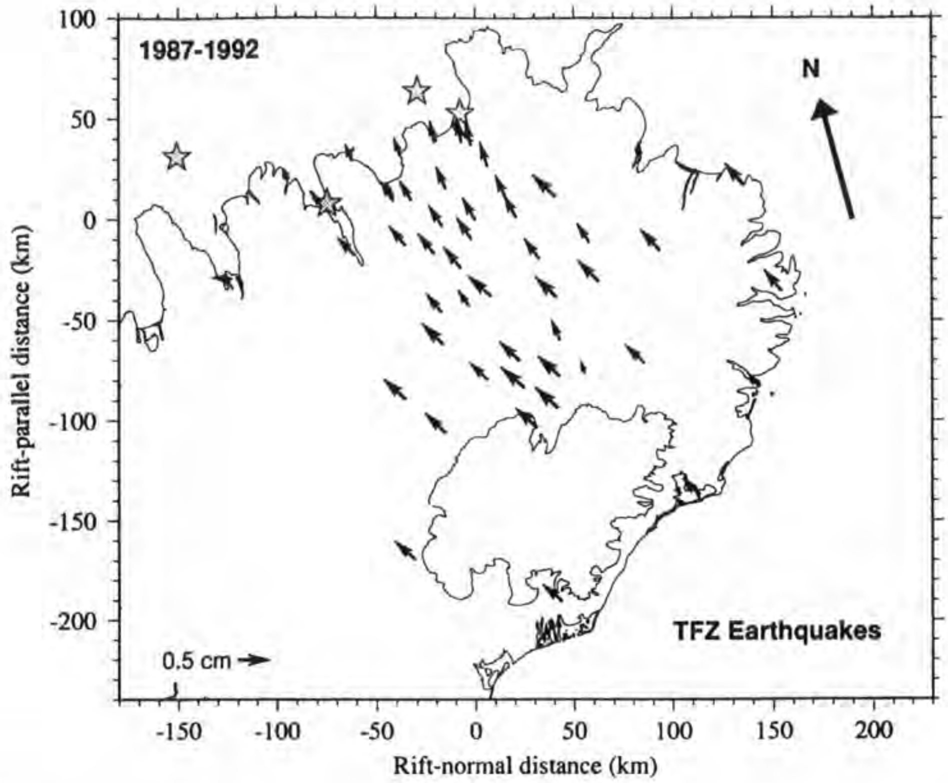

Figure 7.16: Same as Figure 7.10, except for recent, large earthquakes in the TFZ. The stars give the locations of the modelled events.

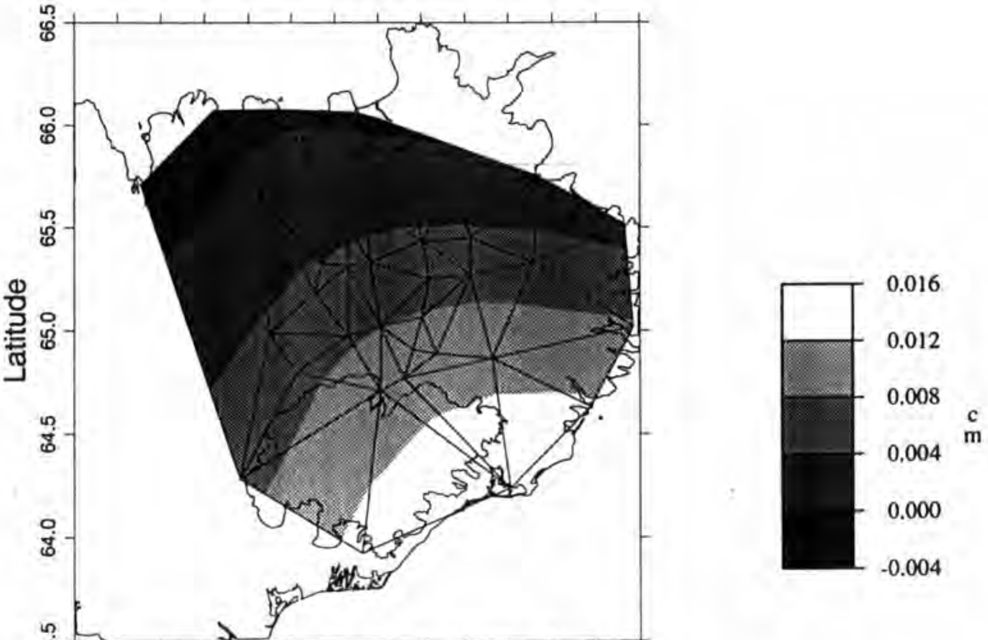

Figure 7.17: Same as Figure 7.11, except for recent, large earthquakes in the TFZ.

All events were assumed to rupture all of the elastic layer. Hence, slip estimates of 2 m and 0.5 m were obtained for the magnitude 7.0 and 6.3 events.

A maximum horizontal displacement of 0.5 cm was predicted as a result of these events, occurring just north of the edge of the Vatnajökull icecap (Figure 7.16). The minimum displacement of ~0.1 cm occurs closest to the TFZ. Motions are directed towards the TFZ.

The vertical displacement field shows that a maximum subsidence of up to 0.04 mm occurred 1987–1992 in the vicinity of the TFZ (Figure 7.17). Uplift occurred over most of the network, increasing with distance from the TFZ, and reaching a maximum of about 0.16 mm in the south of the network. However, as can clearly be seen, vertical displacements resulting from recent, large earthquakes in the TFZ are negligible compared with the accuracy of GPS surveying.

7.4.2.6 Activity in the Askja Magma Chamber

Substantial, recent vertical motions are reported close to the Askja central volcano (Section 2.5). Initial investigations of the probable effect on vertical motion there of the recent Krafla episode show that this cannot explain the vertical motions reported for 1987–1992, since an almost smoothly varying field is predicted (Figure 7.18). It can therefore be concluded that deflation of the magma chamber probably did occur, and this effect must be included in modelling the observed deformation field. A source depth of 2.8 km and an average deflation of 4.8 cm/yr were assumed, as estimated by *Rymer and Tryggvason* [1993].

A simple Mogi point source is used here to predict the deformation field. This assumes a small sphere with varying pressure (a point source) in an elastic halfspace. The horizontal, Δd, and vertical, Δh, displacements on the surface are [*Mogi*, 1958]

$$\Delta d = C\frac{d}{(f^2 + d^2)^{3/2}}, \tag{7.2}$$

$$\Delta h = C\frac{f}{(f^2 + d^2)^{3/2}}, \tag{7.3}$$

where f is the depth to the point source, C is the source strength, and d is the horizontal (radial) distance at the surface from the point source. C is related to the vertical displacement above the point source, Δh_0, by $C = \Delta h_0 f^2$.

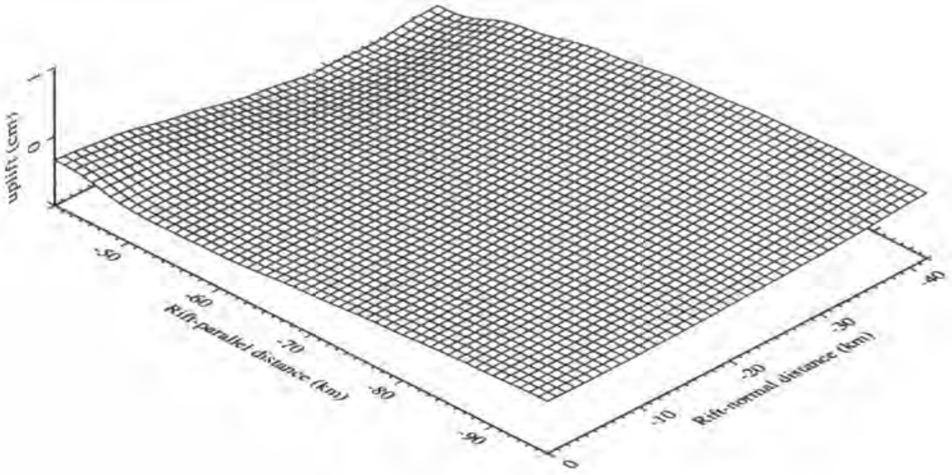

Figure 7.18: Simulated vertical displacements 1987–1992 for an area centred around the Askja caldera due to the recent Krafla dyke intrusion (see Section 7.4.3.1). The Askja caldera is situated at (17, −71) (corresponding to 65° 3.19'N, 16° 46.10'W) and the vertical motion is set to zero at this point. The Krafla caldera is positioned at $x = y = 0$.

The simulated horizontal deformation field for the period 1987–1992 shows a radial pattern of motion, directed inwards towards the caldera (Figure 7.19). Only a very few points that are close to the caldera are significantly affected, with a maximum of 4.1 cm of displacement predicted.

The vertical motion 1987–1992 within the GPS network is shown in Figure 7.20. The majority of the network was unaffected. The point closest to the source subsided by ~2.4 cm 1987-1992, and the subsidence is less than 0.1 cm at all other points.

7.4.2.7 Activity in the Krafla Magma Chamber

Data from tiltmeters in the vicinity of the Krafla caldera indicate substantial vertical motion there 1987–1992 (Section 2.3.4, Table 2.3), interpreted as inflation and deflation of at least two magma chambers beneath Krafla [*Tryggvason*, 1994]. However, much of this tilt is well modelled as viscoelastic relaxation resulting from the recent Krafla episode, as will be shown in Section 7.4.3.2. For this reason, activity in the Krafla magma chamber is not modelled at this stage.

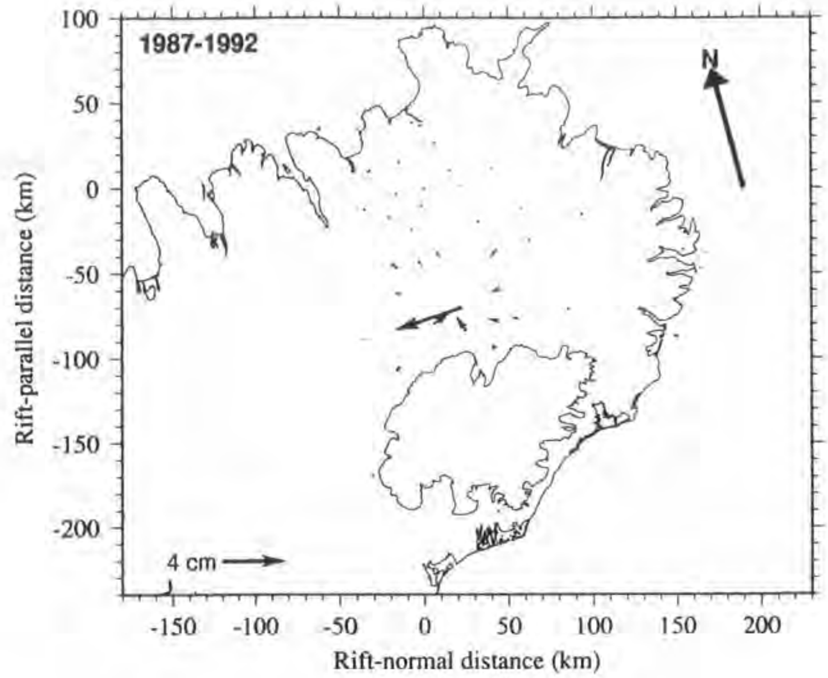

Figure 7.19: Same as Figure 7.10, except for a point source located 2.8 km deep at (17, -71) (corresponding to 65° 3.19'N, 16° 46.10'W), deflating at 4.8 cm/yr in an elastic halfspace.

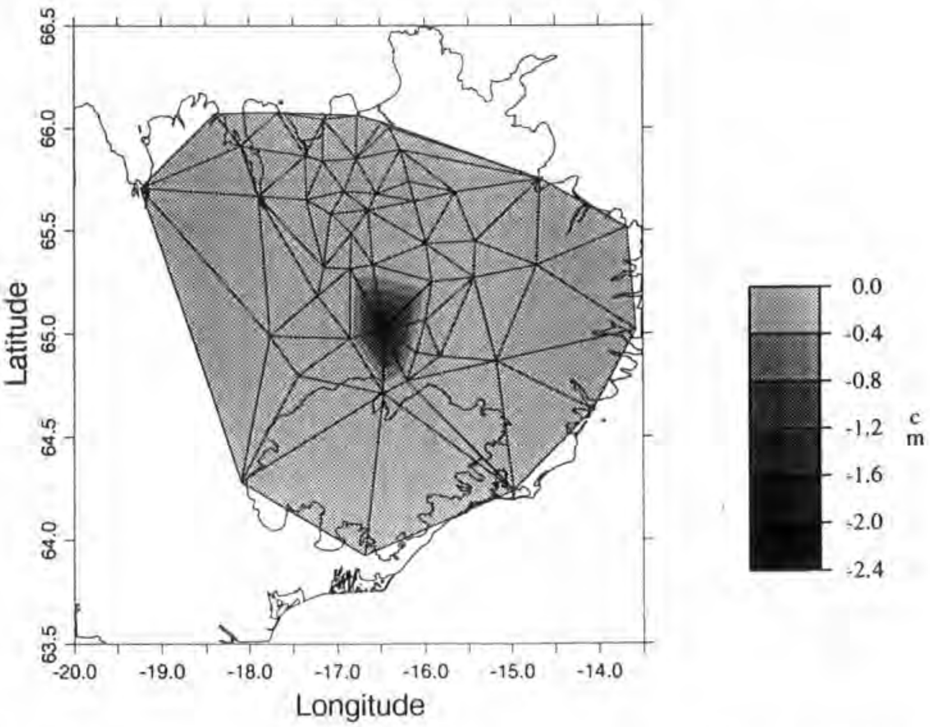

Figure 7.20: Same as Figure 7.11, except for the deflation at 4.8 cm/yr of a 2.8 km deep source located at 65° 3.19'N, 16° 46.10'W in an elastic halfspace.

7.4.2.8 The Total Deformation Field Resulting From Historical Spreading Episodes in the NVZ, Earthquakes in the TFZ, and Activity in the Askja Magma Chamber

The total effect of the processes modelled in Sections 7.4.2.2 to 7.4.2.6 are shown in Figures 7.21 and 7.22. The horizontal deformation field is complicated with contraction of the network predicted across the Krafla volcanic system and expansion across the Askja system (Figure 7.21). Predicted displacements decrease with distance from the rift zones. The maximum displacement is 4 cm, occurs close to the Askja caldera, and is mostly a result of the deflation of the magma chamber 1987–1992. Apart from this, the maximum displacements occur to the north of the Askja system and to the southeast of the Krafla system. A maximum motion of about 1.5 cm is expected there. The displacements shown are relative to the total model, and within this framework, points east of the Askja system undergo negligible motion, as do points in the far south, west and east of the network.

The vertical field shows that the maximum subsidence of 2.7 cm occurs in the vicinity of the Askja caldera (Figure 7.22). Apart from this, the maximum subsidence of 0.8 cm occurs within the Askja volcanic system, and ~0.2 cm in the northwest of the network (in the TFZ). Uplift of 0.4 cm occurs in the Krafla volcanic system. However, the majority of the vertical motion resulting from the processes and episodes in the TFZ and NVZ is very small.

7.4.3 Movements Resulting From the Krafla Spreading Episode

7.4.3.1 The Best-fit Model

The effects of the episodes and processes modelled in Sections 7.4.2.2 to 7.4.2.6 were subtracted from the observed horizontal and vertical deformation fields, and the residual fields modelled as viscoelastic relaxation following the recent Krafla spreading episode. A large number of candidate models were tried, varying the viscosity and dyke thicknesses only. The best-fit model selected was the one that produced the minimum (in a least squares sense) differences between the predicted and observed displacements 1987–1992, the best-constrained epoch. Consistency

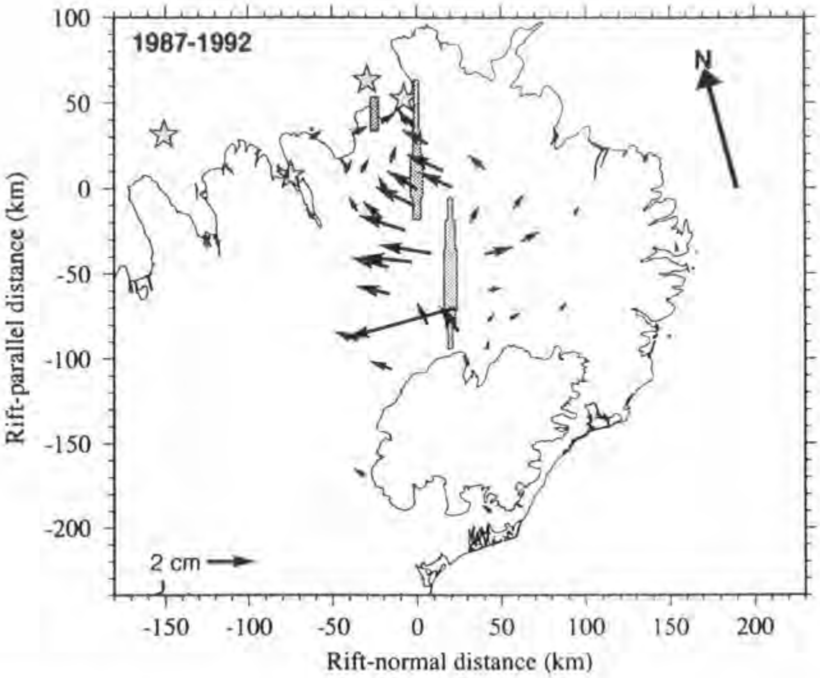

Figure 7.21: Same as Figure 7.10, except the total horizontal deformation field resulting from the processes dealt with in Sections 7.4.2.2 to 7.4.2.6 are shown.

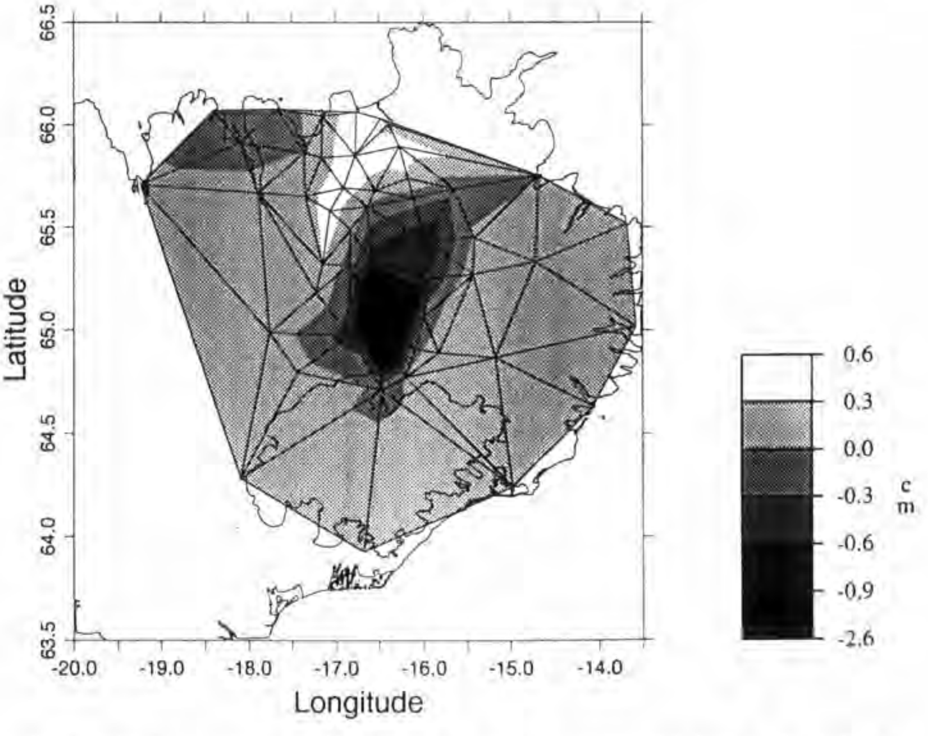

Figure 7.22: Same as Figure 7.11, except the total vertical displacements resulting from the processes dealt with in Sections 7.4.2.2 to 7.4.2.6 is shown. Note that the scale is not linear throughout the whole range.

was maintained with previous estimates for the dyke thickness that were crudely based on the measured amount of expansion within the fissure swarm and the amount of motion outside of the fissure swarm [*Tryggvason*, 1984].

Four end-to-end, simultaneously-injected dykes were used to simulate the along-strike variation in dyke thickness. In reality the dykes were injected over a period of about 10 years. Modelling the intrusions as such however, surprisingly produces negligible differences in the resultant deformation field for 1987–1992 when compared with the simultaneously-injected case. From south to north dyke thicknesses of 4.5 m, 5.0 m, 4.5 m and 3.0 m were used, along with a viscosity of 1.1 x 10^{18} Pa s. All other model parameters were identical to those given in Table 7.2.

Figure 7.23 illustrates the fit of the model to the points in the profile zone (Figure 7.1). Up to 21 cm of expansion is predicted 1987–1990, decreasing to 9 cm further away (Figure 7.23a). The maximum displacement occurs at ~25 km from the rift axis. The motion of the points to the west of the dyke are reasonably well fitted, but the model overestimates motion slightly to the east at intermediate distances. Continued expansion of the network is predicted 1990-1992, with up to 4 cm of motion within ~30 km of the rift, decreasing to 2 cm further away (Figure 7.23b). Motion to the west of the dyke and those of the furthest points are well simulated. However, within 15 km east of the dyke, the motion is significantly underestimated. A maximum expansion of 24 cm is predicted 1987–1992 (Figure 7.23c), occurring at distances of ~40 km from the rift. Further away the motion decreases to ~12 cm. The observed displacements are well predicted by the model, although the observed maximum displacement occurs closer to the rift than is predicted. A reasonable fit to the far field is achieved, with motion underestimated by ~3 cm at distances of 100 km west of the rift.

In plan view, the model predicts a quasi-radial horizontal displacement field, with motion outward from the dyke at all points for the periods 1987–1990, 1990–1992 and 1987–1992 (Figure 7.24). The maximum motion occurs within a few tens of kilometres of the dyke, and decreases with distance beyond. Motion directly to the south of the dyke is considerably smaller than that on either side, and points in the far south of the network are predicted to experience 1–3 cm of motion 1987–1992. χ^2_ν is 3.8, 1.3 and 3.4 for the 1987–1990, 1990–1992, and 1987–1992 epochs respectively. χ^2_ν is reduced to 3.2 for the 1987–1992 epoch if the three points with large residuals in the southeast of the network are neglected. For comparison,

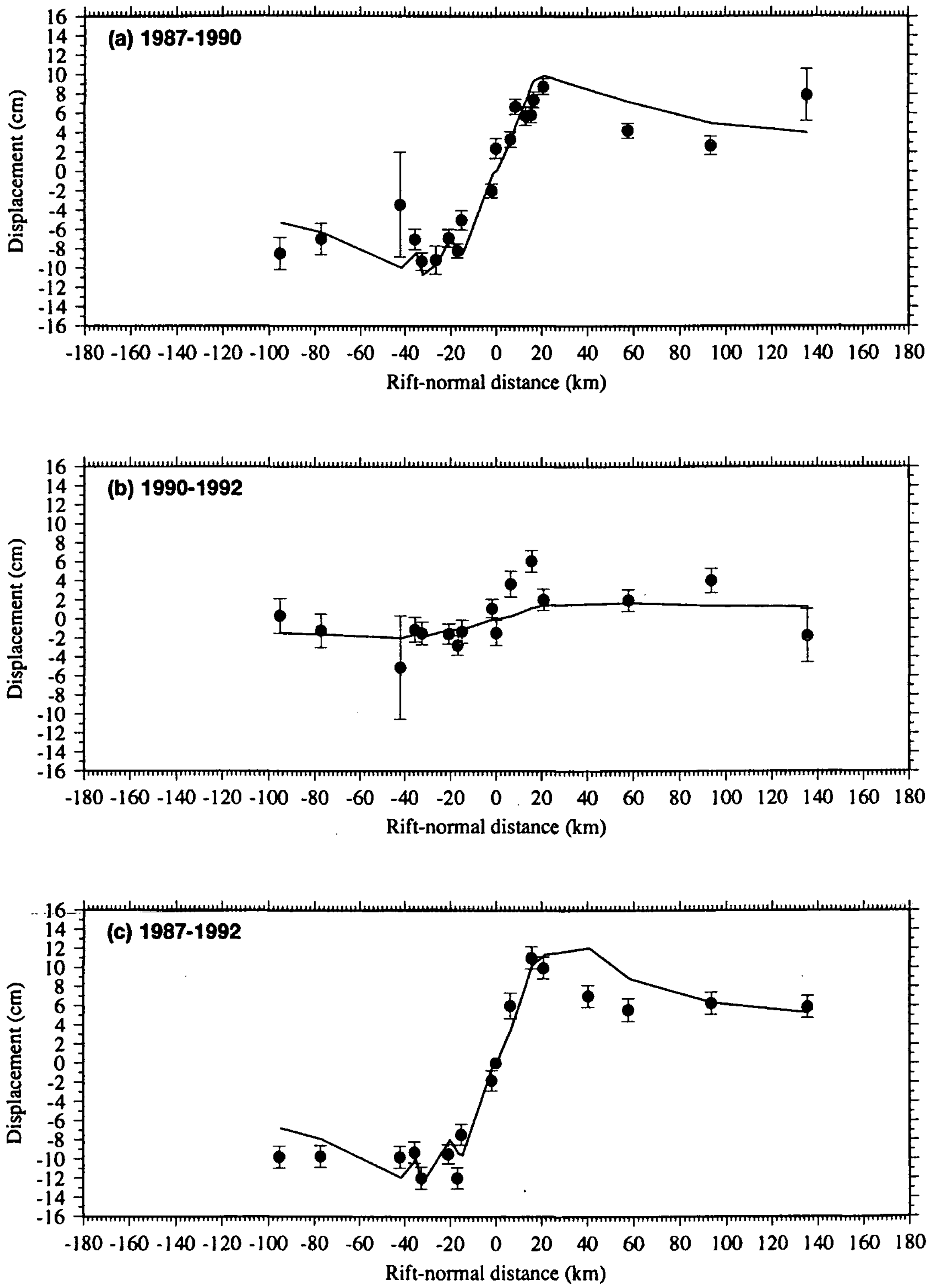

Figure 7.23: Comparison of observed and best-fitting simulated horizontal displacements (a) 1987–1990, (b) 1990–1992, and (c) 1987–1992 of points within the profile zone shown in Figure 7.1. The effects of the processes dealt with in Sections 7.4.2.2–7.4.2.6 have been subtracted from the observed displacements.

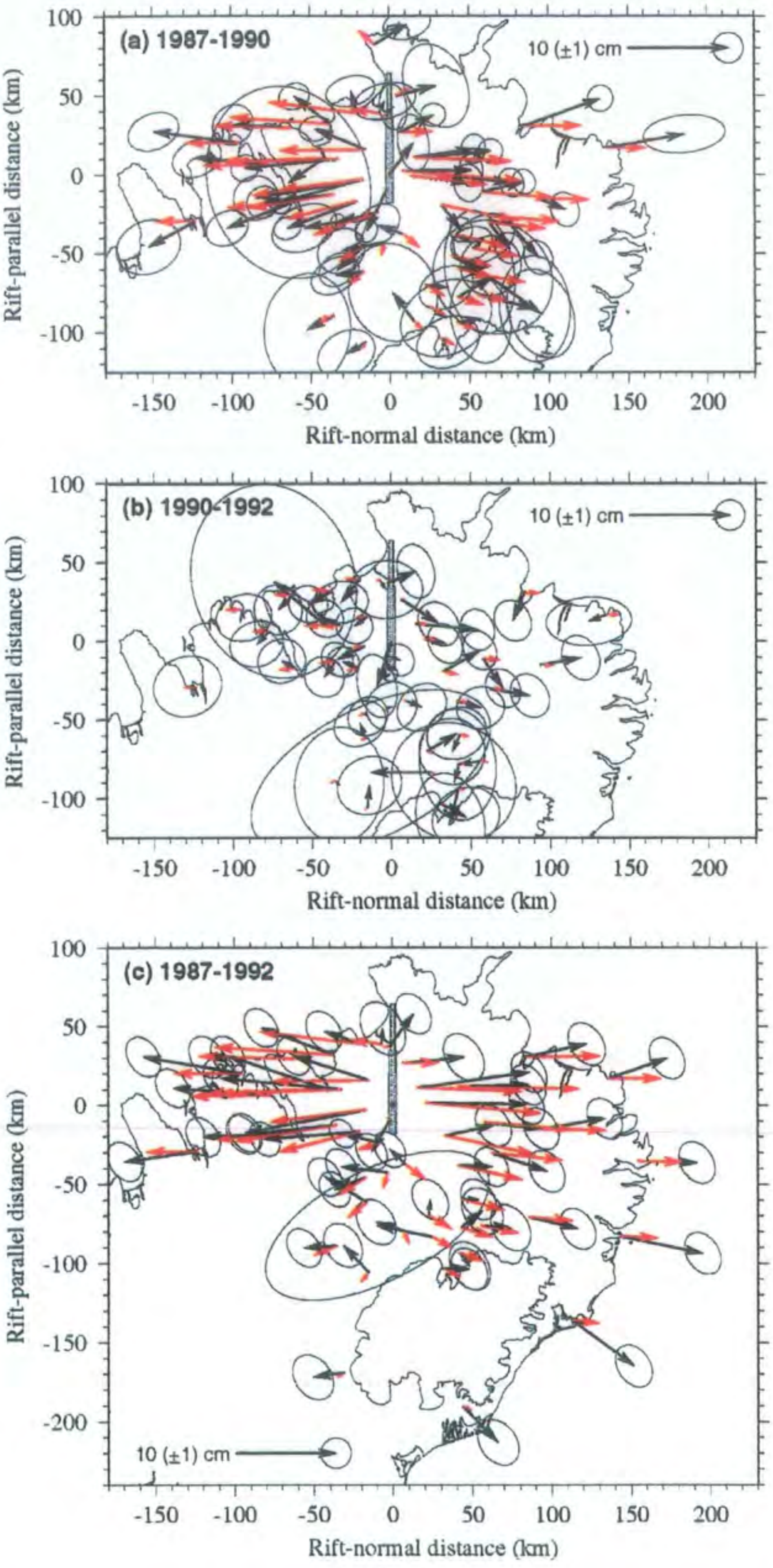

Figure 7.24: Comparison of observed and best-fit simulated displacements (a) 1987–1990, (b) 1990–1992, and (c) 1987–1992. The solid arrows represent the observed displacements, minus the effects of the processes dealt with in Sections 7.4.2.2–7.4.2.6, and the red arrows simulated. The position of the dyke complex and its dimensions are shown schematically.

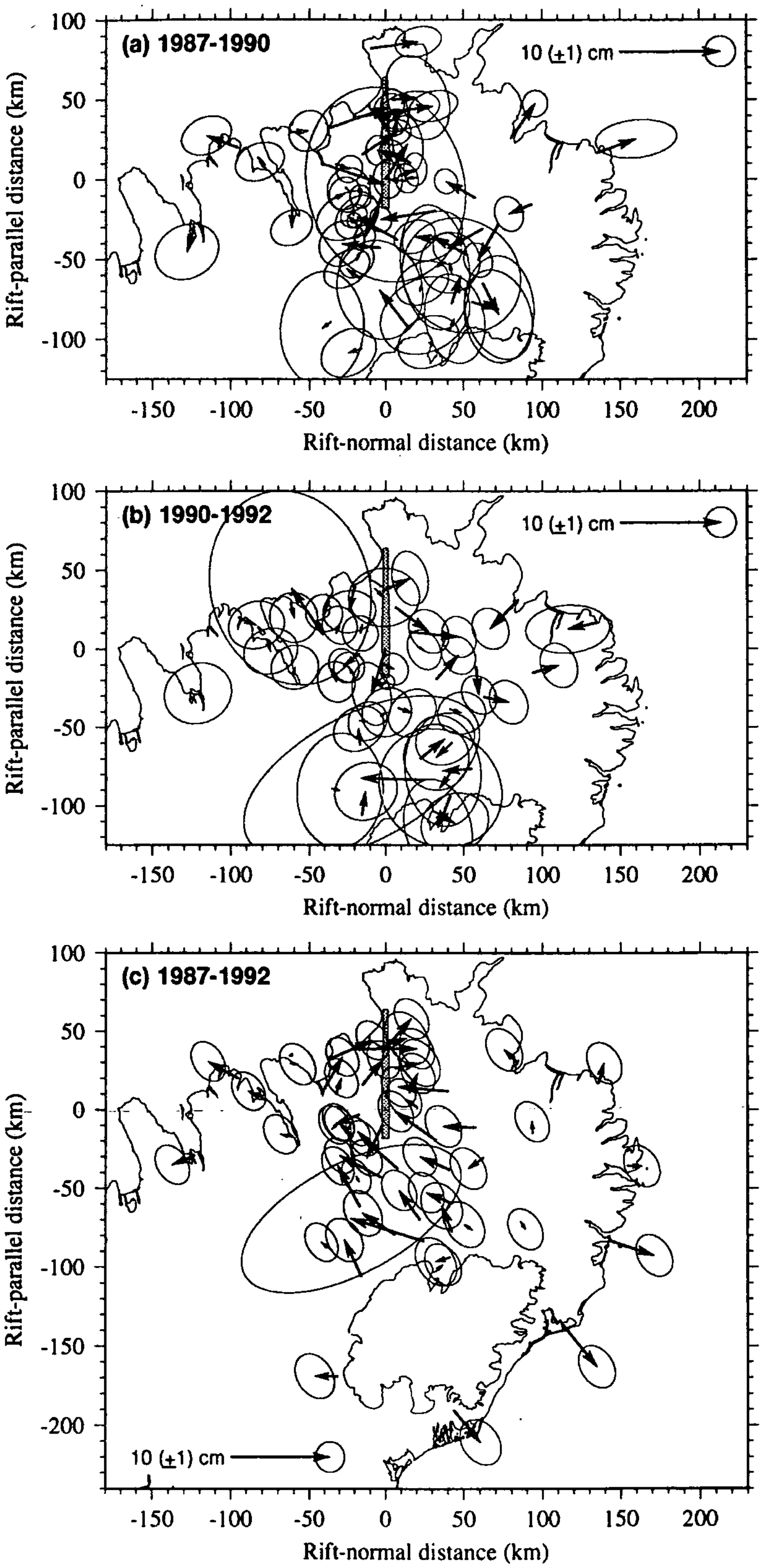

Figure 7.25: The residual vectors remaining after subtracting the best-fit simulated displacements from those observed (a) 1987–1990, (b) 1990–1992, and (c) 1987–1992.

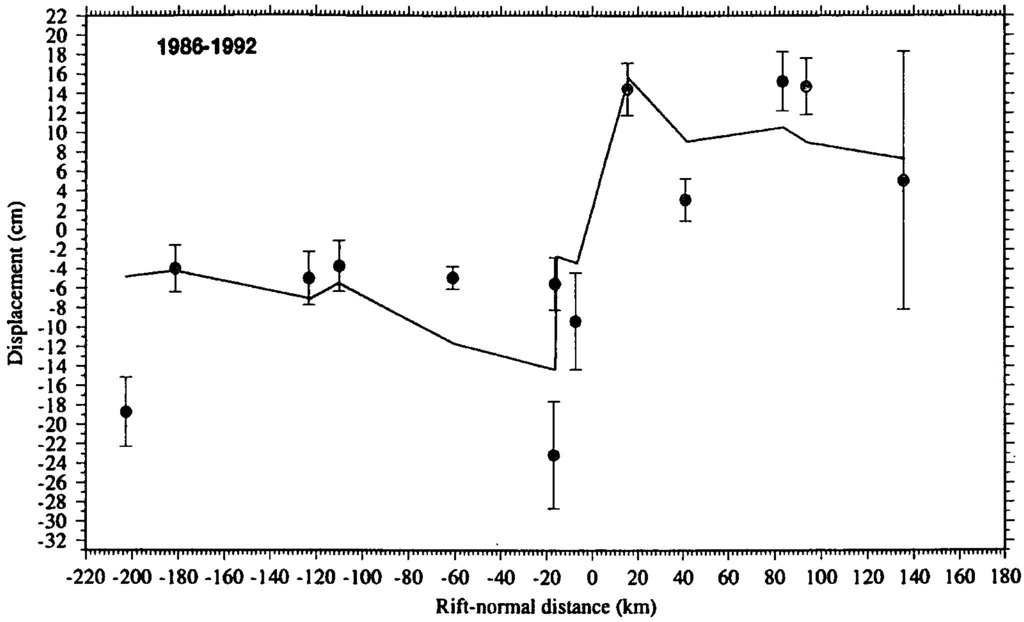

Figure 7.26: Same as Figure 7.23, except for 1986–1992.

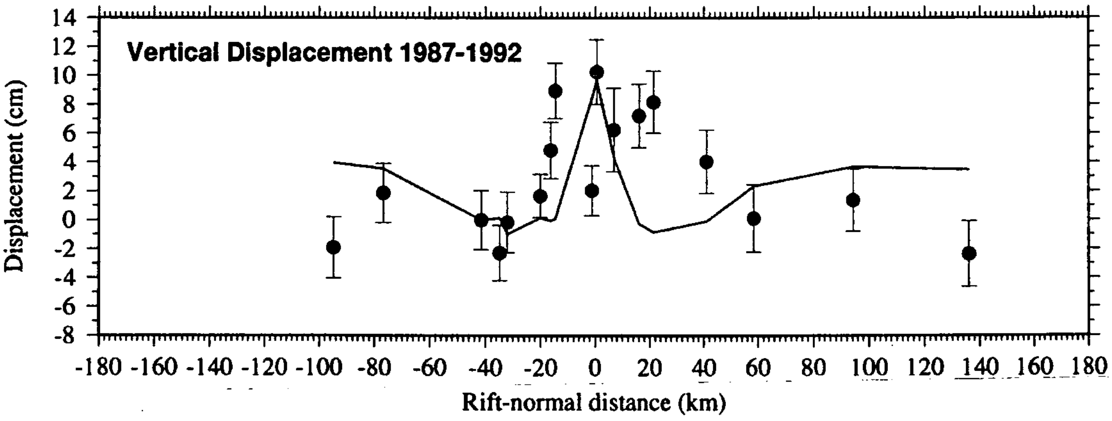

Figure 7.27: Same as Figure 7.23, except for the 1987–1992 vertical deformation field.

the weighted variances of the observations (equation 7.1 for the case where the $v_i^{mod} = 0$) are 12.6, 1.9, and 16.2 for the 1987–1990, 1990–1992, and 1987–1992 epochs respectively. The model thus fits the observed displacements fairly well.

The residual fields for the three epochs are shown in Figure 7.25. There are two significant areas of misfit. The first is close to the dyke complex, where motion is overestimated by up to ~5 cm. The second is in the far south and southeast of the network for the 1987–1992 epoch, where residuals of up to 7 cm remain. No other areas of systematic residuals, significant at the 2σ level are evident.

A maximum of 30 cm of expansion is predicted for 1986–1992, decreasing to 12 cm

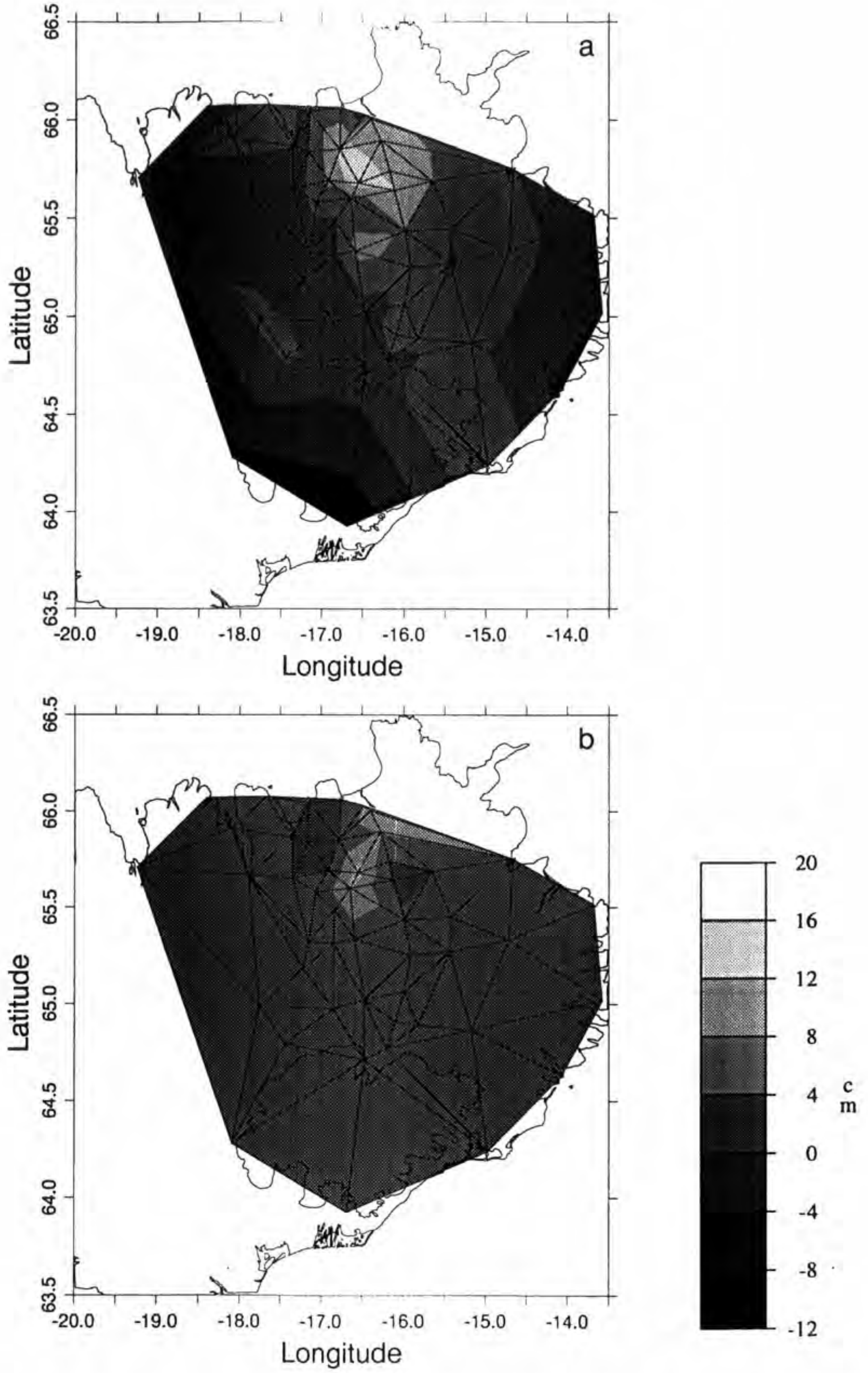

Figure 7.28: (a) Observed vertical displacements minus the effects of the processes dealt with in Sections 7.4.2.2–7.4.2.6, and (b) simulated motions 1987–1992 as a result of the recent Krafla rifting episode, using the model that fits best the 1987–1992 horizontal field.

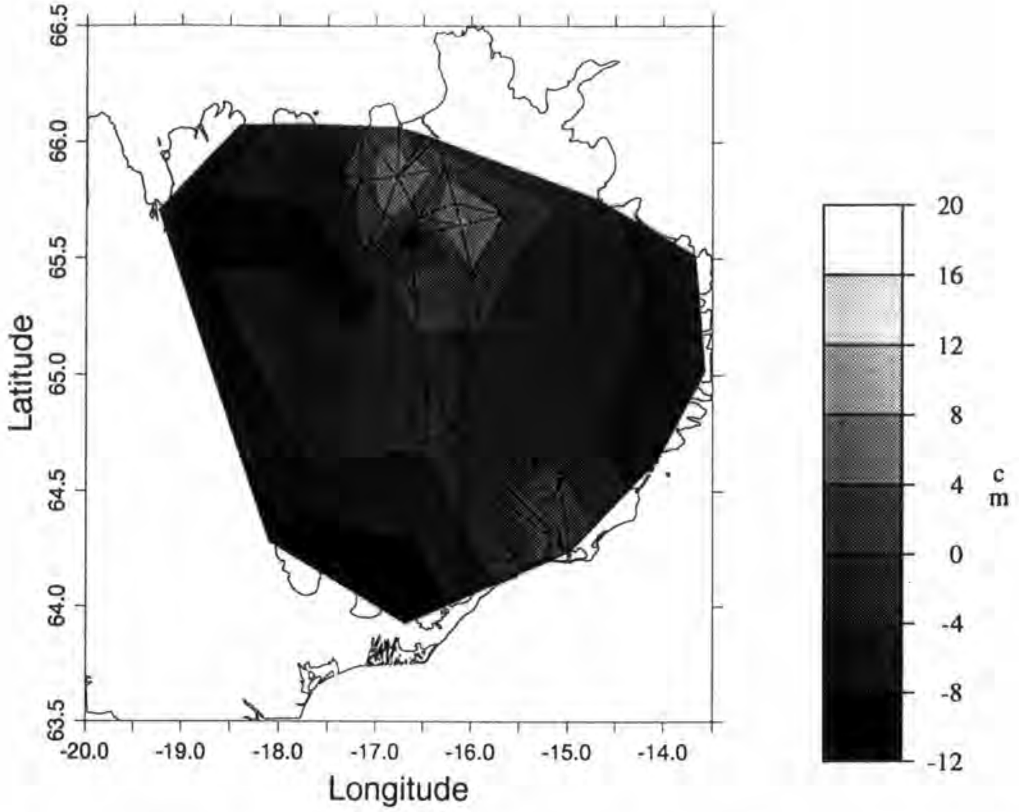

Figure 7.29: The residual vertical field for the epoch 1987–1992 after subtracting the best-fit simulated displacements from the observed.

further away (Figure 7.26). The 1986–1992 epoch exhibits some scatter and large error bars as a result of the poor quality 1986 data, but the displacements are well simulated in general.

Because of the larger errors in the vertical component of GPS surveying results, only the 1987–1992 epoch is modelled. Relative uplift of up to ~11 cm is predicted close to the rift axis for this epoch (Figure 7.27). The uplift decreases to zero at about 20–40 km from the dyke complex. At greater distances relative uplift occurs and is ~4 cm at distances of ~100 km from the dyke. Of the points in the profile zone, only four out of seventeen do not fit the model to within 3σ, and all of these are within ~20 km of the dyke axis.

The observed and predicted two-dimensional vertical fields are shown in Figure 7.28. The motion increases with distance from the rift. Relative uplift of up to ~4 cm is predicted for most of the network. χ^2_ν is 4.3, compared with a weighted variance of the data of 3.4.

The poor statistical fit, and the residual vertical field (Figure 7.29) shows that substantial unexplained vertical motions still remain, in particular in the far south

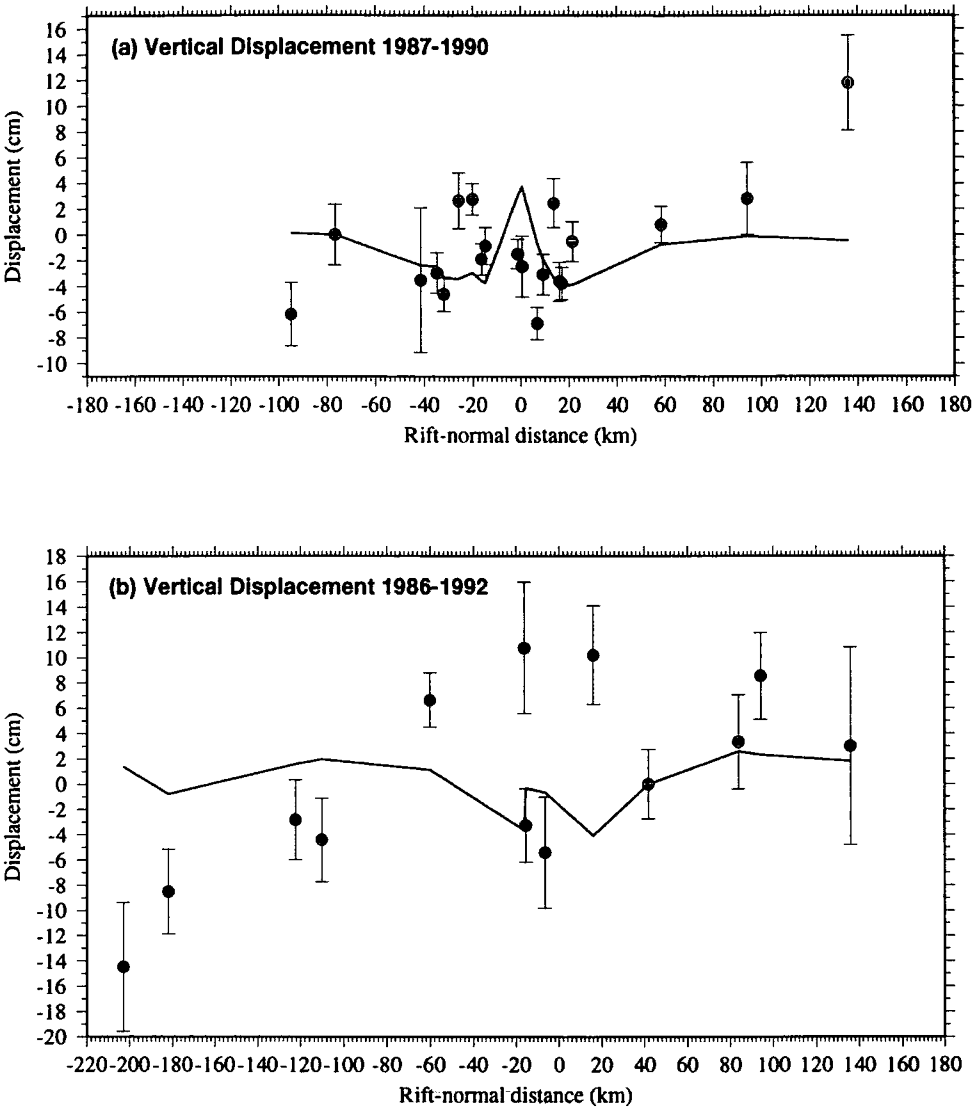

Figure 7.30: Same as Figure 7.27, except for (a) 1987–1990, and (b) 1986–1992.

of the network (up to 12 cm of subsidence), and in the vicinity of the dyke where uplift is underestimated by up to 8 cm. The fit is poorer to the east of the dyke than to the west.

Relative uplift of ~8 cm of the points within the profile zone is predicted 1987–1990, decreasing to ~4 cm further away (Figure 7.30a). Considerable scatter is present in the data from this epoch. However, all but four of the twenty points fit the model to within 3σ. Both χ^2_ν and the weighted variance are 5.9. The 1986–1992 data are poorer still, but again, most of the points fit to within 3σ (Figure 7.30b).

7.4.3.2 Localised Tilt in the Neighbourhood of the Krafla Volcano

Much of the ground tilt in the vicinity of the Krafla magma chamber following the end of the dyking episode can be explained by vertical movements following the Krafla rifting episode. In order to fit these local, tilt data the Krafla episode was modelled using six discrete dykes, injected over a five-year period, corresponding to the December 1975, October 1976, September 1977, January 1978, July 1978 and March 1980 events. These had dyke thicknesses of 2.5 m, 1.2 m, 1.5 m, 1.2 m, 2.4 m and 2.3 m, and lengths of 44 km, 23 km, 38 km, 34 km, 35 km and 34 km respectively [dimensions taken from *Tryggvason*, 1984]. The vertical motion was predicted for six, year-long intervals from 1986 to 1992 (Figure 7.31). A viscosity of 0.8 x 10^{18} Pa s was required to match the observed tilt data.

In the vicinity of the Krafla caldera, uplift is predicted relative to a point 30 km to the southeast throughout the six-year interval, the magnitude of which decreases with time. However, within ±5 km or so of the dyke axis, local subsidence is predicted 1989–1992, the rate of which increases with time.

This model was used to calculate tilt rates to the north and east from 1986 to 1992 at eighteen tilt-station locations (Figure 7.32a). Good agreement between observed and simulated tilt is found for many stations. For example, stations 0000 and 0260 (Figure 7.32b), 0240 (Figure 7.32c), 0070 and 0050 (Figure 7.32d) show good agreement between the predicted and observed east-tilt data. The north tilt component shows, in general, a larger signal. For the majority of these stations, it is clear that there is good agreement after late 1988/early 1989, but significant differences 1986–1988. Stations 0090 (Figure 7.32b), 0240, 0210 (Figure 7.32c) and 0070 (Figure 7.32d) are good examples.

These results suggest that stress redistribution following the Krafla rifting episode can account for the observed tilt data after late 1988/early 1989, but that prior to this time some other process was occurring, which caused tilt in the area. Inflation of the Krafla magma chamber is a likely candidate process [*Tryggvason*, 1994]. A slightly different physical model from that used for the regional deformation field was required, which may indicate local variations in Earth structure in the vicinity of the spreading axis and variations in the dyke shape.

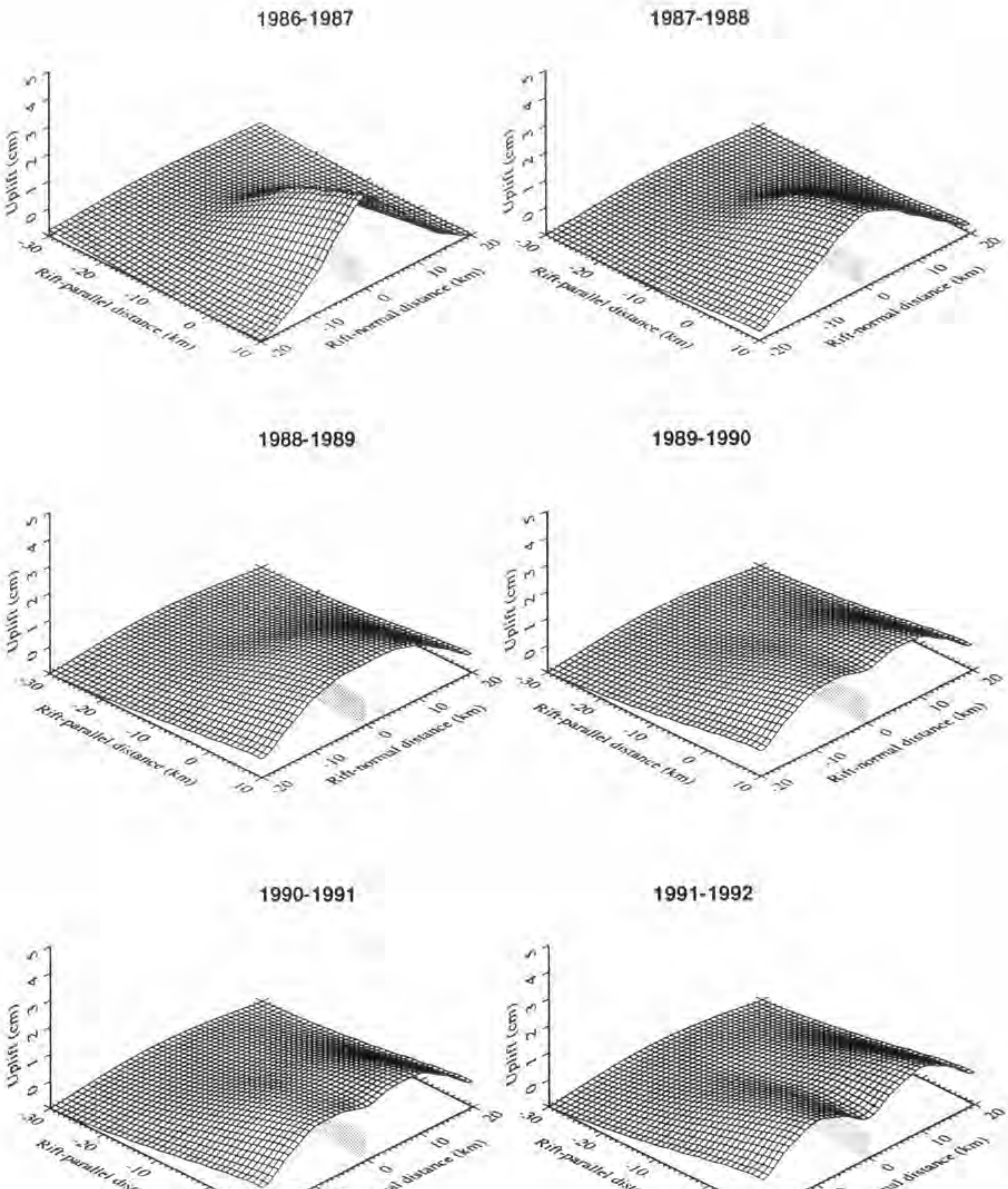

Figure 7.31: Predicted vertical motion within a 40 km^2 area around the southern end of the intruded Krafla dyke complex during six, year-long intervals from 1986 to 1992. The Krafla caldera is situated at $x = y = 0$. The position of the dyke complex is shown lightly shaded.

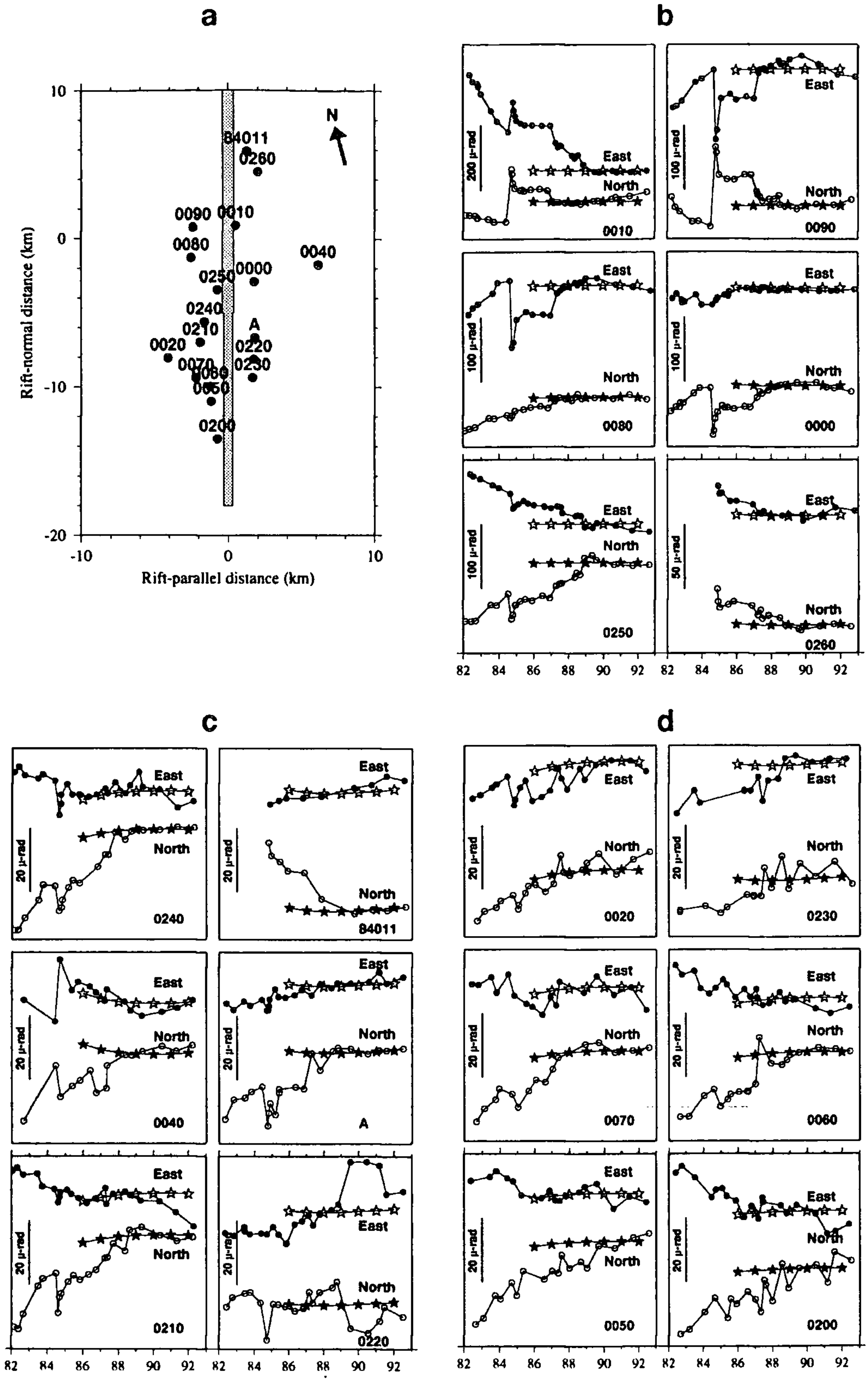

Figure 7.32: (a) Map of the Krafla area showing optical levelling tilt stations. The centre of the Krafla caldera is located at $x = y = 0$. Observed ground tilt 1982–1992 and simulated tilt from Figure 7.31 are shown at six optical levelling stations at distances of (b) less than 5 km, (c) 5–9 km, and (d) farther than 9 km from the centre of the caldera. The scale bar centre left gives the (variable) tilt scale. Increasing uplift is to the east (top curves) and north (bottom curves). The solid circles and open stars show the observed and simulated east tilt, and the open circles and solid stars show the observed and simulated north tilt. The observed tilt data and station locations are taken from *Tryggvason* [1994].

7.4.4 Modelling of the Residual Motion

7.4.4.1 Explanations for the Residual Motion

After accounting for all the major known tectonic events in north Iceland, significant residual motion remains in both the horizontal and the vertical deformation fields. The origins of the deformation are non-unique so it is not possible to determine from the data where the tectonic activity originates that causes these residual motions. In this section the possible effects of known, minor activity that may provide an explanation are explored. Ongoing isostatic uplift due to melting of Vatnajökull is predicted to cause significant vertical motion around that icecap [*Sigmundsson and Einarsson*, 1992]. Recent seismic and eruptive activity in Bardabunga and Grimsvötn, and hypothetical, minor dyke intrusions in the Kverkfjöll, Askja, or Öræfajökull–Snæfell (Figure 1.1) volcanic systems may contribute horizontal and vertical motion.

7.4.4.2 Isostatic Uplift due to Recent Melting of Vatnajökull

Sigmundsson and Einarsson [1992] modelled recent melting of the Vatnajökull icecap (Section 2.2) and calculated the isostatic uplift rate as a function of distance from the centre of the icecap for 1975. A variety of values of asthenosphere viscosity and lithosphere thickness were used (Figure 7.33). These calculations are used to estimate vertical motion for the points of the GPS network 1987–1992 (Figures 7.34 to 7.36).

Using a viscosity of 1 x 10^{18} Pa s, a maximum uplift of 18 cm is predicted for the points closest to the northern and southern edges of the icecap (Figure 7.34). Motions decrease with distance to reach zero at about 50 km from the perimeter of Vatnajökull. The majority of points in the network are unaffected by isostatic uplift according to this model. Horizontal motions as a result of glacial rebound are very small [*F. Sigmundsson*, pers. comm, 1995]. Predicted vertical displacement fields using viscosities of 1 x 10^{19} Pa s and 1 x 10^{20} Pa s are similar in shape but attenuated in amplitude (Figures 7.35 and 7.36).

A comparison of Figures 7.29 and 7.34 clearly shows that the isostatic uplift model of Vatnajökull bears little resemblance to the residual vertical field. Only the

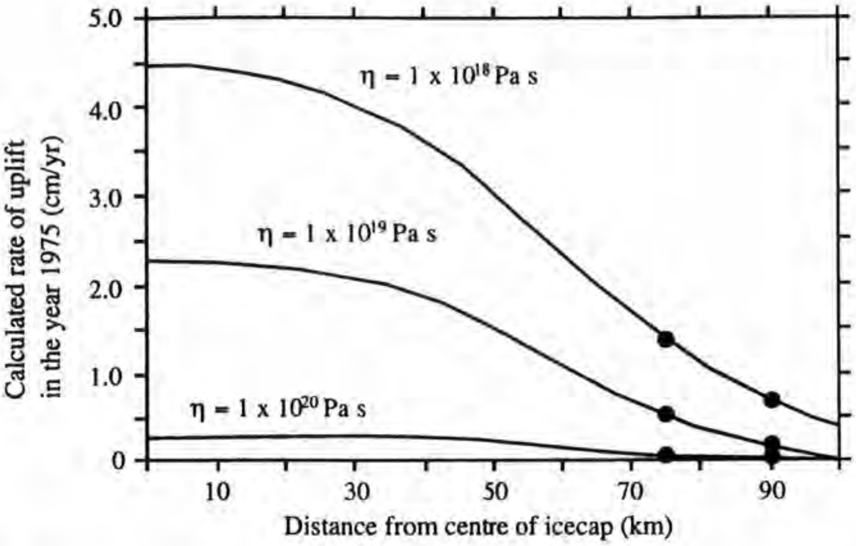

Figure 7.33: Calculated uplift rates for the year 1975 for three upper-mantle viscosities assuming a spherical icecap that experiences 11.4 cm/yr of thinning within the innermost 35 km of the icecap, 23 cm/yr 35–47.5 km, and 57 cm/yr 47.5–52.5 km. The Earth was modelled as a Newtonian viscous fluid halfspace overlain by an elastic layer [*Sigmundsson and Einarsson*, 1992]. The elastic plate was assumed to be 10 km thick. The black dots indicate the predicted uplift rates at the northern and southern ends of lake Langisjór, as determined by the Vatnajökull 1991 survey (Section 4.3.2), adapted from *Sigmundsson and Einarsson* [1992].

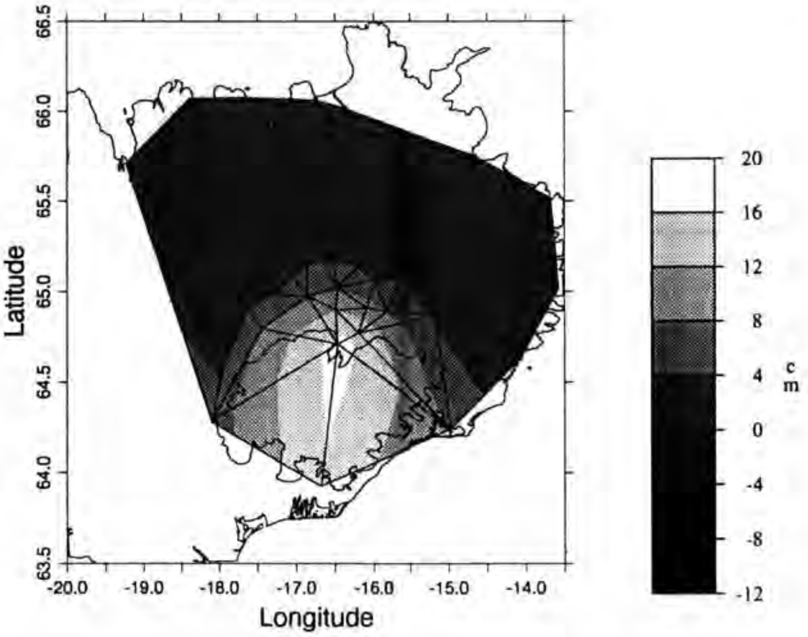

Figure 7.34: Vertical displacements 1987–1992 of points of the GPS network as a result of isostatic adjustments in south Iceland following the removal of iceload during this century. Points more than 90 km from the centre of the assumed spherical icecap undergo no significant motion. The motion of points less than 90 km from the centre are estimated using Figure 7.33 for a viscosity of 1 x 10^{18} Pa s. The icecap centre is at N64.40°, W16.68° [*Sigmundsson and Einarsson*, 1992]. As pointed out for Figure 7.4, linear interpolation between the points is used, so the shape of the contour lines is not meaningful between single pairs of points.

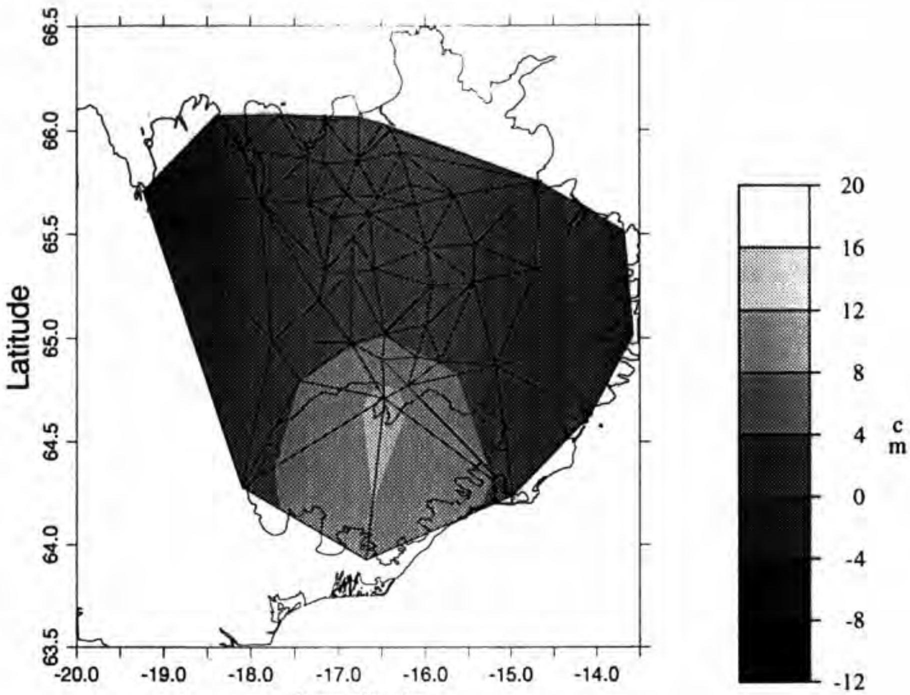

Figure 7.35: Same as Figure 7.34, except a viscosity of 1 x 10^{19} Pa s was used.

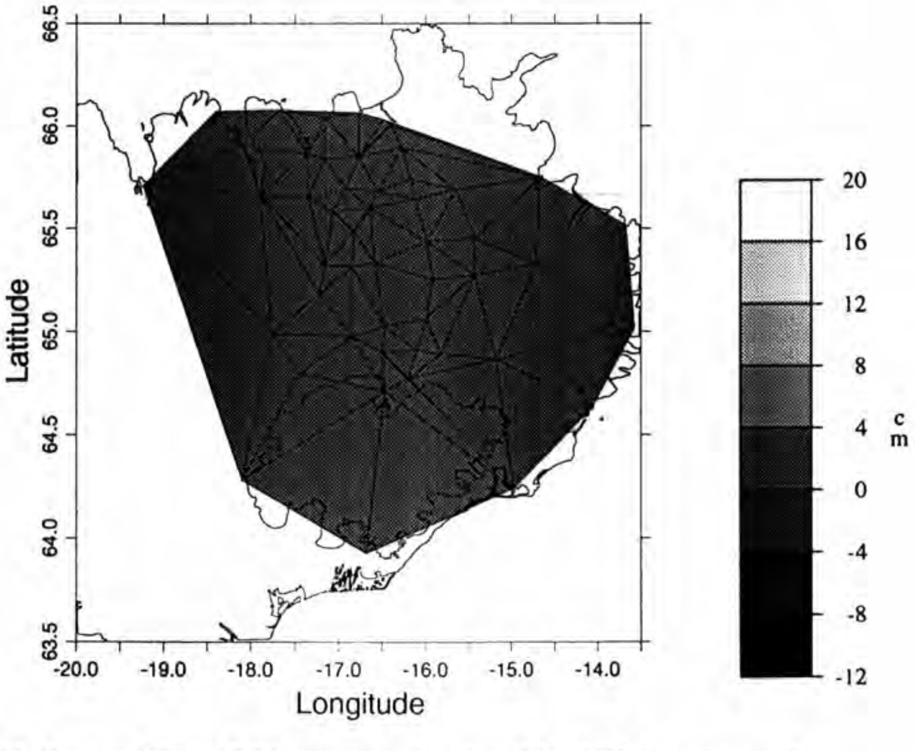

Figure 7.36: Same as Figure 7.34, except a viscosity of 1 x 10^{20} Pa s was used.

residual motion at point Hofn (Figure 4.3) on the southeastern edge of Vatnajökull shows uplift of the magnitude predicted by this model relative to, say, intraplate points distal to the west and east. The residual field (Figure 7.29) shows a large relative subsidence of points to the south and west of the icecap, i.e., an apparent tilt of the icecap up to the northeast, broadly consistent with the predicted effects of isostatic uplift. However, the general pattern of motion is not modelled by any of the viscosity choices used in Figures 7.34 to 7.36.

7.4.4.3 Tectonic Activity in Bardabunga, Grimsvötn, Askja, Kverkfjöll and the Öræfajökull–Snæfell Flank Zone

Although seismic activity in northwestern Vatnajökull was high 1974–1980, the earthquake magnitudes were all less than ~6 (Section 2.5). Modelling of earthquakes with similar magnitudes in the TFZ (Section 7.4.2.5) shows that such events have very little effect on the deformation field, and therefore cannot provide an explanation for the large residual horizontal field to the south and southeast of Vatnajökull (Figure 7.25).

No direct evidence of dyke intrusion accompanying the 1983 eruption of the Grimsvötn volcano (Section 2.5) is reported. However, on the basis of the spatial distribution of earthquakes preceding the eruption, the intrusion of a small dyke may have accompanied this seismo-volcanic activity. A 10 km-long, 1 m-thick dyke, centred at N64.41°, W16.32° along azimuth N62°E is modelled here (Figure 7.37). Other model parameters used are identical to those given in Table 7.2. Such an intrusion can explain a maximum of 1.5 cm of the horizontal residual field 1987–1992, at point I58. The azimuths of the displacement vectors are broadly consistent with those of the residual field. However, the amplitudes of the residual motions are poorly modelled.

The earthquake swarms that occurred close to the Askja volcanic system in 1982 and 1983 [*Einarsson*, 1991] (Section 2.5) may have accompanied the injection of a small dyke. An intrusion 1 m-thick, 36 km-long and extending from 0.1 km to 10 km depth is modelled. Such an intrusion predicts motion of about 5 cm at points I58, I59 and I60 (Figure 7.38), and up to 2 cm at I57 and I61, closely resembling the residual field (Figure 7.29c). However, large motions are predicted close to the northern edge of the icecap which do not appear in the residual field.

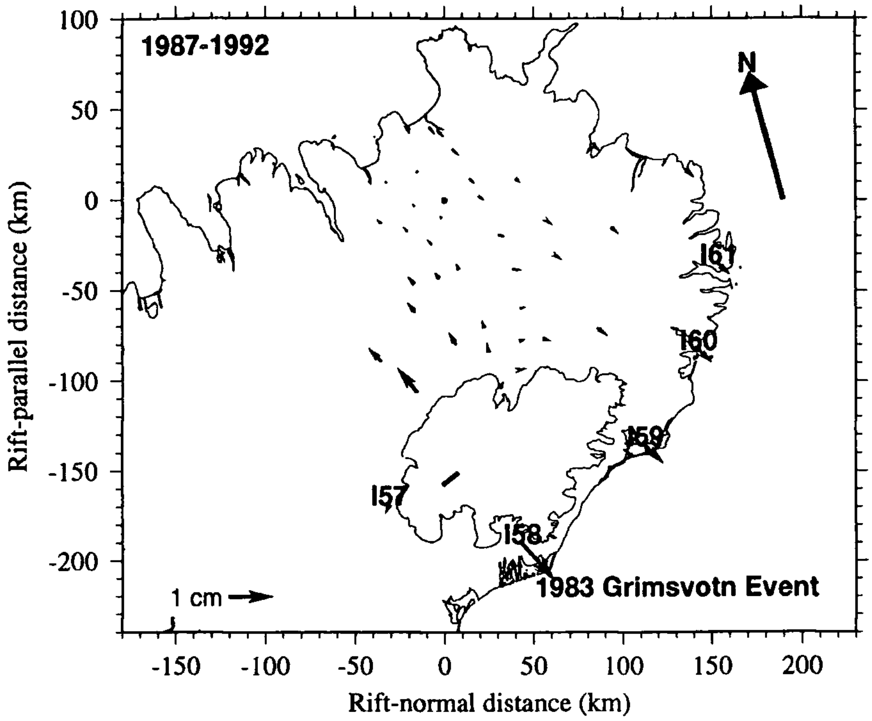

Figure 7.37: Horizontal displacement field 1987–1992 from a hypothetical dyke accompanying the 1983 Grimsvötn eruption. Motion is shown relative to point 128 to enable direct comparison with Figure 7.25c. Black bar indicates the modelled dyke.

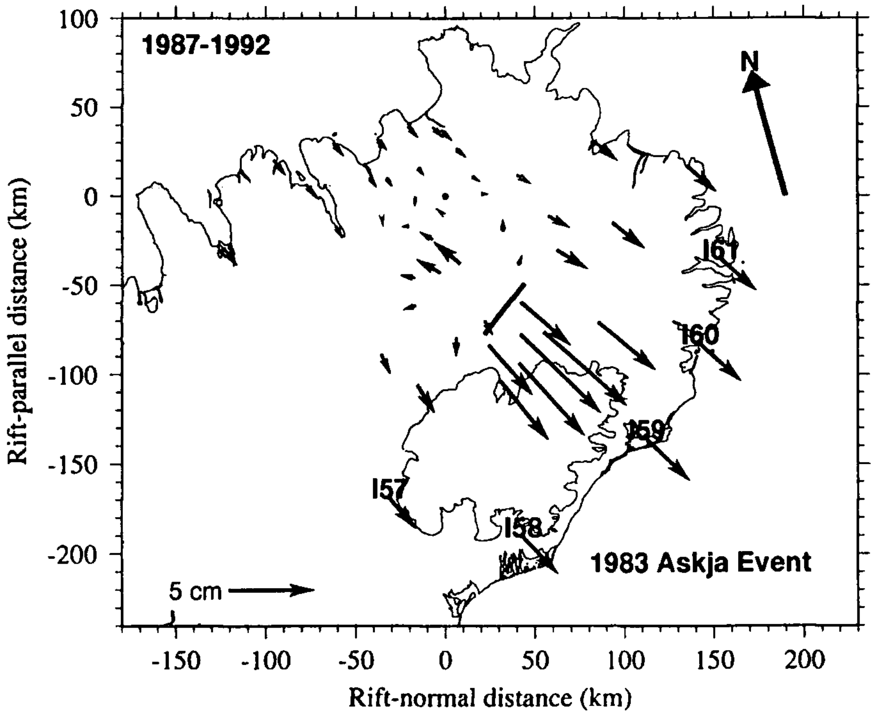

Figure 7.38: Same as Figure 7.37, except for a hypothetical dyke accompanying the 1983 earthquake swarm close to the Askja volcanic system.

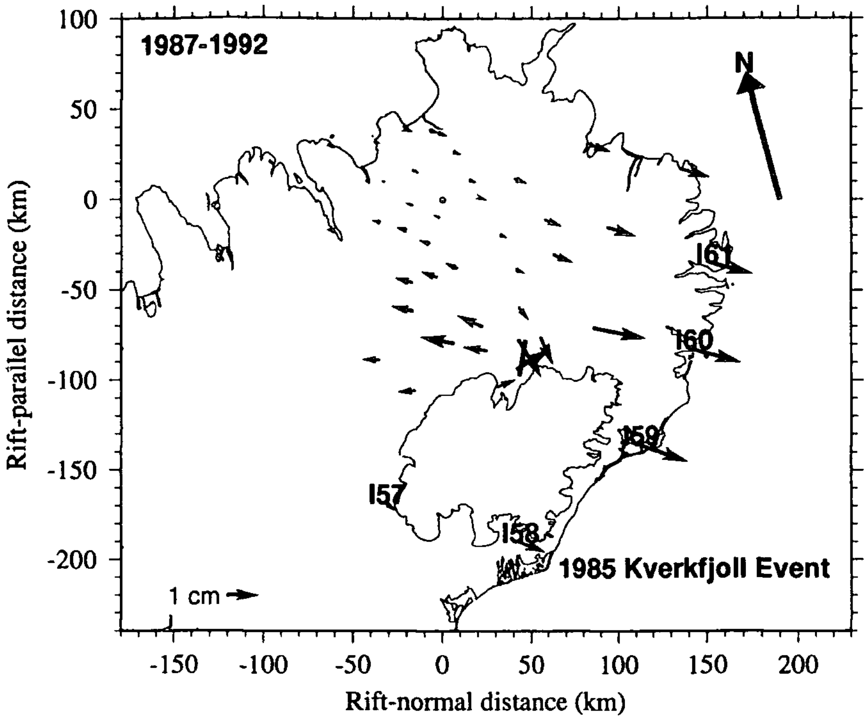

Figure 7.39: Same as Figure 7.37, except for a speculative intrusion in the Kverkfjöll system in 1985.

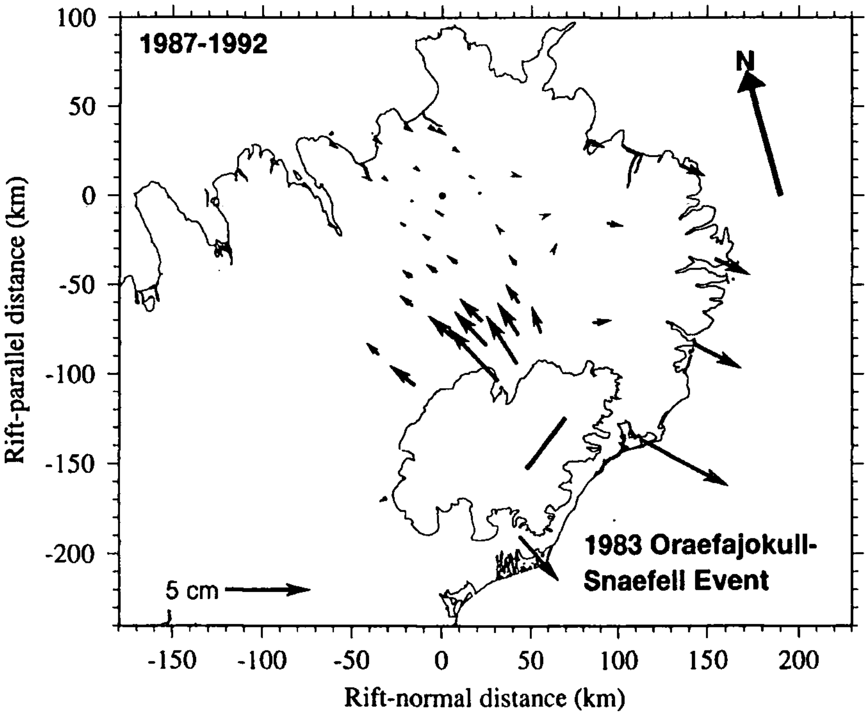

Figure 7.40: Same as Figure 7.37, except for a speculative intrusion in the Öræfajökull–Snæfell flank zone in 1983.

Although there is no supporting observational evidence, a speculative intrusion 20 km-long and 1 m-thick in the Kverkfjöll system is modelled. The dyke is assumed to be centred at N64.85°, W16.29°, to strike along azimuth N30°E, and to have been intruded in 1985. The predicted motions do not model the residual field well (Figure 7.39) in amplitude, and the direction of motion predicted to the south and southeast of Vatnajökull is substantially different from that of the observed residuals.

A speculative intrusion 36 km-long and 2 m-thick in the Öræfajökull–Snæfell flank zone is also modelled, extending from 2 to 10 km depth. The dyke is assumed to be centred at N64.38°, W16.29°, to strike along azimuth N53°E, and to have been intruded in 1984. The predicted displacements model the residual field well to the south of the icecap (Figure 7.40), both in amplitude and direction. However, significant displacements are predicted close to the northern edge of the icecap which are not present in the residual field (Figure 7.25).

7.5 Summary

For a model of continuous dyking at depth in an elastic halfspace, a range of dykes will fit the 1987–1992 deformation field, for example, a tall, thin dyke. Further improvement is doubtless possible if the model is made more complicated, e.g., by combining several dykes, though this work is not pursued in this project.

Motion 1987–1990 and 1990–1992 is simulated well using an elastic-viscous, stress-diffusion model. However, the 1987–1992 epoch, with its improved signal:noise ratio, highlights that a more realistic geophysical model is required, in particular to explain the displacements of the more distant points. A good fit to the data is possible if previous events in the NVZ are taken into account, but unrealistically large dyke thicknesses are required for the preceding episode.

For modelling using the elastic-viscoelastic approach, certain of the parameters were assumed known where good constraints on their values were available from other geophysical results. Dyke thicknesses for historic spreading episodes in the NVZ were chosen assuming that the average widening at all points along the rift is 2 cm/yr. The 1618 Theistareykir, 1724–1729 Mývatn fires and 1874 Askja episodes were modelled, along with recent large events in the TFZ and activity in the Askja magma chamber. A complicated deformation field was revealed. The effect of these events was subtracted from the observed displacement fields and the remaining motion modelled using viscoelastic relaxation following the recent Krafla rifting episode. A best-fit model, selected from a large suite of forward models, uses a viscosity of 1.1 x 10^{18} Pa s. The only significant, horizontal unmodelled motion occurred in the vicinity of the dyke and in the far south of the network 1987–1992. The vertical deformation field is noisier because of the larger errors in the data, and more poorly modelled. This model also explains the localised tilt observations 1989–1992 in the vicinity of the Krafla caldera. However, prior to this time, the tilt cannot be fully explained by this process and some other process was probably occurring, e.g., inflation of the Krafla magma chamber. The residual vertical motion provides no clear supporting evidence for isostatic uplift due to recent melting of Vatnajökull. Recent, tectonic activity in other volcanic systems is a possible explanation for the residual motion, and activity in the Öræfajökull–Snæfell flank zone appears to model the data best.

Chapter 8

Discussion and Conclusions

8.1 The GPS Results

The 1991 GPS data were collected during a period of severe ionospheric disturbance, which resulted in problems in the data analysis. The average repeatability of the survey was ~1 cm in the horizontal and ~3 cm in the vertical. Typical scaled formal errors of ~0.5 cm were obtained in the horizontal and ~1 cm in the vertical. The repeatabilities and scaled formal errors are up to four times larger than those obtained from GPS surveys in southern California [*Larson and Agnew*, 1991]. This is probably a result of the larger ionospheric variations and the poorer satellite configuration in the Iceland region compared to California. The north-south repeatability was comparable to, and the east-west better than, that of the Iceland 1987 survey, probably as a result of the improving satellite constellation and the shorter lines measured in 1991. The scaled formal errors of the 1991 solution indicate that the results were more accurate than earlier surveys in Iceland.

The average repeatability of the 1992 survey was ~1.5 cm in the horizontal and ~4 cm in the vertical. Typical scaled formal errors of ~1 cm were obtained in the horizontal and ~2 cm in the vertical. The north-south repeatability of the 1992 survey was comparable to that of the 1987 survey, whilst the east-west repeatability was better. The repeatability of all three components of the 1992 survey were better than those from 1990. The 1992 scaled formal errors were comparable to those of the 1987 survey, but smaller than those from 1990. Thus, the 1992 results are of a comparable quality to the 1987 results, and of a higher quality than those from 1990. The accuracy of the 1992 results should be typical of the accuracy of similar, future GPS surveys in north Iceland since the full satellite constellation is now in operation, and sunspot activity is declining.

The GEONAP and Bernese 1992 solutions agree well. Poorer agreement is obtained between the vertical components, and may be due to the different processing approaches, for example, to the use of different tropospheric models. The agreement is better for the 1992 results than that for the 1987 results, and considerably better than those for 1990, indicating again that the 1992 results are of a comparable quality to the 1987 results, and of a higher quality than those from 1990. The good agreement between the results from different software packages also lends confidence that the GPS deformation results reflect the true crustal movements, and are not just errors. Such multiple measurements are important in this kind of crustal deformation work, where the ratio of the deformation signal to the noise is relatively low compared with other geophysical measurements, e.g., seismic recordings.

8.2 Modelling of the Deformation Field in North and East Iceland

8.2.1 The Continuous Dyking Model

A reasonable fit to the 1987–1992 data was achieved using the simple model of an 80 km-long, 1000 km-high dyke with an opening of 35 cm. Indeed, the value of χ^2_ν indicates that the fit to the data was almost as good as that of the best-fit viscoelastic model. A statistically perfect fit using the continuous dyking model would certainly be possible if a complex of dykes of various dimensions, times and rates of intrusion were used and probably a large suite of possible combinations would be allowable.

Proponents of the continuous-dyking model envisage a process as follows. At a spreading plate boundary, a large dyke intrusion at shallow depth will produce increased extensional stress levels at its base, encouraging the upward leakage of magma, and resulting in continued, postevent dyking and surface deformation in the same sense as the coevent deformation. The strike-slip and normal fault counterparts of this model have been widely applied to modelling regional motion around the San Andreas and other fault zones [e.g., *Williams*, 1995], and to modelling accelerated, postseismic deformation. At divergent plate boundaries this is to a large extent an *ad hoc* approach, that is not based on independent, supporting data, and has limited ability to contribute to our understanding of the Earth, or our predictive capabilities. The Earth at depth is known from isostatic uplift to flow over long time periods, and the very high temperature gradients in Iceland suggest that low viscosity material occurs at relatively shallow depth. This argues against halfspace models, and in favour of models involving viscous flow. It is possible, however, that, depending on the structure and tectonic setting, these two processes may both occur, either separately or simultaneously.

8.2.2 The Stress Diffusion Model

The best-fit values for the 1987–1990 one-dimensional analysis of the Bernese GPS results closely agree with those obtained by *Foulger et al.* [1992] using GEONAP results. These analyses yield a best-fit diffusivity of 1–2 m^2/s and a half-dyke thickness of 1–1.5 m. Two-dimensional analysis of the Bernese results however, suggested a diffusivity an order of magnitude larger [*Heki et al.*, 1993]. The stress diffusion model can explain most of the motion for the 1987–1990 and 1990–1992 epochs. However, a significantly poorer-fit to the 1987–1992 results, the best-constrained epoch, revealed the basic shortcomings of the model and showed that a more realistic, geophysical model was required.

Analysis of the 1987–1990 results yielded viscosity estimates for the material below the elastic layer of 0.3–2.0 x 10^{18} Pa s (one-dimensional model) and 0.3–2.0 x 10^{19} Pa s (two-dimensional model) [*Foulger et al.*, 1992; *Heki et al.*, 1993]. These estimates were in broad agreement with the viscosity estimates of *Sigmundsson* [1991] and *Sigmundsson and Einarsson* [1992] of 1 x 10^{18}–5 x 10^{19} Pa s from glacio-isostatic uplift rates (Section 2.2). The better-defined displacement field provided by the addition of the 1992 GPS results does not allow improvement of the viscosity estimate as the model is clearly inadequate.

The stress diffusion model is highly idealised and contains many simplifying assumptions, the most important of which is Newtonian behaviour of the viscous layer. This prevents any elastic response at the time of dyking, and results in the overestimation of motion at later times [*Heki et al.*, 1993]. However, this simplistic model was adequate for the early observations, contributed greatly to our understanding of the underlying processes and pointed the way to the more advanced work using the viscoelastic model that is described in this thesis.

8.2.3 The Viscoelastic Model

8.2.3.1 The Effect of Early Events

In order to enhance modelling of the recent Krafla rifting episode, the effects of historical and current events in the NVZ and TFZ were first calculated and subtracted from the observed displacement field. These calculations are subject to considerable uncertainty because of the paucity of constraints of the event magnitudes. In addition, the effects of these early events are small in comparison with the effect of the recent Krafla episode. For this reason it was of peripheral value to correct for these processes prior to modelling the Krafla episode, and indeed it could be argued that making such small and uncertain corrections is merely increasing the noise in the deformation field. However, the influence is small and studying these effects is very illustrative of the style and timescale of deformation following typical large events in Iceland.

Tectonic events in other parts of Iceland were not accounted for, e.g., earthquakes in the SISZ where magnitude 7 sequences occur at intervals of 45–112 years, rifting episodes in the EVZ and WVZ, and the effects of several recent, volcanic eruptions, e.g., that of Hekla in 1991. However, comparable events in the TFZ and NVZ are causing such small displacements within the GPS network at the present time that the effects of events more distant in space or time or smaller in size are insignificant to the present analysis.

8.2.3.2 The Krafla Dyking Episode

8.2.3.2.1 Constraints on Rock Properties

The layer densities were estimated from seismic velocities and a standard velocity-density relationship for Iceland [*Christensen and Wilkins*, 1982]. The variations in seismic velocity, and uncertainty in the velocity-density relationship indicate that density variations and uncertainties of ~10% in both the layer and halfspace are expected. Previous results using a dip-slip source indicate that varying the layer and halfspace densities by 10–20% produces little difference in the predicted displacement fields [*Rundle*, 1981]. From this it is concluded that the density variations expected in Iceland will have little effect on the modelling results.

Observed variations of V_p and the V_p/V_s ratio with depth indicate variations and uncertainties in the average elastic moduli of ~25%. Variations in μ_h are most likely to affect the modelling results since it is this parameter that is varied with k in the introduction of time dependence into the problem (Section 6.4.6). μ_h is expected to vary in the range 3.2–4.6 x 10^{10} Pa. Example calculations have shown that a variation of μ_h by a factor of 10 produces a change of ~50% in the amplitude of the displacement field (compare Figures 2 and 3, *Hofton et al.* [1995]). The expected variations in μ_h of ~22% in Iceland will thus not significantly affect the results of the present analysis.

8.2.3.2.2 Constraints on Structure and the Dimensions of the Krafla Dyke Complex

Elastic Layer Thickness, H, Downdip Width, W, and W/H

Inversion for parameters is not possible as the software is only set up for forward modelling. The sensitivity of the data to the input parameters can thus only be explored by studying suites of forward models. In order to illustrate clearly the effects of varying parameters, the fit to the points within the profile zone shown in Figure 7.1 to various models is considered.

The elastic layer thickness is constrained in the range ~8–12 km, if magnetotelluric evidence for a low resistivity layer at ~10 km depths, and seismological evidence on the depth extent of earthquakes is taken to indicate the thickness of the elastic layer in north Iceland.

Estimates of the height of injected dykes based on the amount of surface widening and volume of injected lava that flowed out of the Krafla magma chamber are ~2 km [*Björnsson*, 1985]. However, lava of differing chemical composition erupted northerly in the fissure swarm, and estimates of ~8.5 km for the dyke heights from geodetic data modelling [*Rubin*, 1992] are strong evidence that the dykes

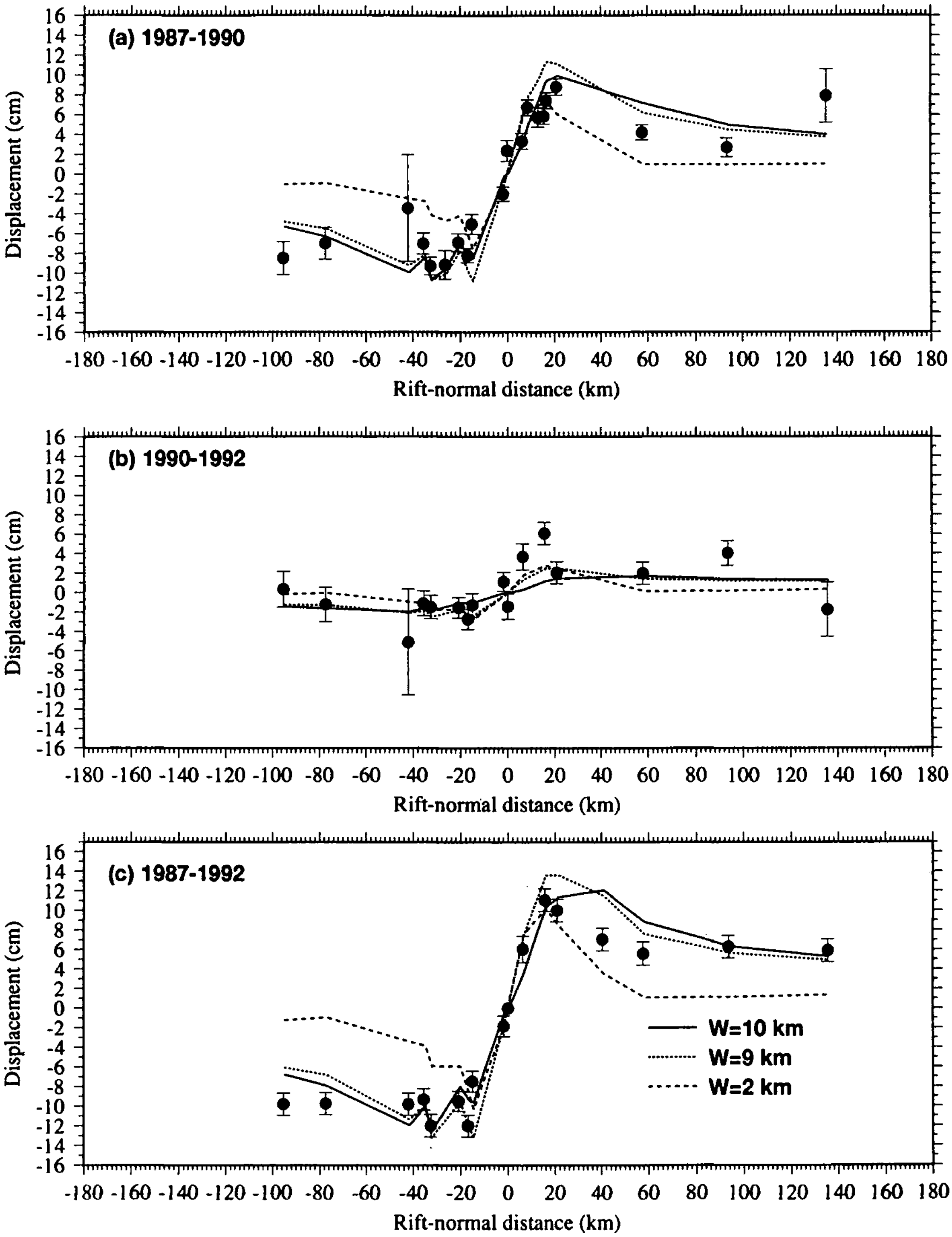

Figure 8.1: Comparison of observed and simulated horizontal displacements (a) 1987–1990, (b) 1990–1992, and (c) 1987–1992 of points within the profile zone shown in Figure 7.1 for dykes extending completely (W = 10 km) (solid curves) and partially (W = 9 km, W = 2 km) (short-dashed curves) through the elastic layer. All other model parameters are identical to those given in Table 7.2. The effect of the processes dealt with in Sections 7.4.2.2–7.4.2.6 have been subtracted from the observed displacements. 1σ error bars are shown.

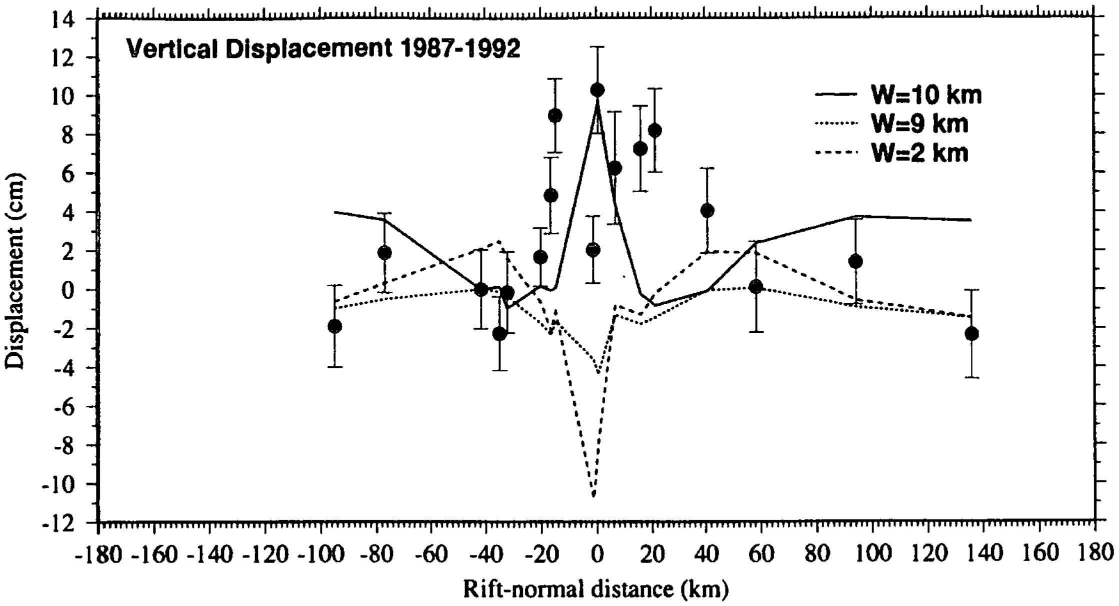

Figure 8.2: Same as Figure 8.1, except for the 1987–1992 vertical deformation field.

may have ruptured the entire elastic layer with the extra material required being injected from greater depths [*Björnsson*, 1985]. Evidence for large dyke heights is available for only some intrusion events however, which may indicate that only some events ruptured the entire elastic layer. Very short dykes can simulate well the displacements within ~20 km of the rift, but the more distant points are poorly simulated, with motion underestimated by many centimetres for the 1987–1992 epoch (Figure 8.1). Vertical subsidence is predicted in the vicinity of the dyke in the cases of dykes that do not rupture the entire elastic layer (Figure 8.2). These factors, in particular the vertical observations, are strong evidence that the dyke complex ruptured to the bottom of the elastic layer.

Within the range 8–12 km, the best-fit value for the elastic layer thickness was found to lie in the range 10–12 km (Figure 8.3). Decreasing the elastic layer thickness increases the amplitude of the displacements of the near-dyke points relative to the more distant points (Figure 8.4). However, the shape of the predicted deformation profile is fairly insensitive to variations in H of a few kilometres.

In the case of the vertical field, as H increases, the amplitude of subsidence on either side of the dyke decreases, and larger values of H produce a better fit to the observations (Figures 8.3 and 8.5). For the cases studied here, a value of H of 30 km fit the vertical field best. The results from modelling the horizontal and vertical deformation fields are thus very different.

A likely explanation for some of the difference between the predictions of the horizontal and vertical fields is that the vertical field is significantly affected by move-

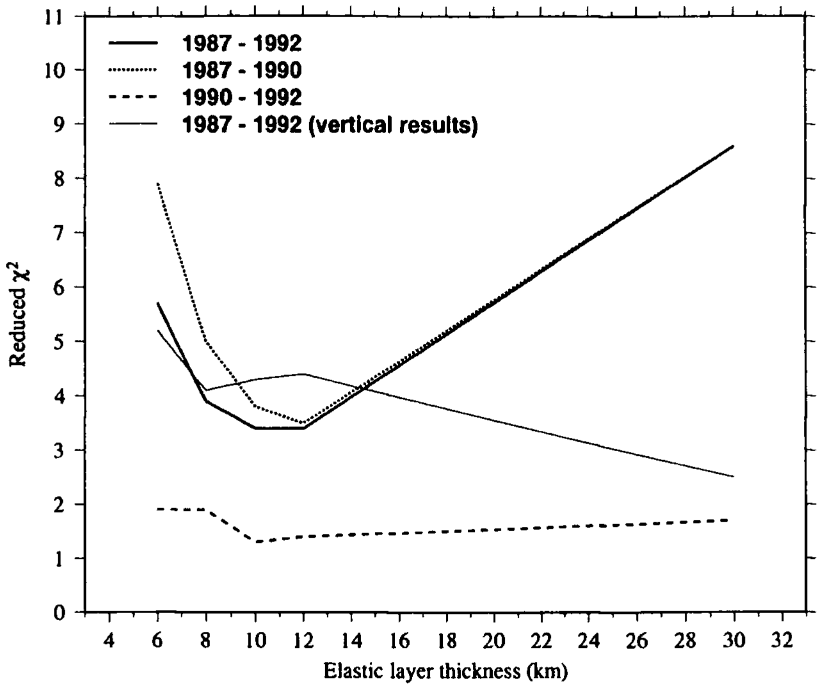

Figure 8.3: Variation of reduced χ^2 (equation 7.1) with elastic layer thickness for the epochs 1987–1992, 1987–1990 and 1990–1992. The thin, solid curve shows the variation of χ^2_ν in the vertical for 1987–1992.

ments on high-angle normal faults. *Rubin* [1992] modelled geodetic data from the Krafla rifting episode and found that a single vertical dyke and two normal faults dipping towards the dyke at 70° best matched the observed data. However, the suggested faults significantly affected displacements only within ~4 km of the dyke, and were able to explain only 80% of the observed vertical displacements [*Rubin*, 1992]. Fault constitutive behaviour and geometry were deemed unlikely to explain the remaining, unmodelled motion, and led *Rubin* [1992] to question the model assumptions of elasticity, homogeneity and isotropy. Modelling the postseismic transients from fault movements may be able to explain the residuals found here in the vicinity of the dyke axis.

The fit to the east of the dyke is poorer than that to the west, and there is asymmetry in both the horizontal and vertical deformation fields. This could result from an asymmetric Earth structure about the rift zone in north Iceland, with a thicker elastic layer to the east of the rift. Such asymmetry is to be expected as a result of the successive eastwards ridge jumps in north Iceland over the past 7 Ma (Section 1.4.3). However, it is fair to say that the dyke model that fits the horizontal field best provides only a broad, qualitative fit to the vertical field, and that investigating the reasons for this is an important area of future research.

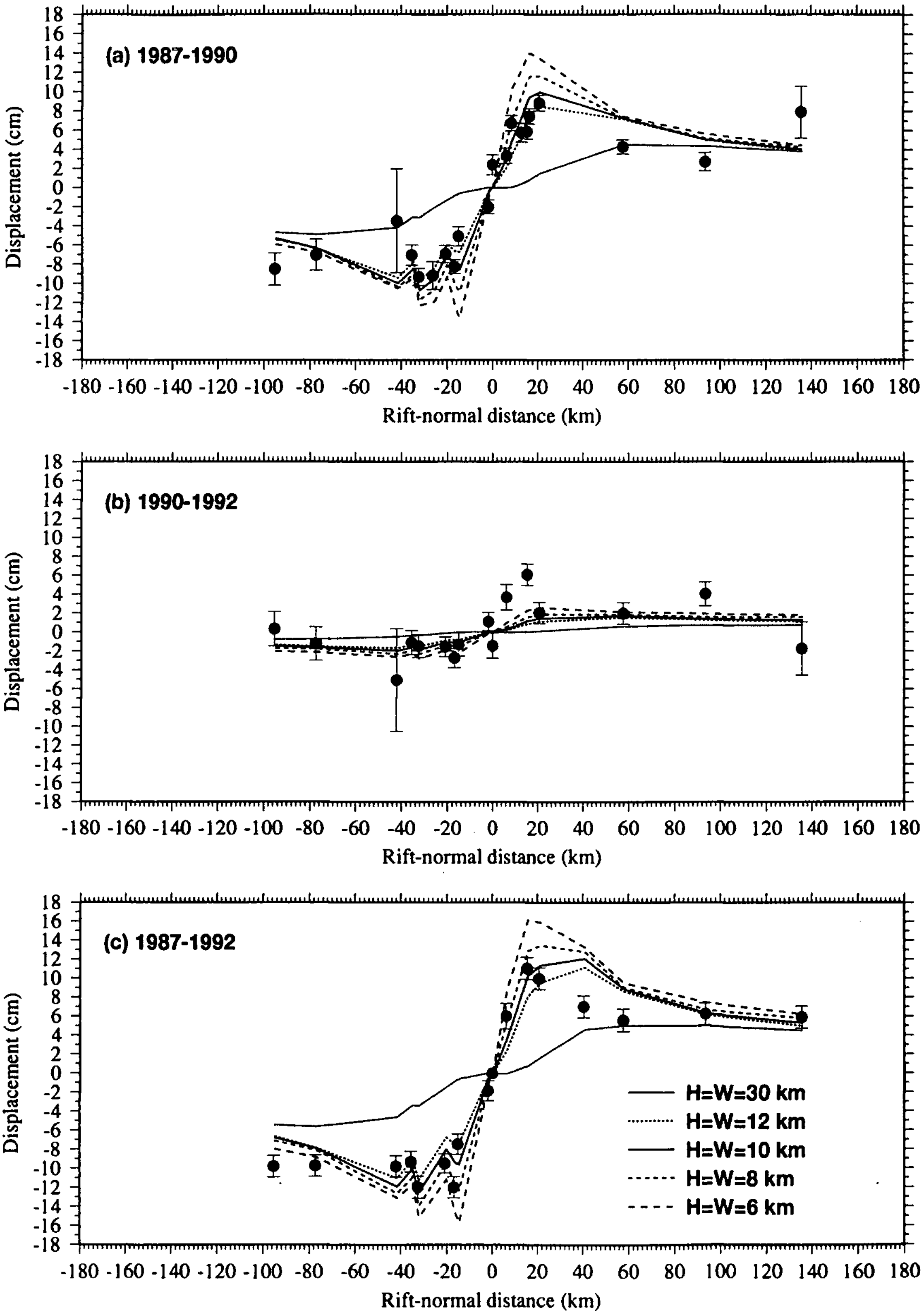

Figure 8.4: Same as Figure 8.1, except the effect of varying the elastic layer thickness (H) is shown. Values of H of 6, 8, 10, 12 and 30 km were used. The dyke complex is assumed to rupture the entire elastic layer.

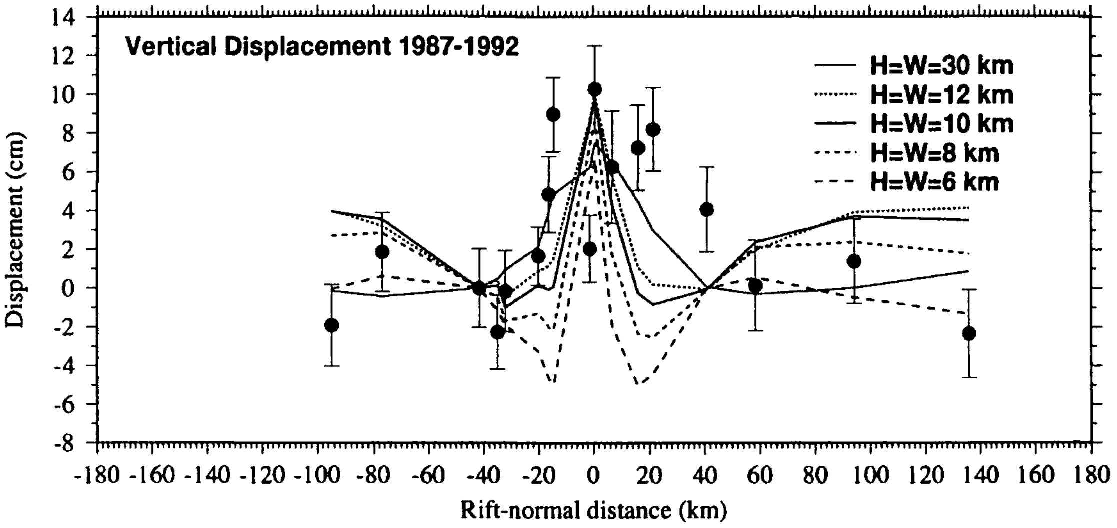

Figure 8.5: Same as Figure 8.4, except for the 1987–1992 vertical deformation field.

Depth, D, to the Top of the Dyke

Prior to 1980, deflation of the Krafla magma chamber was accompanied by injection of magma into the fissure swarm to form dykes, and very little lava was erupted onto the surface. Inverse modelling of geodetic data collected 1975–1980 encompassing ~14 dyke emplacement events indicated depths to the dyke top in the range 1.25–1.5 km [*Rubin*, 1992]. Although surface fissuring accompanied all the events, this evidence suggests that the dykes may not all have extended to the surface.

Compared with a dyke that reaches the surface, one that terminates at a depth of 1 km has little effect on the predicted displacements further than 50 km from the rift (Figure 8.6). Within ~5 km of the rift, however, contraction of the network is predicted for all epochs. At intermediate distances expansion is predicted, but with a significantly smaller amplitude than that observed, and less than that predicted for a dyke that reaches the surface. The predictions for the 1990–1992 epoch are particularly poor.

The data thus favour a dyke complex that extends to the surface. This conclusion is supported by the fact that after 1980 surface lava flows accompanied most of the dyke injections and smaller amounts of rift-widening were observed than in the earlier events [*Tryggvason*, 1984]. An explanation for the results of *Rubin* [1992] may be that some early, individual member dykes of the complex may not have reached the surface, but that later dykes took up proportionally more motion at the surface.

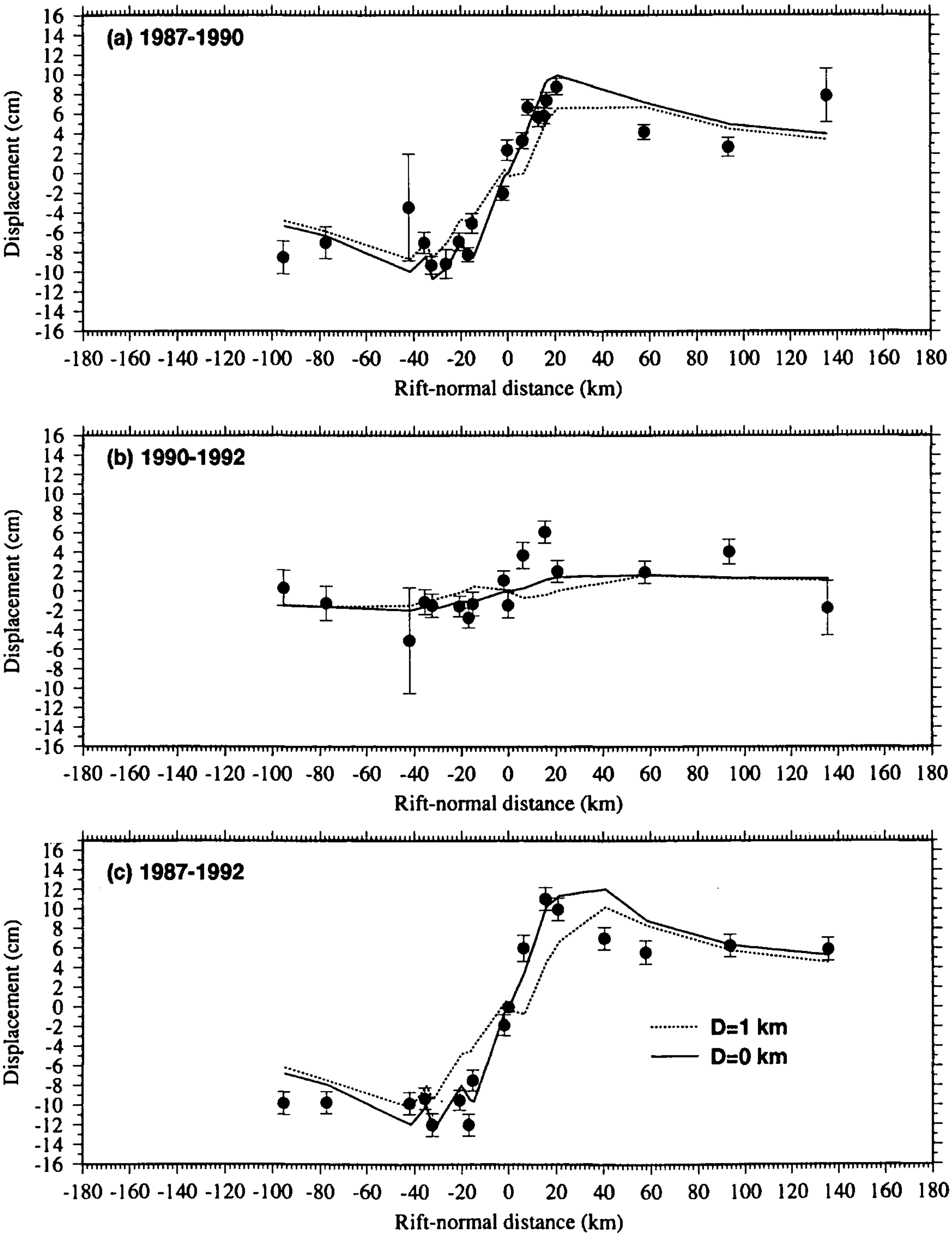

Figure 8.6: Same as Figure 8.1 for $H = 10$ km, except for a dyke with its top at 1 km depth and a downdip width of 9 km (dashed curves). The solid curves indicate the predicted displacements for the same dyke extending to the surface.

Dyke Length, AL

A total length of 82 km was assumed for the Krafla dyke complex, consistent with the best estimates for the length of the activated fissure swarm of 80–90 km, as indicated by seismicity and opening of new ground fissures [*Tryggvason*, 1984]. Example calculations show that decreasing AL by 50% decreases the displacement amplitudes by about a third (Figure 6.9). The error arising from an uncertainty of about 10% is thus relatively small, but would have most effect on the form of the deformation field near the ends of the dykes.

Dyke Dip, ψ

A vertical dyke was assumed in this analysis. However, dyke dips are observed in the field to vary by ~5° [*Gudmundsson*, 1984] and the possible effect of such a dip on the Krafla dyke complex was explored. Extreme end-member cases of dykes dipping at 80° to the east and 80° to the west (–80°) are shown in Figure 8.7. The dominant effect of altering the dyke dip by such a small amount is to shift the predicted displacement profile up or down. No improvement in the fit is obtained over a vertical dyke, and the asymmetry in the observed displacement field cannot be explained by this means.

Dyke Thickness, U

The best set of dyke-thickness estimates for the Krafla spreading episode were presented by *Tryggvason* [1984] (Figure 2.8). These were based on observations of widening between benchmarks on either side of the fissure zone, crudely corrected for contraction of the flanks by assuming an average contraction of 200 mm/km between the fissures, perpendicular to the strike of the fissure swarm. Because of this latter approach, the estimates of *Tryggvason* [1984] may be considered to be upper-bound thicknesses.

Distance measurements from prior to the start of the dyking episode were only available in the region between 13 km north and 12 km south of the centre of the Krafla caldera. Outside this zone distance measurements were made infrequently, and only after the episode had started, thus, "high" and "low" estimates are presented for the width of surface opening in this region (Figure 2.8) [*Tryggvason*, 1984]. From 18–5 km south of the caldera a net thickness, averaged over its length, of ~4.5 m was estimated. From 5 km south to 20 km north a thickness of ~7.5 m

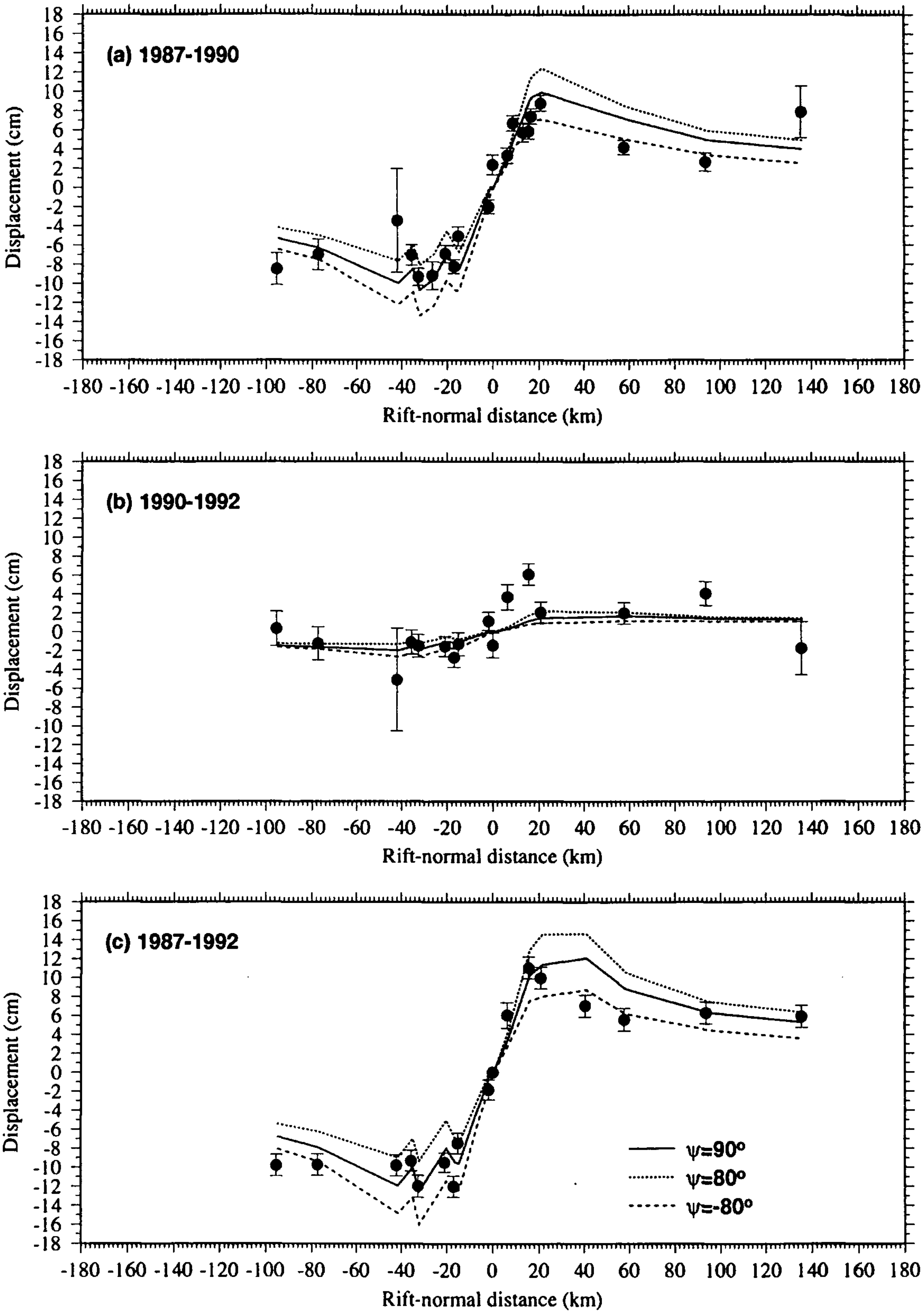

Figure 8.7: Same as Figure 8.1 for $H = 10$ km, except for a dyke dipping at 80° to the east (short-dashed curves) and 80° to the west (-80°) (long-dashed curves). The vertical case is included for comparison (solid curves).

was similarly obtained. Further north high and low estimates are given. These are 5 m and 7 m respectively from 20–35 km north of the caldera, and 3 m and 5 m from 35–64 km (Figure 2.8).

The dyke thickness is likely to vary with depth, for example, an elliptical shape may more accurately reflect the true shape of the injected dykes [*A. Rubin*, pers. comm., 1995]. In addition, if the dykes did not extend to the surface then surface widening is expected to be less than the maximum dyke thickness [*A. Rubin*, pers. comm., 1995] which would lead to an underestimate of dyke thickness. However, the modelling described above suggests that this is not the case so the extreme, possible thicknesses for the intruded dykes are not likely to exceed the published estimates of *Tryggvason* [1984].

The best-fit dyke thicknesses found in this analysis were 4.5 m, 5.0 m, 4.5 m and 3.0 m from 18–5 km south, 5 km south to 20 km north, 20–35 km north and 35–64 km north of the caldera centre respectively. These are consistent with the lower end of the estimates of *Tryggvason* [1984]. Trade-offs between the dyke thicknesses and other model parameters do occur, for example, between H and η. If the elastic layer were thicker, or the viscosity smaller, then larger dyke thicknesses are required to compensate for the effect of these variations on the predicted displacement fields. Variations in the model dyke thicknesses of up to ~30%, and corresponding variation of other model parameters are possible before serious degradation of the fit to the data occurs.

Viscosity, η

A summary of the existing estimates for the viscosity beneath Iceland is given in Table 8.1. These were obtained from glacio-isostatic modelling [*Sigmundsson*, 1991; *Sigmundsson and Einarsson*, 1992], and from one- and two-dimensional elastic-viscous modelling of the deformation field in north Iceland [*Foulger et al.*, 1992; *Heki et al.*, 1993]. The range in these estimates is 0.3–50 x 10^{18} Pa s.

Spatial variations in the viscosity are expected, for example, locally beneath Krafla, and within and outside of the rift zone. This was highlighted by the analysis of the 1987–1990 displacement field using the elastic-viscous model (Section 2.3.4) and the modelling of the localised tilt in the neighbourhood of Krafla (Section 7.4.3.2)

A maximum viscosity of 1.2 x 10^{18} Pa s is consistent with plausible dyke thicknesses

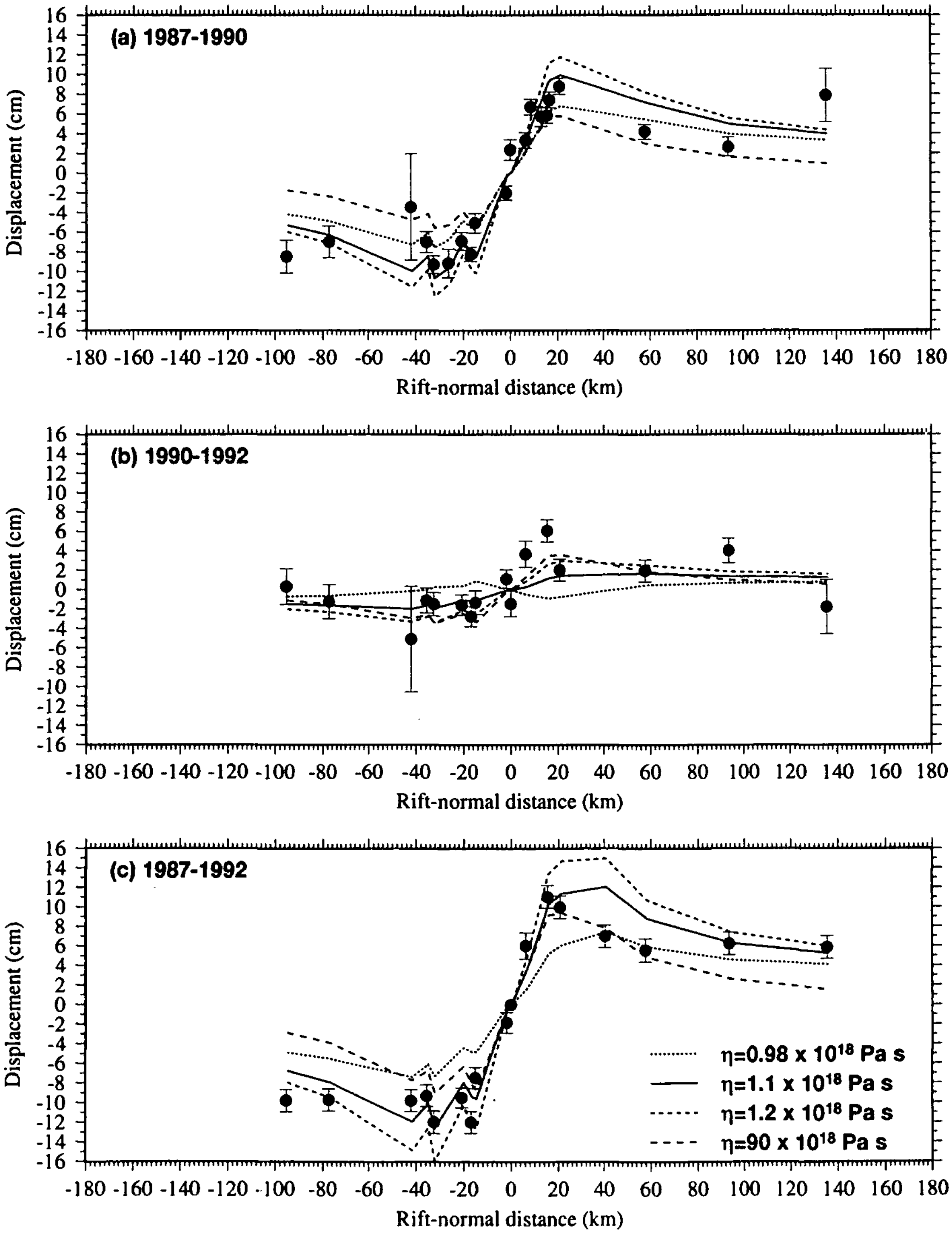

Figure 8.8: Same as Figure 8.1 for $H = W = 10$ km, except for a suite of different viscosities. χ^2_ν is 3.2, 2.0, and 4.2 when η=0.98 x 10^{18} Pa s, and 5.5, 1.3, and 5.6 when η=1.2 x 10^{18} Pa s for the 1987–1990, 1990–1992, and 1987–1992 epochs respectively.

Table 8.1: Viscosity estimates beneath Iceland, inferred from previous geophysical studies.

Viscosity estimate (x 10^{18} Pa s)	Reference
10	*Sigmundsson* [1991]
1–50	*Sigmundsson and Einarsson* [1992]
0.3–2	*Foulger et al.* [1992]
3–20	*Heki et al.* [1992]

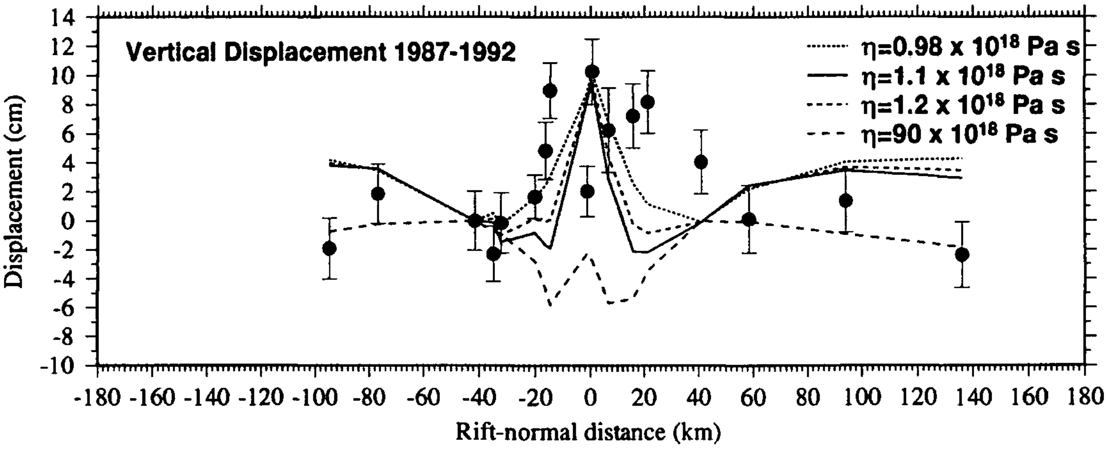

Figure 8.9: Same as Figure 8.8, except for the 1987–1992 vertical deformation field. χ^2_ν is 4.5 and 4.3 when η=0.98 x 10^{18} Pa s and 1.2 x 10^{18} Pa s respectively.

(Figure 8.8). If higher values are assumed then displacements are significantly overestimated. A minimum viscosity of 0.98 x 10^{18} Pa s is possible, and a viscosity of 0.95 x 10^{18} Pa s produces contraction within ~30 km of the dyke, at odds with the observations. The best-fit viscosity was 1.1 x 10^{18} Pa s together with the best-fit dyke thicknesses given above. Radically different viscosities, for example, 90 x 10^{18} Pa s fit poorly the displacements at large distances (Figure 8.8) and in the vertical (Figure 8.9). Varying the dyke thicknesses between the extreme values of *Tryggvason* [1984] was found to require viscosities in the range 1.0 ± 0.1 x 10^{18} Pa s.

Asthenosphere viscosity estimates using data from postglacial rebound studies in Canada and Fennoscandia are in the range 10^{19}–10^{21} Pa s [e.g., *Peltier*, 1986; *Officer et al.*, 1988]. Evidence was also found for a zone of relatively-low viscosity (4 x 10^{19} Pa s) in the upper asthenosphere [*Cathles*, 1975]. The viscosity predicted beneath Iceland is exceptionally low on a global scale and is probably a consequence of the Icelandic hotspot and the mid-ocean ridge [*Sigmundsson*, 1991]. Hot mantle material beneath Iceland would cause low viscosity, a property which may characterise all mid-ocean ridges and hotspots. The contributions of the hotspot and the ridge are not separable, but the two would be expected to reinforce one-another. Hotspots and plate boundaries are probably major contributors to lateral viscosity variations in the Earth.

8.2.3.2.3 Dyking Extending Partially Through the Elastic Layer

If the dykes did not rupture entirely to the base of the elastic layer, then there is a shortfall of motion predicted at large distances, and an additional process must be invoked to account for that motion. It has been proposed that large events in the upper lithosphere induce elevated stress levels in the lower lithosphere and asthenosphere, inducing postevent continuation of motion in the same sense as the coevent motion, along with relaxation in the asthenosphere. Such a process has been used to model motion in thrust zones, where coseismic faulting may be confined to the upper part of the elastic plate only. This causes the load supported by the lower part of the lithospheric plate boundary to be gradually transferred back to the shallow, locked segment of the boundary, effecting the strain buildup for a subsequent event [*Thatcher and Rundle*, 1979]. Such a model is a combination of the viscoelastic and "continued slip" approaches. The equivalent process for a spreading plate boundary is continuous dyking, in which rifting episodes only rupture the shallow part of the elastic layer. Continuous, steady dyking is questionable physically. However, it may occur as short, frequent dyke intrusions at depth, rather than "continuous" dyking.

This process was modelled using the approach of *Savage and Prescott* [1978]. It has previously been applied to strike-slip regimes [e.g., *Thatcher*, 1983], and the extension to dyking is an easy one. The full displacement solution is given by the sum of the steady and transient components. The steady motion is considered to result from the long-term forces that drive the plates (making no assumptions about their origins), and the transient motion from repeated events that partially rift the lithosphere all along the plate boundary.

The total motion between dyking events (the interdyking motion) is given by the summation of: (1) uniform block motion (of the two plates), (2) the response of the elastic layer to steady, shallow "backslip" (i.e., "locking" the boundary at the location of the impending event), (3) the viscous response to (2), and (4) the

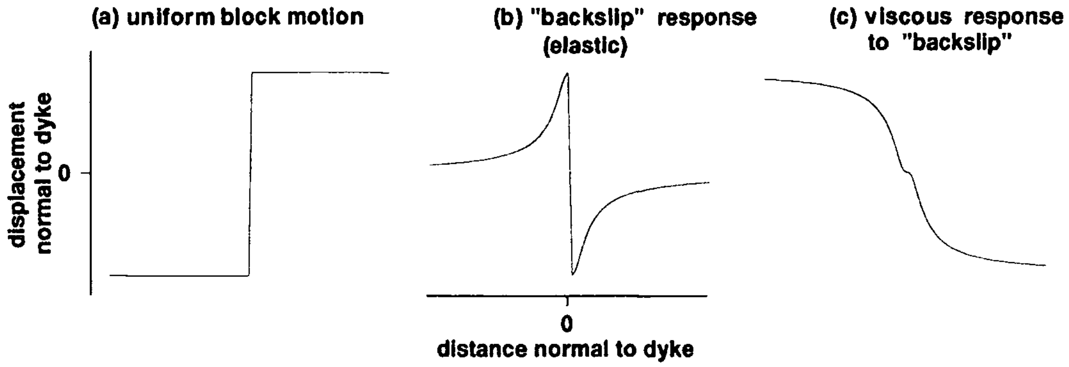

Figure 8.10: Schematic representation of the three components that comprise the steady motion representing the long-term forces that drive the plates. (a) uniform block motion, (b) the response of the elastic layer to steady, shallow "backslip", and (c) the viscous response to (b).

viscoelastic response to past, periodic dyke injections [e.g., *Thatcher*, 1983]. The first three components supply a steady, uniform component of motion, and the fourth a transient, time-dependent part. Once the transient motion has damped out, all that remains is the steady contribution.

(1) is modelled as a simple step function, and represents the motion of two plates freely diverging at a constant rate (Figure 8.10a). Component (2) (Figure 8.10b) is included in order to "lock" the two plates together down to some (prescribed) depth, and is easily modelled using, for example, the formulae of *Okada* [1985] (Section 6.2). The sum of contributions (1) and (2) is the elastic response to continuous, steady dyking below some depth, and is identical to the process modelled in Section 7.2. Component (3) is added to account for the behaviour of a viscoelastic halfspace at depth. This is computed using a previous result of *Thatcher* [1983] who determined that the steady-state, viscoelastic response to fault slip occurring at a uniform rate is identical to the $t = \infty$ response to a step offset at $t = 0$ [*Thatcher*, 1983]. Applying this result to dyking, the $t = \infty$ response of the elastic-viscoelastic model is required to compute component (3) (Figure 8.10c). If dyking does not extend all the way through the elastic layer, and crustal spreading occurs slowly and "continuously" in the lower part of the lithosphere, this method is a consistent approach to modelling plate separation. When $W/H = 1$ the $t = \infty$ response is identical in magnitude but opposite in sign to the codyking response, and thus, in this case all that remains is contribution (4). This result only applies to infinitely-long dykes. An identical result is found for the strike-slip case [*Thatcher*, 1983].

As highlighted above, the horizontal displacement field in north Iceland is insensitive to either this kind of model or one of the two end-member models. The vertical field, however, although suffering from considerably greater noise than the horizontal field, does appear to definitely indicate uplift over the dyke. All models involving continuous dyking, whether partial or complete, would cause subsidence in the rift zone. Future surveys that improve the accuracy of the vertical field will be able to convincingly distinguish between these two processes, which has never before been done.

8.2.3.3 Explanation for the Residual Field

8.2.3.3.1 Isostatic Uplift of Vatnajökull

Although significant, unexplained vertical motion is observed around Vatnajökull 1987–1992, it fits very poorly a model of isostatic uplift centred on the present icecap (Section 7.4.4.2). The general pattern of vertical motion is one of systematic regional tilt up towards the north-northeast. Observational evidence for glacio-isostatic uplift around Vatnajökull comes from two sources. First, the strandlines of Lake Langisjór (Figure 4.3) indicate tilt upwards towards Vatnajökull [*Sigmundsson and Einarsson*, 1992]. Second, uplift close to Vatnajökull was suspected from recent shallowing of the harbour at Hofn [*P. Einarsson*, pers. comm., 1991]. It is interesting to note that both of these effects are confirmed by the GPS results, which also agree with the estimates of rate of motion to within a factor of about 2. However, the overall spatial pattern of motion is highly inconsistent with the model.

The 1987–1992 vertical displacement field obtained using the GEONAP software [*Wübbena*, 1989] reveals a very similar deformation pattern to that obtained using the Bernese results (compare Figures 7.28a and 8.11). This confirms that the vertical motions calculated are not an artifact of the Bernese processing method.

The variation of vertical velocity with distance from the proposed model icecap centre is shown in Figure 8.12a. Points further than 90 km from the centre are not included in the figure. The 1σ errors are at the 0.5 cm/yr level, and very little similarity to the predicted glacio-isostatic uplift fields for the three different upper-mantle viscosities shown is evident (Figure 8.12b). Future remeasurement of the

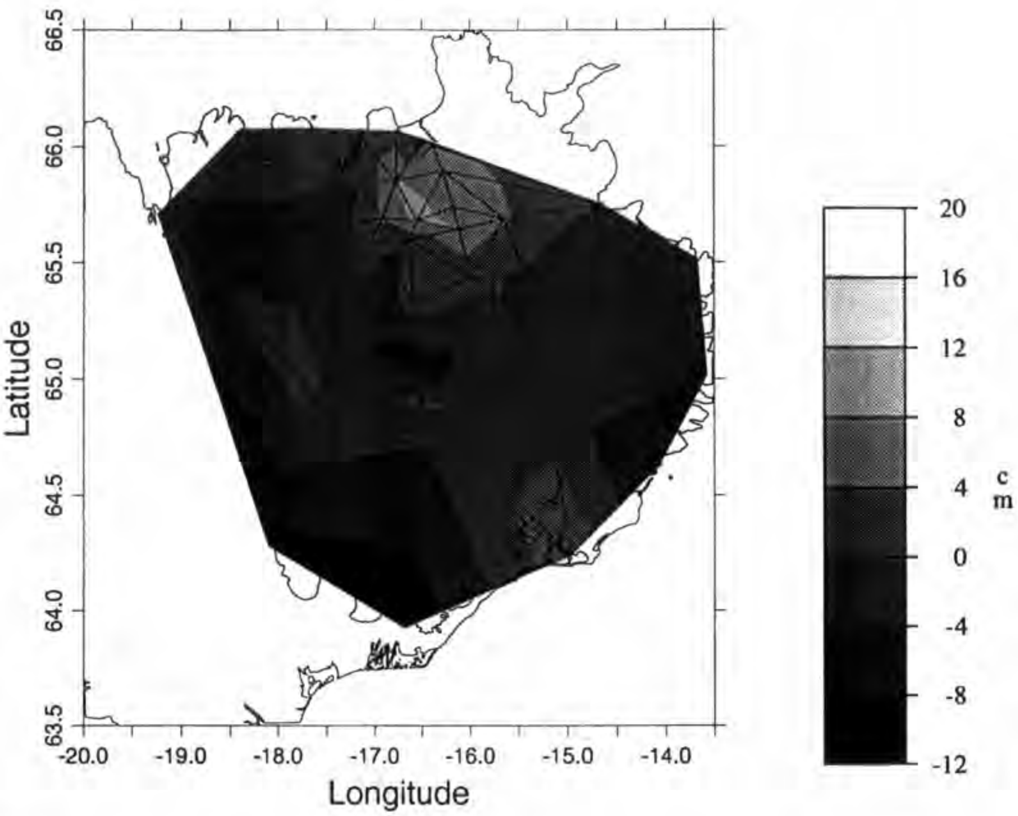

Figure 8.11: The observed vertical field for the epoch 1987–1992 obtained from the GEONAP results. (GEONAP data kindly provided by *C.-H. Jahn* and *C. Völksen*, University of Hannover).

GPS points in this area to improve the accuracy of the vertical velocity field will be important in confirming or otherwise these findings and clarifying the vertical deformation field further.

Errors of ~1 cm were obtained for the vertical component of the 1991 GPS results. Assuming similar errors will characterise a future survey of that network, a combined vertical positional error of about $\sqrt{1^2 + 1^2} = 1.4$ cm will result for the interim displacement field. The deformation rate predicted by the isostatic uplift model across the network is ~1 cm/yr. In order for such deformation, significant at the 3σ level, to be detected, remeasurement of the 1991 network should be conducted ~5 years after the first epoch (in 1996). Observations at points I58 and I59 (Figure 7.1) for the period 1987-1992 suggest up to ~2.5 cm/yr of differential motion across the 1991 network. In that case, significant deformation at the 3σ level might be detected after only ~2 years, and the points in the 1991 network would gainfully be included in the forthcoming 1995 GPS survey of north Iceland.

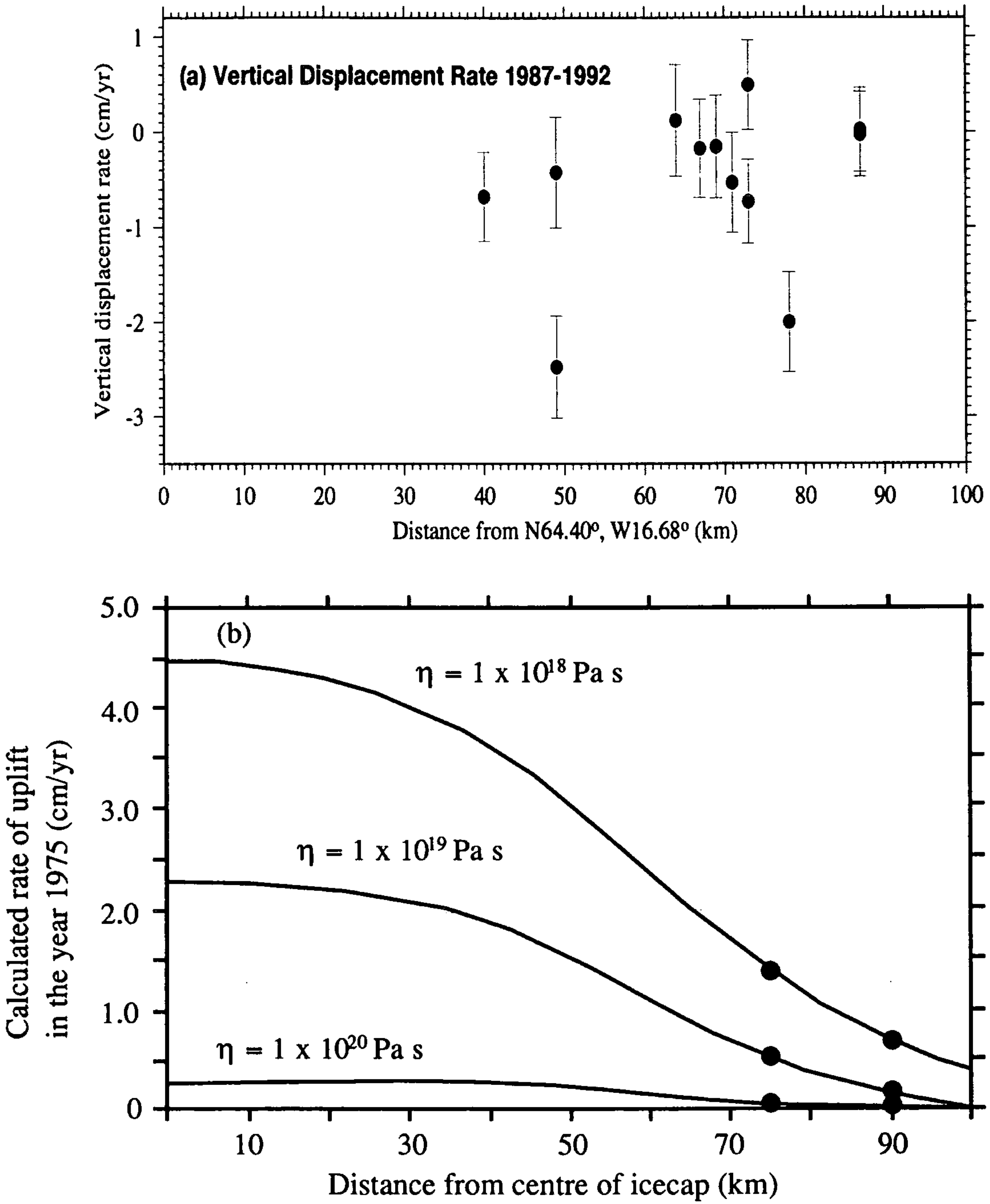

Figure 8.12: (a) Observed vertical displacements 1987–1992 against distance from N64.40°, W16.68°, and (b) calculated uplift rates against distance from the icecap centre at N64.40°, W16.68° for the year 1975 for three upper-mantle viscosities, according to the model of *Sigmundsson and Einarsson* [1992].

8.2.3.3.2 Modelling of Other, Minor Events

Candidate intrusions in Grimsvötn, the Askja and Kverkfjöll volcanic systems and the Öræfajökull–Snæfell flank zone were modelled in an attempt to explain the residual field. None of these models were completely successful, and the latter two are unsupported by any observations of seismic or volcanic activity. Activity in the Öræfajökull–Snæfell zone can explain the orientations of the residual vectors, and 2 m of widening at a depth of 2–10 km in 1983 can match the amplitude of the residuals. Deeper dykes at this location would produce the required orientations, but then larger dyke thicknesses would be required. Later dyking would reduce the required dyke thickness. Such a model, however, predicts displacements of a comparable magnitude both southeast and north of Vatnajökull, but these latter are not observed.

An intrusion on this scale and at this shallow depth is unlikely to have gone undetected and a deeper intrusion may be more likely. There is evidence that magmas erupted in this region come from 10–15 km depth [*V. Hards*, pers. comm., 1995], suggesting the absence of a shallow crustal magma chamber similar to the one beneath the Krafla volcanic system. Lateral dyking may thus not occur in this zone, in keeping with the lack of extensional features. A deep intrusion may also represent slow processes in the viscoelastic layer such as magma rising from large depths to replenish material in the subcrustal layer of partial melt.

8.2.3.3.3 Other Factors

The addition of the better-constrained 1987–1992 epoch has highlighted an apparent asymmetry in the displacement field, easily seen in the profile view. The displacement of the furthest points is ~6 cm less than the peak displacement east of the rift, but only ~2 cm less than the peak on the west (see, for example, Figure 5.16c). This is also evident in the 1987–1990 displacement field, when more points closer to the rift were occupied. This asymmetry in the displacement field may indicate asymmetry of the crustal structure, since the variation of other factors, for example, downdip dyke width and dip, cannot produce the required asymmetry in the deformation pattern.

Lateral variations in the viscosity clearly occur, and this could also provide an explanation for the observed asymmetry, and the residual vectors. Modelling of the tilt data in the vicinity of the Krafla caldera suggested a lower viscosity in this region, and may indicate lower viscosities in general beneath the spreading plate boundary.

Inversion for best-fit parameters is not possible since the software is only set up for forward modelling. With the currently-available data set inversion might not be able to resolve the parameters of interest very well anyway, since different models can produce similar effects, e.g. elastic layer thickness and viscosity.

8.2.3.4 Spreading in North Iceland

The predictions of the viscoelastic model (Figure 6.13) reveal a somewhat surprising result, that is that the direction of motion reverses, possibly more than once, following a large event. This could result in very different processes occurring throughout the rifting cycle, perhaps even compressional tectonic events at certain times. This result is illustrated by the model predictions for the historical events in the NVZ and TFZ. Predicted displacements following the 1618 Theistareykir and the 1724–1729 Mývatn fires episodes indicate contractions of the GPS network for the period 1987–1992, whilst the more recent 1874 Askja episode is contributing a network expansion. In the light of these findings, the terrestrial surveying results of 1965–1971 across the Krafla fissure swarm, which indicated up to 50 cm of contraction (Section 2.3.2), seem less unlikely than was previously thought. The amplitudes of these motions, however, are not well modelled, and localised magmatic activity (e.g., predyking inflation of the Krafla magma chamber) or surveying errors remain more likely explanations.

A relaxation time of ~1.7 years is indicated for north Iceland by the best-fit model. An episode recurrence time of 100–150 years [*Björnsson*, 1985] thus implies that the predictions of Figure 6.16 can be used to approximate spreading in north Iceland. The true picture is more complex than Figure 6.16 indicates, as real dykes are not infinite and deformation resulting from *en échelon*, finite dykes will interfere. However, some general deductions may be drawn.

Near the boundary variable deformation rates occur, and alternate periods of areal expansion and contraction occur before a relatively stable era begins and continues until the onset of the next episode. Accelerated deformation is expected to last ~46 years ($27\tau_a$) following an episode. Far from the boundary episodic motion is still detectable, with high deformation rates expected for ~24 years ($14\tau_a$) after the event, after which little deformation occurs. Continuous, steady motion is not observed within 210 km of the plate boundary.

If continuous plate motion is to occur within about 200 km of the plate boundary then the recurrence time must be of the order of $15\tau_a$ (Figure 6.13). In north Iceland this implies a recurrence time of ~15 x 1.7 years, i.e., ~25 years, much shorter than the actual recurrence interval. To achieve a recurrence time within the accepted range, a relaxation time of 6.7–10 years is required, corresponding to a viscosity of 4.3 x 10^{18}–6.5 x 10^{18} Pa s. If the viscosity beneath Iceland is 1.1 x 10^{18} Pa s, as determined for the best-fit model here, then the "plate boundary zone", i.e., the zone within which motion is significantly episodic, must be considerably more than 350 km wide – the maximum extent of land that flanks the plate boundary in Iceland. This implies that "continuous plate motion" as predicted by models such as the NUVEL-1A model, may not be observable in Iceland.

Evidence for continuous motion is available from trans-Atlantic VLBI measurements over the last 10 years [*Carter and Robertson*, 1989]. The variations in length of those lines is very smooth, as would be expected for lines several thousand kilometres long between the plate interiors, and there is no evidence for irregular plate movements [*Heki et al.*, 1993]. Such distances are out of range for prediction using the elastic-viscoelastic model, since the assumptions, boundary conditions, and mathematical methodology inherent in the model cause increasing inaccuracies with distance.

8.2.3.5 Tectonic Implications

8.2.3.5.1 Deformation in the Krafla Caldera

Postdyking stress redistribution appears to be able to explain tilt in the Krafla area since 1988/1989. The tilt measurements were previously interpreted as continued activity in the Krafla magma chamber, or in some deeper chamber [*Tryggvason*, 1994]. The current analysis indicates that the magma chamber may have become inactive in 1988/1989. A few centimetres of uplift near to Krafla may thus have occurred between the 1987 GPS survey and 1988/1989 and should be taken into account in future modelling.

Stress redistribution following a large volcano-tectonic event may lead volcanologists to believe that volcanic hazard is greater than it really is. This is because transient viscoelastic motion may cause surface deformations that resemble, and are mistakenly interpreted as, indicating magma-chamber activity. In future, after volcanic activity, this stress redistribution should be taken into account before concluding that a volcano continues to be active long after eruptive/intrusive activity is over. This work may be applied, for example, to Long Valley caldera, California, Mount St. Helens, Oregon, and the Phlegrean Fields, Italy.

8.2.3.5.2 Deformation in the Askja Volcanic System

An analysis of a subset of fifteen of the GPS points occupied 1987–1990 in the Askja region was used by *Camitz et al.* [1995] to infer the existence of a 30–45 km-wide plate boundary zone in the Askja volcanic system, beyond which points move at the full spreading rate. This work however, shows that all of the displacement in the region (at better than the 2σ level) can be explained as viscoelastic relaxation following the recent Krafla rifting episode (Figure 8.13).

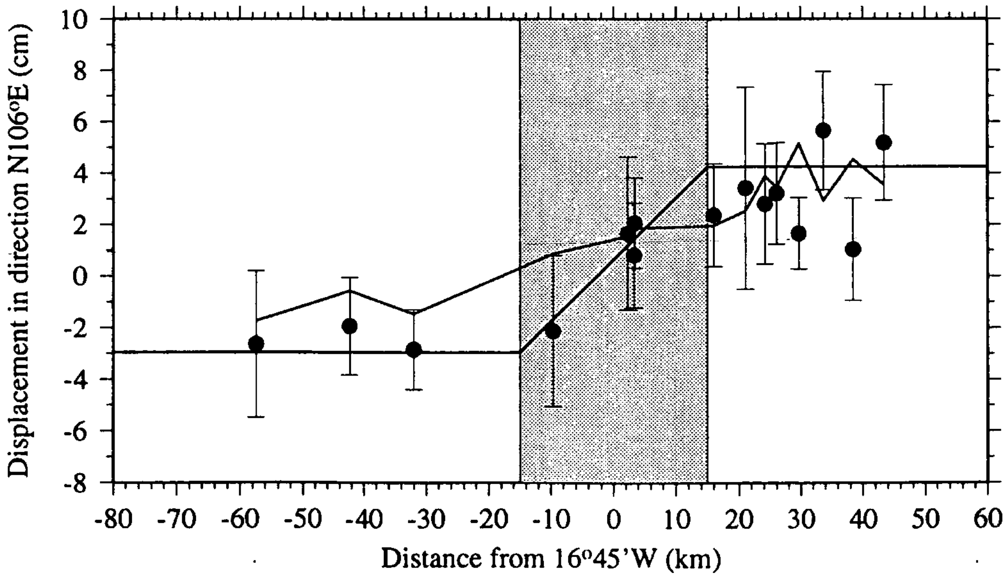

Figure 8.13: Observed and predicted displacements of points within the Askja region 1987–1990 in the direction N106°E (the NUVEL-1 spreading direction) against distance. The effects of the processes dealt with in Sections 7.4.2.2–7.4.2.6 have been subtracted from the observed displacements. 1σ error bars are shown. The shaded region highlights the width of the plate boundary zone and the solid, straight line represents the plate rate inferred by *Camitz et al.* [1995] using the same GPS results.

These two interpretations of the motion around Askja represent physical and kinematic modelling approaches. The kinematic approach is purely a method of describing many velocity observations in greatly summarised form and has been shown by geological studies to be appropriate for motion over very long (geologic) times, and by VLBI and SLR measurements to describe well the relative motion between the distant plate interiors. The work of this thesis shows that such an approach is inappropriate to closely-spaced points in plate boundary zones, in as much as it may fit the deformation field poorly and has no predictive powers. The results from the Askja system 1987–1990 demonstrate that motion that coincidentally agrees with the average plate rates may be observed at certain places and times in the spreading cycle. The results from the Krafla system demonstrate that motion may deviate radically from these rates.

8.2.3.5.3 Implications for Deformation Elsewhere in Iceland

The best-fit model of the Krafla rifting episode was used to predict motion from this source in the TFZ, EVZ, WVZ, and SISZ 1987–1992 (Figure 8.14). The displacements in each region are shown relative to an arbitrary point approximately in the centre of the simulated area. Profiles normal to the plate boundaries in these areas are shown in Figure 8.15. The TFZ was affected most by the recent rifting episode since it is closest. However, substantial displacements also occurred in the EVZ. The WVZ and the SISZ were also affected but to a much lesser degree than the EVZ. Very little motion is predicted in the Reykjanes Peninsula.

Approximately 1 cm/yr of motion is predicted across the TFZ 1987–1992 (Figure 8.15a). In the EVZ ~0.24 cm/yr of motion is predicted (Figure 8.15b), decreasing to ~0.12 cm/yr across the WVZ (Figure 8.15c) and about 0.1 cm/yr is predicted in the direction N105°E, parallel to the SISZ as a whole (Figure 8.15d). However, the major strike-slip faults in the SISZ are orientated north-south and only about 0.01 cm/yr is predicted in this direction (Figure 8.16).

GPS surveying across the SISZ 1986–1992 revealed 8.1 cm of displacement in the direction N104°E, i.e., much larger than that predicted from the recent Krafla rifting episode. A series of magnitude 6.5 to 7.5 earthquakes occurred in this zone between 1896 and 1912 and residual motion from these events may account for most of the motion. *Sigmundsson et al.* [1995] interpreted the measurements as indicating the accumulation of left-lateral shear strain across the SISZ, a result of relative motion

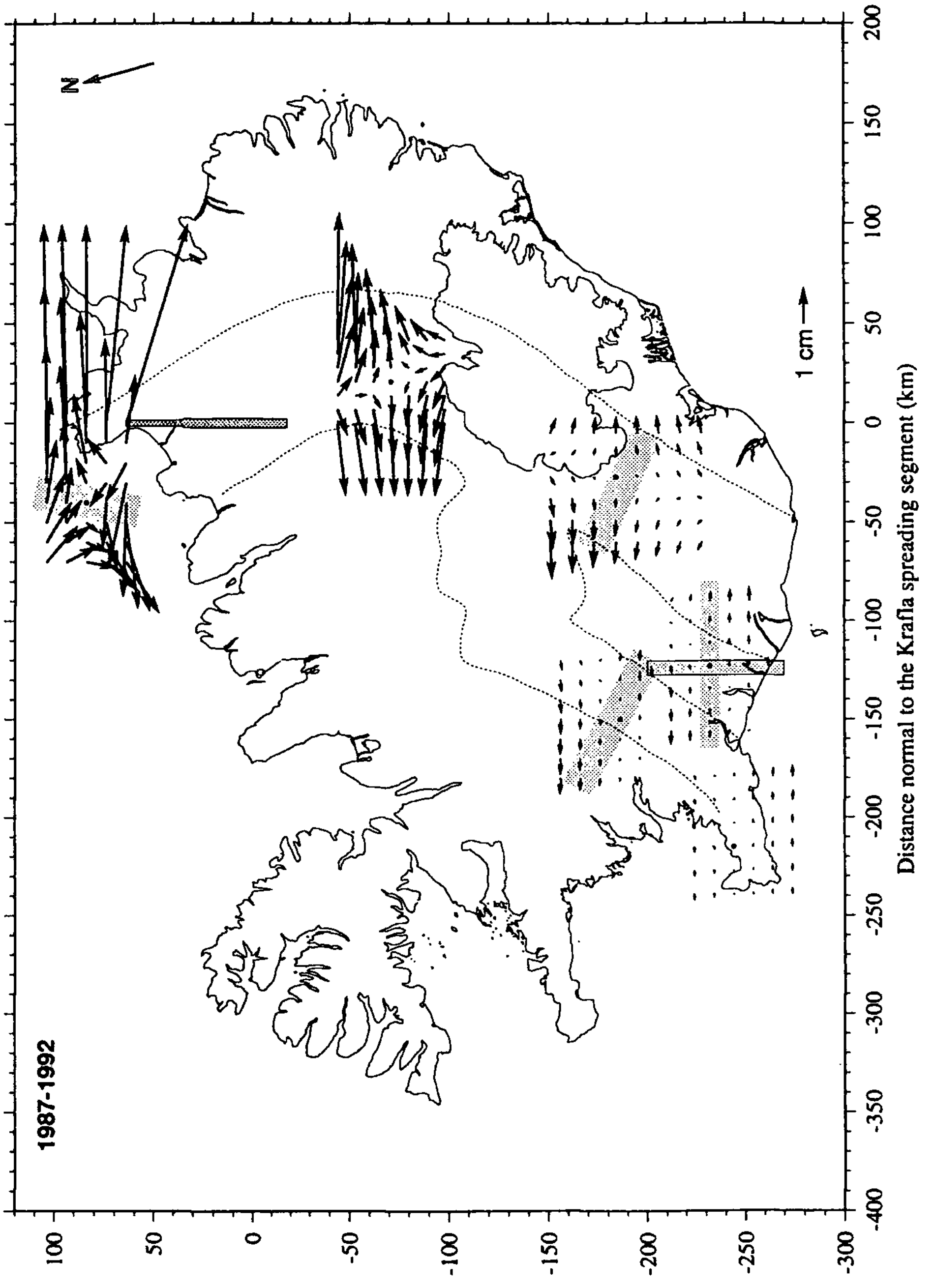

Figure 8.14: Predicted displacements 1987–1992 in Askja, the TFZ, EVZ, WVZ, SISZ and on the Reykjanes Peninsula as a result of the recent Krafla rifting episode. Model parameters are identical to those used in the best-fit model of the Krafla episode. The Krafla dyke is shown shaded and outlined in black, with the caldera positioned at $x = y = 0$. The outer boundary of the neovolcanic zone is shown by the dashed line. The zones used to calculate the profile velocities shown in Figure 8.15 are shaded. The zone used to calculate the profile velocities shown in Figure 8.16 are shaded and outlined in black. These zones were chosen to cross the plate boundary locally at right angles at each location. The scale vector lower right gives the displacement in centimetres.

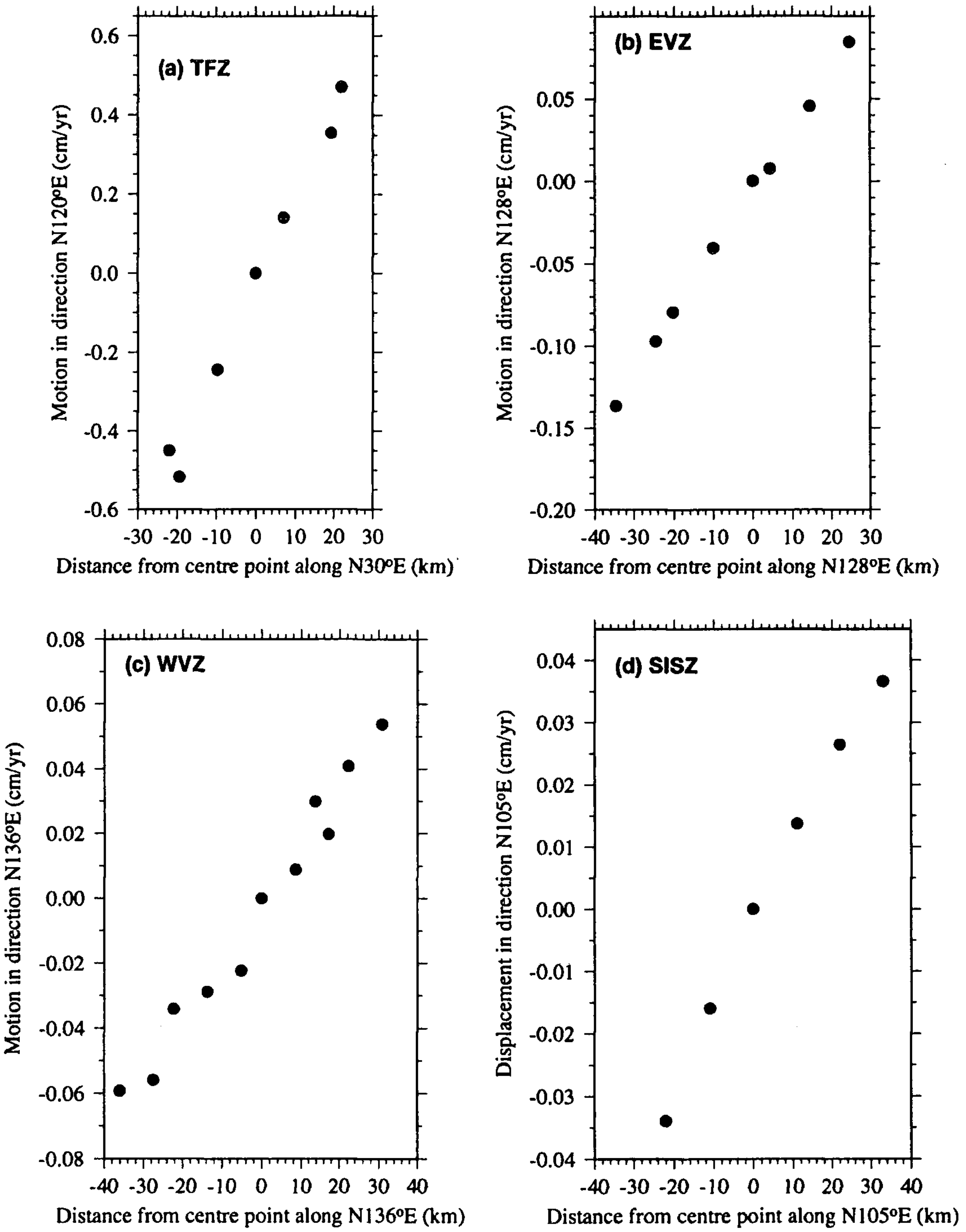

Figure 8.15: Predicted velocities 1987–1992 across (a) the TFZ, (b) the EVZ, (c) the WVZ, and (d) the SISZ as a result of the recent Krafla rifting episode. Points within the zones shown in Figure 8.14 are plotted. These points lie on a cartesian grid orientated parallel to the Krafla system. The zones studied here have different orientations and this is the source of the irregularities evident in each profile.

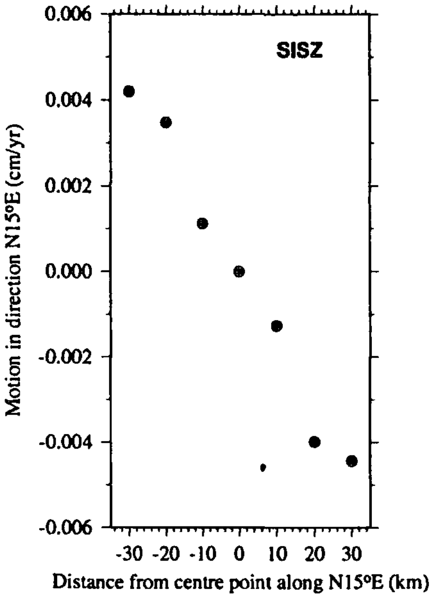

Figure 8.16: Same as Figure 8.15, except for the points within a zone normal to the SISZ.

of the Eurasian and American plates at an estimated velocity of 2.1 ± 0.4 cm/yr in direction N117±11°E. These authors concluded that historical seismicity in the SISZ can be attributed to this accumulation, and that 85 ± 15% of the relative plate motion has been accommodated by the SISZ for the last 1000 years. The current work suggests that modelling the motion as stress redistribution following recent, large events in the neighbourhood would be a more physically realistic interpretative approach.

It was suggested shortly after the Krafla dyking episode that this had loaded the SISZ towards failure. This reasoning was influential in accelerating the seismic hazard monitoring in this zone. However, this analysis shows that very little shear stress was added to the major faults in the SISZ since they are oriented north-south. This may explain why the anticipated events were not triggered by the Krafla episode.

Recent GPS surveying results across the EVZ reveal about ~1.0 ± 0.3 cm/yr of rift-normal expansion for the period 1986–1994 [*S. Jonsson*, pers. comm., 1995]. The model predictions show that the effects of the recent Krafla rifting episode are significant and should be taken into account before modelling the displacement field in this region. However, the effects of older dyking in the EVZ and closer events, e.g., recent activity in the volcano Hekla, may account for most of the current motion there.

Sparse data are consistent with ~1.5 ± 0.3 cm/yr of relative plate motion across the southern tip of the WVZ [*Sigmundsson et al.*, 1995]. The WVZ is affected in a similar manner as the SISZ by the recent Krafla rifting episode, since it is far from the rifted zone. Local events must be modelled in the region to account for the observed motion.

8.2.3.5.4 Forward Predictions for the North Iceland GPS Network

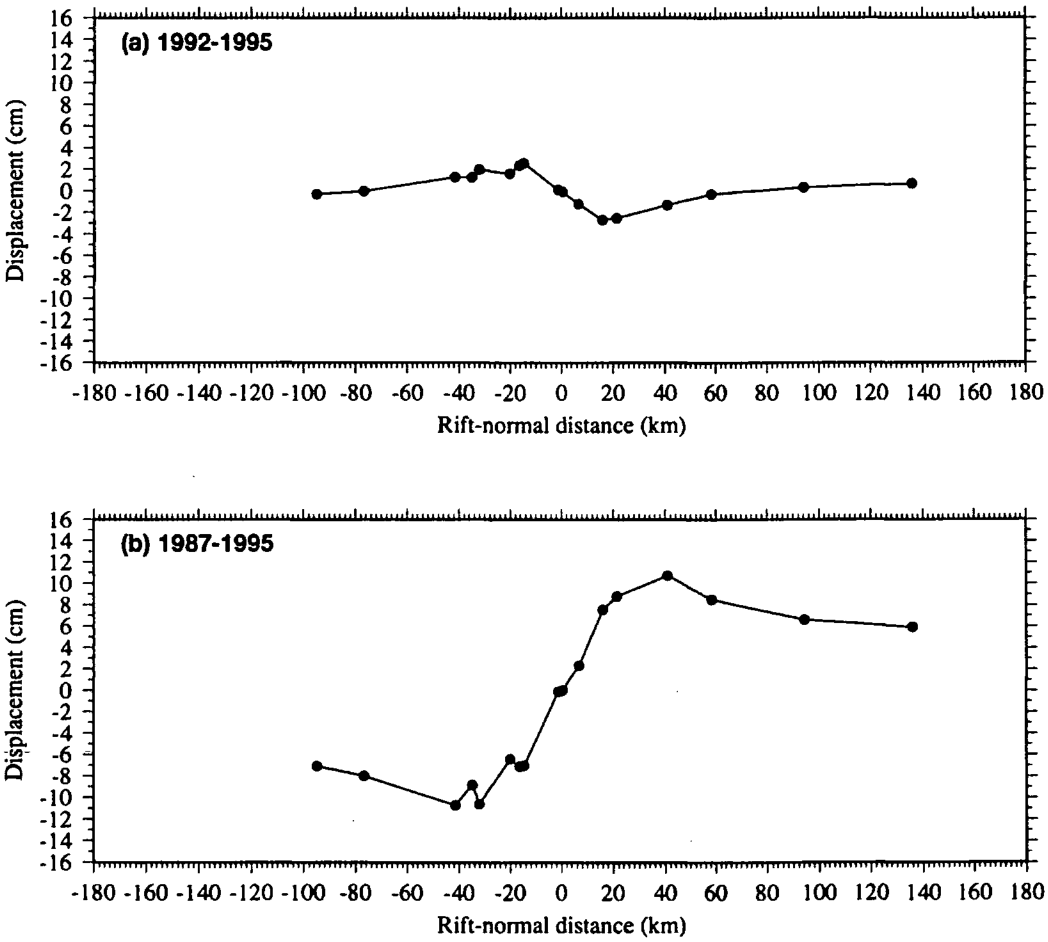

Figure 8.17: Predicted horizontal displacements of the points within the profile zones shown in Figure 7.1 for the epochs (a) 1992–1995, and (b) 1987–1995 as a result of the recent Krafla rifting episode. The best-fit parameters of the elastic-viscoelastic model (Section 7.4.3.1) were used.

Forward predictions for the north Iceland GPS network as a result of the recent Krafla rifting episode are made. Contraction of up to ~6 cm of the points within the profile zone shown in Figure 7.1 is predicted for the epoch 1992–1995 (Figure 8.17a), with the maximum displacements occurring ~20 km from the dyke. The magnitude of the displacements decreases with distance, and no motion of the furthest points is predicted for this epoch. Network expansion of up to 21 cm is thus predicted

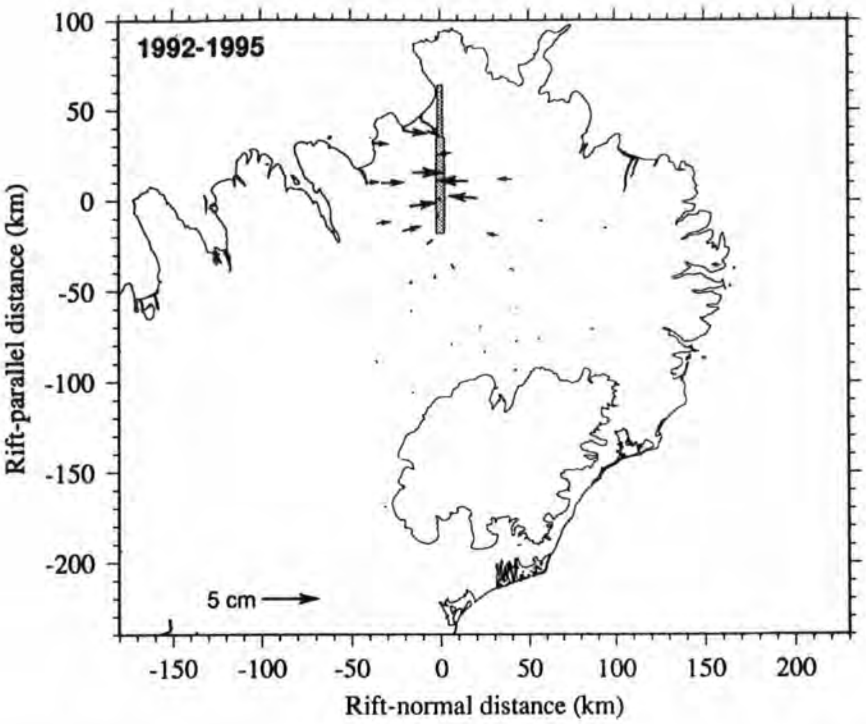

Figure 8.18: Same as Figure 8.17, except the predicted displacements 1992–1995 are shown in plan.

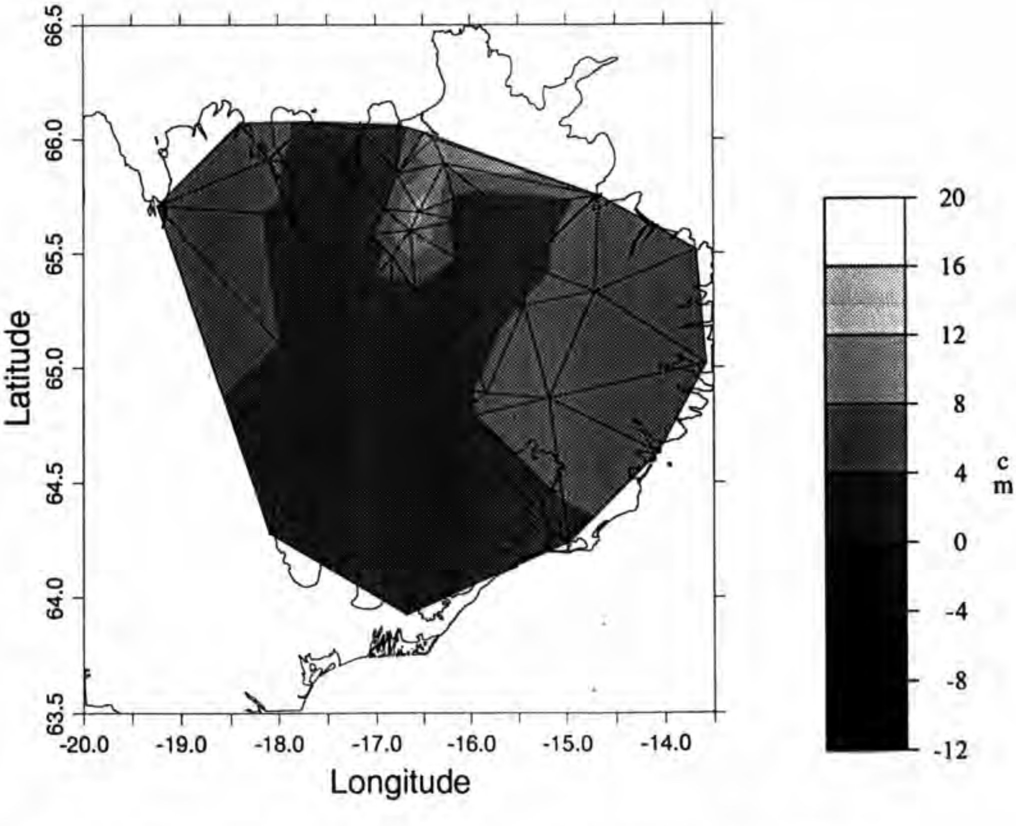

Figure 8.19: Same as Figure 8.17, except for the vertical displacement field 1987–1995.

1987–1995 (Figure 8.17b), decreasing to ~13 cm further away. The maximum displacements occur ~40 km from the dyke.

The network contraction predicted 1992–1995 is shown in plan view in Figure 8.18. Only points up to ~50 km either side of the dyke undergo significant motion as a result of the Krafla episode. All other points are unaffected.

Network uplift is predicted 1987–1995 relative to a point in the west of the network (Figure 8.19). A maximum of 16 cm is predicted in the vicinity of the dyke. Uplift of the farthest points of up to ~4 cm is predicted. In the far south of the network relative uplift of up to 4 cm is predicted to occur 1987–1995. Additional vertical motion of this kind will substantially improve the signal:noise ratio of the measured vertical deformation field.

8.2.3.6 The Shortcomings of the Viscoelastic Model

Although a major improvement in the stress-diffusion model, which simulated a sub-lithospheric viscous layer, the viscoelastic model has substantial limitations. The several simplifying assumptions inherent in the model include an infinitely-thick viscoelastic region, with a simplified linear rheology. A large volume of work exists indicating that actual Earth structure is considerably more complex [e.g., *Meissner and Strehlau*, 1982], involving several layers with contrasting rheologies, and lateral variations. In particular, the incorporation of a mid-crustal ductile layer may be an important improvement over halfspace models.

Laboratory measurements show that actual rock rheology is represented better by a power law rather than a linear viscoelastic relationship [e.g., *Kirby*, 1983]. An important area for future research is to estimate the effects of this on the model results, and to explore whether GPS measurements could distinguish between the two.

The model is unable to model lateral variations in structure and viscosity. The results of the present analysis indicate a possible variation of viscosity with distance from the spreading axis, and also locally beneath the Krafla spreading system. An asymmetric crustal structure is also indicated by the GPS measurements and by the model analysis.

Mathematical simplifications are inherent in the modelling program, for example, the "reduced" problem is presented (Section 6.4.1), and an approximation technique is applied to perform the Laplace inversion. *Rundle* [1981, 1982] found these to produce minimal differences in the predicted displacement fields, but further exploration of their effects in the case of the Krafla model should be done.

8.3 Summary of the Main Conclusions

1. The 1991 and 1992 survey results are of sufficiently high accuracy to be compared to previous and future GPS surveying results in order to determine crustal deformation in Iceland.

2. Significant vertical deformation results may be expected from remeasurement of the 1991 network after ~2–5 years. The results from the 1992 survey are interpreted here as indicating mostly postdyking stress redistribution following the Krafla rifting episode.

3. The continuous dyking-at-depth model can fit the 1987–1992 deformation field using an 80 km-long, 1000 km-high dyke at a depth of 5 km beneath the Krafla volcanic system with an opening of 35 cm.

4. The stress diffusion model is inadequate to model the 1987–1992 north Iceland displacement field, and thus can be eliminated from the possible geophysical models.

5. The elastic-viscoelastic model predicts a best-fit viscosity of 1.1 x 10^{18} Pa s to model the 1987–1990, 1990–1992 and 1987–1992 displacement fields, using an elastic layer thickness of 10 km.

6. The Krafla dyke injection episode ruptured the entire elastic layer, with the lower part of the dyke complex being fed from below, in accordance with the model of *Björnsson* [1985].

7. The effects of previous events in the survey region should be taken into account when modelling the displacement field. However, in the case of the north Iceland displacement field this was of minor importance.

8. The data are not diagnostic of different geophysical models, for example, continuous dyking at depth, viscoelastic relaxation, or a combination of the two. Many different physical models can explain the data. In order to resolve this problem independent data are required, and as realistic a model as possible. However, this is particularly problematic in this kind of crustal deformation work.

9. Crustal asymmetry may exist beneath north Iceland, with a thicker elastic layer to the east of the rift zone.

10. A spatial variation in viscosity exists beneath north Iceland, with values of $\sim 0.8 \times 10^{18}$ Pa s locally beneath Krafla and $0.98-1.2 \times 10^{18}$ Pa s beneath the rift axis. The viscosity beneath Iceland as a whole would have to be substantially higher than these values if a "plate boundary zone" is to occur on land.

11. GPS results confirm the relative uplift of points close to the southern edge of Vatnajökull. However, the overall spatial pattern of motion is highly inconsistent with the model of glacio-uplift as proposed by *Sigmundsson and Einarsson* [1992].

12. Hitherto unreported magmatic or tectonic activity may have occurred in east Iceland recently, most likely in the Öræfajökull–Snæfell flank zone.

13. The Krafla volcano became inactive in 1988/1989.

14. Contrary to early expectations, the Krafla rifting episode has had a minimal effect on bringing the major faults of the SISZ towards failure.

15. Surprisingly, substantial network contraction is predicted for the epoch 1992–1995, along with additional substantial uplift. A resurvey of the 1992 GPS network in 1995 will be powerful to test the results of the modelling presented in this thesis and will improve the definition of the observed displacement field, especially in the vertical.

8.4 Recommendations for Future Work

- Resurvey of the 1991 GPS network, either specifically or by incorporating it into a larger survey, e.g., the forthcoming 1995 resurvey of the north Iceland network.

- Add more GPS points in the far south, southeast and southwest of the 1987–1992 network to constrain better vertical movements around Vatnajökull, and also to study possible tectonic processes in the region of the Öræfajökull–Snæfell flank zone.

- Survey GPS points as far as possible from the rift zone to test the hypothesis that Iceland is wider than the plate boundary zone.

- Model the Krafla dyke intrusion using elliptical dykes rather than square dykes and incorporate an elastic layer that thickens with distance from the rift zone. These two may be achieved using finite element techniques.

- Investigate methods of inverting the data for model parameters instead of using only forward modelling.

- Extend the model to other areas of Iceland, e.g., the EVZ where work is currently at the investigative stage [*S. Jonsson*, pers. comm., 1995] and to the SISZ.

- Investigate the strain fields produced as a result of dyke intrusions, and study the capabilities of the model for predicting the sequence of events in Iceland and inter-segment relationships.

- Investigate the model of continuous dyking at depth in an elastic/viscoelastic medium.

- Extend the model to other volcanoes, e.g., Long Valley, California.

- Investigate whether evidence exists for "opposite" tectonics, e.g., compressive features in Iceland, extensional features in compression zones, and strike-slip faulting in the "wrong" sense in transform zones.

References

Aki, K., and P. G. Richards, *Quantitative Seismology, Vol. 1*, W. H. Freeman and Company, San Francisco, 557 pp., 1980.

Angenheister, G. H., H. Gebrande, H. Miller, P. Goldflam, W. Weigel, W. R. Jacoby, G. Pálmason, S. Björnsson, P. Einarsson, N. I. Pavlenkova, S. M. Zverev, I. V. Litvinenko, B. Loncarevic, and S. C. Solomon, Reykjanes Ridge Iceland seismic experiment (RRISP 77), *J. Geophys.*, *47*, 228–238, 1980.

Båth, M., Crustal structure of Iceland, *J. Geophys. Res.*, *65*, 1793–1807, 1960.

Beblo, M., and A. Björnsson, Magnetotelluric investigation of the lower crust and upper mantle beneath Iceland, *J. Geophys.*, *45*, 1–16, 1978.

Beblo, M., and A. Björnsson, A model of electrical resistivity beneath NE Iceland, correlation with temperature, *J. Geophys.*, *47*, 184–190, 1980.

Beblo, M., A. Björnsson, K. Arnason, B. Stein, and P. Wolfgram, Electrical conductivity beneath Iceland – Constraints imposed by magnetotelluric results on temperature, partial melt, crust and mantle structure, *J. Geophys.*, *53*, 16–23, 1983.

Beloussov, V. V., Against the hypothesis of sea-floor spreading, *Tectonophys.*, *9*, 489–511, 1970.

Ben-Menahem, A., and S. J. Singh, Multipolar elastic fields in a layered half space, *Bull. Seism. Soc. Am.*, *58*, 1519–1572, 1968.

Bernauer, F., Junge Tektonik auf Island und ihre Uhrsachen, in *Spalten auf Island*, ed. O. Niemczyk, Verlag von Konrad Wittwer, Stuttgart, pp. 14–64, 1943.

Bevington, P. R., and D. K. Robinson, *Data Reduction and Error Analysis for the Physical Sciences, Second Edition*, McGraw–Hill, Inc., New York, 1992.

Bjarnason, I., Th., W. Menke, Ó. G. Flóvenz, and D. Caress, Tomographic image of the Mid-Atlantic plate boundary in southwestern Iceland, *J. Geophys. Res.*, *98*, 6607–6622, 1993.

Björnsson, A., Dynamics of rifting in NE Iceland, *J. Geophys. Res.*, *90*, 10151–10162, 1985.

Björnsson, A., K. Sæmundsson, P. Einarsson, E. Tryggvason, and K. Grönvold, Current rifting episode in north Iceland, *Nature*, *266*, 318–323, 1977.

Björnsson, A., G. Johnsen, S. Sigurdsson, and G. Thorbergsson, Rifting of the plate boundary in north Iceland 1975–1978, *J. Geophys. Res.*, *84*, 3029–3038, 1979.

Blewitt, G., An automatic editing algorithm for GPS data, *Geophys. Res. Letts.*, *17*, 199–202, 1990.

Bonafede, M., M. Dragoni, and F. Quareni, Displacement and stress fields produced by a centre of dilation and by a pressure source in a viscoelastic half space: Application to the study of ground deformation and seismic activity at Campi Flegrei, Italy, *Geophys. J. R. astr. Soc.*, *87*, 455–485, 1986.

Bott, M. H. P., Deep structure, evolution and origin of the Icelandic transverse ridge, in *Geodynamics of Iceland and the North Atlantic Area*, ed. L. Kristjansson, pp. 33–47, 1974.

Bott, M. H. P., Deep structure and geodynamics of the Greenland–Scotland ridge; an introductory review, in *Structure and Development of the Greenland-Scotland Ridge: New Methods and Concepts,* eds. M. H. P. Bott et al., Plenum Press, New York, 1983a.

Bott, M. H. P., The crust beneath the Iceland–Faeroe Ridge, in *Structure and Development of the Greenland-Scotland Ridge: New Methods and Concepts,* eds. M. H. P. Bott et al., Plenum Press, New York, 1983b.

Bott, M. H. P., Plate tectonic evolution of the Icelandic transverse ridge and adjacent regions, *J. Geophys. Res.*, *90*, 9953-9960, 1985.

Bott, M. H. P., and D. S. Dean, Stress diffusion from plate boundaries, *Nature, 243*, 339–341, 1973.

Bott, M. H. P., and K. Gunnarsson, Crustal structure of the Iceland-Faeroe Ridge, *J. Geophys.*, *47*, 221–227, 1980.

Bott, M. H. P., S. Saxov, M. Talwani, and J. Theide (Ed.), *Structure and Development of the Greenland-Scotland Ridge: New Methods and Concepts*, 685 pp., Plenum Press, New York, 1983.

Brander, J. L., R. G. Mason, and R. W. Calvert, Precise distance measurements in Iceland, *Tectonophys.*, *31*, 193–206, 1976.

Brandsdottir, B., and P. Einarsson, Seismic activity associated with the September 1977 deflation of the Krafla central volcano in northeastern Iceland, *J. Volcanol. Geotherm. Res.*, *6*, 197-212, 1979.

Camitz, J., F. Sigmundsson, G. Foulger, C.-H. Jahn, C. Völksen, and P. Einarsson, Plate boundary deformation and continuing deflation of the Askja volcano, north Iceland, determined with GPS, 1987–1993, submitted to *Bull. Volcanol.*, 1995.

Carslaw, H. S., and J. C. Jaeger, *Conduction of Heat in Solids*, Oxford University Press, 1959.

Cathles, L. M., *The Viscosity of the Earth's Mantle*, Princeton University Press, Princeton, New Jersey, 1975.

Carter, W. E., and D. S. Robertson, Definition of a terrestrial reference frame using IRIS VLBI observations: Approaching millimetre accuracy, paper presented at Symposium 105, IAG General Meeting Int. Assoc. Geod., Edinburgh, Scotland, 1989.

Chinnery, M., Deformation of the ground around surface faults, *Bull. Seism. Soc. Am.*, *51*, 355–372, 1961.

Christensen, N. I., and R. H. Wilkins, Seismic properties, density and composition of the Icelandic crust near Reydarfjördur, *J. Geophys. Res.*, *87*, 6389–6395, 1982.

Cohen, S. C., Postseismic deformation due to subcrustal viscoelastic relaxation following dip-slip earthquakes, *J. Geophys. Res.*, *89*, 4538–4544, 1984.

Cohen, S. C., and M. J. Kramer, Crustal deformation, the earthquake cycle, and models of viscoelastic flow in the asthenosphere, *Geophys. J. R. astr. Soc.*, *78*, 735–750, 1984.

Cost, T. L., Approximate Laplace transform inversions in viscoelastic stress analysis, *AIAA J.*, *2*, 2157–2166, 1964.

Crouch, S. L., and A. M. Starfield, *Boundary Element Methods in Solid Mechanics*, Allen and Unwin, Winchester, Mass., 1983.

Decker, R. W., P. Einarsson, and P. A. Mohr, Rifting in Iceland: New geodetic data, *Science*, *173*, 530–532, 1971.

Decker, R. W., P. Einarsson, and R. Plumb, Rifting in Iceland: Measuring horizontal movements, *Soc. Sci. Íslandica*, *5*, 61–71, 1976.

DeMets, C., R. G. Gorgon, D. F. Argus, and S. Stein, Current plate motions, *Geophys. J. Int.*, *101*, 425–478, 1990.

DeMets, C., R. G. Gorgon, D. F. Argus, and S. Stein, Effect of recent revisions to the magnetic reversal time scale on estimates of current plate motions, *Geophys. Res. Letts.*, *21*, 2191–2194, 1994.

Dixon, T. H., An introduction to the Global Positioning System and some geological applications, *Rev. Geophys.*, *29*, 249–276, 1991.

Duba, A., S. Heikamp, W. Meurer, G. Nover, and G. Will, Evidence from borehole samples for the role of accessory minerals in lower-crustal conductivity, *Nature*, *367*, 59–61, 1994.

Einarsson, P., S-wave shadows in the Krafla caldera in northeast Iceland, evidence for a magma chamber in the crust, *Bull. Volcanol.*, *41*, 1–9, 1978.

Einarsson, P., Seismicity along the eastern margin of the North American plate, in *The geology of North America, Volume M, The Western North Atlantic Region*, eds. P. R. Vogt and B. E. Tucholke, The Geological Society of America, 1986.

Einarsson, P., Intraplate earthquakes in Iceland, in *Earthquakes at North Atlantic Passive Margins: Neotectonics and Postglacial Rebound*, eds. S. Gregersen and P. W. Basham, Kluwer Academic Publishers, pp. 329–344, 1989.

Einarsson, P., Earthquakes and present-day tectonism in Iceland, *Tectonophys.*, *189*, 261–279, 1991.

Einarsson, P., *Benchmarks of GPS-measurements in Iceland 1986–1991*, Science Institute, University of Iceland, 1992.

Einarsson, P., and B. Brandsdottir, Seismological evidence for lateral magma intrusion during the July 1978 deflation of the Krafla volcano in northeast Iceland, *J. Geophys. Res.*, *47*, 160–165, 1980.

Einarsson, P., and B. Brandsdottir, Seismic activity preceding and during the 1983 volcanic eruption in Grimsvötn, Iceland, *Jökull*, *34*, 13–23, 1984.

Einarsson, P., and J. Eiríksson, Earthquake fractures in the districts Land and Rangarvellir in the South Iceland Seismic Zone, *Jökull*, *32*, 113–120, 1982.

Einarsson, Tr., *A Survey of Gravity in Iceland*, Soc. Sci. Íslandica, Reykjavik, 22 pp., 1954.

Einarsson, Tr., The Icelandic fracture system and the inferred causal stress field, in *Iceland and Mid-Ocean Ridges*, ed. S. Björnsson, Soc. Sci. Íslandica, Reykjavik, pp. 128–139, 1967.

Einarsson, T., and K. J. Albertsson, The glacial history of Iceland during the past three million years, *Phil. Trans. R. Soc. Lond.B*, *318*, 637–644, 1988.

Elsasser, W. M., Convection and stress propagation in the upper mantle, in *The Application of Modern Physics to the Earth and Planetary Interiors*, ed. S. K. Runcorn, pp. 223–245, Wiley, London, 1969.

ETOPO5: Digital relief of the surface of the earth – bathymetry/topography data, *Rep. 88-M66-2*, Natl. Oceanic and Atmos. Admin., Boulder, Colo., 1988.

Fiske, R. S., and W. T. Kinoshita, Inflation of Kilauea volcano prior to its 1967–1968 eruption, *Science*, *165*, 341–349, 1969.

Flóvenz, Ó. G., Seismic structure of the Icelandic crust above layer three and the relation between body wave velocity and the alteration of the basaltic crust, *J. Geophys.*, *47*, 211–220, 1980.

Flóvenz, Ó. G., and K. Gunnarsson, Seismic crustal structure in Iceland and surrounding area, *Tectonophys.*, *189*, 1–17, 1991.

Foulger, G. R., A GPS geodetic survey of the Northern Volcanic Zone of Iceland 1987, *EOS Trans. AGU 68:1236*, 1987.

Foulger, G. R., Hengill triple junction, S.W. Iceland. 1. Tectonic structure and the spatial and temporal distribution of local earthquakes, *J. Geophys. Res.*, *93*, 13,493–13,506, 1988a.

Foulger, G. R., Hengill triple junction, S.W. Iceland. 2. Anomalous focal mechanisms and implications for processes within the geothermal reservoir and at accretionary plate boundaries, *J. Geophys. Res., 93*, 13,507–13,523, 1988b.

Foulger, G. R., C. -H. Jahn, G. Seeber, P. Einarsson, B. R. Julian and K. Heki, Post-rifting stress relaxation at the divergent plate boundary in Northeast Iceland, *Nature, 358*, 488–490, 1992.

Foulger, G. R., G. Beutler, R. Bilham, P. Einarsson, S. Fankhauser, W. Gurtner, U. Hugentobler, W. J. Morgan, M. Rothacher, G. Thorbergsson, and U. Wild, The Iceland 1986 GPS geodetic survey: tectonic goals and data processing, *Bull. Géodésique, 67*, 148–172, 1993.

Gebrande, H., H. Miller, and P. Einarsson, Seismic structure of Iceland along RRISP-profile I, *J. Geophys., 47*, 239–249, 1980.

Gerke, K., Crustal movements in the Mývatn and Thingvallavatn-area, both horizontal and vertical, in *Geodynamics of Iceland and the North Atlantic Area*, ed. L. Kristjansson, Reidel, Dordrecht, Holland, pp. 263–275, 1974.

Goldflam, P., W. Weigel, and B. D. Loncarevic, Seismic structure along RRISP-profile I on the southeast flank of the Reykjanes Ridge, *J. Geophys., 47*, 250–260, 1980.

Gordon, R. G., Orbital dates and steady rates, *Nature, 364*, 760–761, 1993.

Grove, J. M., *The Little Ice Age*, Routledge, London, 1988.

Gudmundsson, A., Form and dimension of dykes in eastern Iceland, *Tectonophys., 95*, 295–307, 1983.

Gudmundsson, A., Tectonic aspects of dykes in northwestern Iceland, *Jökull, 34*, 81–96, 1984.

Gudmundsson, B., and P. Einarsson, GPS measurements in Iceland 1986, station descriptions, Iceland Geodetic Survey Report, 1986.

Gudmundsson, B., and P. Einarsson, GPS measurements in Iceland 1987, station descriptions, Iceland Geodetic Survey Report, 1987.

Gudmundsson, G., and K. Sæmundsson, Statistical analysis of damaging earthquakes and volcanic eruptions in Iceland from 1550–1978, *J. Geophys., 47*, 99–109, 1980.

Gurtner, W., G. Mader, and D. MacArthur, A common exchange format for GPS data, *GPS Bulletin of the Commission VIII of the International Coordination of Space Techniques for Geodesy and Geodynamics (CSTG)*, May–June, 1989.

Hackman, M. C., *A Study of Crustal Deformation in Iceland Using Boundary Element Modeling and the Global Positioning System*, Ph.D. thesis, University of Colorado, 1991.

Hager, B. H., R. W. King, and M. Murray, Measurement of crustal deformation using the Global Positioning System, *Annu. Rev. Earth Planet. Sci., 19*, 351–82, 1991.

Hanks, T. C., and H. Kanamori, A moment magnitude scale, *J. Geophys. Res.*, *84*, 2348–2350, 1979.

Haskell, N. A., The dispersion of surface waves on multilayered media, *Bull. Seism. Soc. Am.*, *43*, 17–34, 1953.

Heki, K., A network adjustment program for the Bernese Global Positioning System data analysis software, *Jour. Geod. Soc. Japan*, *38*, 309–312, 1992.

Heki, K., G. R. Foulger, B. R. Julian, and C. -H. Jahn, Plate dynamics near divergent plate boundaries: Geophysical implications of postrifting crustal deformation in NE Iceland, *J. Geophys. Res.*, *98*, 14,279–14,297, 1993.

Helgason, J., Shifts of the plate boundary in Iceland: some aspects of Tertiary volcanism, *J. Geophys. Res.*, *90*, 10,084-10,092, 1985.

Helgason, J., and M. Zentilli, Field characteristics of laterally emplaced dikes: Anatomy of an exhumed Miocene dike swarm in Reydarfjördur, eastern Iceland, *Tectonophys.*, *115*, 247–274, 1985.

Hermance, J. F., An electrical model for the sub-Icelandic crust, *Geophysics*, *38*, 3–13, 1973.

Hermance, J. F., Crustal genesis in Iceland: Geophysical constraints on crustal thickening with age, *Geophys. Res. Letts.*, *8*, 203–206, 1981.

Hermance, J. F., R. E. Thayer, and A. Björnsson, The Telluric-magnetotelluric method in the regional assessment of geothermal potential, in *Proceedings of Second U. N. Symposium on the Development and Use of Geothermal Resources, vol. 2*, pp. 1037–1048, U.S. Government Printing Office, Washington D.C., 1976.

Hofton, M. A., J. B. Rundle, and G. R. Foulger, Horizontal surface deformation due to dike emplacement in an elastic-gravitational layer overlying a viscoelastic-gravitational half-space, *J. Geophys. Res.*, *100*, 6328-6339, 1995.

Jacoby, W. R., H. Zdarsky, and U. Altmann, Geodetic and geophysical evidence for magma movement and dyke injection during the Krafla rifting episode in North Iceland, in *Evolution of Mid Ocean Ridges*, IUGG 8, Geophysical Monograph 57, ed. J. M. Sinton, American Geophysical Union, pp. 65–77, 1989.

Jahn, C.-H., A Highly Precise GPS-epoch Measurement in the Northeast Volcanic Zone of Iceland, in *Cahiers du Centre Européen de Géodynamique et de Séismologie*, pp. 292–304, eds. P. Paquet, J. Flick, J. and B. Ducarme, Luxembourg, 1990.

Jahn, C.-H., G. Seeber, G. R. Foulger, and A. Björnsson, A GPS survey in the north-east volcanic zone, Iceland 1987–first results, in *Procedings of the General Meeting of the International Association of Geodesy Edinburgh, Global and Regional Geodynamics*, pp. 173–181, Springer-Verlag, New York, 1990.

Jahn, C.-H., G. Seeber, G. R. Foulger, and P. Einarsson, GPS epoch measurements across the mid-Atlantic plate boundary in northern Iceland 1987–1990, paper presented at Union Symposium U-5, IUGG, XX General Assembly, Int. Union of Geod. and Geophys., Vienna, 1991.

Jahn, C.-H., G. Seeber, G. R. Foulger, and P. Einarsson, GPS epoch measurements spanning the mid-Atlantic plate boundary in Northern Iceland 1987–1990, in *Gravimetry and Space Techniques Applied to Geodynamics and Ocean Dynamics*, eds. B. E. Schutz, A. Andersen, C. Froidevaux, and M. Parke, IUGG 17, Geophysical Monograph 82, American Geophysical Union, 1994.

Jakobsson, S. P., Chemistry and distribution patterns of Recent basaltic rocks in Iceland, *Lithos, 5*, 365–386, 1972.

Johnsen, G. V., A. Björnsson, and S. Sigurdsson, Gravity and elevation changes caused by magma movemnts beneath the Krafla caldera, northeast Iceland, *J. Geophys., 47*, 132–140, 1980.

Jovanovich, D. B., M. I. Husseini, and M. A. Chinnery, Elastic dislocations in a layered half space, I, Basic theory and numerical methods, *Geophys. J. R. astr. Soc., 39*, 205–217, 1974.

Kanngieser, E., Vertical component of ground deformation in north Iceland, *Ann. Geophys., 1*, 321–328, 1983.

Kirkby, S. H., Rheology of the lithosphere, *Rev. Geophys. Space Phys., 21*, 1458–1487, 1983.

Klein, F. W., P. Einarsson, and M. Wyss, Microearthquakes on the Mid-Atlantic plate boundary on the Reykjanes Peninsula in Iceland, *J. Geophys. Res., 78*, 5084–5099, 1973.

Klein, F. W., P. Einarsson, and M. Wyss, The Reykjanes Peninsula, Iceland, earthquake swarm of September 1972 and its tectonic significance, *J. Geophys. Res., 82*, 865–888, 1977.

Knopoff, L., Energy release in earthquakes, *Geophys. J. R. astr. Soc., 1*, 44–52, 1958.

Larson, K. M., and D. C. Agnew, Application of the Global Positioning System to crustal deformation measurement, 1., Precision and accuracy, *J. Geophys. Res., 96*, 16,567–16,584, 1991.

Lee, E. H., Stress analysis in viscoelastic bodies, *Quart. Appl. Math., 13*, 183–190, 1955.

Lehner, F. K., V. C. Li, and J. R. Rice, Stress diffusion along rupturing plate boundaries, *J. Geophys. Res., 86*, 6155–6199, 1981.

Leick, A., *GPS Satellite Surveying*, John Wiley and Sons, New York, 1990.

Lichten, S. M., and J. S. Border, Strategies for high precision GPS orbit determination, *J. Geophys. Res., 92*, 12,751–12,762, 1987.

Littell, F. B., and J. C. Hammond, World longitude operation, *Astronomical Journal, 38*, pp. 185, 1928.

Long, R. E., and M. G. Mitchell, Teleseismic P-wave delay time in Iceland, *Geophys. J. R. astr. Soc., 20*, 41–48, 1970.

Love, A. E. H., *Some Problems of Geodynamics*, Cambridge, 1911.

McKenzie, D., The generation and compaction of partially molten rock, *J. Petrol., 25*, 713–765, 1984.

Mackenzie, K., J. McClain, and J. Orcutt, Constraints on crustal structure in Eastern Iceland based on external inversions of refraction data, *J. Geophys. Res., 87*, 6371–6382, 1982.

Marquart, G., and W. Jacoby, On the mechanism of magma injection and plate divergence during the Krafla rifting episode in northeast Iceland, *J. Geophys. Res., 90*, 10,178–10,192, 1985.

Maruyama, T., Statical elastic dislocations in an infinite and semi-infinite medium, *Bull. Earthquake Res. Inst. Univ. Tokyo, 42*, 289–368, 1964.

Meissner, R., and J. Strehlau, Limits of stresses in continental crusts and their relations to the depth-frequency distribution of shallow earthquakes, *Tectonics, 1*, 73–89, 1982.

Melosh, H. J., Vertical movements following a dip-slip earthquake, *Geophys. Res. Letts., 10*, 47–50, 1983.

Menke, W., and V. Levin, Cold crust in a hot spot, *Geophys. Res. Letts., 21*, 1967–1970, 1994.

Minster, J. B., and T. H. Jordan, Present day plate motions, *J. Geophys. Res., 83*, 5331–5354, 1978.

Mogi, K., Relations between the eruptions of various volcanoes and the deformation of the ground surfaces around them, *Bull. Earthquake Res. Inst., 36*, 99–134, 1958.

Möller, D., Terrestrische geodätische Arbeiten zur Erfassung horizontaler rezenter Oberflächenbewegungen, *Zeitschrift für Vermessungswesen, 114*, pp. 10–25, Stuttgart, 1989.

Möller, D., and B. Ritter, Geodetic measurements and horizontal crustal movements in the rift zone of NE Iceland, *J. Geophys., 47*, 110–119, 1980.

Möller, D., B. Ritter, and K. Wendt, Geodetic measurement of horizontal deformations in northeast Iceland, *Earth Evol. Sci., 2*, 149–154, 1982.

Minster, J. B., and T. H. Jordan, Present day plate motions, *J. Geophys. Res., 83*, 5331–5354, 1978.

Morgan, J. P., and M. C. Kleinrock, Transform zone migration: Implications of bookshelf faulting at oceanic and Icelandic propagating ridges, *Tectonics, 10*, 920–935, 1991.

Nielsen, N., Tektonik und Vulkanismus unter Berücksichtigung der Wegener-Hypothese, *Geologische Rundschau, 21*, 347–349, 1930.

Niemczyk, O., and E. Emschermann, Sonderdreiecksmessung auf Island zur Feststellung feinster Erdkrustenbewegungen, in *Spalten auf Island*, ed. O. Niemczyk, Verlag von Konrad Wittwer, Stuttgart, pp. 80–113, 1943.

Nunns, A. G., Plate tectonic evolution of the Greenland-Scotland Ridge and surrounding region, in *Structure and Development of the Greenland-Scotland Ridge: New Methods and Concepts*, ed. M. H. P. Bott et al., Plenum Press, New York, 1983.

Officer, C. B., W. S. Newman, J. M. Sullivan, and D. R. Lynch, Glacial isostatic adjustment and mantle viscosity, *J. Geophys. Res., 93*, 6397–6409, 1988.

Okada, Y., Surface deformation due to shear and tensile faults in a half space, *Bull. Seism. Soc. Am., 75*, 1135–1154, 1985.

Oskarsson, N., S. Steinthórsson, and G. E. Sigvaldasson, Iceland geochemical anomaly: Volcanotectonics, chemical fractionation and isotope evolution of the crust, *J. Geophys. Res., 90*, 10,001–10,025, 1985.

Pálmason, G., *Crustal Structure of Iceland from Explosion Seismology*, Soc. Sci. Íslandica, pp. 187, 1971.

Pálmason, G., A continuum model of crustal generation in Iceland; Kinematic aspects, *J. Geophys., 47*, 7–18, 1980.

Pálmason, G., and K. Sæmundsson, Iceland in relation to the Mid-Atlantic Ridge, *Annu. Rev. Earth Planet. Sci., 2*, 25–50, 1974.

Pálmason, G., S. Arnorsson, I. B. Fridleifsson, H. Kristmannsdottir, K. Sæmundsson, V. Stefánsson, B. Steingrimsson, J. Tomasson, and L. Kristjansson, The Icelandic crust: Evidence from drillhole data on structure and processes, *American Geophysical Union, Ewing Series, 3*, 43–65, 1978.

Peltier, W. R., Deglaciation-induced vertical motion of the North-American continent and transient lower mantle rheology, *J. Geophys. Res., 91*, 9099–9123, 1986.

Pollard, D. D., P. T. Delaney, W. A. Duffield, E. T. Endo, and A. T. Okamura, Surface deformation in volcanic rift zones, *Tectonophys., 94*, 541–584, 1983.

Press, F., Displacements, strains and tilts at teleseismic distances, *J. Geophys. Res., 70*, 2395–2412, 1965.

Rocken, C., *The Global Positioning System: A New Tool for Tectonic Studies*, Ph.D. thesis, University of Colorado, 1988.

Roth, F., Deformations in a layered crust due to a system of cracks: modeling the effects of dike injections or dilatancy, *J. Geophys. Res., 98*, 4548–4551, 1993.

Rothacher, M., G. Beutler, W. Gurtner, T. Schildknecht, and U. Wild, *Documentation for Bernese GPS software version 3.2*, Univ. Bern, 1990.

Rubin, A., M., Dike-induced faulting and graben subsidence in volcanic rift zones, *J. Geophys. Res., 97*, 1839–1858, 1992.

Rundle, J. B., Viscoelastic crustal deformation by finite quasi-static sources, *J. Geophys. Res., 83*, 5937–5945, 1978.

Rundle, J. B., Static elastic-gravitational deformation of a layered half space by point couple sources, *J. Geophys. Res., 85*, 5354–5363, 1980.

Rundle, J. B., Vertical displacements from a rectangular fault in layered elastic-gravitational media, *J. Phys. Earth, 29*, 173–186, 1981.

Rundle, J. B., Viscoelastic-gravitational deformation by a rectangular thrust fault in a layered earth, *J. Geophys. Res., 87*, 7787–7796, 1982.

Rundle, J. B., An approach to modeling present-day deformation in southern California, *J. Geophys. Res., 91*, 1947–1959, 1986.

Rundle, J. B., and D. D. Jackson, A three-dimensional viscoelastic model of a strike-slip fault, *Geophys. J. R. astr. Soc., 49*, 575–591, 1977.

Rydelek, P. A., and I. S. Sacks, Asthenospheric viscosity and stress diffusion: A mechanism to explain correlated earthquakes and surface deformations in northeast Japan, *Geophys. J. Int., 100*, 39–58, 1990.

Rymer, H., and E. Tryggvason, Gravity and elevation changes at Askja, Iceland, *Bull. Volcanol., 55*, 362–371, 1993.

Saastamoinen, J., Atmospheric correction for the troposphere and stratosphere in radio ranging of satellites, in *Use of Artificial Satellites for Geodesy*, Geophysical Monograph 15, American Geophysical Union, DC, 1972.

Sæmundsson, K., Evolution of the axial rifting zone in northern Iceland and the Tjörnes Fracture Zone, *Geol. Soc. Am. Bull., 85*, 495–504, 1974.

Sæmundsson, K., Fissure swarms and central volcanoes of the neovolcanic zones of Iceland, *Geol. J. Spec. Issue, 10*; 415–432, 1978.

Sæmundsson, K., Outline of the geology of Iceland, *Jökull, 29*, 7–28, 1979.

Sæmundsson, K., Subaerial volcanism in the western North Atlantic, in *The geology of North America, Volume M, The Western North Atlantic Region*, eds. P. R. Vogt and B. E. Tucholke, The Geological Society of America, 1986.

Savage, J. C., and W. H. Prescott, Asthenosphere readjustment and the earthquake cycle, *J. Geophys. Res., 83*, 3369–3376, 1978.

Savage, J. C., and M. M. Clark, Magmatic resurgence in Long Valley caldera, California: possible cause of the 1980 Mammoth Lakes earthquakes, *Science, 217*, 531–533, 1982.

Schapery, R. A., Approximate methods of transform inversion for viscoelastic stress analyses, *Proc. Fourth U. S. Natl. Congr. Appl. Mech., 4th*, 1075–1085, 1961.

Schmeling, H., Partial melt below Iceland: A combined interpretation of seismic and conductivity data, *J. Geophys. Res., 90*, 10,105–10,116, 1985.

Sigmundsson, F., Post-glacial rebound and asthenosphere viscosity in Iceland, *Geophys. Res. Letts., 18*, 1131–1134, 1991.

Sigmundsson, F., and P. Einarsson, Glacio-isostatic crustal movements caused by historical volume change of the Vatnajökull icecap, Iceland, *Geophys. Res. Letts., 19*, 2123–2126, 1992.

Sigmundsson, F., P. Einarsson, and R. Bilham, Magma chamber deflation recorded by the Global Positioning System: The Hekla 1991 eruption, *Geophys. Res. Letts., 19*, 1483–1486, 1992.

Sigmundsson, F., P. Einarsson, R. Bilham, and E. Sturkell, Rift-transform kinematics in south Iceland: Deformation from Global Positioning System measurements, 1986–1992, in press, *J. Geophys. Res.*, 1995.

Sigurdsson, H., and R. S. J. Sparks, Rifting episode in north Iceland in 1874–1875, and the eruption of Askja and Sveinagjá, *Bull. Volcanol., 41*, 149–167, 1978.

Sigurdsson, O., Surface deformation of the Krafla fissure swarm in two rifting events, *J. Geophys., 47*, 154–159, 1980.

Sigvaldason, G. E., S. Steinthorsson, N. Oskarsson, and P. Imsland, Compositional variation in recent Icelandic tholeiites and the Kverkfjöll hotspot, *Nature, 251*, 579–582, 1974.

Singh, S. J., Static deformation of a multilayered half space by internal sources, *J. Geophys. Res., 75*, 3257–3263, 1970.

Stefánsson, R., R. Bödvarsson, R. Slunga, P. Einarsson, S. Jakobsdottir, H. Bungum, S. Gregersen, J. Havskov, J. Hjelme, and H. Korhonen, Earthquake prediction in the South Iceland Seismic Zone and the SIL project, *Bull. Seism. Soc. Am., 83*, 696–716, 1993.

Steinthórsson, S., and W. Jacoby, Crustal accretion in and around Iceland, *J. Geophys. Res., 90*, 9951–9952, 1985.

Steketee, J., On Volterra's dislocations in a semi-infinite elastic medium, *Can. J. Phys., 36*, 192–205, 1958.

Stephens, S., GIPSY frontend users guide, *JPL Publ., D-3918*, 1986.

Sturkell, E., F. Sigmundsson, P. Einarsson, and R. Bilham, Strain accumulation 1986-1992 across the Reykjanes Peninsula plate boundary, Iceland, determined from GPS measurements, *Geophys. Res. Letts.*, *21*, 125–128, 1994.

Sykes, L. R., Mechanism of earthquakes and nature of faulting on mid-ocean ridges, *J. Geophys. Res.*, *72*, 2131-2153, 1967.

Talwani, M., and O. Eldholm, Evolution of the Norwegian–Greenland Sea, *Geol. Soc. Am. Bull.*, *88*, 969-999, 1977.

Thatcher, W., Nonlinear strain buildup and the earthquake cycle on the San Andreas fault, *J. Geophys. Res.*, *88*, 5893–5902, 1983.

Thatcher, W., and J. B. Rundle, A model for the earthquake cycle in underthrust zones, *J. Geophys. Res.*, *84*, 5540–5556, 1979.

Thatcher, W., and J. B. Rundle, A viscoelastic coupling model for the cyclic deformation due to periodically repeated earthquakes at subduction zones, *J. Geophys. Res.*, *89*, 7631–7640, 1984.

Thatcher, W., T. Matsuda, T. Kato, and J. B. Rundle, Lithospheric loading by the Riku-U earthquake, northern Japan: Implications for plate flexure and asthenospheric rheology, *J. Geophys. Res.*, *85*, 6429-6435, 1980.

Thayer, R. E., A. Björnsson, L. Alvarez, and J. F. Hermance, Magma genesis and crustal spreading in the northern neovolcanic zone of Iceland: Telluric-magnetotelluric constraints, *Geophys. J. R. astr. Soc.*, *65*, 423–442, 1981.

Thomson, W. T., Transmission of elastic waves through a stratified medium, *J. Appl. Phys.*, *21*, 89–93, 1950.

Thorarinsson, S., The median zone of Iceland, in *The World Rift System*, Geol. Survey of Canada, Paper 66–14, pp. 187-211, 1965.

Tryggvason, E., Arrival times of P waves and upper mantle structure, *Bull. Seism. Soc. Am.*, *54*, 727-736, 1964.

Tryggvason, E., Seismicity, earthquake swarms and plate boundaries in the Iceland region, *Bull. Seism. Soc. Am.*, *63*, 1327–1348, 1973..

Tryggvason, E., Widening of the Krafla fissure swarm during the 1975–1985 volcano-tectonic episode, *Bull. Volcanol.*, *47-1*, 1984.

Tryggvason, E., Surface deformation at the Krafla volcano, North Iceland, 1982–1992, *Bull. Volcanol.*, *56*, 98-107, 1994.

Vink, G. E., A hotspot model for Iceland and the Vøring Plateau, *J. Geophys. Res.*, *89*, 9949–9959, 1984.

Vogt, P. R., Plate kinematics during the last 20 m.y. and the problem of "present" motions, in *The geology of North America, Volume M, The Western North Atlantic Region*, eds. P. R. Vogt and B. E. Tucholke, The Geological Society of America, 1986.

Wanach, B., Ein Beitrag zur Flage der Kontinentalverschiebung, *Zeitschrift für Geophysik, 2*, 161–163, 1926.

Ward, P. L., New interpretation of the geology of Iceland, *Geol. Soc. Am. Bull., 82*, 2991–3012, 1971.

Ward, P. L., and S. Björnsson, Microearthquakes, swarms, and the geothermal areas of Iceland, *J. Geophys. Res., 76*, 3953-3982, 1971.

Wegener, A., Die Entstehung der Kontinente, *Petermanns Geogr. Mitt., 58*, 305–309, 1912.

Wegener, A., *Die Entstehung der Kontinente und Ozeane*, Vieweg, Braunschweig, 1915.

Wells, D. E., N. Beck, D. Delikaraoglou, A. Kleusberg, E. J. Krakiwsky, G. Lachapelle, R. B. Langley, M. Nakiboglu, K. P. Schwarz, J. M. Tranquilla and P. Vaniĉek, *Guide to GPS Positioning*, Canadian GPS Associates, Fredricton, N. B., Canada, 1986.

Wendt, K., D. Möller, and B. Ritter, Geodetic measrurements of surface deformations during the present rifting episode in northeast Iceland, *J. Geophys. Res., 90*, 10,163–10,172, 1985.

White, R. S., D. McKensie, and R. K. O'Nions, Oceanic crustal thickness from seismic measurements and rare Earth element inversions, *J. Geophys. Res., 97*, 19,683–19,715, 1992.

Williams, S. D. P., *Current Motion on Faults of the San Andreas System in Central California Inferred from Recent GPS and Terrestrial Survey Measurements*, Ph. D. thesis (in preparation), University of Durham, 1995.

Wübbena, G., The GPS adjustment software package – GEONAP – concepts and models, in *Procedings of the fifth International Geodetic Symposium on Satellite Positioning*, pp. 452–461, Las Cruces, New Mexico, 1989.

Yang, M., and M. N. Toksöz, Time-dependent deformation and stress relaxation after strike slip earthquakes, *J. Geophys. Res., 86*, 2889–2901, 1981.

Zverev, S. M., I. P. Kosminskaya, G. A. Krasilschikova, and G. G. Mikhota, The crustal structure of Iceland and of the Iceland–Faeroe–Shetland region, *Soc. Sci. Íslandica, 5*, 72–95, 1976.

Zverev, S. M., I. V. Litvinenko, G. Pálmason, G. A. Yaroshevskaya, N. N. Osokin, and M. A. Akhmetjev, A seismic study of the rift zone in northern Iceland, *J. Geophys., 47*, 191–201, 1980a.

Zverev, S. M., I. V. Litvinenko, G. Pálmason, G. A. Yaroshevskaya, and N. N. Osokin, A seismic crustal study of the axial rift zone in southwest Iceland, *J. Geophys.,47*, 202–210, 1980b.

Zverev, S. M., I. V. Litvinenko, G. Pálmason, and G. A. Yaroshevskaya, Seismic model of Eastern Iceland, in *Geological-Geophysical Studies of the Ocean Floor*, 139 pp., Acad. Sci. USSR, Moscow, 1985.

Appendix A

Readme Text Accompanying Programs NFLTGRH and NFLTGRV

A.1 Introduction

NFLTGRH and **NFLTGRV** compute the horizontal and vertical displacements at the surface of an elastic layer overlying a viscoelastic halfspace due to dyke emplacement along a finite or infinite plane.

Gravity acts in both the layer and half space.

Gravitational effects can be "turned off".

The displacement is calculated at specified (X, Y) coordinates where the X-coordinate is the distance parallel to the fault (relative to the fault centre) and the Y-coordinate is the distance perpendicular to the fault.

The fault dips in the positive Y direction.

Postseismic displacements at specified times are calculated, along with the coseismic displacements.

To compile : *make nfltgrh* or *make nfltgrv.*

Usage : *nfltgrh* or *nfltgrv.*

(The directory must contain the four input files).

Output files : *output.*

A.2 Input Files

A.2.1 File *input*

There are four required input files for **NFLTGRH** and **NFLTGRV**. The first of these is file *input*, which is a collection of the input parameters.

An example *input* file is:

Table A.1: Example input file for programs **NFLTGRH** and **NFLTGRV**.

Data input file for NFLTGRH and NFLTGRV		
Name	Value	Comment
H	30.d0	layer thickness (units km)
HMIN	0.d0	minimum vertical depth ie depth to top of dyke (units km)
W	30.d0	dyke width down dip (units km)
AL	200.d0	dyke semilength ie dyke is twice this length (units km) – for infinitely long dyke use 1.e5 < AL < 1.e8
THETA	90.d0	dip angle in degrees
U	200.d0	amount of dislocation (units determine units of output)
ALAM	3.0d0	lame constant for top layer (units 10^{11} dyne/cm^2)
ALAM1	3.0d0	lame constant for halfspace (units 10^{11} dyne/cm^2)
AMU	3.0d0	lame constant for top layer (units 10^{11} dyne/cm^2)
AMU1	3.0d0	lame constant for halfspace (units 10^{11} dyne/cm^2)
YSTART	0.1d0	start value for y coordinate (perpendicular to strike)
DYOBS	10.0d0	step increase in y
NNY	50	number of y coordinate values
XSTART	0.0d0	start value for x coordinate (parallel to strike)
DXOBS	10.d0	step increase in x
NNX	1	number of x coordinate_values
INDIC	0	if INDIC is > than 0, then the value of INDIC should correspond to the no. of coord pairs entered in inputc ie in this case user specified points are used (YSTART,XSTART, DYOBS,DXOBS,NNY,NNX not used when INDIC > 0)
TSTART	0.d0	time after event when computation starts
DELT	10.d0	time value increments – in units of relaxation time
NTIME	6	number of time value increments (must be <100) (if INTIME=1 then NTIME=no. of values given in time file) (TSTART,DELT not used when INTIME=1)
NMTERM	6	number of exponential terms in prony series – actual coefficients (timepoles) written in poles file
INTIME	0	if INTIME=1,individual times read in using time file
NREL	1	if NREL is 1, you get asthenospheric relaxation if NREL is 2, you get lithospheric relaxation if NREL is 3, you get poroelastic relaxation
RHOL	3.0d0	density of layer (units g/cm^3)
RHOH	3.0d0	density of halfspace (units g/cm^3)
RHOFCT	1.d0	density factor. RHOFCT means density acts. To minimise gravitational effects, set RHOFCT to 0.1

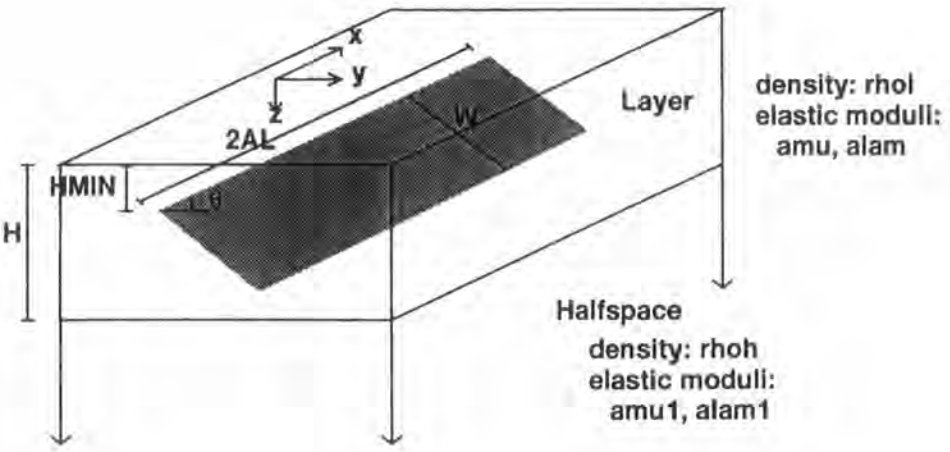

Figure A.1: Geometry of fault plane, and schematic illustration of model parameters.

The fault plane geometry and a schematic illustration of the input parameters are shown in Figure A.1.

Notes:

(a) W : the fault must not extend into the halfspace : choose W carefully.

(b) AL : if AL $> 1 \times 10^5 < 1 \times 10^6$ then an infinitely-long fault is used.

(c) THETA : a minimum of 5° for the dip angle is advisable.

(d) The postseismic times are normalised by the relaxation time τ, where $\tau = 2\eta/\mathrm{G}$, η is the Maxwell viscosity, and G is the elastic modulus of the Maxwell fluid.

(e) NREL : three relaxation models are possible:

If NREL=1 then AMU1 relaxes.

If NREL=2 then AMU, ALAM relax, Poisson's ratio in halfspace is constant.

If NREL=3 then AMU1, ALAM1 relax, BULK MODULUS in halfspace is constant.

NB: Only NREL=1 case has been investigated for the dyke emplacement model.

(f) NNY $*$ NNX : the maximum number of points (NNX $*$ NNY) is 50.

(g) NTIME : the maximum number of times (NTIME) is 100.

(h) INDIC, INTIME : file *input* in this form calculates the observation points and postseismic times implicitly. To specify (X, Y), INDIC must be set to a value > 0 that corresponds to the number of coordinate pairs written in file inputc. To use specific postseismic times, INTIME should be set to 1 and NTIME should have a value corresponding to the number of times in the *inputt* file.

A.2.2 File *inputp*

This specifies the time poles for the Prony series.

An example *inputp* file is:

Table A.2: Example inputp file for programs **NFLTGRH** and **NFLTGRV**.

inputp: coefficients for the Prony series (usually set to 6 as given by NMTERM
000.5d0
001.0d0
005.0d0
010.0d0
050.0d0
100.0d0

Note:

These values are picked arbitrarily and should not require changing. Small differences result when a more rigourous method is used to determine these values [*Rundle*, 1982].

A.2.3 File *inputc*

This is used to specify explicit points if these are required. Otherwise benchmarks are calculated according to the parameters given in the *input* file.

An example *inputc* file is:

Table A.3: Example inputc file for programs **NFLTGRH** and **NFLTGRV**.

inputc: contains (X,Y) coords for Ux, Uy calculation	
******·******	******·******
0.0	-250.0
0.0	-200.0
0.0	-150.0
0.0	-100.0

Note:

The maximum number of benchmarks allowed is 50.

A.2.4 File *inputt*

This specifies the post event observation times, else these times are calculated according to parameters given in the *input* file.

An example *inputt* file is:

Table A.4: Example inputt file for programs **NFLTGRH** and **NFLTGRV**.

```
inputt file: postseismic observation times (in units of relaxation time)
(no. of entered values must = ntime used in input file).
******·******
          1.d0
          2.d0
          3.d0
          4.d0
          1.d2
          1.d4
```

Note:

The maximum number of postseismic times is 100.

A.3 Output File

A sample part of an output file is:

```
Source is dyke
 layer thickness:            h =  30.00 km
 minimun vertical depth: hmin =   0.00 km
 fault length down dip:     w =  30.00 km
 fault semilength:         al = 200.00 km
 dip angle:             theta =  90.00 degrees
 dislocation:               u = 200.00

 lame constants.  layer:
                        amu =  3.000 dyne*cm**-2
                       alam =  3.000
              halfspace:
                       amul =  3.000
                      alaml =  3.000


 finite rectangular fault

 amul relaxes

 densities.       layer:
                       rhol =  3.000 g*cm**-3
              halfspace:
                       rhoh =  3.000
```

```
nb : x step size may be too small.

time poles are:
                  0.50000000
                   1.0000000
                   5.0000000
                   10.000000
                   50.000000
                   100.00000

x=        0.    y=   0.10000000

dx: elastic part=        0.     additional part=  0.25817049E-18
dy: elastic part=   99.997942      additional part=  0.43396450E-04

t=   1.0000000     postseismic ux= -0.15133188E-14 uy=  0.70882470E-02

t=   2.0000000     postseismic ux= -0.20530625E-14 uy=  0.17253509E-02

t=   5.0000000     postseismic ux= -0.13242152E-14 uy= -0.91460038E-02

t=   8.0000000     postseismic ux= -0.15262305E-14 uy= -0.13466648E-01

t=   50.000000     postseismic ux= -0.64118795E-15 uy= -0.17743058E-01

t=   10000.000     postseismic ux= -0.15469885E-13 uy= -0.16473004E-01

x=        0.    y=    10.100000

dx: elastic part=        0.     additional part=  0.31585733E-18
dy: elastic part=   98.369010      additional part=  0.40338216E-02

t=   1.0000000     postseismic ux= -0.11157197E-14 uy=   1.3148527

t=   2.0000000     postseismic ux= -0.16048470E-14 uy=   1.1288247

t=   5.0000000     postseismic ux= -0.18636778E-14 uy=  0.39594900

t=   8.0000000     postseismic ux= -0.21738786E-14 uy=  0.52912991E-01

t=   50.000000     postseismic ux= -0.95047216E-15 uy= -0.38422324

t=   10000.000     postseismic ux= -0.78461255E-14 uy= -0.30919481

x=        0.    y=    20.100000

dx: elastic part=        0.     additional part=  0.21609786E-18
dy: elastic part=   91.444037      additional part=  0.66224332E-02

t=   1.0000000     postseismic ux= -0.10023248E-14 uy=   4.7176122

t=   2.0000000     postseismic ux= -0.15596520E-14 uy=   5.6698285

t=   5.0000000     postseismic ux= -0.30424390E-14 uy=   5.6405331

t=   8.0000000     postseismic ux= -0.30115304E-14 uy=   5.3482901

t=   50.000000     postseismic ux= -0.16070378E-14 uy=   4.4857321

t=   10000.000     postseismic ux=  0.94439504E-15 uy=   4.4228503
```

ETC.

A.4 Run Times

For program **NFLTGRH** the displacements at 50 benchmarks using 6 Prony series coefficients takes ~6 hours on a SUN 4 (~2.5 hours on a Sparc 10).

For program **NFLTGRV** the displacements at 50 benchmarks using 6 Prony series coefficients takes ~2 hours on a Sparc 10.

A.5 Useful References

Rundle, J. B., Viscoelastic crustal deformation by finite, quasistatic sources, *J. Geophys. Res., 83*, 5937-5945, 1978.

Rundle, J. B., Static-elastic gravitational deformation of a layered half space by point couple sources, *J. Geophys. Res., 85*, 5355-5363, 1980.

Rundle, J. B., Viscoelastic-gravitational deformation by a rectangular thrust fault in a layered earth, *J. Geophys. Res., 87*, 7787-7796, 1982.

Hofton, M. A., Rundle, J. B., and G. R. Foulger, Surface deformation due to dyke emplacement in an elastic-gravitational layer overlying a viscoelastic- gravitational half-space, in press, *Journal of Geophysical Research*, 1995.

To appear in the *Journal of Geophysical Research*, 1995.

Horizontal surface deformation due to dike emplacement in an elastic-gravitational layer overlying a viscoelastic-gravitational half-space

M. A. Hofton
Department of Geological Sciences, University of Durham, Durham, England.

J. B. Rundle
Cooperative Institute for Research in Environmental Sciences, University of Colorado, Boulder.

G. R. Foulger
Department of Geological Sciences, University of Durham, Durham, England.

Abstract

We extend a technique previously used to model surface displacements resulting from thrust faulting in an elastic-gravitational layer over a viscoelastic-gravitational half-space to the case of dike emplacement. The method involves the calculation of the Green's functions for a dike point source contained in an elastic-gravitational layer over an elastic-gravitational half-space. The correspondence principle is then applied to introduce time dependence. The resultant Green's functions are integrated over the source region to obtain the near-field displacements. Several example calculations are presented involving 90°, 60°, and 30° dipping dikes, extending completely and partially through the elastic layer. We also illustrate the time dependent deformation due to buried dikes. Dikes extending completely through the elastic layer produce a larger-amplitude long-wavelength component than those extending partially through the elastic layer. Inflexion points are seen in the dike-normal horizontal deformation profiles when the base of the dike intersects the top of the half-space, providing a means of differentiating between vertical surface dikes extending completely and partially through the elastic layer. All results show that the use of a viscoelastic half-space underlying an elastic layer introduces a long-wavelength component into the deformation field that cannot be predicted by elastic half-space models.

Introduction

An important goal of modern crustal deformation studies is to understand the transient postevent ground deformation sometimes seen following large earthquakes and dike emplacement events. Stress relaxation in a nonelastic region situated below the surface elastic zone is one possible mechanism for transient strain [e.g., *Thatcher and Rundle*, 1979; *Thatcher et al.*, 1980; *Cohen*, 1984]. A second possible explanation is continued slip at depth on the fault or dike plane.

Elastic models involving dislocation sources in a homogeneous half-space [e.g., *Chinnery*, 1961; *Okada*, 1985] or in a layered half-space [e.g., *Jovanovich et al.*, 1974] cannot explain time dependent transient behavior. One method of introducing time dependence is by including a viscoelastic half-space. *Nur and Mavko* [1974], *Rundle and Jackson* [1977], *Spence and Turcotte* [1979], *Rundle* [1978, 1980], *Savage and Prescott* [1978], *Matsu'ura and Tanimoto* [1980], and others have studied the time dependent behavior with thrust or strike-slip sources. Authors dealing with dilatational sources include *Roth* [1993], who found a solution for an opening crack contained in a layered elastic half-space that could be extended to simulate a system of dikes, and *Heki et al.* [1993], who proposed a viscous diffusion model for postdiking stress relaxation at divergent plate boundaries.

We extend the work of *Rundle* [1980, 1981] to include the case of dike opening in an elastic layer overlying a viscoelastic half-space, the application of which will be especially useful in predicting transient deformation in areas of active tectonic rifting and at mid-ocean ridges. We limit the choice of materials in the viscoelastic region to those whose rheological properties have linear constitutive laws since even though the deformations are large, the strains are small as these depend on the small differences between time dependent displacements and the steady plate velocity. Because the strains are small, we can use a linear model; the nonlinear terms will all be negligible compared to the magnitude of the linear terms. A Maxwell rheology is also assumed which implies the inelastic region behaves as an elastic solid over short time periods and as a Newtonian fluid over long timescales. This is considered by the authors to be the most appropriate linear rheology for long-term deformation processes within the Earth.

We include gravitational effects in our calculations. For deformation at the surface of an elastic half-space, gravitational effects become significant over wavelengths greater than 1000 km [*Rundle*, 1980] but have little relevance to deformation near the source region. In viscoelastic structures, stresses in some regions of the Earth decrease as flow occurs: the initial elastic stresses induce flow in the medium, generating a change in the displacements and gravitational stresses as a result. Equilibrium is eventually attained between the gravitational and elastic stresses in the flowing region. However over short time intervals gravitational effects are small [*Rundle*, 1981], and the inclusion of gravitational effects is significant only when the event is assumed to reoccur, producing a cyclic distribution of events.

In this paper, surface displacements following dike emplacement are modeled using Green's functions. The solutions for the elastic-gravitational problem are first computed. Then the correspondence principle which relates the elastic-gravitational solution to the Laplace-transformed viscoelastic-gravitational solution is applied. Finally, the resultant Green's functions are integrated over the finite source region to obtain the time dependent, near-field displacements. A brief review of the method developed by *Rundle* [1980, 1981] is given here.

Solution to the Infinite Space Problem

Rundle [1981] found that for displacements resulting from a dip-slip event in a layered elastic-gravitational medium, self-gravitation effects arising from the nonzero value of G_0, the gravitational constant, were generally much smaller than gravitational effects relating to the surface acceleration, g. Making use of this, *Rundle* [1981] considered the governing equations [*Love*, 1911]

$$\nabla^2\vec{u} + \frac{1}{1-2\sigma}\nabla\nabla\cdot\vec{u} + \frac{\rho_0 g}{\mu}\nabla(\vec{u}\cdot\hat{e_z}) - \frac{\rho_0}{\mu}\nabla\phi - \frac{\rho_0 g}{\mu}\hat{e_z}\nabla\cdot\vec{u} = 0, \qquad (1)$$

$$\nabla^2\phi = -4\pi\rho_0 G_0 \nabla\cdot\vec{u}, \qquad (2)$$

where $\vec{u}$ is the perturbed displacement vector in the deformed cylindrical coordinate system (r,θ,z), ϕ is the gravitational potential in this coordinate system, $\hat{e_r}$, $\hat{e_\theta}$, and $\hat{e_z}$ are the unit vectors, σ is Poisson's ratio, ρ_0 is the density and μ is the rigidity. As $z \rightarrow \infty$, all perturbed quantities are presumed to tend to zero, so setting $G_0 = 0$ implies ϕ is constant. In this case we may write

$$\nabla^2\vec{u}+\frac{1}{1-2\sigma}\nabla\nabla\cdot\vec{u}+\frac{\rho_0 g}{\mu}\nabla(\vec{u}\cdot\hat{e_z})-\frac{\rho_0 g}{\mu}\hat{e_z}\nabla\cdot\vec{u}=0. \tag{3}$$

Using the vector base

$$\begin{aligned}\vec{P_m} &= J_m(kr)e^{im\theta}\hat{e_z}, && (4)\\ \vec{B_m} &= \left(\frac{\partial J_m(kr)}{\partial kr}\hat{e_r}+im\frac{J_m(kr)}{kr}\hat{e_\theta}\right)e^{im\theta}, && (5)\\ \vec{C_m} &= \left(im\frac{J_m(kr)}{kr}\hat{e_r}-\frac{\partial J_m(kr)}{\partial kr}\hat{e_\theta}\right)e^{im\theta}, && (6)\end{aligned}$$

where $J_m(kr)$ are cylindrical Bessel functions, $i=\sqrt{-1}$, and k corresponds to the wave number in dynamical problems [cf. *Ben Menahem and Singh*, 1968], we can expand $\vec{u}$ in terms of equations (4) to (6) as

$$\vec{u}=\sum_{m=0}^{\infty}\int_0^{\infty}k\,dk[W_m(z)\vec{P_m}+U_m(z)\vec{B_m}+V_m(z)\vec{C_m}]. \tag{7}$$

The solution given by $V_m(z)$ is not considered as it is found to be identical to the solution in the nongravitating case. $U_m(z)$ and $W_m(z)$ are given by *Rundle* [1981] as

$$\begin{pmatrix}U_m(z)\\ V_m(z)\end{pmatrix}=\begin{pmatrix}1\\ p_1^+(k)\end{pmatrix}e^{a_1 z}+\begin{pmatrix}1\\ p_1^-(k)\end{pmatrix}e^{-a_1 z} +k\begin{pmatrix}1\\ p_2^+(k)\end{pmatrix}e^{a_2 z}+k\begin{pmatrix}1\\ p_2^-(k)\end{pmatrix}e^{-a_2 z}, \tag{8}$$

where

$$\begin{aligned}\pm a_1 &= \pm(k^2+k\eta\sqrt{\zeta})^{1/2}, && (9)\\ \pm a_2 &= \pm(k^2-k\eta\sqrt{\zeta})^{1/2}, && (10)\\ \zeta &= \frac{1-2\sigma}{2(1-\sigma)}, && (11)\end{aligned}$$

$$p_j^{\pm}(k)=\pm 1-\frac{k\eta\sqrt{\zeta}}{(a_j+k)}\,\frac{1+\sqrt{\zeta}}{a_j-k\sqrt{\zeta}},\quad j=1,2, \tag{12}$$

and

$$\begin{aligned}\eta &= \frac{\rho_0 g}{\mu}=\rho g, && (13)\\ \rho &= \frac{\rho_0}{\mu}. && (14)\end{aligned}$$

The gravitational wave number k_g, found by setting $a_2(k)=0$, is defined as

$$k_g=\eta\sqrt{\zeta}. \tag{15}$$

For $k<k_g$, a_2 is purely imaginary, and for $k>k_g$, a_2 is real.

Solution to the Layered Half-Space Problem

Rundle [1980] used a polar coordinate system (r,θ,z) with unit vectors $\hat{e_r},\hat{e_\theta}$, and $\hat{e_z}$, and with the z axis oriented down into the medium at the surface of a layered, elastic-gravitational half-space. The elastic moduli in the nth layer are denoted by λ_n and μ_n, and the density by ρ_n. The solution in the nth layer is given by

$$\vec{u^n}=\sum_{m=0}\int_0^{\infty}k\,dk\,\vec{u^n_m}, \tag{16}$$

where $\vec{u^n_m}$ is given by

$$\vec{u^n_m}=x^n_m\vec{P_m}+y^n_m\vec{B_m}+z^n_m\vec{C_m}, \tag{17}$$

and the kernel functions x^n_m, y^n_m and z^n_m are

$$\begin{aligned}x^n_m &= -e^{-kz}A^-_{mn}+e^{kz}A^+_{mn}+p_1^-e^{-a_1 z}B^-_{mn}\\ &\quad+p_1^+e^{a_1 z}B^+_{mn}+kp_2^-e^{-a_2 z}D^-_{mn}\\ &\quad+kp_2^+e^{a_2 z}D^+_{mn}, && (18)\\ y^n_m &= e^{-kz}A^-_{mn}+e^{kz}A^+_{mn}+e^{-a_1 z}B^-_{mn}\\ &\quad+e^{a_1 z}B^+_{mn}+ke^{-a_2 z}D^-_{mn}+ke^{a_2 z}D^+_{mn}, && (19)\\ z^n_m &= e^{-kz}C^-_{mn}+e^{kz}C^+_{mn}. && (20)\end{aligned}$$

Here $\pm a_1$ and $\pm a_2$ are defined by equations (9) and (10). The same formulation is applied to the stresses across the layer boundaries to obtain similar expressions for the normal tractions across a plane.

As can be seen from equations (18) to (20), the problem can be divided into two separate parts, the "R" problem (that includes the x^n_m and y^n_m terms) and the "L" problem (that includes the z^n_m terms). The solutions to these problems are given by *Rundle* [1980, (equations 88–96)].

Source Functions

The source functions $[D_m]$ for the six elementary displacement dislocation sources have been derived by *Ben Menahem and Singh* [1968]. In the notation of *Singh* [1970], (jk) refers both to the direction of the force system and the normal to the plane across which it is applied. For a dike inclined at an angle ψ to the horizontal

$$(jk)=(3,3)\cos^2\psi+(2,2)\sin^2\psi-(2,3)\sin 2\psi, \tag{21}$$

with each component given by

$$\begin{aligned}
(jk) = (2,2): \quad & (D_0)_1 = 2\gamma\,(3\delta - 1)/(\delta + 1), \\
& (D_0)_4 = \mu\gamma\,(7\delta - 1)/(\delta + 1), \\
& (D_2)_4 = \mu\gamma, \\
& (D_2^L)_2 = -2\mu\gamma i, \qquad (22) \\
(jk) = (3,3): \quad & (D_0)_1 = 2\gamma, \\
(jk) = (2,3): \quad & (D_1)_2 = -2\gamma i, \\
& (D_1^L)_1 = -2\gamma.
\end{aligned}$$

Here $\gamma = \Delta U d\Sigma/4\pi$, where ΔU is the relative displacement across the crack, $d\Sigma$ is an element of area on the crack, and δ=1/(3-4σ).

Hence we have three different source function contributions to the diking problem, one describing opening in the vertical direction ($m = 0$), a second describing opening in the horizontal direction ($m = 2$) and a shearing component ($m = 1$). Using equations (16) and (17) and summing these three contributions, the displacement at the surface may be written as

$$\begin{aligned}
\vec{u} = \int_0^\infty k\,dk \Big\{ & \Big[x_0^{1(33)}(0)\vec{P}_0 + y_0^{1(33)}(0)\vec{B}_0 \Big] \cos^2\psi \\
& + \Big[x_0^1(0)\vec{P}_0 + y_0^1(0)\vec{B}_0 + x_2^1(0)\vec{P}_2 + y_2^1(0)\vec{B}_2 \\
& + z_2^1(0)\vec{C}_2 \Big] \sin^2\psi - \Big[x_1^1(0)\vec{P}_1 + y_1^1(0)\vec{B}_1 \\
& + z_1^1(0)\vec{C}_1 \Big] \sin 2\psi \Big\}. \qquad (23)
\end{aligned}$$

The superscript (33) distinguishes the kernel functions of the $(jk) = (3,3)$ component from the $(jk) = (2,2)$ component. Substituting equations (4) to (6) for $\vec{P}_m$, $\vec{B}_m$ and $\vec{C}_m$, replacing $e^{im\theta}$ and $ie^{im\theta}$ by $\cos m\theta$ and $-\sin m\theta$, respectively, to obtain the real part, and splitting the displacement vector into its three components, we obtain

$$\begin{aligned}
u_r = -\int_0^\infty k\,dk \Big\{ & y_0^{1(33)}(0) J_1(kr) \cos^2\psi \\
& + \Big(y_0^1(0) J_1(kr) - \Big[y_2^1(0) \Big(\frac{J_1(kr) - J_3(kr)}{2} \Big) \\
& - \frac{1}{i} z_2^1(0) \Big(\frac{J_1(kr) + J_3(kr)}{2} \Big) \Big] \cos 2\theta \Big) \sin^2\psi \\
& - \Big[\frac{1}{i} y_1^1(0) \Big(\frac{J_0(kr) + J_2(kr)}{2} \Big) \\
& + z_1^1(0) \Big(\frac{J_0(kr) + J_2(kr)}{2} \Big) \Big] \sin\theta \sin 2\psi \Big\}, \qquad (24)
\end{aligned}$$

$$\begin{aligned}
u_\theta = \int_0^\infty k\,dk \Big\{ & \Big[\frac{1}{i} z_2^1(0) \Big(\frac{J_1(kr) - J_3(kr)}{2} \Big) \\
& - y_2^1(0) \Big(\frac{J_1(kr) + J_3(kr)}{2} \Big) \Big] \sin 2\theta \sin^2\psi \\
& + \Big[\frac{1}{i} y_1^1(0) \Big(\frac{J_0(kr) + J_2(kr)}{2} \Big) \\
& + z_1^1(0) \Big(\frac{J_0(kr) - J_2(kr)}{2} \Big) \Big] \cos\theta \sin 2\psi \Big\}, \qquad (25)
\end{aligned}$$

$$\begin{aligned}
u_z = \int_0^\infty k\,dk \Big\{ & x_0^{1(33)}(0) J_0(kr) \cos^2\psi \\
& + x_0^1(0) J_0(kr) \sin^2\psi + x_2^1(0) J_2(kr) \cos 2\theta \sin^2\psi \\
& + \frac{1}{i} x_1^1(0) J_1(kr) \sin\theta \sin 2\psi \Big\}. \qquad (26)
\end{aligned}$$

Equations (24) to (26) give the solution to the elastic-gravitational problem of a point nucleus of dilation in an elastic-gravitational layer over an elastic-gravitational half-space.

Introduction of Viscoelasticity

As the first step, the correspondence principle of linear viscoelasticity is applied [*Lee*, 1955]. This requires that the elastic quantities λ and μ in each component of the elastic solution be replaced by their Laplace transformed quantities $s\bar{\lambda}(s)$ and $s\bar{\mu}(s)$ to obtain $\bar{u}(s)$ where the bar signifies the Laplace-transformed quantity and s is the parameter conjugate to time. Then $\bar{u}(s)$ is inverted to give $u_v(t)$, the solution to the viscoelastic problem. The technique used to perform the inversion involves the Prony series where the function $u_v(t)$ is approximated by a function $u_v^*(t)$ composed of a series of decaying exponentials. Following *Schapery* [1961] and *Cost* [1964] we set

$$u_v(t) \cong \sum_{ij}^{N} A_i \tau_i (1 - e^{-t/\tau_i}) = u_v^*(t), \qquad (27)$$

where $\cong$ means "approximately equal to in the least squares sense" and where $\{\tau_{ij}\}$ is a set of N relaxation times. In this problem we set

$$\{\tau_{ij}\} = \{0.5\tau_a, \tau_a, 5\tau_a, 10\tau_a, 50\tau_a, 100\tau_a\},$$

where τ_a, the characteristic relaxation time, is defined by $\tau_a = 2\eta/\mu_h$ in which η is the viscosity of the Maxwell fluid and μ_h is the elastic modulus of the half-space. The A_i are then a set of unknown constants to be determined. This approximation method has the advantage of smooth time domain results in the time interval required and involves as few function evaluations as possible. The error obtained using the numerical method is thus minimized. Then $u_v^*(t)$ can be integrated over the source region to obtain the required solution.

Results

Post-diking horizontal deformation is predicted over timescales of 0 to $50\tau_a$. Effects due to the inclusion of gravity and from the variation of the fault parameters μ_h, D, W, and ψ (Figure 1) are studied. Note that the figures (Figures 2 to 4, 6, 8 to 10) illustrating postdiking displacements where gravitational effects are not included show nondimensional horizontal motion perpendicular to the dike plane, i.e., in the y direction, over an area scaled in terms of H. The figures (Figures 5 and 7) which include gravitational effects do not have their horizontal motion and lengths scaled in a similar manner. In the gravitational problem several independent length scales now exist: H, the layer thickness, and k_g^L and k_g^H, the gravitational wave numbers for the layer and half-space. A nondimensionalizing of the kernel functions for the gravitational case results in a ratio of gravitational effects to elasticity effects, e.g., $\rho g H/\mu$ [*Rundle*, 1982].

The case of a vertical dike extending completely through the elastic layer ($W/H = 1$) is shown in Figure 2. The predicted codiking deformation is large close to the source and decreases as the distance from the source increases. The postdiking response behaves in the opposite sense with little deformation predicted in the near-source region and substantial deformation at distances several dike widths from the source. Rebound of the nonelastic region in response to the rapid outward movement from the diking leads to the formation of an inflexion in the displacement field close to the source. The amplitude of the postdiking deformation field is increased as a result of increasing μ_h (compare Figures 2 and 3). This also leads to the formation of a more pronounced peak in the field several dike widths away from the source. In addition, increasing μ_h increases the magnitude of the completion time of the postdiking deformation. Viscosity is directly proportional to rigidity; hence increasing μ_h implies that the viscoelastic region has become less "fluid" and responds more slowly to postdiking stress changes but with a larger magnitude response. Decreasing the downdip width of the dike such that it extends halfway through the elastic layer from the surface produces minimal differences in the codiking deformation field. (compare Figures 3 and 4). However, the postdiking deformation field now has a more pronounced peak related to the thickness of the elastic layer, and it has no inflexion in the near-source region. The presence of this inflexion in the displacement field is a direct consequence of the base of the dike touching the top of the half-space. Decreasing the downdip width of the surface dike by a small fraction removes the presence of the inflexion from the postdiking deformation fields. Hence the case of a dike extending completely through the elastic layer can be distinguished from the case of a surface dike which extends partially through the elastic layer by inspection of the postdiking deformation fields. The inclusion of gravitational effects produces no significant differences in the horizontal deformation field over all time intervals for the dike of downdip width H, but decreasing the downdip width of the dike results in a significant attenuation of the long time interval postdiking deformation fields (compare Figures 4 and 5).

Burying the dike has a profound effect on the predicted postdiking deformation field. The codiking response has a smaller amplitude than that predicted using the surface dike sources, with the maximum displacement occurring at a greater distance from the source. The inflexion seen in the near-source region of the postdiking deformation field (Figure 6) is of a larger amplitude and covers a greater area than that predicted for a surface dike of twice the downdip width. The inclusion of gravitational effects results in an attenuation of the deformation field (compare Figures 6 and 7); however, when compared to the surface diking case these effects become apparent over a much shorter timescale. This difference in time scales is due to the closeness of the dike end to the halfspace. The stresses die off from the fault ends like $1/r$, so for the case of a buried dike extending to the base of the elastic layer the halfspace will experience shorter wavelength stresses and faster stress relaxation than if the dike extended from the surface to the midpoint of the elastic layer [*Rundle*, 1982].

The dominant effect of altering the dip of the dike is the formation of an asymmetrical deformation field in both the codiking and postdiking response (compare Figures 4 and 8 and Figures 6 and 9). Other features are similar to those observed in the corresponding vertical dike cases with the asymmetric features being introduced by the dip of the dike. Increasing the dip of the dike increases the scale of the asymmetrical effect (compare Figures 8 and 10). The inclusion of gravitational effects into these cases results in the same effects as those observed for the vertical dike case. That is, for the surface dike no apparent differences are observed until longer time periods, and for the buried dike these differences occur within shorter timescales.

Regions of uplift and subsidence can be associated with areal strain compression and expansion patterns [*Bilham and King*, 1989]. The horizontal strain field is given by the derivative of the horizontal deformation curves; hence regions of uplift and subsidence can be inferred. A dike extending completely through the elastic layer produces uplift above the dyke, no appreciable motion either side of the dike, i.e., in the flank zones, and uplift further away. No appreciable motion is predicted in the far field. This pattern is repeated for a buried dike extending to the base of the elastic layer, except the flank zones now undergo subsidence. A surface dike extending halfway through the layer produces uplift of the flank zones with subsidence elsewhere and no appreciable motion in the far field.

Summary and Discussion

A previous method is extended in order to calculate the horizontal postdiking surface displacements as a result of a dike emplacement in an elastic layer above a viscoelastic half-space. The effects of gravity can be included in both the layer and the half-space but are found to produce minimal differences in the displacement fields until longer time intervals are considered. In addition, results indicate that it is possible to determine whether a dike extends completely or partially through the elastic layer by an inspection of the postdiking deformation fields.

The boundary conditions contained in the present version of the model, however, do not account for data that are affected by repeated events. The method appropriate to these circumstances is outlined by *Savage and Prescott* [1978], and the application of this will form a particularly valuable tool for interpreting observed geodetic horizontal surface deformation in areas of active tectonic rifting and for forward modeling at mid-ocean ridges. One region in which the model is currently applicable is in northeast Iceland where a major rifting episode commenced in 1975. In the following decade up to 8 m of crustal widening occurred along an 80 km-long-section of the accretionary plate boundary [*Björnsson*, 1985]. Repeated geodetic surveying results in this area using Global Positioning System (GPS) satellite surveying [*Heki et al.*, 1993; *Jahn et al.*, 1994] have revealed a horizontal deformation field that shows a clear postdiking transient signal that may be attributable to viscoelastic asthenospheric relaxation.

Furthermore, this model predicts the presence of a long-wavelength component in the postdiking deformation field following a single event, a result also obtainable by modeling continued diking at depth in an elastic half-space. One possible distinction between these two models lies in the analysis of the distribution of observed deformation with time. Here we demonstrate a nonlinear spatial variation of displacement with time. For a similar distribution of displacements to occur using the continued diking at depth in an elastic half-space hypothesis, a dike continually evolving in depth, downdip width, and length would have to be incorporated into the model. Data sets of a sufficiently high quality, for example, the northeast Iceland GPS data set [*Heki et al.*, 1993; *Jahn et al.*, 1994], are now becoming available, enabling the possibility of distinguishing between these two methods. If a difference can be detected, then this will lead to a better understanding of the physical processes responsible for plate boundary processes.

Acknowledgments The authors wish to thank J. C. Savage, R. S. Stein, S. C. Cohen and A. Donellan for their careful reviews.

References

Ben-Menahem, A., and S. J. Singh, Multipolar elastic fields in a layered half-space, *Bull. Seismol. Soc. Am., 58*, 1519–1572, 1968.

Bilham, R., and G. King, The morphology of strike-slip faults: Examples from the San Andreas fault, California, *J. Geophys. Res., 94*, 10,204–10,216, 1989.

Björnsson, A., Dynamics of rifting in NE Iceland, *J. Geophys. Res., 90*, 10,151–10,162, 1985.

Chinnery, M. A., Deformation of the ground around surface faults, *Bull. Seismol. Soc. Am., 51*, 355–372, 1961.

Cohen, S. C., Postseismic deformation due to subcrustal viscoelastic relaxation following dip-slip earthquakes, *J. Geophys. Res., 89*, 4538–4544, 1984.

Cost, T. L., Approximate Laplace transform inversions in viscoelastic stress analysis, *AIAA J., 2*, 2157–2166, 1964.

Jahn, C.-H., G. Seeber, G. R. Foulger, and P. Einarsson, GPS epoch measurements spanning the mid-Atlantic plate boundary in northern Iceland 1987–1990, in *Gravimetry and Space Techniques Applied to Geodynamics and Ocean Dynamics, Geophys. Monogr. Ser., vol. 82*, edited by B. E. Schutz et al., pp. 109–123, AGU, Washington, D. C., 1994.

Jovannovich, D. B., M. I. Husseini, and M. A. Chinnery, Elastic dislocations in a layered half space, I, Basic theory and numerical methods, *Geophys. J. R. Astron. Soc., 39*, 205–217, 1974.

Heki, K., G. R. Foulger, B. R. Julian and C.-H. Jahn, Plate dynamics near divergent boundaries: Geophysical implications of postrifting crustal deformation in NE Iceland, *J. Geophys. Res., 98*, 14279–14297, 1993.

Lee, E. H., Stress analysis in viscoelastic bodies, *J. Appl. Mech., 13*, 183–190, 1955.

Love, A. E. H., *Some Problems of Geodynamics*, Cambridge University Press, New York, 1911.

Matsu'ura, M., and T. Tanimoto, Quasi-static deformations due to an inclined, rectangular fault in a viscoelastic half-space, *J. Phys. Earth., 28*, 103–118, 1980.

Nur, A., and G. Mavko, Postseismic viscoelastic rebound, *Science, 183*, 204–206, 1974.

Okada, Y., Surface deformation due to shear and tensile faults in a half-space, *Bull. Seismol. Soc. Am., 75*, 1135–1154, 1985.

Roth, F., Deformations in a layered crust due to a system of cracks: Modeling the effect of dike injections or dilatancy, *J. Geophys. Res., 98*, 4543–4551, 1993.

Rundle, J. B., Viscoelastic crustal deformation by finite, quasi-static sources, *J. Geophys. Res., 83*, 5937–5945, 1978.

Rundle, J. B., Static elastic-gravitational deformation of a layered half-space by point couple sources, *J. Geophys. Res., 85*, 5354–5363, 1980.

Rundle, J. B., Vertical displacements from a rectangular fault in layered elastic-gravitational media, *J. Phys. Earth., 29*, 173–186, 1981.

Rundle, J. B., Viscoelastic-gravitational deformation by a rectangular thrust fault in a layered earth, *J. Geophys. Res., 87*, 7787–7796, 1982.

Rundle, J. B., and D. D. Jackson, A three dimensional viscoelastic model of a strike slip fault, *J. Geophys. Res., 49*, 575–592, 1977.

Savage, J. C., and W. H. Prescott, Asthenosphere readjustment and the earthquake cycle, *J. Geophys. Res., 83*, 3369–3376, 1978.

Schapery, R. A., Approximate methods of transform inversion for viscoelastic stress analysis, *Proc. U.S. Natl. Congr. Appl. Mech., 4th*, 1075–1085, 1961.

Singh, S. J., Static deformation of a multilayered half-space by internal sources, *J. Geophys. Res., 75*, 3257–3263, 1970.

Spence, D. A., and D. L. Turcotte, Viscoelastic relaxation of cyclic displacements on the San Andreas fault, *Proc. R. Soc. London A, 365*, 121–144, 1979.

Thatcher, W., and J. B. Rundle, A model for the earthquake cycle in underthrust zones, *J. Geophys. Res., 84*, 5540–5556, 1979.

Thatcher, W., T. Matsuda, T. Kato, and J. B. Rundle, Lithospheric loading by the Riku-U earthquake, northern Japan: Implications for plate flexure and asthenospheric rheology, *J. Geophys. Res., 85*, 6429–6435, 1980.

This preprint was prepared with the AGU LaTeX macros v3.1. File jgr'pp formatted 1995 February 1.

Figure 1. Geometry and coordinate system for a rectangular, dipping dike in an elastic-gravitational layer over a viscoelastic-gravitational half-space. H is the thickness of the layer, D is the depth of the dike, $2L$ is the along strike length, W is the downdip width, and ψ is the dip.

Figure 2. Nondimensional surface horizontal deformation against distance normal to a dike extending completely through the elastic layer. Model parameters are $H = 30$ km, $2L = 20H/3$, $\rho_l = \rho_h = 3.0$ g/cm^3, $\mu_l = \lambda_l = \lambda_h = 3\text{x}10^{10}$ Pa, $\mu_h = 3\text{x}10^9$ Pa, $D/H = 0$, $W/H = 1$, and $\psi = 90°$. The codiking response is calculated using the formulae of *Okada* [1985] for a dike in an elastic half-space where $\mu = \lambda = 3\text{x}10^{10}$ Pa. The shaded area represents the elastic-gravitational layer, the horizontal dashed line is the layer half-space boundary, and the heavy solid line shows the dike geometry. The solid curve is the initial elastic (codiking) response, and the dashed curves represent the deformation due to viscoelastic stress relaxation after $2\tau_a$, $5\tau_a$, and $50\tau_a$. Each displacement profile has been evaluated at the midpoint of the fault plane.

Figure 3. Same as Figure 2 except $\mu_h = 3\text{x}10^{10}$ Pa.

Figure 4. Same as Figure 2 except $D/H = 0$, $W/H = 0.5$, and $\mu_h = 3\text{x}10^{10}$ Pa.

Figure 5. Same as Figure 4 except gravitational effects are included in the model. Surface deformation is now in centimeters per meter of opening.

Figure 6. Same as Figure 2 except $D/H = 0.5$, $W/H = 0.5$, and $\mu_h = 3\text{x}10^{10}$ Pa.

Figure 7. Same as Figure 6 except gravitational effects are included in the model. Surface deformation is now in centimeters per meter of opening.

Figure 8. Same as Figure 2 except $\psi = 60°$, $D/H = 0$, $W/H = 0.5$, and $\mu_h = 3\text{x}10^{10}$ Pa.

Figure 9. Same as Figure 2 except $\psi = 60°$, $D/H = 0.5$, $W/H = 0.5$, and $\mu_h = 3\text{x}10^{10}$ Pa.

Figure 10. Same as Figure 2 except $\psi = 30°$, $D/H = 0$, $W/H = 0.5$, and $\mu_h = 3\text{x}10^{10}$ Pa.

Figure 1

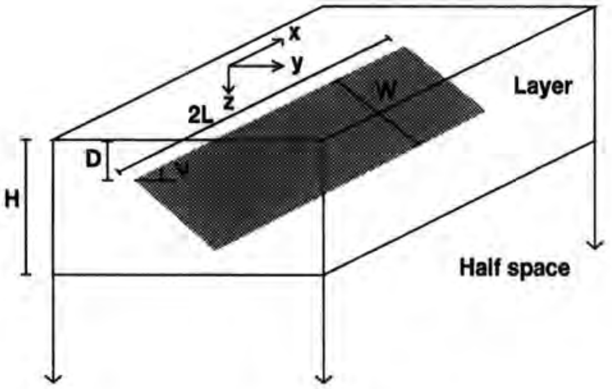

Figure 2

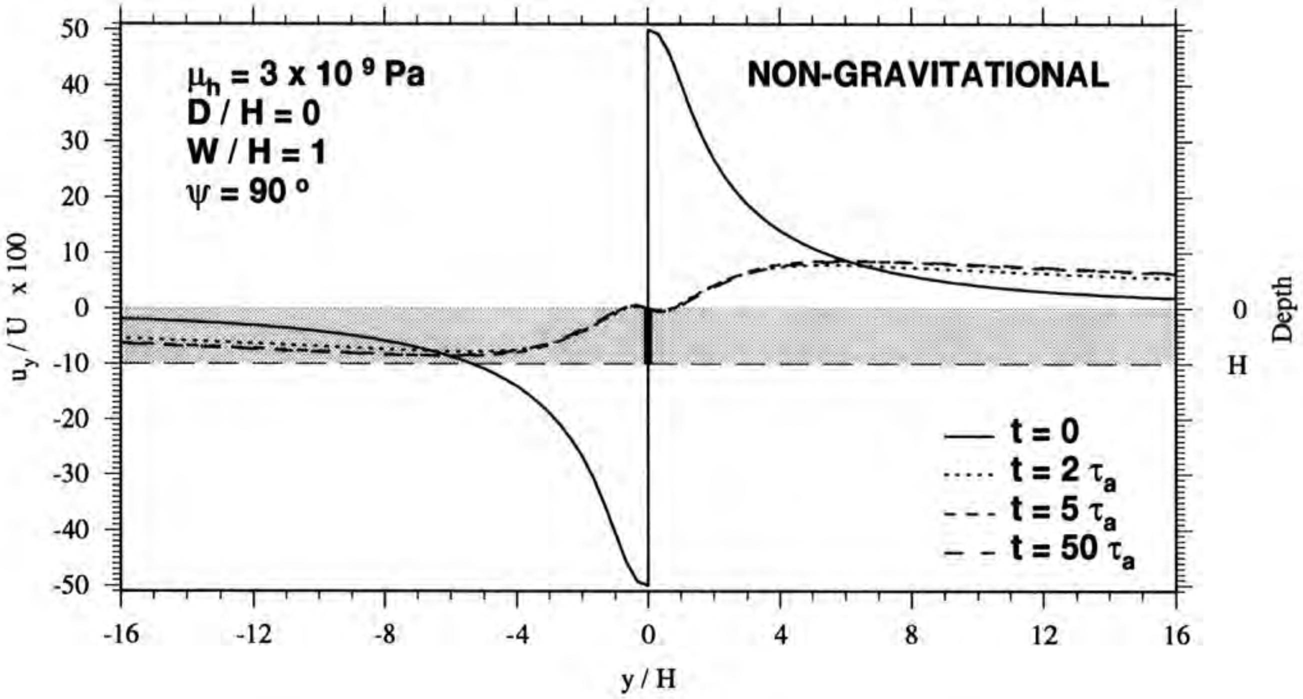

Figure 3

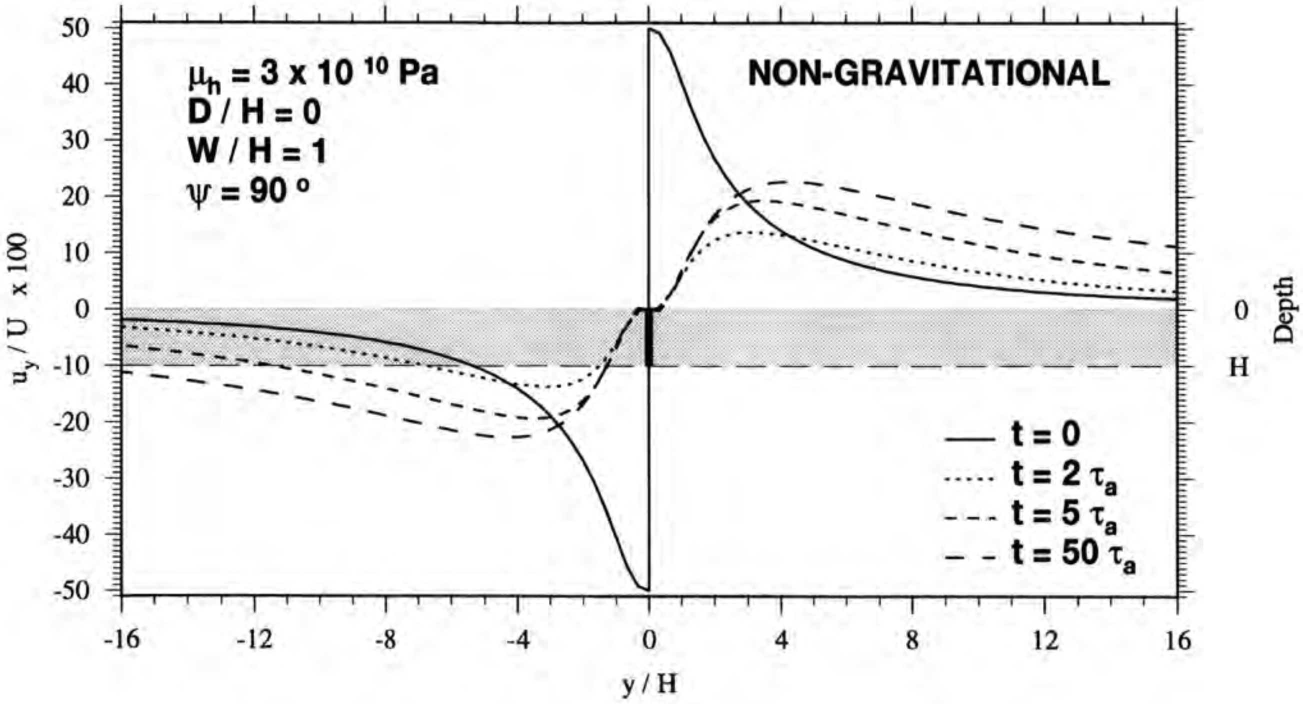

Figure 4

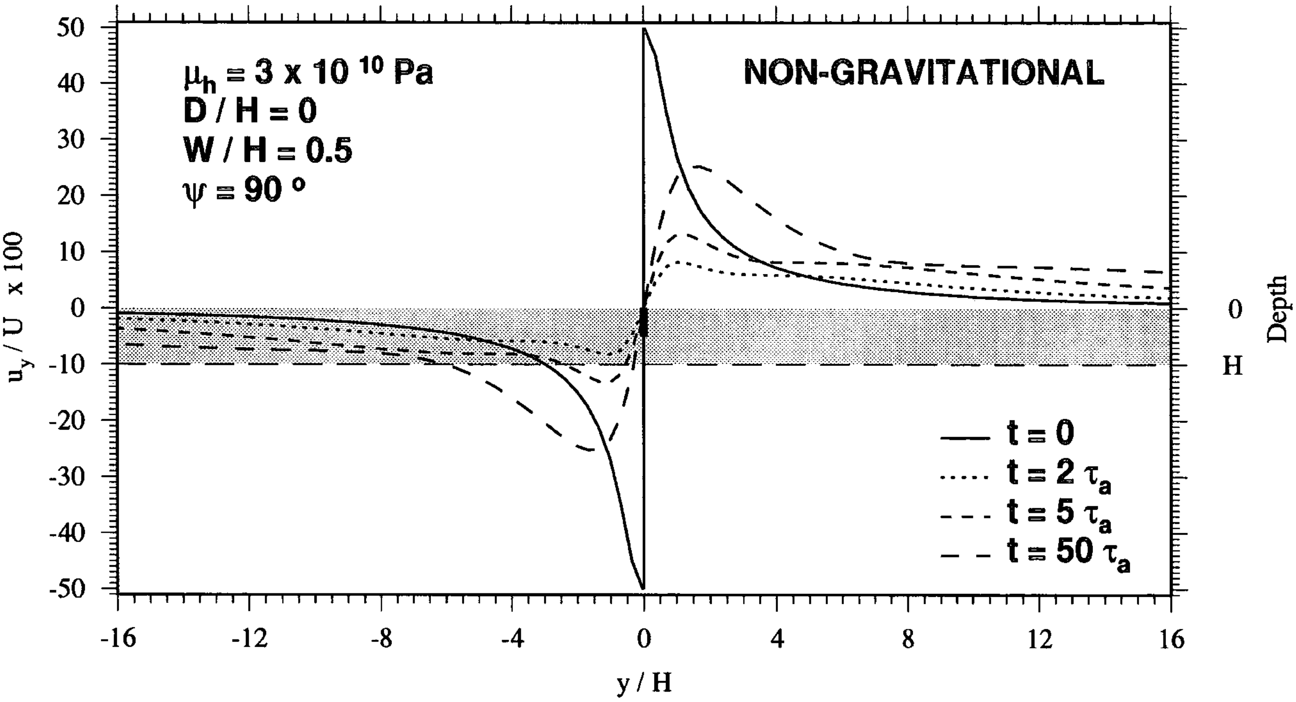

Figure 5

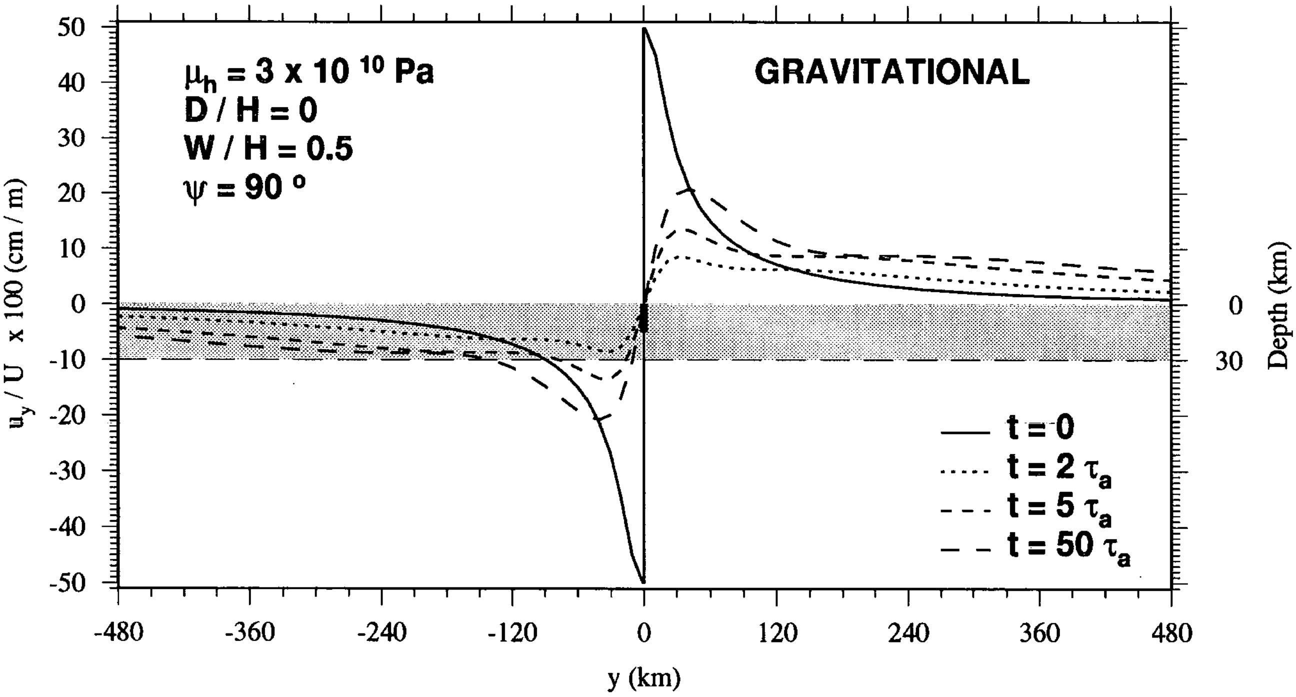

Figure 6

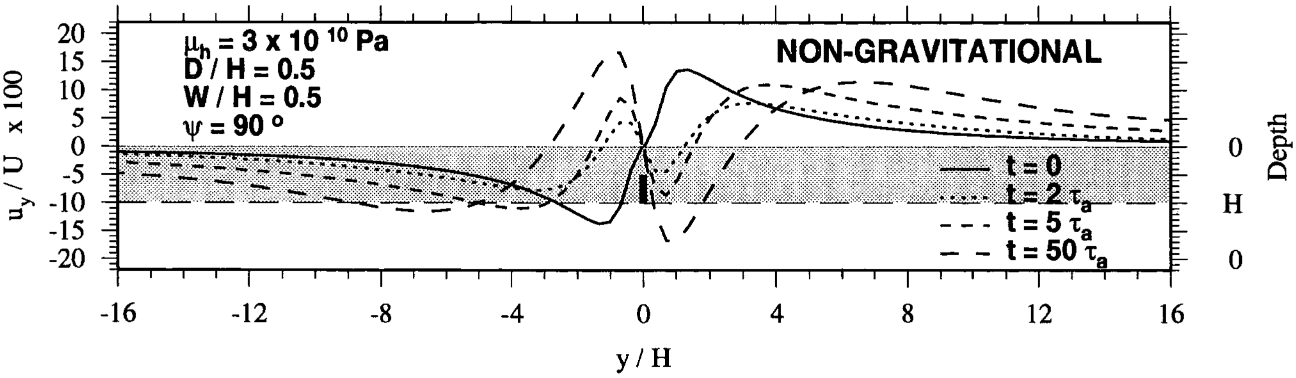

Figure 7

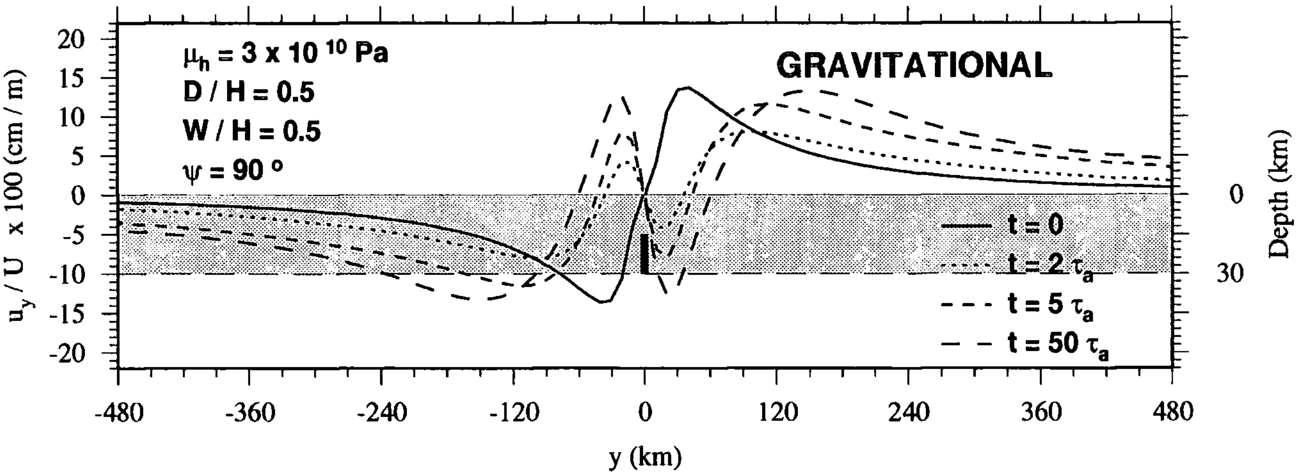

Figure 8

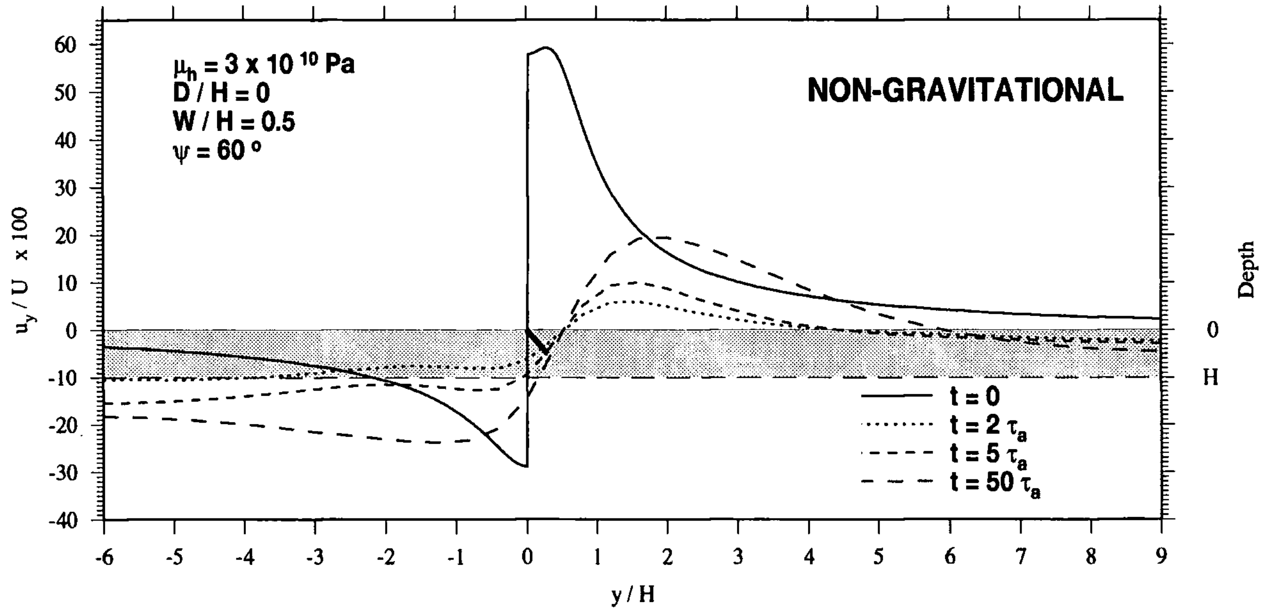

Figure 9

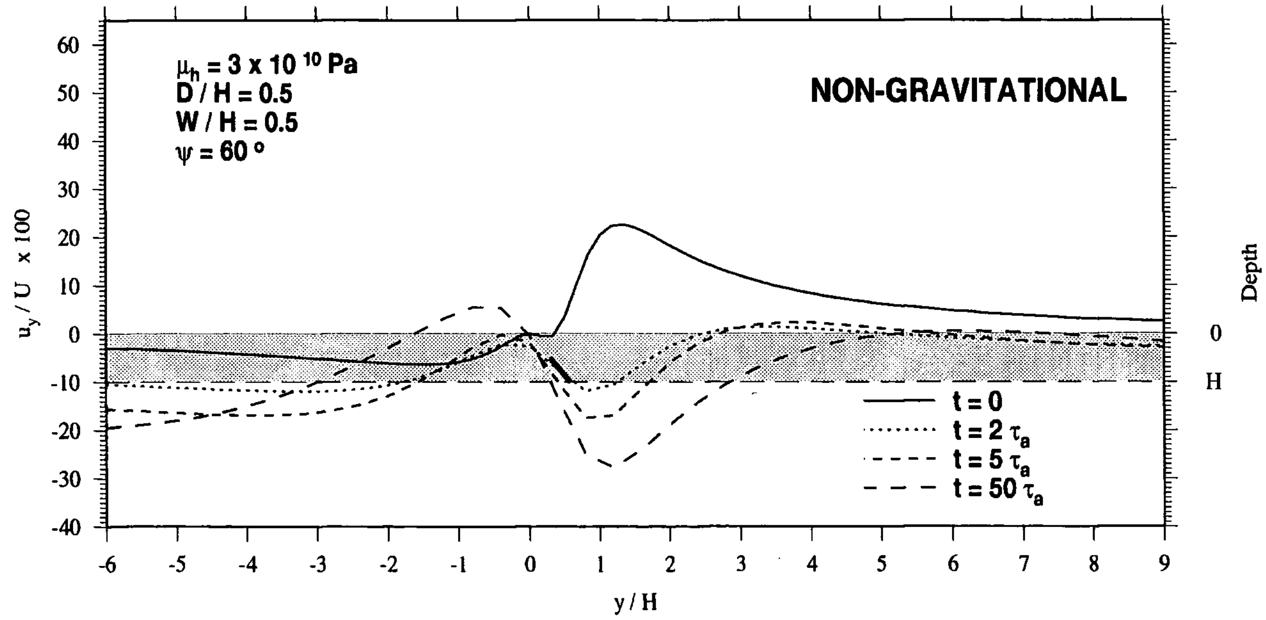

Figure 10

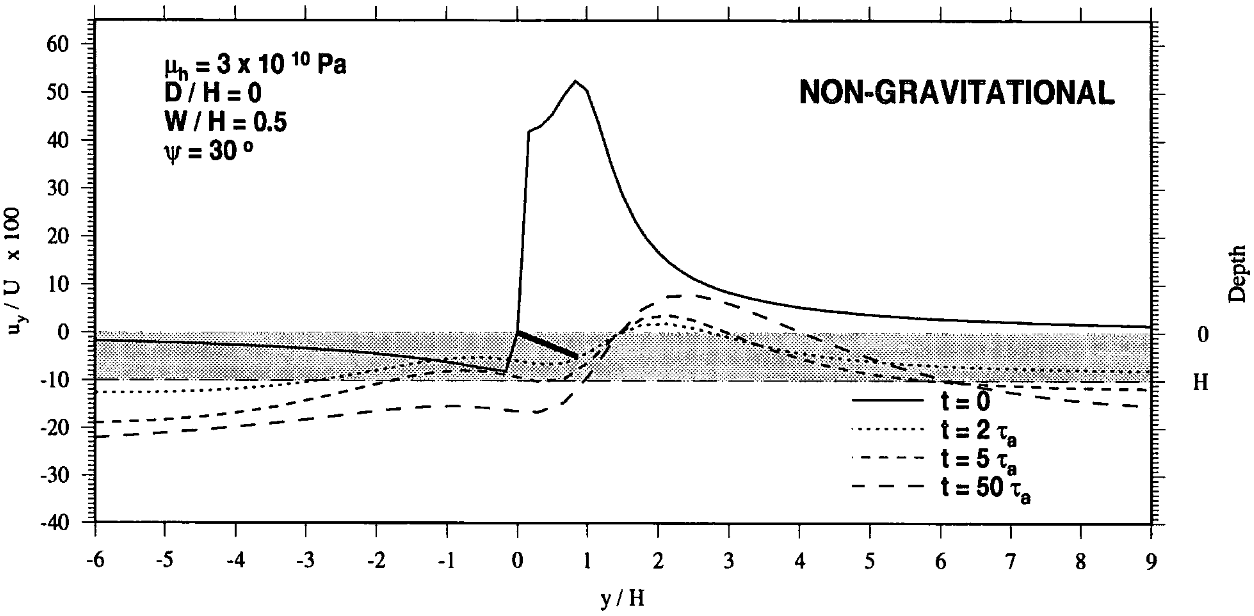
μ_h = 3 x 10 ^{10} Pa
D / H = 0
W / H = 0.5
ψ = 30 °
NON-GRAVITATIONAL
u_y / U x 100
60
50
40
30
20
10
0
-10
-20
-30
-40
Depth
0
H
t = 0
t = 2 τ_a
t = 5 τ_a
t = 50 τ_a
-6
-5
-4
-3
-2
-1
0
1
2
3
4
5
6
7
8
9
y / H

Proceedings of the CRCM '93, Kobe, December 6-11, 1993, pp.99-105

Regional Post-diking Deformation in Northeast Iceland: A Third Epoch of GPS Measurements in 1992

G. R. FOULGER*, M. A. HOFTON
Dept. of Geological Sciences, University of Durham, South Rd., Durham, DH1 3LE, UK

B. R. JULIAN
U. S. Geological Survey, MS 977, 345 Middlefield Rd., Menlo Park, CA 94025, USA

C.-H. JAHN
Institut für Erdmessung, Universität Hannover, Nienburger Str. 6, D-3000 Hannover 1, Germany

and Kosuke HEKI
Kashima Space Res. Cent., Comm. Res. Lab., 893-1 Hirai, Kashima, Ibaraki 314, Japan

Abstract

A massive dike-intrusion episode between 1975 and 1980 in the Krafla volcanic system in northeastern Iceland has been followed by years of regional deformation that were first detected by comparing the results of GPS surveys made in 1987 and 1990 (Foulger *et al.*, 1992; Heki *et al.*, 1993; Jahn, 1992). Data from a third survey in 1992 show that the region continues to expand, although at a reduced rate. Comparing the 1987 and 1992 results greatly improves the accuracy with which the deformation field is determined. The field is roughly symmetrical about the plate boundary, with velocities that increase with distance from the plate boundary, but are fairly constant at large distances. Velocities of several times the time-averaged plate rate persist at least to distances of 120 km from the plate boundary. Candidate geophysical models include regional stress relaxation and continued, deep, aseismic dike intrusion. The deformation field cannot discriminate between these two physical models, which both fit the data well for suitable parameter values. Structural information suggests, however, that the surface brittle layer is thin in Iceland and that the model of stress relaxation in a viscoelastic Earth is more plausible.

1. Introduction

The regional-scale anelastic deformation that follows major tectonic episodes such as great earthquakes is the main source of information on the rheology of the Earth on decade time scales. Such deformation is, however, relatively small, and distributed over laterally extensive regions. Because of the rarity of great earthquakes in areas previously accurately surveyed, and because terrestrial surveying techniques, which have been used exclusively up until quite recently, cannot easily detect small strains distributed over large regions, good geodetic measurements of this phenomenon are rare.

We describe GPS measurements of the regional deformation that occurred around the spreading plate boundary in northeastern Iceland in the interval from 8 to 13 years after a major dike-intrusion episode along the plate boundary resulted in several meters of surface extension. This is one of the best-constrained observations of post-tectonic regional deformation so far reported.

2. Iceland and the tectonics of Northeast Iceland

Excessive volcanism at a ridge-centered hotspot in the north Atlantic has constructed a thick pile of basaltic material that projects above sea-level to form the 100,000 km^2 island of Iceland. More than 600 km of spreading plate boundary occur on land in Iceland, the largest subaerial exposure of this kind of plate boundary in the world. In northeastern Iceland the neovolcanic zone (where post-glacial lavas occur) is 40 km wide and contains 5 *en-echelon* spreading segments (Figure 1). Each consists of a 50 to 100 km wide swarm of normal faults, open and eruptive fissures, a central volcano, and a high-temperature geothermal area.

Spreading along the plate boundary occurs as occasional, intense tectonic episodes in the spreading segments. During these episodes, volcanism, seismicity and intrusion of dikes of the order of meters thick occur along the fissure swarms. It is thought that each spreading segment in northeast Iceland becomes active at intervals of a few centuries and that generally only one segment is active at a time. A number of such episodes are documented historically (*e.g.* Björnsson et al., 1979) and a well-monitored episode in the Krafla segment (Figure 1), began in 1975. In December of that year, a magma chamber beneath the Krafla central volcano deflated and magma was intruded along the fissure swarm forming a dike about 60 km long and causing up to 2 m of surface crustal widening. Magma chamber inflation continued at a high rate for the next 10 years. Deflations accompanied by dike injections occurred every few months, totaling about 9 dikes in the first 4 years, after which time magma escaping from the magma chamber was erupted onto the surface from fissures. Up to 8 m of crustal widening occurred in total along the Krafla fissure swarm (Björnsson, 1985).

---

*Fax: +44-91-374-2510, Email: G. R. Foulger@durham. ac. uk

Erdmessung, Univ. Hannover, Germany, and Dept. Geological Sciences, Univ. Durham, U. K. Seven Ashtech dual-frequency P-code receivers were used and observations were made at intervals of 30 s over a single daytime window of about 5 hours, to minimise noise from ionospheric turbulence. About 18 satellites were recorded during these sessions. Anti-spoofing was in effect on weekends and no observations were made at those times.

6. Processing of the 1992 data

As with 1987 and 1990 surveys, the data were processed both at Univ. Hannover using GEONAP software, and at Univ. Durham using the Bernese v. 3 software and the cycle-slip editor TurboEdit (Blewitt, 1990). The results of processing using the Bernese software are briefly described below.

Ionospheric disturbances were much less severe in 1992 than in 1990, and high-quality results similar to those from 1987 were obtained. L1 and L2 ambiguities were determined reliably for 91% of the data. A standard Saastamoinen tropospheric model and a satellite elevation cut-off angle of 15° were used, in keeping with previous experience of processing GPS data from Iceland. Broadcast orbits were used to calculate 1-day standard orbital arcs, and these were used throughout the processing. The calculated point coordinates were combined in a network adjustment to produce a final set of coordinates and corresponding covariance matrix (Heki, 1992). Point coordinate repeatability (WRMS) for the whole network was 1.4 cm. The results from the Bernese software agree well with those calculated using GEONAP at Univ. Hannover.

7. Results of the 1992 survey

Comparing the results of the 1990 and 1992 surveys indicates deformation exceeding the 1-σ uncertainty level for the most of the points in the central part of the network (Figure 3). This deformation is similar in style to that for the period 1987—1990, *i. e.* an east-west expansion, but is smaller in magnitude (up to a maximum of about 8 cm compared with 18 cm for 1987 — 1990). A maximum expansion rate of about 6 cm a^{-1}, significant at the 3-σ level, was therefore detected for the period 1987 — 1990, but this decreased to 4 cm a^{-1} during the period 1990 — 1992. The best-defined deformation field is obtained by comparing the 1987 and 1992 results, which not only provide the largest deformation signal but also give the smallest uncertainties, because ionospheric disturbances were weaker during these two surveys than in 1990 (Figures 2 and 3). A clearly significant east-west expansion of the network is detected with a considerably improved signal-to-noise ratio over the 1987 — 1990 results, and a better defined deformation field shape. The maximum spreading rate for the period 1987 — 1992 was about 4.5 cm a^{-1}. The vertical displacement field shows considerable scatter, but uplift of the central part of the network is significant at the 2-σ level.

The new 1992 survey results show that the crustal extension rate decreased with time between 1987 and 1992. The improved definition of the deformation field shows that the relative velocities of points remain significant throughout our network, which is approximately 250 km wide from east to west. In addition, although the deformation field is fairly symmetrical about the Krafla spreading segment, thought to be the center of expansion, the rate of motion is variable, with low velocities close to the spreading segment and higher velocities farther away.

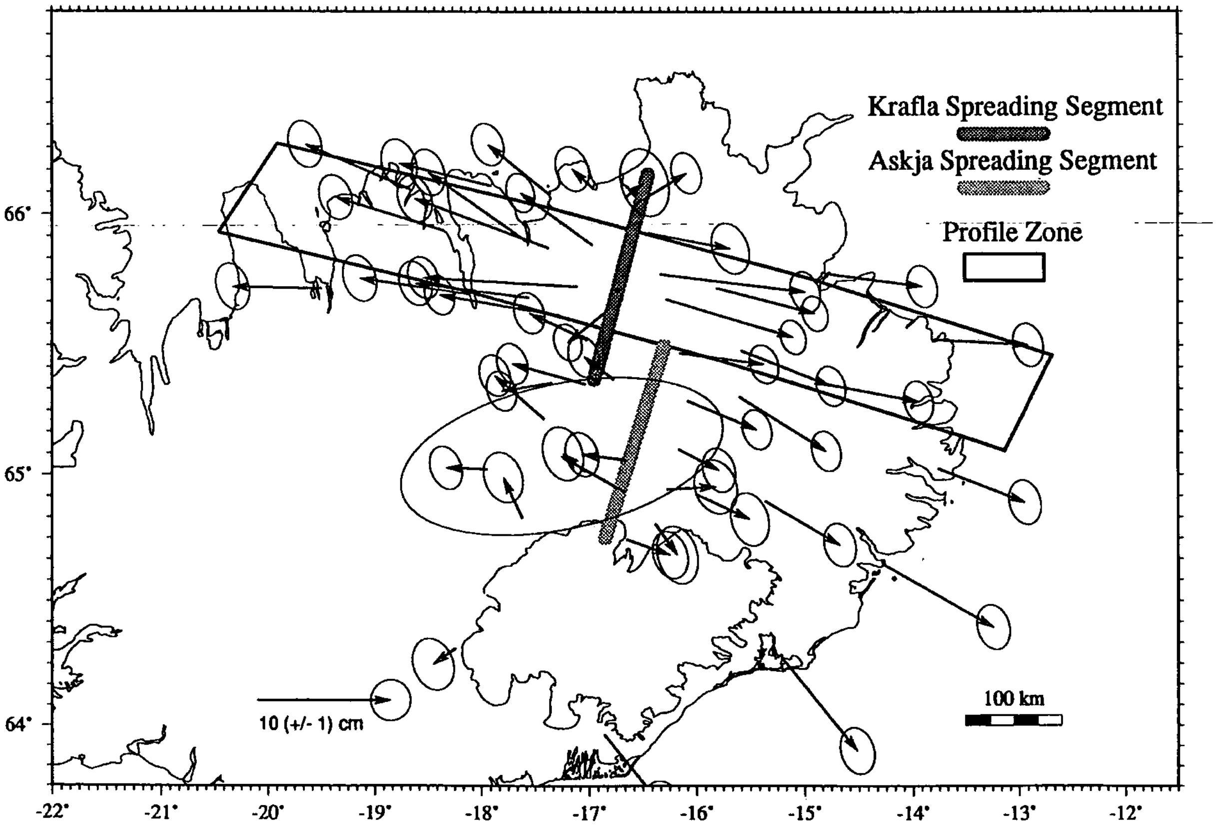

Fig. 2. Map of northeast Iceland showing point displacements for the period 1987—1992. Ellipses at each arrowhead indicate 1-σ errors. Arrow at lower left gives scale. The zone of points used to construct the profiles shown in Figure 3 is enclosed by a box.

In the two-dimensional analysis the finite length of the dike and the additional effect of minor magma chamber inflation were also taken into account assuming that the chamber could be approximated to a point source of inflation (Mogi, 1958).

This model explains the 1987—1990 observations to first order, but several unrealistic simplifying assumptions are inherent in it. For example, Newtonian behaviour of the viscous layer would not allow any immediate response at the time of dike intrusion, which is known to have occurred, and would result in unrealistically large motions at later times (Savage and Prescott, 1978). The assumption of an infinite length for the dike, used for the 1-dimensional model, would result in overestimation of the far-field motion, but ignoring earlier events would tend to underestimate the true motion at distance. Inflation of the Krafla magma chamber would tend to increase the amplitude of movements close to the dike. The improved definition of the deformation field provided by the 1992 results clearly shows that this simple model cannot account for second-order features in the data, in particular the shapes of the velocity fields on each flank (Figure. 4). Including older dike-intrusion episodes can improve the fit, but requires unrealistically large dike widths (over 10m) for the older episodes. We conclude that a more realistic geophysical model is necessary to adequately model our improved data.

8. 2. Stress relaxation in an elastic/ viscoelastic earth model

To remedy the defects in the simple elastic/viscous model described above, we consider a geometrically and rheologically more realistic model, consisting of an elastic layer overlying a Maxwellian viscoelastic half space, including the effects of gravity. We use the method of Rundle (1980), which applies the correspondence principal (*e. g.* Cathles, 1975) to the problem of a layered elastic half space, in effect allowing the elastic moduli to be complex. We extend the method to tensile (dike-opening) sources.

It is again assumed that a dike is instantaneously intruded into the elastic layer. Both the elastic layer and the underlying viscoelastic half space react elastically initially, after which time stress in the half space is released slowly by viscous creep. Deformation occurs within and at the surface of the elastic layer as a result of traction at the interface between the two materials. This work is currently at the investigative stage, but initial results show that this model can fit the observed deformation better than stress relaxation in an elastic/viscous structure. In particular, predicted velocities at distances a few tens of kilometers away from the dike fall off much more slowly with distance than for the simple elastic/viscous model.

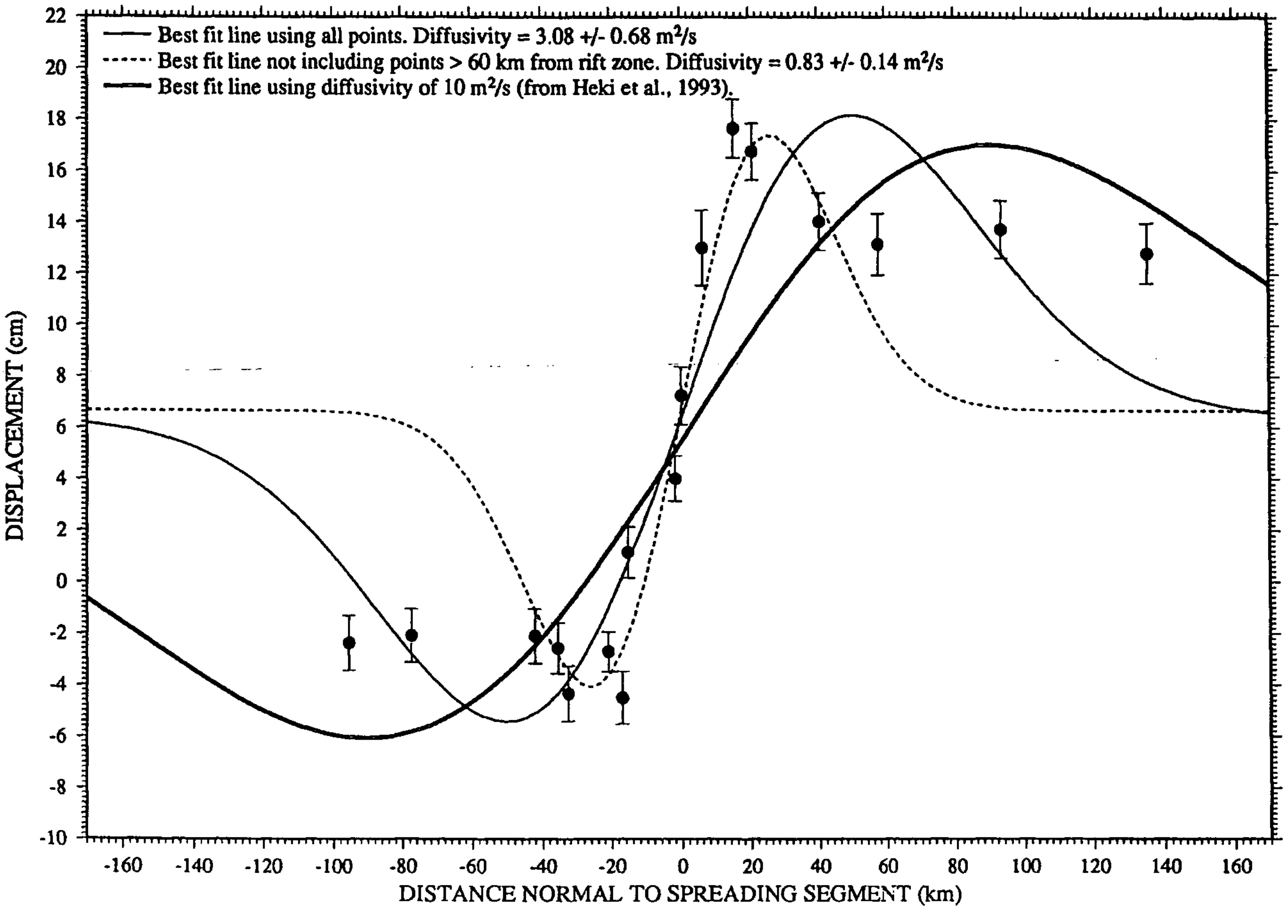

Fig. 4. Horizontal displacements observed between 1987 and 1992, as a function of distance from the plate boundary, compared with theoretical curves for three models of stress diffusion in a thin elastic layer overlying a thin viscous layer. The one-dimensional formulation was used to compute these curves, which incorporates the simplifying assumptions of an infinite dike length, zero "background" movements and no other sources of deformation.

Geothermal gradients predict that temperatures exceed 1,000℃ at these depths. Such material must necessarily behave viscoelastically. In the presence of such evidence, and because it is intrinsically the simpler physical model, we favor the model of stress relaxation in a viscoelastic model over that of continued dike intrusion at depth in an elastic half-space.

Acknowledgments

We thank the many field workers who conducted the surveying work. The contribution of Univ. Durham was funded by NERC grant GR9/834. The contribution of the Univ. Hannover was financed by grants from DFG. We have learnt from thought-provoking exchanges with Jim Savage.

References

Beblo, M. and A. Björnsson (1980): A model of electrical resistivity beneath northeast Iceland, correlation with temperature, J. Geophys., **47**, 184—190.

Björnsson, A. (1985): Dynamics of crustal rifting in NE Iceland, J. Geophys. Res., **90**, 10151—10162.

Björnsson, A., G. Johnsen, S. Sigurdsson and G. Thorbergsson (1979): Rifting of the plate boundary in north Iceland 1975—1978, J. Geophys. Res., **84**, 3029—3038.

Blewitt, G. (1990): An automatic editing algorithm for GPS data, Geophys. Res. Lett., **17**, 199—202.

Cathles, L.M. (1975): The Viscosity of the Earth's Mantle, Princeton University Press, 386p.

Foulger, G.R., C-H Jahn, G. Seeber, P. Einarsson, B.R. Julian and K. Heki (1992): Post-rifting stress relaxation at the accretionary plate boundary in Iceland, measured using the Global Positioning System, Nature, **358**, 488—490.

Foulger, G., G. Beutler, R. Bilham, P. Einarsson, S. Fankhauser, W. Gurtner, U. Hugentobler, W. J. Morgan, M. Rothacher, G. Thorbergsson, and U. Wild (1993): The Iceland 1986 GPS geodetic survey: tectonic goals and data processing results, Bull. Geod., **67**, 148—172.

Heki, K. (1992): A network adjustment program for the Bernese Global Positioning System data analysis software, J. Geod. Soc. Japan, **38**, 309—312.

Heki, K,. G.R. Foulger, B. R. Julian and C.-H. Jahn (1993): Plate dynamics near divergent boundaries: geophysical implications of postrifting crustal deformation in NE Iceland, J. Geophys. Res., **98**, 14279—14297.

Jahn, C.-H. (1992): Recent crustal movements in the neovolcanic zone of Iceland between 1987 and 1990 using GPS, Proceedings of the 6th International FIG-Symposium on Deformation Measurement, Hannover, Germany.

Jahn, C-H., G. Seeber, G.R. Foulger, and P. Einarsson: GPS epoch measurements spanning the Mid-Atlantic plate boundary in northern Iceland 1987—1990, J. Geophys. Res. (in press)

Mogi, K. (1958): Relations between the eruptions of various volcanoes and the deformation of the ground surfaces around them, Bull. Earthq. Res. Inst., **36**, 99—134.

Möller, D. and B. Ritter (1980): Geodetic measurements and horizontal crustal movements in the rift zone of NE-Iceland, J. Geophys., **47**, 110—119.

Niemczyk, O. (1943): Spalten auf Island, Wittwer, Stuttgart.

Okada, Y. (1992): Internal deformation due to shear and tensile faults in a half space, Bull. Seismol. Soc. Am., **82**, 1018—1040.

Rundle, J. B. (1980): Static elastic-gravitational deformation of a layered half space by point couple sources, J. Geophys. Res., **85**, 5355—5363.

Savage, J. C. (1990): Equivalent strike-slip earthquake cycles in half-space and lithosphere-asthenosphere Earth models., J. Geophys. Res., **95**, 4873—4879.

Savage, J. C. and W. H. Prescott (1978): Asthenosphere readjustment and the earthquake cycle, J. Geophys. Res., **83**, 3369—3376.

Sigmundsson, F. (1991): Post-glacial rebound and asthenosphere viscosity in Iceland, Geophys. Res. Lett., **18**, 1131—1134.

Torge, W., T. Grote, R. Roeder, M. Schnuell and H.-G. Wenzel (1992): Introduction of absolute gravimetic techniques into a high-precision gravity and vertical control system in northern Iceland, Deutsch Geodetic Kommission, Reihe B, No. 297.

Wanninger, L. and C.-H. Jahn (1993): Effects of severe ionospheric conditions on GPS data processing, Proceedings of the IAG Symposium 109, Permanent Satellite Tracking Networks for Geodesy and Geodynamics, Springer Verlag, Berlin, 140—151.